Molecular Imaging Agent Design for Quantifying Beta Cell Mass in Type 1 Diabetes

by

Liang Zhang

A dissertation submitted in partial fulfillment
of the requirements for the degree of
Doctor of Philosophy
(Chemical Engineering)
in the University of Michigan
2017

Doctoral Committee:

Professor Mark A. Burns, Co-Chair
Assistant Professor Greg M. Thurber, Co-Chair
Professor Lola Eniola-Adefeso
Professor Jennifer J. Linderman
Professor Thomas D. Wang

Liang Zhang

liangzha@umich.edu

ORCID ID: 0000-0001-5766-2302

Dedication

This dissertation is dedicated to

Tao

Mom and Dad

Meme

Acknowledgments

I would like to thank my advisors, Professors Greg Thurber and Mark Burns for their guidance, support, patience, encouragement, and wisdom throughout my doctoral studies. I would also like to express my gratitude to my committee members, Jennifer, Lola, and Thomas for their support.

I am fortunate to have met many talented and fun individuals throughout my PhD. Some of these amazing people include Ray Seo, Wenjun Huang, Kyle Huston, Eric Holt, Molly Kozminsky, Jeff Lowe and Lynn Secondo; I am grateful for our fun times. I cannot thank these individuals enough for their support and friendship.

I must emphasize how lucky I am to have two wonderful lab groups. I want to thank Burns Lab members Brian Johnson, Eric Livak-Dahl, Jaesung Lee, Steven Wang, Lavinia Li, Wenchi Lin, Zach Pritchard, Martin de Beer, Ioana Ciuta, Sarah Mena, and Alyse Krausz for their support. I especially want to thank Brian, Eric, Jaesung, Steven, Lavinia, and Wenchi for their help during my first two years in the program when I knew so little about research (I know slightly more now!). Instrumental to my fantastic PhD experience also includes Thurber Lab members Sumit Bhatnagar, Cornelius Cilliers, Kirti Dhingra, Tejas Navaratna, Lydia Atangcho, Bruna Menezes, Eshita Khera, and Ian Nessler. I want to express my gratitude to Sumit and Cornelius for their support, encouragement, and advice during my preliminary examination. I especially want to thank Sumit for his invaluable help in building the lab during the early years as well as support and advice on multiple projects.

I am very lucky to have multiple outstanding undergraduate students, Matt Riley, Aaron Priluck, Jianshan Liao, Nadia Auchus, and Zhongyuan Zhang work with me on research projects. They were a major driving force for the lab's productivity during our lab's start-up.

I'd like to acknowledge the funding that supported my graduate studies. This includes the National Institute of Health and the National Science Foundation. I would also like to express my sincerest thanks to the Janicek family; John Janicek's generous legacy gift provided significant funding for my doctoral studies.

Lastly, I want to thank my family. I want to thank my mom and dad for supporting me throughout my life; we now have a third doctor in the family. Tao, thank you for being by my side. I love you all dearly.

Table of Contents

List of Figures

List of Tables

List of Schemes

Abstract

Type 1 diabetes affects over one million Americans and an additional 40,000 new cases are diagnosed each year. The disease is characterized by the destruction of insulin-secreting beta cells in the pancreas by the immune system. Consequently, patients with type 1 diabetes rely on exogenous insulin for life. Due to the small volume of beta cells in healthy pancreas, it is extremely challenging to monitor disease progression (particularly at early stages when adequate control of blood sugar levels is still maintained) and assess treatment efficacy in patients with type 1 diabetes. Therefore, an accurate method to monitor and quantify the beta cell mass (BCM) through imaging has been an important goal of the diabetes community.

This thesis describes the unique anatomy and physiology of the beta cells within the Islets of Langerhans and calculates the optimal physicochemical properties needed for a BCM molecular imaging probe. The molecular weight of exendin probes are near ideal for targeting the endocrine pancreas, and this molecule was analyzed in more detail. Receptor trafficking properties and plasma clearance play a major role in determining beta cell targeting versus background signal and were measured for a series of probes. Due to rapid downregulation of the receptor, slow plasma clearance does not allow for continual beta cell uptake and increases background, so more rapid clearance results in higher target to background signal . Additionally, the receptor expression of GLP1-R was measured for the first time and provided evidence for low exocrine expression of GLP1-R in addition to the high endocrine expression. Because this could explain poor clinical contrast of exendin probes, exocrine expression was investigated in

more detail. Using a transgenic mouse model, a very low expression of GLP1-R was confirmed on exocrine cells. Although absolute expression is very low (850 receptors per cell on exocrine cells versus 53,000 receptors per cell on beta cells), the much higher prevalence of exocrine cells (99%) relative to beta cells (1%) results in a significant total signal from the exocrine pancreas. Preliminary results show it is possible to preferentially block exocrine uptake to provide more specific beta cell signal. Multiple doses were administered to first saturate the exocrine with non-detectable peptide followed by a imaging agent dose to label the beta cells. The dosing strategy completely blocked exocrine GLP-1R in healthy animal models. Because peptides often have poor stability and lower affinity due to the lack of secondary structure, exendin was used as a model system to study the impact of helix stabilization on improving peptide physicochemical properties. Using a unique cross-linker with exendin and GLP1 peptides, the helicity, protease stability, and affinity could be improved. The increase protease stability of the cross-linked peptides and use of exendin as a therapeutic led us to test the subcutaneous bioavailability. Near-100% bioavailability was achieved through peptide stabilization, and the bioavailability of a slow-clearing version was also improved. The linker lipophilicity could be controlled to modulate the absorption and clearance rates of the fluorescent peptide. Overall, this thesis provides a theoretical analysis of imaging BCM, novel tools to manipulate peptide image probe properties, and experimental evidence of methods to improve the design of molecular imaging agents for beta cell mass.

Chapter 1

Introduction

1.1 Publication Information

Zhang, L., and G.M. Thurber. *Imaging in Diabetes* in Imaging and Metabolism. Springer.

Modifications have been made to the book chapter to adapt the content to this text.

1.2 Background

Diabetes refers to a group of metabolic disorders where insulin insensitivity and/or a lack of insulin production results in elevated blood glucose levels. These broadly include type 1 diabetes (previously known as "juvenile onset" diabetes, T1DM), type 2 diabetes (previously "adult onset"), and additional less prevalent variants (e.g. monogenic diabetes). Unregulated blood glucose levels have a negative impact on multiple organ systems and consequently pose a risk for stroke, heart disease, kidney failure, blindness, high blood pressure, and other chronic conditions that impair the quality of life. Currently, there are over 400 million cases of diabetes worldwide and the rate continues to rise[1]. Patients with diabetes must rely on medications and lifestyle changes to maintain glucose homeostasis. Aside from the morbidity, the financial burden of the disease constitutes approximately 10% of all health care costs in developed countries[2]. No cure currently exists and present strategies to prevent disease complications place a significant strain on healthcare systems. Therefore, it is important to understand the disease pathophysiology for the medical community and patients. The ability to image and follow disease progression would play a crucial role in understanding disease etiology and allow accurate monitoring during clinical trials for potential clinical translation of treatments.

Ultimately, improved treatments, transplants, and understanding of basic and clinical pathophysiology of the disease may lead to a permanent cure.

Physiology of the pancreas/islets

Despite the multi-organ involvement of the disease, the pancreas is a critical organ due to its central role in regulating blood sugar levels and metabolism. Located behind the stomach in humans, the pancreas is part of both the endocrine and digestive systems. Macroscopically, it consists of three regions – the head, body, and tail (Figure 1.1A). Distinct tissues within the organ carry out the functions for each organ system. The exocrine pancreas primarily serves the digestive system and forms ~99% of the organ mass[2]. It is formed by acini, with each acinus consisting of secretory epithelial cells. The lumen at the center of each layer mediates the drainage of cellular secretions into a series of connected ducts. The ducts join to form the pancreatic duct, which empties into the duodenum. These secretions aid in digestion and include enzymes such as trypsin, chymotrypsin, elastase, ribonuclease, amylase, lipase, and others. The endocrine pancreas forms approximately 1% of the pancreas mass and carries out several functions through multiple distinct cell types. These functions include the secretion of insulin, glucagon, somatostatin, peptide YY, neuropeptide Y and pancreatic polypeptide (PP) directly into the blood for tight glucose regulation (endocrine function). Although the pancreas is mostly exocrine tissue by mass, the organ's role in diabetes research is closely associated with the functionality of endocrine pancreas.

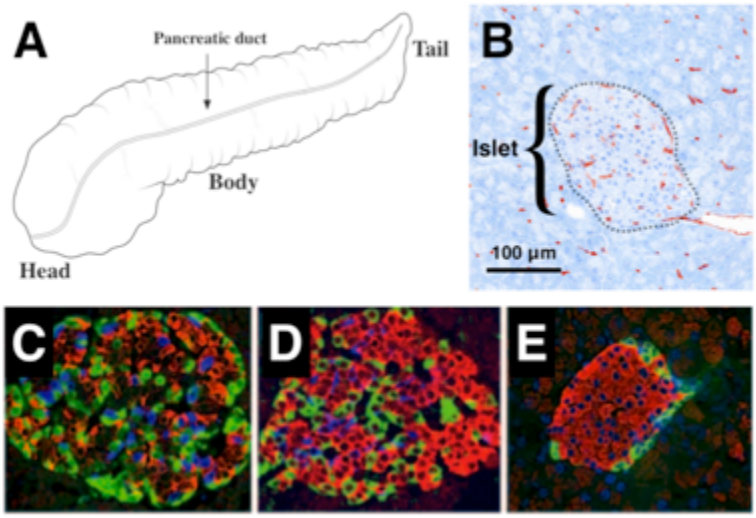

Figure 1.1 Structure of the pancreas.
A. Schematic of the pancreas with head, body, and tail portions labeled. The pancreatic duct runs along the organ and empties into the duodenum (not shown). B. Histology slide of a mouse islet with the blood vessels (CD31) stained in brown (hematoxylin counterstain). Adapted from Keliher et al., 2012. Notice the extensive vessels on the islet surface and within. A human (C), monkey (D), and mouse (E) islet of Langerhans stained for beta cells (insulin, red), alpha cells (glucagon, green), and delta cells (somatostatin, blue). The proportion of beta cells in humans is lower (~%60) than mice (~80%)[3]

The endocrine pancreas is comprised of distinct microstructures known as islets of Langerhans. These individual clusters of cells range from 40-300 microns in diameter and account for 1-2% of pancreatic tissue (varying between species, Figure 1.1B), although they receive 10-20% of arterial flow, a disproportionately higher amount compared to exocrine tissue[4]. They also have a higher density of vessels, with surface area measurements of 505 cm^2/cm^3 for the islets versus 182 cm^2/cm^3 for the exocrine tissue[5, 6]. Cell types within each islet include alpha, beta, delta, and PP cells with differences in cytoarchitecture across species. These cells secrete glucagon (alpha cells), insulin (beta cells), somatostatin (delta cells), and pancreatic polypeptide (PP) with beta cells responsible for the central role of secreting insulin and lowering blood glucose. Although the ratios of different cell types vary between the head, body, and tail of

the pancreas, the beta cells are the most prevalent cells type (70-80% in mice) with the remaining fraction comprised of alpha cells, delta, and PP cells[7]. Incretins form another signaling axis in the regulation of metabolism. These peptides are secreted by the epithelial cells in the intestines and induce beta cell production of insulin. Two common incretin peptides include glucagon-like peptide-1 (GLP-1) and gastric inhibitory peptide (GIP).

Disease background

The most common types of diabetes are type 1 diabetes mellitus and type 2 diabetes mellitus. Type 1 diabetes is an autoimmune disorder characterized by T-cell destruction of the insulin-producing beta cells in the pancreas. The drastic reduction in beta cell functionality results in hyperglycemia and requires patients to depend on life-long insulin treatments to lower blood glucose levels for survival. Because the destruction occurs in adolescents and the early stages are largely asymptomatic, there is much to learn about disease progression. Though disease etiology is complex and the pathogenesis poorly understood, the examination of patient islet tissue from biopsies reveal the presence of insulitis in most patients (>50%). Much of this knowledge relies on histopathology from the 1960s and there is limited availability from pre-diabetic patients due to the difficulty of obtaining samples from individuals at risk to develop the disease[8]. From these early studies and more recent data, disease progression is divided into two phases, the initial occult phase followed by overt diabetes. The occult phase, marked by insulitis, involves the aggressive infiltration of leukocytes. The transition to overt diabetes occurs once the majority of beta cells (60-80%) are destroyed and the remaining beta cell mass can no longer adequately control blood sugar levels. Healthy fasting blood glucose levels should be less than

100 mg/dL, and levels between 100 and 125 mg/dL are considered prediabetes, while levels over 125 mg/dL indicate diabetes.

The much more prevalent type 2 diabetes is reaching epidemic levels given the worldwide increase in obesity[9]. Accounting for 90-95% of all cases, type 2 diabetes is a complex heterogeneous metabolic disorder responsible for simultaneous dysfunctions in multiple organs. Disease etiology is complex with physical inactivity and genetic predisposition as the two critical causes for disease onset[10]. Onset of hyperglycemia is caused by multiple defects in glucose homeostasis including increased liver glucose production, decreased insulin secretion in islets, and insulin insensitivity. Although screening and diagnosis of the disease is readily available and established, no cure currently exists. The majority of cases can be prevented by lifestyle changes such as routine exercise and dietary modifications, but most patients will eventually require medication. Numerous effective and FDA-approved medications exist to alleviate symptoms, and research into new agents continues. Metformin is an oral pill often used as first-line therapy to lower hepatic glucose production. Sulfonylureas can be used to increase insulin secretion, and glitazones are insulin sensitizers. Glucagon-like peptide-1 (GLP-1) agonists (e.g. exenatide, liraglutide, dulaglutide) are incretin mimetics that can control blood sugar and promote weight loss. These agents must be injected, but research into slower clearing agents has reduced the frequency of dosing. Oral formulations of these peptides are actively being researched. Rather than supplying exogenous incretins, DPP-4 inhibitors, such as sitagliptin and saxagliptin, slow the degradation rate of GLP-1. They have the advantage of oral administration but do not promote weight loss. The newest class of diabetes drugs is sodium-glucose co-transporter 2 (SGLT-2) inhibitors. Glucose is readily filtered from the blood by the kidneys, but these

transporters facilitate reabsorption to avoid loss of glucose in the urine. By inhibiting this transporter, blood glucose levels are reduced. These agents promote modest weight loss without a risk of low blood sugar, but the most common side effects include vaginal yeast and urinary tract infections. Finally, in some cases exogenous insulin is indicated[11].

Role of Imaging in Diabetes

Attempts to cure diabetes have primarily focused on restoring or preserving beta cell function within the pancreas. This has proven challenging as no clinical procedure currently exists to quantify the beta cell mass (BCM) non-invasively in patients. Instead, biochemical tests using blood samples are used to estimate beta cell mass functionality, but these methods are insensitive to the early phase of the disease when the pancreas has excess capacity to control blood sugar levels[12]. An imaging technique with the resolution and sensitivity to quantify the BCM would greatly benefit the diabetes community but has so far remained out of reach. For type 2 diabetes, understanding the role that BCM plays in the disease could open up new avenues for treatment. Imaging could play an even more significant role in type 1 diabetes by increasing insight into the early stages of immune attack and monitoring immunomodulatory therapy, transplant, and other treatment strategies. Accurately quantifying the beta call mass during clinical trials would provide invaluable information on disease etiology and treatment efficacy, but the low fraction of beta cells in the pancreas is challenging to monitor.

Particularly for type 1 diabetes, extensive research has been conducted on islet transplantation, since this treatment has the potential for curative results. One of the most successful and well-studied methods is the Edmonton Protocol where islets from multiple donors

are infused in the portal vein of the liver[13]. To date, long-term cures from transplantation are rare[14] due to several causes. The transplanted islets are susceptible to the same type of immune rejection as any organ transplant (and patients must maintain life-long immunosuppressive therapy) and must also counter the autoimmune attack responsible for the initial loss of the islets. Additionally, the microvasculature must connect with the islets, since many are beyond the size where oxygen can efficiently diffuse from the surface to cells in the center[15]. Finally, the local microenvironment in the transplant site may impact long-term efficacy[7]. The ability to track transplanted islets would improve transplantation technique and post-surgical monitoring[16].

1.3 Imaging Modalities in Diabetes

A significant effort has been placed on developing imaging agents for the pancreas due to its central role in diabetes. The focus of this chapter is primarily on methods to quantify the BCM given the importance in diagnosis and treatment monitoring of type 1 diabetes and potential implications in type 2 diabetes. However, several studies and reviews of molecular and metabolic imaging strategies for tissues outside of the pancreas are also presented to show the breadth of imaging applications in these diseases.

Detecting changes in BCM and early stages of the immune attack *in vivo* hold high clinical relevance but no current combination of imaging agent and modality is ideal. At present, several imaging modalities are used in diabetes research each with their complementary strengths and weaknesses. These include magnetic resonance imaging (MRI), positron emission tomography (PET), single photon emission computed tomography (SPECT), fluorescence imaging, bioluminescence imaging, ultrasound (US), and x-ray computed tomography (CT).

With the exception of bioluminescence, the remaining modalities have seen or have potential for clinical translation (albeit limited for fluorescence). Tradeoffs such as spatial resolution, specificity, and the use or lack of non-ionizing radiation are considered in the following sections. Although it is a valuable research tool, bioluminescent techniques will not be discussed due to low imaging depth and difficulty of clinical translation. Each of the above imaging modalities will be described in turn, but first, some of the unique considerations when imaging the endocrine pancreas, particularly for molecular imaging of beta cells in type 1 diabetes, will be discussed to provide context for the reported studies.

Imaging Limitations and Design Considerations for Pancreatic Imaging

Quantitative analysis of molecular imaging of islets reveals several challenges to BCM quantification[17]. The two biggest obstacles are the small size of individual islets (40-300 μm) and the incredibly low volume fraction of islets in the pancreas. The small islet size relative to the resolution of current imaging modalities results in significant partial volume effects. Because an islet only occupies a fraction of a voxel in an image, any contrast, be it intrinsic or from exogenous imaging agents, is 'diluted' over the entire voxel volume. Voxel dimensions for PET and SPECT imaging are on the order of 1 cm^3 under ideal imaging conditions, which can be difficult to replicate in a clinical setting. Recent literature indicate that quantification of radiotracers in structures lower than 3 cm in diameter will be subject to such partial volume effects and will require correction factors for accurate quantification[18]. Voxel sizes for US, CT, and MRI are smaller (~1 mm^3), but these modalities suffer from a much lower sensitivity for exogenous contrast agents and are still well above the size of individual islets. Optical imaging

has both high resolution and adequate sensitivity, but the lower depth of imaging limits this to invasive procedures[19].

The partial volume effects alone would not be a problem if the volume fraction were relatively large. For example, if islets occupied 50% of the tissue volume, this would only lower the measured contrast ~2-fold. Although islet volume fractions vary between species and disease states, and the low absolute value and distribution of islets in the pancreas can make it challenging to estimate[20-22], most measurements indicate 1-2% of the total pancreas mass is occupied by islets. This results in a 50 to 100-fold reduction in islet contrast due to the partial volume effect, which places severe limitations on probe selection and design.

Given the small size and low volume fraction discussed above, the intrinsic contrast between islets and the surrounding exocrine pancreas is insufficient for beta cell mass measurements using US, MRI, or CT. Therefore, exogenous contrast agents have been used to monitor various aspects of diabetes, particularly type 1. These can be divided into targeted and non-targeted exogenous contrast agents.

The type of contrast agent is generally dictated by the sensitivity of the imaging modality. For molecular contrast, meaning a specific binding interaction between the contrast agent and a target, the sensitivity must be high. Some of the most highly expressed disease related targets, such as cell surface receptors over-expressed on cancer cells, have ~1 million receptors per cell[23]. Using a cell density of 5×10^8 cells/mL, if the targeting has no method for amplification (e.g. continuous internalization and recycling, a catalytic mechanism to trap probe, etc.), the

maximum concentration of target would be ~800 nM. Even if a highly expressed target were completely saturated, this is far from the millimolar concentrations needed for CT contrast agents and well below the micromolar concentrations typically needed for MRI contrast. This also does not account for partial volume effects. Microbubbles are available for US contrast but targeting is limited to blood vessels. This leaves PET, SPECT, (both with picomolar sensitivity) and fluorescence (nanomolar sensitivity) for targeted molecular imaging. Non-targeted exogenous contrast agents in MRI, US, and CT must rely on changes in local physiology such as blood flow (small molecule contrast agents) or blood volume/permeability (for macromolecular contrast agents)[24]. An important exception is iron oxide nanoparticles for MRI contrast. These nanoparticles can be detected at lower concentrations than the common chelated gadolinium MRI contrast agents. Nanoparticles extravasate in areas of increased vascular permeability and are taken up by local macrophages, particularly in inflammatory environments. Efforts to target nanoparticles to specific receptors, however, have generally not worked due to poor washout of the nanoparticles from tissue (resulting in the enhanced permeation and retention, EPR, effect)[25]. Therefore, they target specific cells but not through the typical molecular binding of most targeted contrast agents.

Focusing on molecular imaging agents, which can be designed to provide signal specifically from the islets, PET, SPECT, and fluorescence are three modalities that have the necessary sensitivity. Despite this sensitivity, the selectivity for islets is challenging given their small volume fraction. Sweet et al. analyzed the targeting requirements for such a probe with estimates on the required selectivity and affinity that highlight the formidable challenges in probe development. In addition to the low volume fraction and partial volume effects, they also

considered the challenge of measuring a loss in signal over time before the critical functional islet mass threshold is reached and a patient exhibits overt diabetes. For imaging probes that can reach intracellular targets, the probes must be 1000-fold more specific for beta cells than exocrine cells. Even cell surface targeting probes that completely lack binding to exocrine cells require extremely high affinity and rapid clearance to lower the signal from the extracellular space[17]. Despite these stringent requirements, there are probes that are close to meeting these criteria, although further work is required. For two of the probes, vesicular monoamine transporter 2 (VMAT2) and glucagon-like peptide-1 (GLP-1) receptor targeted agents, discussion on the presence of receptor expression in the exocrine pancreas is particularly salient in light of these strict requirements. Overall, an effective clinical agent will require a combination of a high expressing target, a high-fidelity probe with strong binding affinity, little to no interactions/uptake in off-target exocrine tissue, and fast systemic clearance. In spite of the challenges, progress has been made in using several modalities to image various aspects of diabetes:

MRI

MRI offers relatively high spatial resolution in a non-invasive manner free from ionizing radiation. Many clinical instruments are capable of imaging with voxel dimensions of 1mm × 1mm × 1mm, but sub-millimeter resolution is possible with higher field strengths[19]. High soft tissue contrast and potential for use with imaging probes make this a useful tool in diabetes imaging. The modality also allows for prolonged visualization of the region of interest compared to radionuclides. To date, MRI has been used to image transplanted islets as well as to study insulitis in animal models. The high resolution and lack of ionizing radiation makes MRI an

attractive option for diabetes imaging, particularly in pediatric populations, but the inability to distinguish between exocrine and endocrine pancreas without contrast agents limits the modality to particles reacted *ex vivo* such as islet transplantation, particles taken up *in vivo* for imaging insulitis (Figure 1.2), and gadolinium contrast agents to measure changes in tissue physiology in the clinic.

There are multiple studies using MRI to study the efficacy of islet transplantation as a means of replacing the BCM for patients with type 1 diabetes. During islet transplantation surgery, significant cellular losses may occur due to multiple reasons including autoimmune rejection, mechanical stress on the cells, glucose toxicity, and damage incurred within the islets such as microvascular damage during the isolation process[7]. To study ways of minimizing islet failure during transplantation, cells are first labeled with a contrast agent prior to surgery. In mouse models, Turvey and colleagues were able to purify islets, load the cells with superparamagnetic iron oxide (SPIO) nanoparticles, and then visualize the particles in diabetic and healthy mice on T2-weighted MR images[26]. Distinguishing between functional and non-functional islets proved challenging although further studies by Kriz et al. suggested it may be possible to detect decreases in islet mass[27].

Insulitis is marked by multiple microvascular changes including increases in vessel permeability to small molecules, volumetric flow rate of blood to endocrine tissue, and the islet vascular volume[7]. These changes can be readily investigated using MRI contrast agents. Medarova et al. were able to detect vascular changes using a streptozotocin induced mouse model of type 1 diabetes[28]. T1-weighted MR images revealed increased accumulation of the gadolinium-based contrast agent compared to healthy mice. Another example includes MR

imaging using $CD8^+$ lymphocytes, where cells first internalize dextran-coated SPIO nanoparticles *in vitro*, resulting in intracellular accumulation. The re-administered cells were used to track the immune response in animal models of type 1 diabetes using NOD mice and detected decreases in the parenchymal pancreas in NOD mice when compared to control animals[29, 30].

Gaglia et al. were able to visualize islet inflammation caused by microvascular changes through MR imaging of dextran-coated magnetic nanoparticles (MNP) taken up by monocytes/macrophages in the clinic[31, 32]. An earlier study using ferumoxtran as a negative T2 contrast agent was able to elucidate differences in delta T2 between patients with type 1 diabetes and healthy controls. The change in T2 signal is associated with macrophage uptake of the MNPs. Heterogeneity in MNP accumulation was also detected, and these heterogeneities are supported from past pancreatic histology from cadavers. A more extensive study using FDA-approved ferumoxytol and imaging advances such as higher field strength, optimized pulse sequences, and improved visualization tools measured increased levels of pancreatic inflammation in patients with type 1 diabetes and detected pronounced heterogeneities in pancreatic tissue.

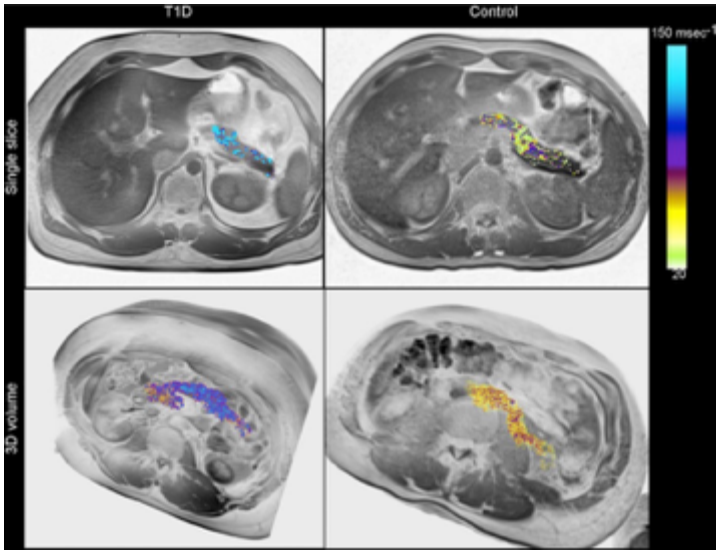

Figure 1.2 MR imaging of insulitis.
The iron-replacement therapy agent ferumoxytol accumulates in macrophages. The increase in $\Delta R2^*$ is higher in the pancreas of recent onset type-1 diabetic patients (left) than the controls (right), shown for a slice (top) or 3D reconstruction (bottom). The data indicate heterogeneous nanoparticle distribution, consistent with insulitis models in animal models[31].

PET/SPECT

Significant progress has been made towards a non-invasive monitoring technique using targeted nuclear probes. PET and SPECT are modalities that offer some of the highest sensitivity (picomolar detection) with tradeoffs in resolution compared to CT and MRI. Recent efforts to pair PET and SPECT with CT or MRI have helped address this shortcoming by overlaying a high-resolution anatomical image with the molecular PET/SPECT data. PET has a higher sensitivity than SPECT due to the coincidence detection rather than using a less efficient collimator for image formation. However, PET isotopes can be challenging to synthesize and many have short decay half-lives. The high sensitivity of these nuclear imaging techniques allows for multiple approaches in diabetes research including the use of radiolabeled ligands to target beta cells specifically for BCM quantification and imaging insulitis to understand disease histopathology.

Targeted Molecular Imaging

Targeting cell receptors provides a robust method for labeling abnormal cells as well as monitoring disease progression and evaluating therapeutic response. A detectable label, which is typically chemically conjugated to the targeting moiety, allows researchers to track the targeting ligand in the tissue of interest. Two of the most promising biomarkers for targeted molecular imaging include vesicular monoamine transporter 2 (VMAT2) and glucagon-like peptide-1 receptor (GLP-1R)[2]. Neither ligand is perfect, and the search for alternative imaging probes continues[33, 34]. However, both of these targets and associated imaging agents dihydrotetrabenazine (DTBZ and exendin derivatives, respectively) have demonstrated potential in proof-of-principle studies in the clinic and will be discussed in more detail. Antibody-targeted imaging and metabolic tracers are also mentioned as alternatives.

Vesicular monoamine transporters regulate the uptake of cytoplasmic monoamines to the secretory granules in neuroendocrine cells. Although VMAT2 was first used in the 1990s as a target for PET brain imaging in Parkinson's disease, more recent immunohistochemical staining revealed VMAT2 expression in the islets of Langerhans, making it an attractive target for beta cell imaging as well. DTBZ is a strong binder for VMAT2, with subnanomolar K_d values and greater than 10,000-fold selectivity over VMAT1 (also expressed in the endocrine pancreas), and holds promise given that DTBZ is a clinically approved PET tracer. [^{11}C]-DTBZ has been traditionally used for neural imaging of VMAT2 with high specificity, and Freeby et al. were able to estimate rat BCM in models of spontaneous type 1 diabetes using this probe[35]. The probe also detected decreases in BCM in STZ-induced diabetic rats, although accumulation was not

detectable in baboons. Variable expression across species makes interpretation challenging, and rodent studies may show the targeting of pancreatic nerve tissue rather than islets themselves[36].

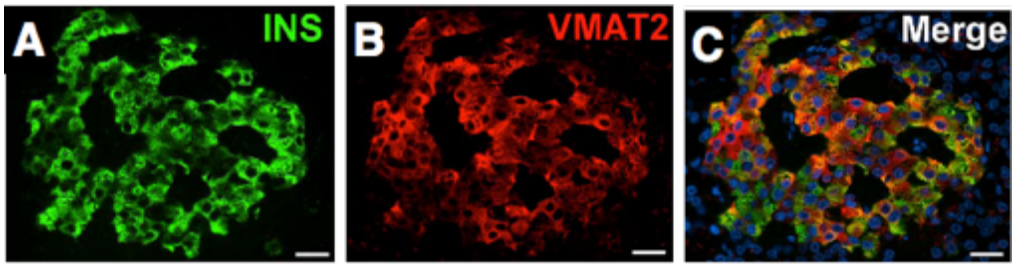

Figure 1.3 VMAT2 targeted PET agents.
Immunofluorescent staining of a healthy human islet; insulin (A), VMAT2 (B), and DAPI (blue, C). Merged image indicates most insulin expressing cells also express VMAT2 (C). Scale bars are 30 um[37].

The short half life of C-11 (20 min) can lead to some challenges, so researchers have created F-18 derivatives (110 min half life) with high affinity[38]. *In vivo* imaging of pancreatic BCM in type 1 diabetic patients compared to healthy controls with these agents has yielded promising results, but challenges remain. Using the VMAT2 radiotracer [^{18}F]-fluoropropyl-dihydrotetrabenazine (^{18}F-FP-(+)-DTBZ), Normandin et al. and Freeby et al. have measured significant differences in pancreatic standardized uptake and binding potential in healthy volunteers and patients[39, 40]. Higher-than-expected uptake of the radiotracer was measured in the body and tail of patient pancreata despite the near complete loss of functionality. Non-specific uptake of the radiotracer and/or possible exocrine expression of VMAT2 are possible explanations for the higher signal, although estimates for exocrine expression by Freeby et al. suggest a low contribution to overall measurements (<10%). Non-specific contributions were estimated using the negative enantiomer and showed that uptake in pancreata accounted for at most 15% of the total signal[2]. The measured reduction in binding potential in patients compared to healthy controls (26% reduction) and the decreases in binding capacity (63% reduction)

suggest VMAT2-targted tracers hold clinical promise. However, since multiple groups have obtained findings that indicate patients with long-standing diabetes, where the BCM should be negligible, show pancreatic accumulation of labeled DTBZ (e.g. Goland et al.[41]), further investigation is required. Improvements in accuracy and decreases in off-target signal are needed for efficient clinical translation including accounting for VMAT2 expression in PP cells[18]. Expression differences in common lab species make this a challenging endeavor[36].

Glucagon-like peptide-1 receptor (GLP-1R) is a member of Family B1 of G protein-coupled receptors. Activation of the receptor plays an important role in glucose homeostasis where the natural ligand GLP-1 helps stimulate insulin secretion in pancreatic beta cells[42]. Therefore, this receptor is a target of several clinically approved treatments for type 2 diabetes[43]. GLP-1R is highly expressed in islets, making GLP-1 and its analogues strong candidates for beta cell imaging. The high expression, along with high vascularization of tissue within the islets, has led to the development of multiple GLP-1 analogues for beta cell targeting. Native GLP-1 is rapidly degraded by dipeptidyl peptidase (DPP-IV) resulting in a < 2 min half-life in the blood[44]. To avoid high lysosomal breakdown of GLP-1, Gao et al. incorporated a lactam bridge along the peptide backbone, leading to higher binding affinity as well[45]. Perhaps even more promising is the exendin-4 peptide, originally isolated from *Heloderma suspectum*, more commonly known as the Gila monster. Multiple bioactive compounds were isolated from the venom of this foot-long lizard, one of only two poisonous lizards, including exendin-4[46]. This peptide displays remarkable *in vivo* stability. Wild type exendin-4 shares 53% homology to GLP-1 and binds to GLP-1R with subnanomolar affinity[47]. The peptide is currently approved for treatment of type 2 diabetes, and the interaction between the ligand and GLP-1R is well characterized. Gotthardt

visualized GLP-1R receptor positive tissues through SPECT imaging using [^{111}In]-DTPA-Lys^{40}-Exendin-4 through *in vivo* imaging and biodistribution measurements in rats and mice[48]. Mukai demonstrated successful blocking of GLP-1R using pre-administration of excess non-radioactive exendin followed by subsequent delivery of truncated exendin in the form of [^{125}I]-Bolton-Hunter Exendin (9-39)[49]. The development of [^{18}F]-Exendin (9-39) by Toyoda et al. showed promising uptake in the pancreas at 30 min with receptor specificity confirmed by similar blocking experiments[50]. However, intracellular trapping of the agonist form (wild-type exendin-4) may improve retention compared to the non-internalized exendin (9-39) antagonist. More recently, Brom et al. demonstrated pronounced differences in pancreas uptake with ^{111}In-labelled exendin in five patients with type 1 diabetes[51]. Quantitative PCR results from human tissue also suggested a favorable expression of GLP-1R in the islets compared to exocrine pancreas, indicating low off-target signal in patients. Similar to VMAT2 imaging, challenges remain. Karlsson and colleagues point out that the Brom et al. results may not account for the shrinking pancreas size, which may confound measurements in healthy versus diseased pancreata[33].

Despite the promising clinical results, a significant obstacle facing GLP-1 imaging is low GLP-1 receptor expression in non-beta cells. Although a diffuse signal was reported for human exocrine pancreas slides labeled with radioactive GLP-1[52], recent studies have presented a clearer picture of the localization of this expression in humans and animal models[53, 54]. Zhang et al. used quantitative flow cytometry and biodistribution measurements to estimate the expression on beta cells and non-beta cells and found ~55,000 GLP-1 receptors per beta cell in a transgenic MIP-GFP mouse model[55]. Based on the specific uptake (%ID/g difference between blocked and unblocked mice) and a 1% beta cell fraction, the beta cell targeting only accounted for 50% of

the specific signal. The other half appeared to be diffusely spread throughout the mouse pancreas. A lower expression in the exocrine pancreas (~850 GLP-1 receptors per cell[55]) could explain this non-beta cell specific labeling and is consistent with other studies showing exocrine expression.

The low beta cell fraction in the pancreas makes the specificity of the target crucial to the success of a probe, and GLP-1R faces similar challenges as VMAT2 in this regard. Willekens argue that the uptake of exendin in mouse models indicate binding to a receptor other than GLP-1R[56]. This is based on their findings of 1) a similarly high transcription ratio between endocrine and exocrine tissue in mice and rats but 2) a much lower *in vivo* uptake between these two tissues. The comparable transcript levels indicate that expression may be similar in the exocrine pancreas between these species, but this is challenging to verify at the protein (translational) level due to the poor specificity of GLP-1R mouse antibodies[57]. Functional expression of GLP1-R has been reported in mouse acinar cells[58], and slightly higher translation in mouse exocrine pancreas (resulting in higher target expression) could be the culprit for the low (5:1) uptake between endocrine and exocrine pancreas in mice versus 50:1 for rats. The 20 pmol dose of radiolabelled exendin may saturate the exocrine pancreas while the endocrine pancreas is strongly labeled but well below saturation due to higher expression. Higher doses, such as 200 pmol to 2 nmol used in fluorescence imaging, saturate both endocrine and exocrine tissue, resulting in higher endocrine to exocrine ratios.

Understanding the differences between mouse and rat pancreas (and other species such as pig and non-human primate[53, 59]) is crucial for preclinical studies, but ultimately the human

pancreas is most important for clinical translation. Animal studies are critical for understanding the disease, but they can sometimes be misleading, such as variable density of beta cells in islets[3] and differences in prevalence as a result of gender differences and unpredictability of disease onset in non-obese diabetic (NOD) mice[60-62]. Other animal models such as BioBreeding (BB) rats are lymphopenic and display a near absence of $CD4^+$ and $CD8^+$ T cells, deviating from type 1 diabetes in humans[63]. For targeted molecular imaging for diabetes research, differences between animals and humans can significantly impact results as well. Given the challenges in imaging beta cell mass, even small changes in receptor expression or beta cell number can influence imaging outcomes in preclinical models. Willekens et al. state that the rat pancreas is similar to humans given the low levels of In-111 exendin seen in some type 1 diabetic patients. Brom et al. show very low non-specific uptake in humans, which appears promising. Alternatively, the variability seen in pancreas uptake could be impacted not just by variability in patient BCM but also variable exocrine pancreas expression, pancreas size, and potentially non-specific uptake due to inflammation[51]. There are several studies indicating GLP-1R expression in the human exocrine pancreas with radiolabelled GLP-1[52] and extensively validated antibodies[53, 54]. Whether this off-target expression is sufficient to interfere with beta cell quantification is currently unclear.

Although In-111 is not an ideal radioisotope for imaging (SPECT tracer versus PET, beta and Auger electron emissions, a longer half-life than needed), it is important to note that In-111 exendin does have some of the best imaging agent targeting properties for a cell surface receptor. The low plasma protein interactions result in extremely low non-specific interactions as seen by the high blocking efficiency when delivered with high doses of cold exendin[48, 51]. Tc-99m and

Ga-68 can suffer from non-specific interactions that decrease endocrine pancreas uptake and/or increase non-specific signal[64]. Cu-64 labeled peptides appear to have better pharmacokinetics than technetium and gadolinium[65], but the islet uptake is slightly lower and the blocked pancreas (non-specific) uptake slightly higher than In-111[66]. Whether the higher sensitivity of PET outweighs these effects remains to be determined. In-111 is also a residualizing isotope, which is important for rapidly internalized agonists, such as exendin-4, that are trapped within the cell to avoid washout of probes that occurs even with seemingly high single-digit nanomolar affinity[6, 25]. This is in contrast to isotopes such as iodine and F-18 that can wash out of the target cells upon internalization and degradation (depending on the linker and associated chemistry[67]).

Antibodies specific to beta cell surface proteins that bind with high affinity have also been investigated as probes for BCM imaging and quantification. Several monoclonal antibodies (mAbs) have been reported that bind specifically to beta cells[68, 69]. These large (~150 kDa) proteins recognize specific epitopes through their variable regions, and their slow clearance results in efficient targeting. IC2, a rat IgM monoclonal antibody, is known to bind to sulfatide expressed on the beta cell surface in the insulin granula[70]. Results of the study using [^{111}In]-DTPA-IC2 were promising and demonstrated high uptake and specificity as well as high correlation between antibody accumulation in the pancreas and BCM between diabetic and healthy animals. However, several limitations exist for radiolabeled antibodies in the clinic, particularly the high background activity due to slow systemic clearance. Hampe and colleagues used fragments of K14D10 IgG to demonstrate that antibody fragments are able to clear systemic circulation quickly and bind to beta cells with high affinity[71]. However, analysis of the pharmacokinetics of protein imaging agents indicate the most efficient uptake occurs for either

very low molecular weight probes (< 3 kDa)[6] or monoclonal antibodies[25], with low molecular weight probes providing more efficient background clearance than the latter.

Serotonin synthesis is localized in islets and measurements of biosynthesis activity can be used to potentially quantify beta cells. One strategy uses a radiolabeled serotonin precursor hydroxy-tryptophan (HTP). Serotonin synthesis in healthy pancreata will result in the accumulation of radiolabeled precursor whereas pancreas from patients with type 1 diabetes will lack the molecular machinery required for synthesis[72]. Although both exocrine and endocrine cells take up HTP, the precursor molecule is quickly trafficked out of the cell unless it's metabolized. Eriksson and colleagues demonstrated accumulation of [^{11}C]5-HTP in the pancreas of healthy volunteers, noticeably in the tail and body regions where islets are more abundant. Compensating for loss of pancreas volume in patients, there was an observable decrease in tracer accumulation in diabetic pancreata (0.0028 %ID/g vs., 0.0046 %ID/g for patients and volunteers, respectively) between 40 and 60 minutes post-administration[34]. Because all neuroendocrine tissue undergoes serotonin biosynthesis, the tracer is not specific to beta cells, indicating that the near total beta cell loss found in patients with longstanding type 1 diabetes will result in only partial signal loss. Despite these challenges, [^{11}C]5-HTP has potential for use in islet transplantation and regenerative therapies.

Highly specific ligands to markers unique to beta cells are a challenge to develop. One of the reasons the debate over the significance of low-level expression in non-beta cell tissue for several imaging probes continues is due to the challenging circumstances from the small islet size and partial volume effects. For example, in cancer imaging, a few thousand EGFR receptors

per cell in healthy tissue would not be a major concern when imaging a tumor with a million EGFR receptors per cell. However, the 1% mass fraction of islets makes even low expression extremely pertinent. Also important is the non-specific uptake of probe in healthy tissue, particularly for residualizing radioisotopes that will be trapped in background tissue even once the plasma and interstitial probe has cleared. Even subtle changes to the molecule, such as the radiolabel, can impart large changes in protein interaction and non-specific uptake rates. These considerations, and differences between animal species used for preclinical testing and humans, remain an important consideration for all probes, including VMAT2 and GLP-1R.

Nuclear Imaging of Insulitis

To date, non-invasive PET methods for imaging insulitis include labeled lymphocytes and labeled peptide and protein ligands specifically targeting lymphocytes. The labeling of lymphocytes is performed *ex vivo* and cells are re-administered intravenously post-labeling. Ideally, the systemic circulating lymphocytes will migrate to the inflamed pancreatic tissue due to cytokine and chemokine signaling. Results from re-administered lymphocytes showed poor pancreas targeting in patients and animal work indicated uptake in the pancreas for both the control and test groups. As a result, the technique using labeled lymphocytes does not appear to be specific. A promising alternative for insulitis imaging involves radiolabeling interleukin-2 (IL-2) with SPECT tracers. In short, uptake of [^{123}I]-IL-2 resulting from lymphocyte invasion in the pancreas of non-obese diabetic (NOD) mice was quantifiable. Promising *in vitro* and *in vivo* results including high specificity and retention prompted administration of radiolabeled IL-2 in humans. Patients with a high risk of type 1 diabetes were also dosed and showed clear pancreatic

uptake as well[73]. Additional SPECT tracers have been used including Tc-99m with similar qualitative results. However, additional improvements are needed for accurate quantification. A more detailed discussion can be found in Signore et al[7].

Fluorescence

Fluorescence imaging uses visible or near-infrared light to detect a dye with high spatial resolution (< 1 μm) and sensitivity (nM range). The excitation wavelength photon excites the dye, and a longer wavelength photon is emitted. Near-infrared fluorescent dyes are often used due to reduced background (autofluorescence) and higher tissue-penetrating properties of the light. Similar to radiolabeled ligands for PET/SPECT, a fluorophore is attached to a targeting ligand to generate the probe. Commonly, a commercially available dye is chemically conjugated to the targeting ligand using common chemistries (ester-amine reactions, maleimide-sulfhydryl linkages, azide-alkyne click chemistry or copper-free click reactions, etc.) to create the imaging probe, which is then administered to a patient or animal to label specific antigens. Although near infrared light can travel through several centimeters of tissue[74], the tissue is highly scattering. Even a large difference in contrast between the target and background can be lost as the signal 'blurs' under increasing tissue depth. Due to the scattering and absorption associated with fluorescence imaging, it is not possible to develop a fluorescent probe that will allow for non-invasive real-time monitoring of BCM, where MRI or PET/SPECT may be more appropriate. However, the high resolution and ease of handling of fluorescent materials compared to radionuclides—including the ability to resolve subcellular structure and trafficking—make it an invaluable tool for research use in imaging agent design. Some pertinent parameters that can be

measured using fluorescent molecular imaging include receptor expression quantification, binding affinity, internalization rate measurements, plasma protein interactions, and imaging agent stability.

With the availability of reactive fluorophores and fluorescent proteins, including near infrared (NIR) probes with higher penetration depths, there is increased use of fluorescent microscopy for determining localization of biomolecules under normal and diseased conditions. Hara et al. stably generated transgenic mice with the specific expression of green fluorescent protein (GFP) in the insulin-producing beta cells[75]. The tool has improved flow cytometry analysis and quantification of BCM *ex vivo,* although low imaging depth and poor optical properties of GFP preclude this method's use for *in vivo* quantification. Given the low absorption of near infrared light by hemoglobin, NIR probes are quickly gaining popularity for labeling targeting ligands. For example, Reiner et al. chemically conjugated an NIR fluorophore via copper-catalyzed click chemistry to exendin-4 to generate a highly specific beta cell binder and demonstrate the loss in signal following streptozotocin treatment of mice[76].

Fluorescence Imaging for Molecular Probe Design

The high resolution and real-time imaging of fluorescent probes make them excellent tools for insight into molecular probe design. For example, the rapid internalization and intracellular trapping of exendin derivatives visualized through live cell imaging provides insight into the necessary affinity for these imaging agents. Distinct from the original analysis performed by Sweet et al.[17], the fast internalization rate results in effectively irreversible binding, so the requirement for binding affinity for internalized and residualizing probes (those trapped within

cells following internalization) is not as strict as originally postulated. (In Sweet et al. it is assumed no internalization occurs and binding is at equilibrium.) Internalization and trapping using residualizing isotopes and/or linkers is an effective method to lower the required binding affinity and reduce washout of probe[6]. Notably, the slowly internalized exendin antagonist (exendin 9-39) is not an appropriate imaging agent, likely because it is not rapidly internalized and therefore it is subject to the strict affinity requirements for low molecular weight probes[25].

In addition to cellular trafficking, fluorescent derivatives can provide insight into absolute expression of imaging targets. Flow cytometry analysis of digested pancreas from mice that were administered fluorescent exendin-4 has provided absolute measurements of the accessible GLP-1 receptor expression *in vivo.* Absolute expression levels can be difficult to measure, but they can assist researchers in determining the optimal dose, blocking doses, and required affinity. Fluorescent derivatives for VMAT2 targeting are more challenging to develop given its intracellular location. However, the recent report of a fluorescent derivative may aid in the understanding of VMAT2 targeting in the context of diabetes[77]. For these targets and others, a subsaturating dose is typically ideal to achieve maximum contrast between binding of probe in the target versus background tissues. This is balanced against a need for sufficient signal depending on the imaging modality. (For example, fluorescent doses are often higher than radiolabeled doses for animal imaging.)

Given the extremely small fraction of islets in pancreatic tissue, non-specific targeting and uptake, even in low quantities, can result in drastic overestimates for BCM. Fluorescently labeled ligands have been used to correlate non-specific *in vivo* uptake with plasma protein

binding and non-specific *in vitro* cellular uptake[6]. This may enable rapid *in vitro* screening for molecules with low non-specific uptake *in vivo*. Fluorescently labeled exendin-4 derivatives were used to show that probes with increased plasma protein binding also had higher non-specific cellular uptake rates, which can contribute to background signal. Even if the bound exendin were internalized and trapped within beta cells, a long washout period before imaging would provide little benefit if the non-specific signal were also internalized. The longer washout would reduce extracellular probe that could intravasate into the blood and clear systemically, but the internalized probe would leak out of the beta cells and other cells at approximately the same rate. It is important to be cognizant of the impact of fluorophore conjugation on imaging agent properties similar to how chelators impact radiolabeled probes (along with the targeting ligand itself). The lipophilicity of a fluorophore can significantly impact clearance rates and the degree of off-target interactions. A parallel exists in radioimaging where additional chelator hydrophilicity may reduce sticking[78, 79]. This may be one reason why the In-111 labeled exendin was able to show large differences in the clinic[51]. Chelated In-111 is known to have very low interactions with plasma proteins, and In-111 has shown excellent specificity by having very low uptake in blocked controls in animal models[80].

Ultrasonography and Computed Tomography

Abdominal ultrasonography (US) and computed tomography (CT) are common techniques used for traditional pancreatic imaging. Due its non-invasive nature, lack of ionizing radiation, and abundance in the clinic, US is one of the most frequent diagnostic tools. Although organ functionality and anatomical structures can be visualized, US is rarely used to detect the structural changes that occur during type 1 diabetes, and the modality faces numerous challenges

for quantifying and visualizing islets[7]. Computed tomography (CT) is an imaging technique used to visualize the anatomy of the pancreas due to differences in x-ray attenuation between tissues. Within the pancreas, however, both exocrine tissue and the islets share a similar density, making it difficult to differentiate between the two with available CT scanners. Though not suited for islet visualization, CT has been used to monitor tissue modifications during pancreas transplantation[81]. These methods have also been used to measure the size of the pancreas. The lower organ weight seen in some studies may complicate the interpretation of loss in beta cell mass, which could reflect a lower pancreas volume. Though not as common as type 1 and type 2 diabetes, monogenic diabetes mellitus displays multiple characteristics that are detectable with traditional US and CT imaging including increased US reflectivity and reduced X-ray attenuation on CT[82]. Therefore, these modalities play an important secondary role in pancreas imaging.

Multi-modal Imaging

The tradeoffs of different imaging modalities for detecting and treatment of type 1 diabetes including islet transplantation therapy and beta cell quantification suggest there may not be one ideal modality for this purpose, mirroring conclusions found in other diseases such as cancer. Because of these non-overlapping weaknesses, multi-modal imaging, which combines methods such as PET/MRI, has gained use for clinical diagnostics. For example, PET images can provide functional information whereas MRI provides the complementary high-resolution anatomical images[83]. Medarova et al. have detailed a method of islet transplantation that allows for facile monitoring post-surgery using both MR imaging and optical imaging in mice[84]. The MN-NIRF (superparamagnetic iron oxide nanoparticles conjugated with a near-infrared probe) particles label islets with fluorescent imaging to corroborate MRI results. Combinations of

fluorescence and PET have been used to target *N*-glycoprotein with a monoclonal antibody specific for transmembrane protein 27 (TMEM27) and achieved measurable uptake in insulinoma xenografts in mouse models[85]. The expansion of multi-modal imaging will likely expand given the intrinsic drawbacks of each individual modality.

1.4 Molecular Imaging Outside the Pancreas in Diabetes

Molecular and metabolic imaging outside of the pancreas is primarily focused on quantifying changes in metabolism and insulin resistance in organs such as the liver and skeletal muscle given the importance in type 2 diabetes. Additional studies have focused on pathological effects in organs such as the kidney and heart, which are common in the disease. Even with the important pathological role of insulin resistance, the failure of beta cells is considered the main culprit in the conversion to diabetes[86]. Although most diabetes research involves visualizing the pancreas, imaging other organs has increased our understanding of the pathogenesis of the disease, and examples of such studies are outlined below.

The most common techniques for examining metabolic changes associated with diabetes use radiolabeled metabolites for PET and SPECT imaging, magnetic resonance spectroscopy, and more recently, hyperpolarized MRI. Radiolabeled agents for metabolic studies include ^{18}F-fluorodeoxyglucose (FDG) for quantifying glucose metabolism, [^{11}C]-palmitate and [^{123}I]-BMIPP (beta-methyl-p-iodophenyl-pentadecanoic acid) for measuring fatty acid utilization with PET and SPECT, respectively, and [^{11}C]-glutamate and [^{11}C]-methionine for amino acid metabolism[87, 88]. For example, impaired glucose transport and phosphorylation in response to insulin using PET has been demonstrated in skeletal muscle, the most important tissue for insulin

resistance, and results suggest there are deficiencies in glucose phosphorylation in the pathogenesis of type 2 diabetes[89]. This is consistent with magnetic resonance spectroscopy studies[90], and similar results have been shown for the liver[91]. [^{11}C]-palmitate has shown the reduced conversion of fatty acids into triglycerides in muscle for obese patients, a major risk factor in type 2 diabetes. Brehm and colleagues measured reductions in insulin-stimulated ATP synthase flux due to increases in lipid availability for patients with insulin-sensitivity. These fatty acids are important regulators of glucose metabolism, further impacting insulin-mediated glucose utilization[92]. Other studies have focused on the pathological effects of diabetes in different organ systems. Recently, a hyperpolarized redox sensor, [^{13}C]-dehydroascorbate (DHA) has been used to show reduced redox capacity prior to the onset of nephropathy in a diabetic mouse model[93]. Particular emphasis has been placed on imaging the heart due to the increased risk of cardiovascular disease in diabetic patients. Blood flow imaging (^{201}Tl, ^{99m}Tc tetrofosmin, ^{99m}Tc-sestamibi) and glucose metabolism (FDG) have been used to detect mismatch between perfusion and viable tissue after myocardial infarction[87], which is more prevalent in diabetics. Specifically for diabetes, studies on metabolism include magnetic resonance spectroscopy, which has shown increased triglyceride content in the heart[94]. Molecular imaging will continue to develop in these areas to improve our understanding of the multi-organ pathological impact of the disease.

1.5 Future Directions for Imaging Beta Cells

Molecular imaging in diabetes has primarily focused on the endocrine pancreas given its central role in controlling glucose metabolism. The small size and low volume fraction of islets of Langerhans in the pancreas place considerable limitations for current imaging modalities. To date, a robust and widely adopted approach for quantifying beta cell mass remains elusive. This is a major limitation for researchers in the field when studying disease onset, progression, and

treatment options. The use of highly specific targeting ligands to bind defined biomarkers on beta cells in PET and SPECT imaging are making progress towards the goal of clinical quantification of beta cell mass. The high resolution and ease of use of fluorescence imaging make this an increasingly valuable tool for aiding in the design of improved imaging agents. In addition to quantifying beta cell mass through imaging, the early stages of type 1 diabetes characterized by insulitis and the multi-organ effects of metabolism in type 2 diabetes have also been investigated as well using multiple modalities including MRI, PET, SPECT, fluorescence imaging, and bioluminescence. Each modality has a unique set of strengths and drawbacks and each plays a crucial imaging role in studying the disease. The non-invasive nature of MRI and PET/SPECT and sensitivity to molecular markers (e.g. molecular resonance spectroscopy and hyperpolarized MRI contrast agents and radioactive PET and SPECT tracers) make these key modalities for clinical translation.

One of the biggest challenges for the future of this field remains the development of a robust imaging method for beta cell mass. What new approaches could help facilitate the development of such a probe (or adaptation of current probes to yield more reliable results)? Absolute quantification of target expression (across species and in humans), delivery rates (blood flow, vascular surface area, etc.) under various disease states, and probe properties (plasma clearance, cellular uptake and retention, binding affinity, etc.) can greatly facilitate the development of improved agents and interpretation of experimental results. For example, knowing the absolute number of GLP-1 receptors on endocrine versus exocrine cells rather than relative expression can facilitate strategies for improving specificity. Some of the basic principles of targeting specificity can be incorporated into screening methods[34] provided the *in*

vitro expression profiles capture the *in vivo* situation. At the same time, it is important to revisit the assumptions of earlier analyses, since new probes may act by different mechanisms. For example, GLP-1R agonists and tryptophan precursors act by cellular trafficking and residualization rather than a simple binding interaction, thereby side-stepping some of the affinity limitations outlined in earlier analyses. Fortunately, a plethora of models exist to describe the pharmacokinetics of these types of agents (including FDG) that can be used to scale the results to animal and possibly human studies[24, 95].

In silico simulations of molecular distribution continue to improve and may be adapted for pharmacokinetic simulations of imaging agents. For the purpose of the discussion here, simulations differ from models in that simulations require little to no experimental data to predict *in vivo* outcomes. In contrast, models often use extensive experimental data and are fit to the results. For intracellular targets, simulations of first-in-animal and first-in-man drug distribution could be adapted (with suitable adjustments for targeting in tissues) to describe specific and non-specific distribution of small molecule probes[96]. Similarly, non-steady state simulations of probe distribution[6, 97] can aid in the design of extracellular targeted agents. The use of *in silico* techniques can help guide experiments with current probes as well. As mentioned previously, recent evidence indicates that GLP-1R is expressed at very low levels in the exocrine pancreas in several species, including humans. Based on estimates of GLP-1R expression in mice and quantitative blocked and unblocked biodistribution, the expression is ~850 receptors per cell. However, this lower expression is significant versus endocrine uptake in the whole pancreas due to the low volume fraction of beta cells. If this low level expression in the exocrine pancreas could be blocked specifically without completely blocking the beta cell receptor expression, the

beta cell specificity of a subsequent radiolabeled agent would be greatly improved. The low molecular weight of exendin is close to optimal for an extracellular target in fenestrated tissue such as the pancreas, but it is still limited by permeability (the permeability surface area product, or PS/V) and not blood flow. Assuming the fenestrated permeability is similar between the endocrine and exocrine pancreas, the relative uptake is determined by the surface area. Estimates of S/V (cm^2/cm^3) for endocrine and exocrine pancreas are 505 and 182 respectively[5, 98]. Although delivery to the exocrine pancreas is expected to be about 3-fold lower, the amount of probe required to block these receptors is >10-fold lower than what would completely block islet uptake. Therefore it is theoretically possible to block this low exocrine signal without blocking the beta cell receptors using a low dose of unlabeled peptide, and *in silico* simulations can be used to identify the appropriate scheme. (In contrast, the close association between non-target cells expressing VMAT2 and reversible binding of DTBZ versus the 'irreversible' internalization of GLP-1R make blocking less feasible for VMAT2.) 'Cold dosing' using non-radioactive probes, has extensive precedent in the literature including the use with radiolabelled antibodies[99, 100] and in antibody drug conjugate delivery[101]. It is important to clarify here that 'low dose' refers to a dose that does not saturate the islets but does saturate the lower expression within exocrine tissue. Therefore, it may be much higher than the trace amounts of radioactive probe injected. A potential complication would be nausea and emesis seen with large doses of exendin, although these symptoms may be controlled for a single imaging session or an antagonist could be used. This may provide one avenue to improve specificity.

Another concern for agents delivered to sites of inflamed tissue includes accounting for changes in local transport properties due to the inflammation itself. For example, many probes

will have a higher effective permeability in the inflamed tissue during insulitis, potentially increasing local probe uptake. A structurally similar non-binding probe could be used to quantify the impact of inflammation on imaging agent concentration in the inflamed local environment. This could be critical if some of the significant inter-individual variability seen in clinical trials is due to differences in delivery and not just differences in beta cell mass[102]. SPECT offers the possibility of gating on two gamma ray energies, providing 'two-color' imaging, and adaptations for use with PET are being explored[103]. This could be employed for binding and non-binding controls[95] to normalize results to differences in probe delivery from inflammation. Recently, Mathijs and colleagues used this dual isotope approach for delineating the pancreas relative to surrounding organs, such as the kidneys, in mouse imaging[104].

1.6 Design of Novel Exendin-based Probes

Due to its optimal molecular weight and strong binding affinity for GLP-1R, the exendin model system is used to quantify the beta cell mass *in* vivo. Alanine scans of exendin-4 and data from Clardy et al. indicate multiple amino acid residues may be modified with little impact on binding affinity[105, 106] for fluorophore conjugation. Seemingly safe residues include lysine at the 12th position, methionine at the 14th position, and leucine at the 21st position. Given the presence of free amines in exendin-4, NHS ester and carbodiimide chemistries will not be used. Rather, click chemistry, with advantages such as bioorthogonality, stability, and low toxicity will be employed to conjugate various NIR dyes[107]. A recent solution for functionalizing proteins with bioorthgonal reactivity is to introduce L-azidohomoalanine into the peptide sequence during solid phase peptide synthesis or through methionine substitution in bacteria[108-112]. The free azide (N_3) can be used to react to free alkynes on fluorophores or linkers.

Molecular weight is one probe parameter that can be easily adjusted using the azide moiety and is known to influence *in vivo* trafficking and transport properties such as vessel permeability, internalization, binding affinity, and biexponential decay parameters[25, 113-115]. For example, increasing molecular weight of a peptide may slow plasma clearance, but it may hinder cell surface binding. Kim et al [116, 117] successfully synthesized PEGylated dimeric exendin-4 slower plasma clearance, and greater antihyperglycemic efficacy (exendin-4 is an FDA-approved drug for treating symptoms of Type 2 diabetes) but decreased binding affinity. For a therapeutic drug, the benefits of a higher molecular weight exendin are obvious. However, the molecular weight tradeoffs for exendin as an imaging agent are difficult to predict, hence the need for a mathematical model. For example, an extremely small imaging agent will leak out of plasma and quickly bind to GLP-1R; unbound probe will then quickly leak back to plasma. This in theory will give low background when imaging because probe residence time in the islets is relatively short; however, β-cells have little time to bind and internalize probe (internalized probe cannot leak out of cells back into plasma and is advantageous for imaging). On the other hand, a larger probe has a longer residence time in the islets, potentially causing a higher background signal when imaging. On the upside, β-cells will have more time to bind and internalize the probe, which improves imaging signal at longer times post injection. For the aforementioned reasons, both smaller and larger probes have the potential to be robust imaging agents, and modeling based on data collected from different molecular weight probes will help identify the optimal size.

Ensuring low non-specific uptake of probe in tissue surrounding the pancreas will result in high signal to background ratio during imaging. Biodistribution studies indicate kidney uptake of exendin is 2-3 orders of magnitude higher on a per mass basis than other organs [76, 118-120].

Because the kidneys are situated directly beneath the pancreas, reducing NIR-tagged exendin uptake in the kidney will help visualize the pancreas during imaging. Many peptides are degraded by proteases situated on the brush border of proximal tubule cells. Dipeptides are then endocytosed in the proximal tubule to recycle the amino acids, and associated tags are often trapped in these cells. Reducing proteolysis in the kidney may decrease renal uptake. However, Vegt et al showed cells expressing megalin in the kidney facilitated renal reabsorption of radiolabelled exendin[118]. Upon binding to megalin, exendin is endocytosed and degraded; the radiolabel may residualize depending on its chemical properties. Modifying exendin to resist proteolysis and megalin-mediated internalization and/or using a non-residualizing fluorophore/linker may help decrease kidney signal.

1.7 Stabilized Peptides

Peptides are in an ideal molecular weight range for efficient tissue targeting but suffer from protease instability. One strategy to improve protease stability, binding affinity, and helicity is through helix stabilization. Stabilizing, or conformationally restricting, the alpha helical secondary structure of peptides has been an exciting new technique for protein engineering[121]. The poor performances of many current peptide biologics are often a result of their poor stability. By engineering them to be more stable, proteins can function under a wide range of harsh conditions such as extremes in temperature and pH or protease digestion. Although the use of salt bridges, lactam bridges, and disulfides have been used previously as natural means of stabilizing alpha helices, recent breakthroughs, including novel side-chain cross-linking

chemistry and the expression of non-natural amino acids in bacteria, have renewed a growing interest in 'stapled' peptides[121-125].

Alpha helices are the most prevalent secondary protein structure. One turn of an alpha helix consists of 3.6 amino acid residues stabilized by intrachain hydrogen bond interactions between the i and i+4 residues. For this reason, previous work at stabilizing various peptides often crosslinked i, i+4 or i, i+7 residues[126, 127]. Despite progress being made at studying how to stabilize peptides, there has been slower progress on stabilization of peptides that bind to specific targets, such as exendin.

Stabilizing exendin to resist proteolysis may allow it to clear from the kidneys without being reabsorbed, resulting in lower unwanted kidney signal during imaging. Bird et al demonstrated that by introducing multiple small staples across the backbone of the peptides including exendin, the resultant structures were more resistant to enzymatic digestion and had improved helicity[124]. Exendin, a peptide mostly helical by nature[42], could benefit from additional helicity with higher affinity for cell surface receptors.

In conclusion, there are key challenges that must be overcome to develop an imaging agent for the clinic moving forward. One, there must be improvements in the specificity of PET and SPECT beta cell targeting probes as they represent the most advanced and well-characterized approaches for BCM assessment in humans. The promising results in the clinic for both VMAT2 and GLP-1R targets still show overlap between healthy controls and type 1 diabetics, which is short of the desired goal of quantifying a graded loss in beta cell mass. Two, the clinical application must be clearly defined for different imaging modalities. For example, given the radiation concern in pediatric populations, can a composite score of MRI measured inflammation, autoantibody titer, and other clinical data (e.g. functional tests) provide enough information for measuring patient response to treatment? Each of these methods has drawbacks individually, but progress in several areas may allow reasonable measurements of clinical response. One could envision PET/SPECT imaging playing a critical role in clinical trials for developing new treatments while MRI methods would be used for clinical practice to avoid the safety risk associated with ionizing radiation. Lastly, there is a need for more emphasis in imaging agent design. Due to the complexity of imaging beta cells, a clinically reliable probe needs to display ideal pharmacokinetic properties including high target uptake, low systemic concentrations during imaging, very low non-specific sticking to proteins, and next to zero off-target uptake for maximum contrast. Given the expense of developing new probes and imaging techniques, particularly those requiring large animals, *in vitro* and *in silico* experiments can help guide the rational design of probes, efficiently set up animal experiments, and help interpret the results to maximize the information gained from animal imaging. These probes can facilitate our

understanding of diabetes, open up opportunities for new drug targets, and monitor progress in clinical trials to improve the outcome for this increasingly prevalent and costly disease.

Chapter 2

Mechanistic And Quantitative Insight Into Cell Surface Targeted Molecular Imaging Agent Design

2.1 Publication Information

Zhang, L.*, S. Bhatnagar*, E. Deschenes, and G.M. Thurber. *Mechanistic and quantitative insight into cell surface targeted molecular imaging agent design.* Scientific Reports, 2016; 25424

Modifications have been made to the published document to adapt the content to this text. The goal of this chapter is to identify key properties for successful peptide-based molecular targeted imaging agents. Identifying these properties will help aid in the development of a successful imaging agent for targeting beta cells for type 1 diabetes.

2.2 Abstract

Molecular imaging agent design involves simultaneously optimizing multiple probe properties. While several desired characteristics are straightforward, including strong affinity and low non-specific background signal, in practice there are quantitative trade-offs between these properties. These include plasma clearance, where fast clearance lowers background signal but can reduce target uptake, and binding, where high affinity compounds sometimes suffer from lower stability or increased non-specific interactions. Further complicating probe development, many of the optimal parameters vary depending on both target tissue and imaging agent properties, making empirical approaches or past experience difficult to translate. Here, we focus on low molecular weight compounds targeting extracellular receptors, which have some of the highest contrast values for imaging agents. We use a mechanistic approach to provide a quantitative framework for weighing trade-offs between molecules. Our results show that

specific target uptake is well-described by quantitative simulations for a variety of targeting agents, whereas non-specific background signal is more difficult to predict. We compare two *in vitro* experimental methods for estimating background signal *in vivo* – non-specific cellular uptake and plasma protein binding. Together, these data provide a quantitative method to guide probe design and focus animal work for more cost-effective and time-efficient development of molecular imaging agents.

2.3 Background

Targeting cell surface receptors provides a robust method for identifying abnormal tissue, monitoring disease progression, and quantifying therapeutic response[128]. Typically, a detectable label (e.g. radioactive isotope, fluorescent dye, MRI, CT, or ultrasound contrast agent) is chemically conjugated to a targeting ligand to create the imaging agent. These agents are then administered to a patient or animal to target tissues that express antigens specific to the targeting ligand. Monitoring the targeting compound *in vivo* provides valuable insight into diverse biological processes such as cell signaling, tumor growth rates, and drug response depending on the system studied.

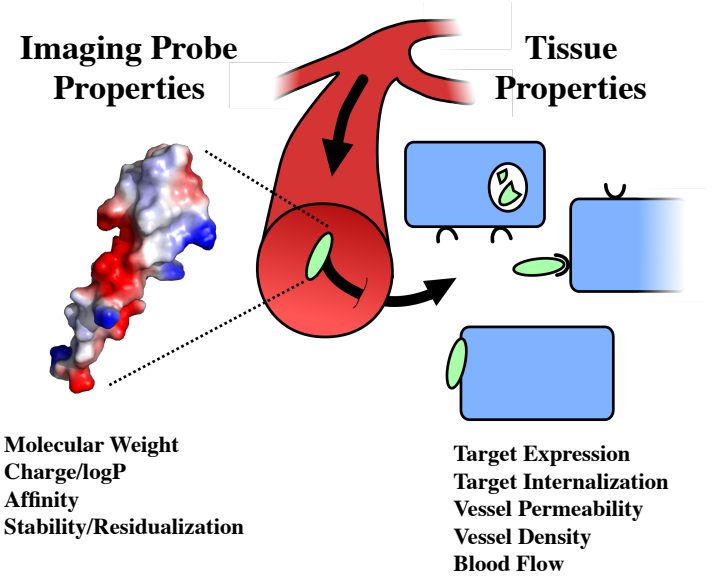

Scheme 2.1 Diagram of interplay between imaging probe properties and tissue properties

In vivo cell surface targeting is a complex interplay between tissue and imaging agent properties (Scheme 2.1). Investigators can manipulate the chemical or physical properties of the ligand by adding or removing functional groups to alter molecular weight, charge, affinity, and stability[25, 129, 130]. For example, molecular weight can be manipulated with recombinant proteins[131, 132] or through PEGylation of small molecules to slow blood clearance[129, 133]. Plasma protein binding can also be manipulated through the net charge and charge distribution of small molecules[134, 135]. More recently, stabilization of peptide secondary structure has been used to increase cellular uptake and resistance to proteases, allowing for imaging at longer times[124, 136, 137]. Equally important are the tissue properties and local physiology, which can vary widely between different tissues and in healthy versus diseased states[138, 139]. Depending on the target tissue, intrinsic transport parameters such as blood flow (Q) and blood vessel surface area to volume (S/V) vary. The diverse local physiology results in tissue-specific optimal imaging agent properties, making it difficult to generalize from empirical rules or extrapolate from previous

results. Likewise, computational approaches originally developed for therapeutics often require extensive experimental data or assume a pseudo-steady state drug concentration, which is not appropriate for imaging agent design. Many imaging agent models have been used to quantitatively analyze experimental data[95], but these compartmental models were not designed to predict distribution based on probe properties. Therefore, most imaging agents are developed on a case-by-case basis with low throughput and cost intensive animal experiments. While a qualitative understanding of *in vivo* conditions offers insight on which parameters play a role in targeting, a quantitative model that is both mechanistic and predictive allows for much more efficient design of imaging probes.

To help guide the design of novel imaging agents against extracellular targets, we present a quantitative and mechanistic model for describing target tissue uptake and background signal. These simulations build on previously published models that incorporate the time-varying and spatially heterogeneous tissue concentrations present under non-equilibrium conditions following a bolus dose. The trade-offs in molecular properties can then be quantitatively compared for selection of the most promising agents to move forward with imaging probe development.

2.4 Results

A simplified system was used to identify the most important parameters for maximizing contrast under optimal conditions. Assuming a high affinity binder with no blood flow limitations, first-order uptake in background tissues, and probe degradation rates that are much slower than plasma clearance and internalization (SI), the maximum target to background ratio (TBR) can be expressed as

$$TBR = \left[\frac{\left(\frac{PS}{V} \right)_{\text{target}}}{\varepsilon k_{\text{int},ns}} \right]$$

where P is the vascular permeability of the target tissue, S/V is the tissue vessel surface area to volume ratio, ε is the tissue interstitial void volume, and $k_{int,ns}$ is the non-specific internalization rate in background tissue. Based on these results, the salient design parameters for targeting contrast are molecular weight (impacting P), stability/residualization of the label, and non-specific interactions. The optimal values of these parameters depend on the tissue blood flow, vessel-type, vessel surface area, target expression, and internalization rate.

Table 2.1 Tissue physiology versus molecular weight

Tissues	Plasma flow (mL/min/g)	Vasculature type	S/V (cm^{-1})	Imaging agent Mw (50% extraction, Da)
Bone	0.29	Non-fenestrated, loose junctions	144	<570
Heart	4.06	Non-fenestrated, loose junctions	211	<100
Kidney	1.91	Fenestrated	350	<3600
Liver	0.9	Sinusoidal, reticulo-endothelial	250	--
Lung	24	Non-fenestrated, loose junctions	250	<80
Muscle	0.13	Non-fenestrated, loose junctions	70	<600
Pancreas (endo)	0.29 (g pancreas^{-1})	Fenestrated	505	<3000
Pancreas (exo)	0.41	Fenestrated	182	<6900
Spleen	0.57	Sinusoidal, non reticulo-endothelial	400	--
Tumor	0.055	Fenestrated, immature	20-100	<2200

Previous reports indicate that at molecular weights less than about 35 kDa, the efficiency of uptake in a tissue (% injected dose per gram) increases with reduced molecular weight due to increased permeability[25]. Eventually, the extraction fraction approaches 100% providing an upper limit on the benefit of small size. Molecular weight cutoffs were established for optimal extraction of the imaging agent from the circulation to the target tissue. The extraction fraction is a function of molecular weight, plasma flow rate, effective permeability, and S/V[24]. The correlation between effective permeability as a function of molecular size was fit for fenestrated, non-fenestrated, and tumor vessels. As previously reported by Schmidt et al., tumor data indicated 4.5 and 500 nm radius pores with fractional area to thickness ratios of 17.6 and 0.65 cm^{-1} for small and large pores, respectively. Fenestrated vessels indicated 8 and 35 nm radius pores with fractional area to thickness ratios of 30 and 2 cm^{-1} for small and large pores, respectively. Non-fenestrated vessels suggested pore radii of 0.7 and 60 nm with fractional area to thickness ratios of 10 and 2 cm^{-1} for small and large pores, respectively. Using these permeability fits and a 50% extraction fraction cutoff, we predict that for targeting tumor, a molecule below 2200 Da will effectively extravasate out of the blood vessel into the target tissue (Figure 2.1). Similar analyses are performed for organs and tissues with fenestrated or non-fenestrated vasculature. For tissue with non-fenestrated vessels, such as bone, heart, liver, and muscle, the molecular weight cutoff for 50% extraction is low due to high blood flow rates and low permeability: bone (<570 Da), heart (<100 Da), lung (<80 Da), muscle (<600 Da). Fenestrated organs resulted in higher molecular weight cutoffs as seen by kidney (<3600 Da), endocrine pancreas (<3000 Da), and exocrine pancreas (<6900 Da).

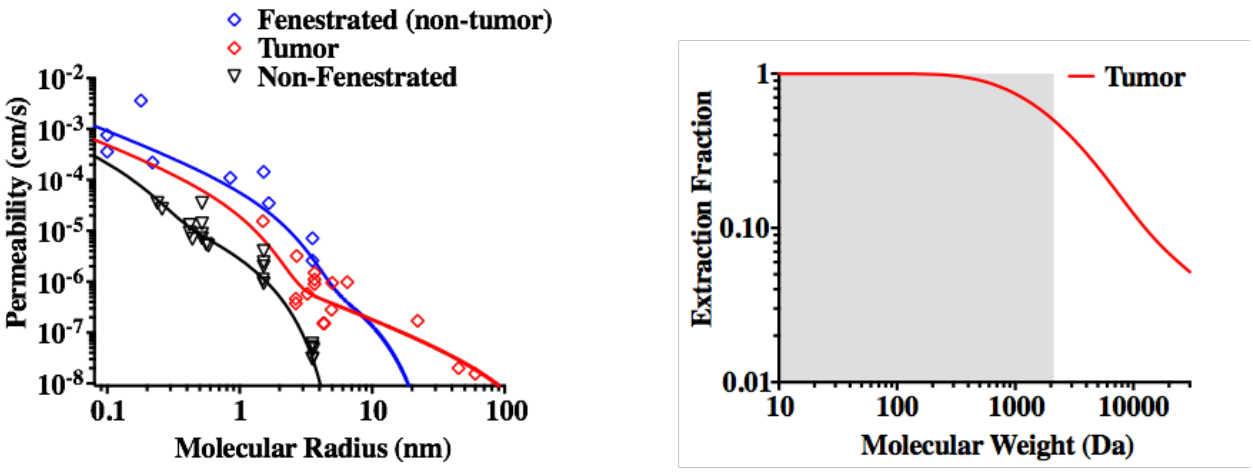

Figure 2.1 Optimal molecular weight probes for different tissue types
The values are based on 50% extraction fraction using the vessel type, blood flow, and vessel surface area. Tumors have elevated macromolecular permeability, but the elevated interstitial pressure may contribute to lower effective permeability than fenestrated tissue for low molecular weight compounds. The data and fit for tumor values are identical to ref.[25] (left). The 50% extraction fraction is an arbitrary cutoff based on diminishing returns as seen for the tumor (right).

To examine the impact of affinity, we selected two series of compounds in this size range against a tumor antigen, HER2, and an endocrine pancreas target, GLP-1R, and compared experimentally measured versus predicted uptake. In the case of the high HER2 expressing tumor cell line (SKOV-3 > 10^6 receptors/cell), predicted uptake approaches the maximum value 14-15 %ID/g at binding potential (BP = target concentration relative to dissociation constant, $[T]/K_d$) values of 50 or greater (K_d < 20 nM) for these slowly internalized affibodies. Experimental results indicate affibody molecules with measured K_d < 20 nM indeed achieve 14-15 %ID/g experimentally (e.g. PEP07127 with a 3.8 nM K_d, Figure 2.2). For a tumor with ~30-fold lower expression (LS174T tumors = 30,000 receptors/cell), the affinity must be 30-fold higher for the same BP. Therefore, the K_d must be < 0.7 nM for high uptake. In agreement with these results, PEP07127 has low uptake in LS174T xenografts, but ZHER2:342 (K_d = 0.022 nM) achieves high ~15%ID/g uptake.

The *in silico* predictions in most cases agreed with experimental results. These simulations assume complete residualization (all the internalized probe is trapped within the cell indefinitely). Metallic radionuclides such as technetium and indium are known to be residualizing labels[140-144] over the time scale of the experiment, while halogen radionuclides such as iodine are non-residualizing[145, 146]. This could explain the lower iodinated compound experimental values in Figure 2.2.

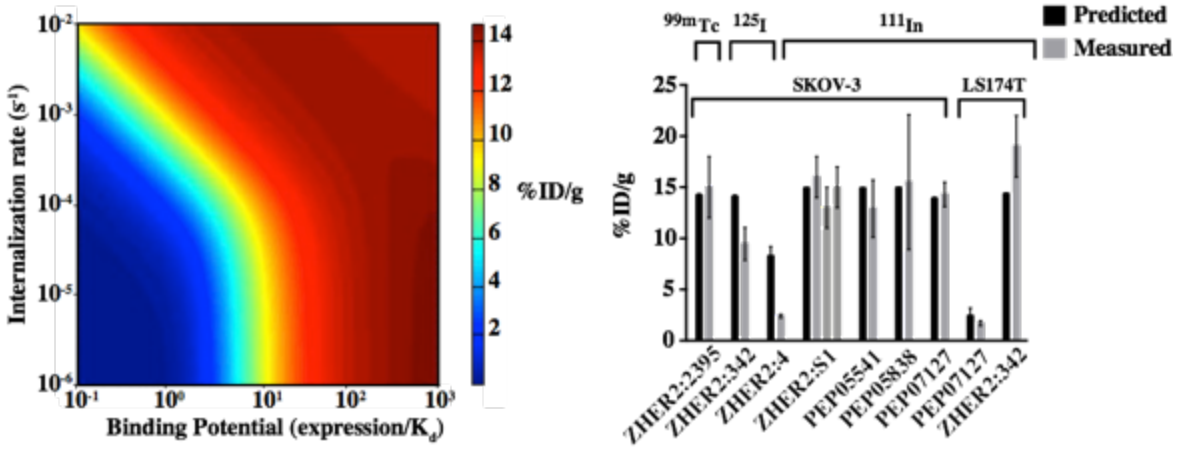

Figure 2.2 Computational model of tumor targeting with peptide agents versus experimental results
Using the physiology of a tumor, the targeting efficiency (%ID/g) is graphed versus the internalization rate and binding potential (a function of target expression and affinity, left). These results are compared with a series of affibody molecules varying in affinity, radiolabel, and target expression (right).

The predicted uptake in the endocrine pancreas is very different from the tumor in both magnitude and shape. The higher blood flow and permeability results in much larger maximum uptake values but also more stringent binding affinity requirements (a general shift to the right of Figure 2.3). Because GLP-1R expression (54,000 receptors per cell) is closer to SKOV-3 levels, a high affinity requirement would be expected. However, the internalization rate of GLP-1R is much faster ($2x10^{-3}$/s), trapping probe inside the cell before it can dissociate. Therefore, a K_d of

~10 nM is needed for efficient targeting. In agreement with these predictions, a decrease in affinity from 2.6 nM to 8.3 nM had a minimal impact on pancreatic uptake[147].

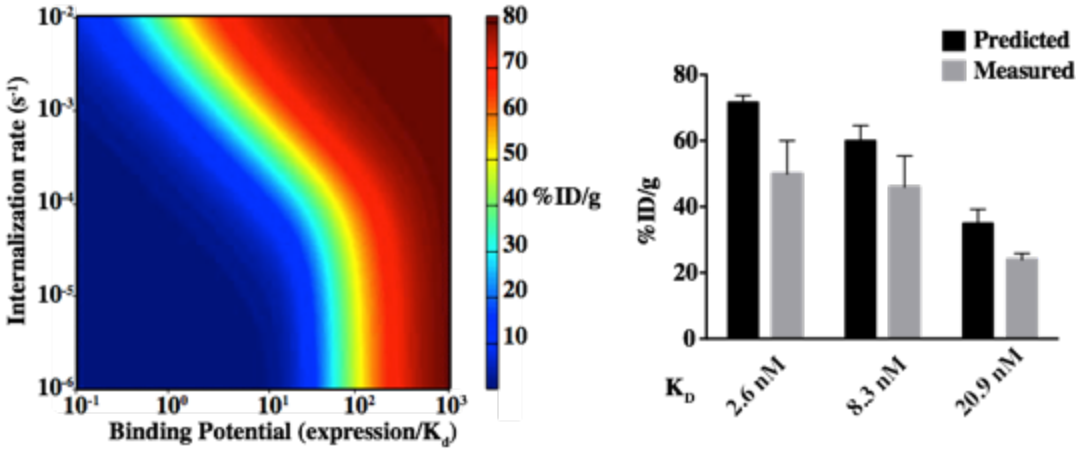

Figure 2.3 Computational model of endocrine pancreas targeting with peptide agents versus experimental results
The physiology of pancreatic islets results in much higher potential targeting %ID/g due to higher blood flow and vascular density. The more efficient transport also shifts the contour lines to the right, requiring higher affinity due to faster washout (left). A comparison of predictions with published data on exendin based peptides of varying molecular weight and affinity highlights how the rapid internalization reduces the stringency in binding affinity despite the faster transport (right).

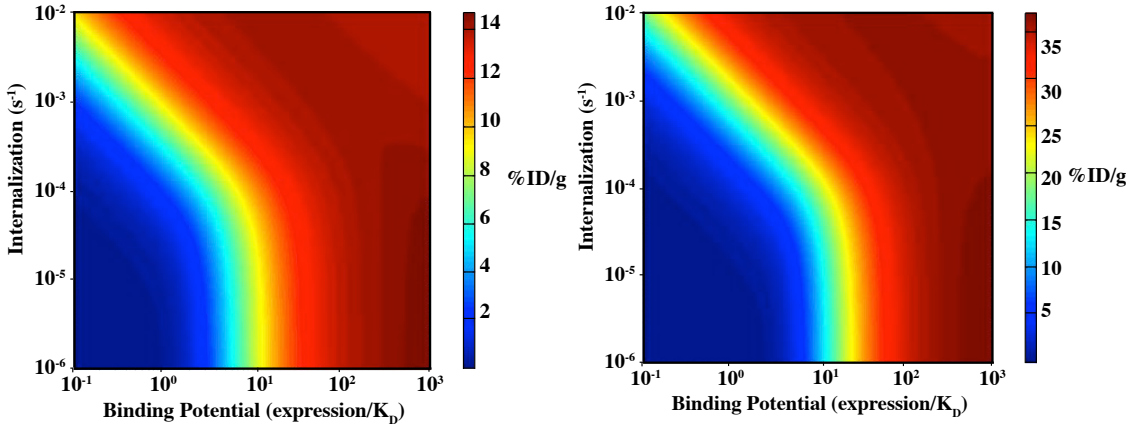

Figure 2.4 Impact of vascular density on simulations
Contour plots for tumor uptake of a small peptide to demonstrate the effect of blood vessel surface area to volume (S/V). Left plot uses an S/V value of 60 cm^{-1}; Right plot uses an S/V value of 200 cm^{-1}. Two noticeable differences between the plots include 1) a higher maximum tumor uptake with a greater S/V (top) and 2) near-maximum uptake occurs at a higher binding potential (higher expression or lower affinity) for greater S/V.

To quantify the background signal, two additional probe data sets were examined – low molecular weight prostate specific membrane antigen (PSMA) ligands and integrin binding ligands. Plots of TBR versus blood clearance for both integrin and PSMA binders (Figure 2.5) show similar trends. In the case of PSMA binders, at 4 h post-injection, much higher TBRs (tumor to muscle ratio) can be achieved for compounds with low blood concentration ($R^2 = 0.69$, MIP1095 omitted). MIP1072 and MIP1404, the compounds with the highest 4 h TBR at 171 and 157, respectively, maintained relatively low blood uptake of 0.06 and 0.02 %ID/g, respectively. MIP1405, MIP1427, and MIP1428 achieved TBR values of 72, 31, and 42 respectively and displayed relatively slow blood clearance with 4 h blood uptake values of 0.26, 0.28, and 0.14 %ID/g. Integrin binders show a similar relationship between TBR and blood uptake ($R^2 = 0.34$, compound **17** omitted). These results indicate that in this size range (well below the renal filtration cut-off), more rapid plasma clearance benefits TBR by reducing the background. Although properties such as plasma protein binding may slow clearance and allow more time for target uptake, this effect is mitigated by the fact that plasma protein binding also reduces extravasation rates of the free probe.

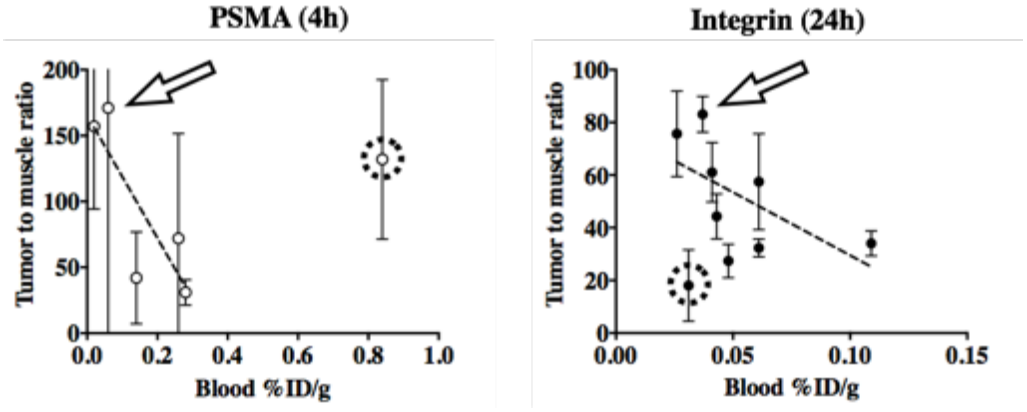

Figure 2.5 Impact of non-specific uptake in background tissue (i)
For both low molecular weight PSMA binders (left) and integrin binders (right), the highest TBR values (arrows) occur for low blood signal. The lines indicate a general trend of lower TBR with higher blood signal. The circled data were excluded as described in the text. Although faster

clearance has the potential to lower target uptake and reduce TBR, these results indicate this is generally not the case in this size range.

A correlation between charge and TBR was also investigated using uptake values from the PSMA and integrin targeting compounds. A plot of TBR versus the overall charge of all compounds at pH 7.4. The plot suggests no evident trend between charge and uptake (R^2=0.05, R^2=0.01 for PSMA and integrin binders, respectively) likely due to the importance of chelation chemistry in determining overall molecular charge and highlighting one challenge in prediction from pure structure.

A series of three affibodies was studied by Tolmachev et al. to examine the impact of affinity and physicochemical properties of small proteins on targeting[148]. Comparing peptides PEP05838 and PEP05541, the sequence was more hydrophobic[149] for PEP05838, resulting in higher liver uptake (Figure 2.6). The lowest uptake occurred for PEP07127, which notably differed by a hydrophilic residue in the middle of an otherwise hydrophobic patch on the surface. However, based on sequence alone, PEP07127 had an intermediate hydrophilicity, indicating secondary structure can play a driving role even for residue changes on a single alpha helix. Similar to integrin and PSMA binders, the blood clearance was compared to TBR.

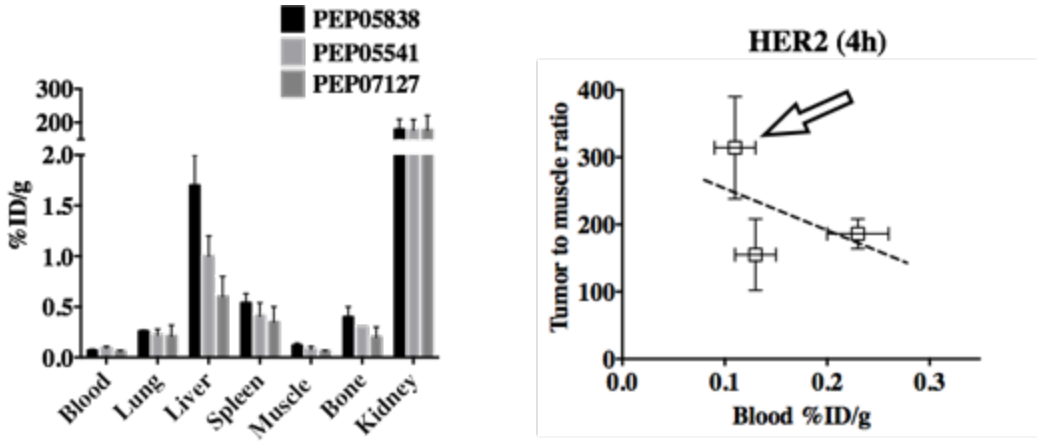

Figure 2.6 Impact of non-specific uptake in background tissue (ii)
For proteins/peptides, even a single alpha helix can result in secondary structure playing a significant role in determining non-specific uptake (C). The substitution of a single amino acid in the middle of a hydrophobic patch on PEP07127 reduced background tissue concentrations, resulting in the highest TBR and fastest blood clearance (D).

The data indicate that rapid plasma clearance is beneficial for molecular imaging agents in this size range, and we hypothesized that non-specific interactions could quantitatively explain the differences in clearance from the blood. However, there is no simple correlation between physicochemical properties of small molecules or sequence of peptides and efficient clearance due to the large number of non-specific low affinity (ionic, hydrophobic, colloidal) interactions that are difficult to predict from structure alone. To prospectively explore the impact of physicochemical properties on clearance, a series of fluorescent integrin binding peptidomimetic agents was synthesized using different fluorescent dyes to manipulate the physicochemical properties. Two different assays were used to measure non-specific interactions – a non-specific cellular uptake assay and an equilibrium plasma protein binding assay. The cell-based assay used excess non-fluorescent probe to block specific interactions and measured the increase in fluorescence signal over time, and the plasma protein binding assay was used as a surrogate for overall non-specific interactions. Plasma clearance of the probes was measured in C57BL/6 mice

over 24 h. The most hydrophobic agent had very rapid early phase decay but had higher signal at later times, while the more hydrophilic probes had increased clearance at 24 h. Rapid redistribution into tissues lowers the plasma concentration initially, but whole body clearance from tissues has a larger impact on TBR[150]. Both the non-specific cellular uptake and plasma protein binding correlated with plasma clearance and can be run in a high-throughput manner (Figure 2.7). The methods each had different strengths. The plasma protein binding assay is cell-free, resulting in less variability, and protein binding also affects uptake in the target tissue[151], so it is useful for correlating with both uptake and background signal. However, for certain compounds it is difficult to achieve equilibrium using dialysis. In these cases, such as with larger peptides, proteins, and compounds that interact strongly with the dialysis membrane, the cellular uptake assay can be used.

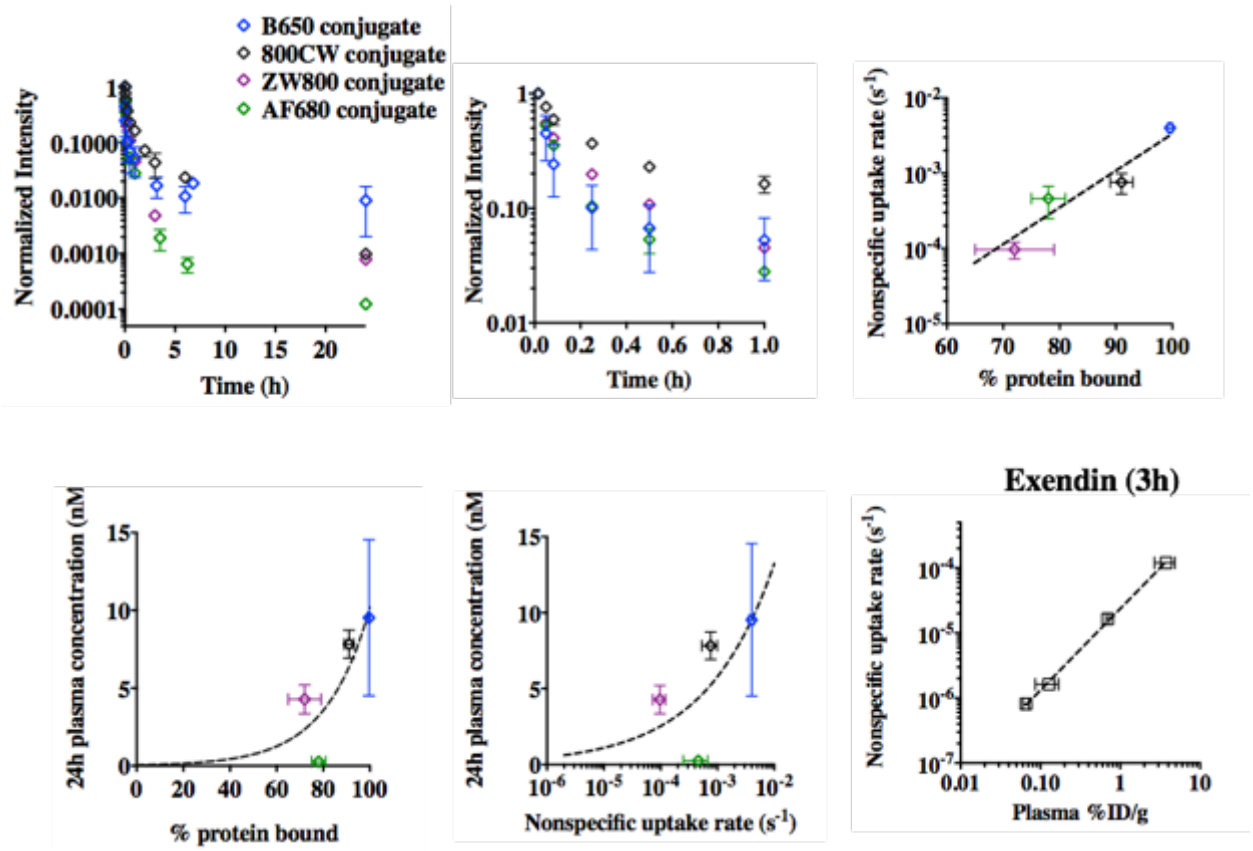

Figure 2.7 High throughput methods for quantifying non-specific uptake
Lower plasma protein binding and non-specific cell uptake generally correlate with faster plasma clearance for a series of integrin probes with the exception that very lipophilic compounds can redistribute rapidly in the tissue, causing high background but low plasma signal (A) particularly at early times (e.g. BODIPY 650 conjugate, B). Plasma protein binding, a common assay for small molecule drugs, correlates with non-specific cell uptake in vitro (C). For plasma protein binding, there are diminishing returns when lowering the fraction below ~60% bound (D). Based on the non-specific cell uptake assay, which is useful for agents that cannot undergo rapid equilibrium dialysis (e.g. due to molecular weight or membrane sticking), a non-specific in vitro cell uptake rate of less than ~10^{-5} s^{-1} also has diminishing returns (E) providing quantitative guidance on probe selection. Four exendin derivatives where plasma protein binding could not be measured directly show that the non-specific cell uptake assay correlates with plasma clearance (F).

Given the increasing use of near-infrared fluorescence in preclinical studies and clinical applications (for intraoperative imaging), we measured the protein binding of a series of fluorescent dyes (Table 2.2, some dyes displayed higher variation than other compounds). While

the targeting ligand and linker also impact the overall plasma protein binding, the relative scale of these values can be useful in estimating overall probe PPB.

Table 2.2 Plasma protein binding of near-infrared dyes and conjugates

Compound	Ex/Em (nm)	% Plasma Protein Bound
BODIPY 650 conjugate	646/660	99.6 ± 0.4
Alexa Fluor 680 conjugate	684/707	78 ± 3
IRDye 800CW conjugate	774/789	91 ± 2
ZW800 conjugate	768/786	72 ± 7
BODIPY 650 carboxylate	646/660	99.8 ± 0.3
Alexa Fluor 680 carboxlyate	684/707	81 ± 6
IRDye 800CW carboxylate	774/789	89 ± 3
ZW800-1 carboxylate	768/786	81 ± 5*
ICG-dye	~800/826	99.5 – 99.75*
SIDAG dye	755/778	57*
Alexa Fluor 647 carboxylate	651/672	76 ± 1
DDAO carboxylate	646/659	98.8 ± 0.2

2.5 Discussion

Molecular imaging agents can provide detailed insight into *in vivo* biological phenomena in a minimally invasive manner. However, the development of these agents is time consuming and costly. There are often tissue and target-dependent trade-offs between properties that maximize signal, foiling empirical approaches and extrapolation from published values. To

improve the design of imaging agents and help focus preclinical experiments on the most promising molecules, we analyzed and quantified the mechanistic trade-offs for probe development.

Parameters that determine target uptake for *in vivo* imaging can be categorized as either an imaging probe property or a tissue property (Scheme 2.1). Molecular weight and charge play a role in uptake and clearance, while affinity and label residualization impact target retention. These imaging agent values are all relative to the tissue properties, making generalizations difficult. For radionuclides, the choice of radioisotope and chelator are also critically important. Certain aspects such as ease of synthesis and stability of the complex *in vivo* are beyond the scope of this analysis. However, other properties, such as the radioisotope decay half-life (where isotopes with short half-lives are acceptable for rapidly cleared agents), residualization rate of the radioisotope, and chelation chemistry (which impacts plasma protein binding and non-specific interactions) all have an impact on the parameters discussed here.

The molecular properties of the targeting probe are under the direct control of the researcher, and these must be optimized according to the target tissue type for maximum signal and contrast. Based on a previous analysis of targeting efficiency in tumors, two local maxima exist for target uptake – one at single kDa molecular weight ranges and one close to the size of antibodies[25]. For imaging agents, clearance is important for contrast, so lower molecular weight probes result in higher target to background ratios. Antibodies rarely have tumor to organ ratios above 100 and are typically 3-10[152, 153]. However, several low molecular weight probes cited in this work reach ratios above 100, and importantly, these high TBR values developed within several hours after injection versus days for antibodies. Therefore, we focused on the optimization of low molecular weight compounds in this analysis.

Based on size versus permeability and clearance, a lower molecular weight is more efficient in target uptake. However, we sought to determine the optimal size of an agent, since eventually blood flow limitations negate any benefits from smaller size. Molecular weight cutoffs were established for various tissues using a 50% extraction fraction criterion (related to the vessel depletion number[24]). Predictions indicate non-fenestrated organs with small pore sizes such as bone, heart, lung, and muscle have a significantly lower size cutoff compared to the fenestrated kidney and pancreas. The predictions also indicate that in organs with high plasma flow such as heart (4.06 mL/min/g) and lung (24 mL/min/g), the extraction fraction can be very low for many probes (albeit a low fraction of extremely high delivery).

The blood flow and extraction fraction determine the amount of probe reaching the tissue, but this does not account for binding and retention of the imaging agent at the target. While antibodies can readily be engineered for high affinity (~ 1 nM K_d), high affinity low molecular weight compounds can be more challenging to design[154-157]. Given this common trade-off between molecular weight and affinity (such as dimerization increasing apparent affinity but also molecular weight[158]), we next determined the required dissociation constant for efficient localization.

A predictive and mechanistic model was used for comparison with published values of tumor and endocrine pancreas uptake for two classes of targeting molecules (Figure 2.3,Figure 2.4) – HER2 binding affibodies (MW ~ 6 kDa) and GLP-1R binding peptides (MW ~ 5 kDa for monomer). Tumor cell lines with high (SKOV-3) and low (LS174T) expression of HER2 were simulated for the HER2 agents. To account for varying expression levels, the binding potential was compared to the internalization rate. Varying either [T] or K_d to manipulate BP gave the same results. Predicted uptake values were calculated assuming tracer (subsaturating) doses.

However, tumor xenografts with low expression levels can readily be saturated, and several data points were excluded due to reported evidence of target saturation[159]. Because plasma protein interactions are not well-characterized for these molecules in the literature, a single value of plasma protein binding was assumed (42% bound); this is the experimentally estimated value for fluorescent exendin, a peptide with similar molecular weight and alpha helical secondary structure. However, the value could be higher due to possible interactions with other plasma proteins[160].

The simulation results agreed well with the literature reported values for HER2. With the very high expression levels in SKOV-3 cells, a 3.8 nM binder (PEP07127) is sufficient for high uptake, but a 50 nM K_d (ZHER2:4) lowers the signal. In contrast, the lower expression on LS174T xenografts results in lower uptake of the 3.8 nM binder and requires a 22 pM affinity (ZHER2:342) for high retention. (Note that the required affinity is also a function of the molecular weight, and for low affinity interactions, higher targeting efficiency can often be achieved by increasing the molecular weight above the optimal range discussed here[25].)

The model predictions are also in agreement with uptake of exendin monomers, dimers, and trimers in the endocrine pancreas despite very different tissue physiology. For the slowly internalized affibody-HER2 complex[161, 162] (3.9×10^{-6} s^{-1}), a very high affinity (< 1nM) was required for maximum uptake with moderate receptor expression (LS174T). In contrast, the much more rapidly internalized GLP-1 receptor (2×10^{-3} s^{-1}) has a lower requirement (< 10 nM) for high uptake even with similar expression levels as LS174T (54,000 GLP-1 receptors versus 30,000 HER2 receptors per cell) as seen with the 8.3 nM binder. Uptake is only noticeably reduced with a K_d of 20.9 nM. The model slightly over-predicts uptake, which could be a function of error in any of the model parameters that were not fit, such as plasma protein

binding, wt% of beta cells, permeability, etc. Importantly, these simulations highlight the differences in affinity requirements based on tissue properties and target internalization. Since these probes are given at tracer doses, internalization does not amplify the signal like it would for a saturating dose. However, it does reduce the required affinity since the probe is internalized and trapped prior to dissociation. These data demonstrate that the required affinity is a function of target expression, tissue physiology, and internalization rates.

Unlike target uptake rates that can be predicted with reasonable accuracy from sigmoidal binding curves and measured extravasation rates, the background signal is more challenging to predict. Low molecular weight agents are cleared more rapidly than higher molecular weight agents[163, 164], but for small molecules well below the nominal renal molecular weight cut-off, non-specific interactions play a large role. For these agents, molecules that interact strongly with plasma proteins will have slower clearance times[165, 166]. While this may allow more time for uptake, this also reduces extravasation in the target tissue[165], resulting in little to no net gain. In addition, non-specific interactions can increase background signal.

Although there may be no net gain in target uptake relative to plasma protein binding, we hypothesized that molecules with weak plasma protein interactions and fast blood clearance times would have lower background uptake *without a loss* in target uptake, resulting in higher TBR when imaging. This is in contrast to known trends for larger proteins where lower molecular weight results in a higher TBR but at the expense of lower target uptake[131]. Importantly, plasma protein binding can be measured in a high-throughput manner in contrast to animal biodistribution experiments, thereby providing a screening tool. To demonstrate this trend, two published series of low molecular weight targeting ligands with varying affinity and clearance rates targeting either PSMA or integrin of the form αvβ3 were considered. At long

times post-injection, both sets of molecules showed that the highest TBR values were obtained with the lowest blood %ID/g. There was also a general correlation with higher TBR with lower blood signal, although two outliers existed in the data, and the data are scattered due to the many additional factors that impact TBR beyond background clearance (e.g. affinity). One exception in the PSMA set (Figure 2.5 dotted circle, left) is compound MIP1095, which exhibited both slow clearance and a high TBR. This molecule exhibited the strongest affinity for all PSMA binders tested (K_d = 240 pM), the highest tumor uptake (34.3 %ID/g), and the highest skeletal muscle uptake (0.26 %ID/g). This outlier demonstrates one of many quantitative trade-offs, where having a strong affinity at the cost of poor clearance can still result in a high TBR. All properties (not just plasma clearance) must be quantitatively considered together.

The nine bivalent integrin-targeting agents designed with various spacer lengths also support the notion that molecules that have a low blood uptake at 24 h post-injection are able to achieve a higher TBR. Again, the highest TBR values corresponded to the lowest blood signal. One outlier is compound **17** (Figure 2.5 dotted circle, right), where both blood concentrations and TBR at 24 h were low at 0.031 %ID/g and 18, respectively. However, this results from unusually high muscle uptake of > 0.6 %ID/g, much higher than all the other compounds in the series and actually increasing from 4 to 24 h. This suggests specific uptake of the probe in muscle or an experimental artifact.

Weak and non-specific interactions between molecules are challenging to predict. These interactions are being investigated for large proteins such as antibodies, and comparisons with these findings provide some insight[167, 168]. Hydrophobic and charged patches on the surface of these proteins can increase colloidal interactions, changing the pharmacokinetic properties. Notably in the case of antibodies, non-specific tissue interactions *increase* clearance from the

normally long-circulating molecules[169], while plasma protein interactions typically *decrease* the clearance of the normally rapidly-cleared small hydrophilic molecules discussed here.

PSMA and integrin ligand results show there is no simple correlation between TBR and overall charge. Many of the charges come from the chelating agent, and chelator selection is a critical component of probe design[170, 171]. Some chelated metals have very low non-specific interactions like indium-DTPA while others have higher plasma protein binding and overall lipophilic properties like Tc-99m-DTPA[150, 172]. More hydrophilic chelators have been designed, but here again these do not completely correlate with physicochemical properties[78], making predictions from structure alone challenging.

Tolmachev and colleagues' analysis of non-target uptake for affibodies as a function of hydrophobicity provides insight into peptide agent design compared to non-peptide small molecule ligands[148]. Compound PEP07127, due to an L18S amino acid substitution, disrupted a hydrophobic patch present in the original compound. Even for this small region on an alpha helix, the secondary structure played a role in non-specific interactions. As pointed out by these authors, the results are pertinent to the development of high affinity proteins and peptides, where many binding interfaces have hydrophobic regions driving high affinity[148], highlighting a direct trade-off between affinity and background signal. Hackel et al. investigated the impact of surface charge and hydrophilicity modification on fibronectin compounds[173]. By manipulating the surface properties, they were able to control the distribution in the two major clearance organs, liver and kidney. Our current analysis does not focus on clearance organs, but for the integrin and PSMA binders, more efficient clearance from the blood generally correlated with lower signal in the liver and kidneys for these non-peptide agents.

The affibody results highlight the fact that predicting the impact of amino acid substitutions on the abundant *in vivo* low affinity interactions that depend on sequence and structure is extremely complex and challenging, particularly in the context of screening compounds where the structure may not be known. Rather, taking a lead from the protein engineering field[167, 168, 174], experimental methods of measuring non-specific interactions in a high-throughput manner may be more fruitful. Hydrophobic and other non-specific interactions impact off-target uptake of these molecules and directly lower tumor to organ ratios. Conversely, the highest TBR value occurred for the compound with the lowest blood signal, consistent with the integrin and PSMA imaging agent series. The clearance is likely a direct result of increased plasma protein interactions, which is challenging to quantify for peptides. Accurate plasma protein quantification for lower molecular weight molecules is possible using several techniques, such as rapid equilibrium dialysis or ultrafiltration, and these were investigated next.

To compare two methods of measuring non-specific interactions for correlating with plasma clearance, we generated a series of small molecule fluorescent peptidomimetics using different fluorescent dye structures to manipulate the physicochemical properties. Non-specific interactions due to lipophilicity have been characterized for many visible light fluorophores[175, 176] but less is known about these interactions for near infrared (NIR) fluorophores, which have *in vivo* advantages for imaging. *In vivo* clearance and non-specific uptake rates of peptidomimetics using NIR fluorophores such as AF680, 800CW, and ZW800 demonstrate the impact of non-specific interactions on imaging agent design. The plasma clearance was measured over 24 h (Figure 2.7A) and compared to plasma protein binding measured by rapid equilibrium dialysis and non-specific uptake in cell culture. The cell uptake rates correlated with plasma protein binding, indicating these assays may be providing similar information on non-specific

interactions (Figure 2.7C). The probes with lower plasma protein binding typically had more rapid alpha phase clearance and lower plasma signal at 24 h. Given the correlation with higher TBR in Figure 2.5 and Figure 2.6, this could be incorporated into high throughput screening methods for determining propensity to clear from tissue. Note that the most lipophilic agent (BODIPY 650 conjugate) had a fast early (alpha phase) clearance but higher signal at 24 h. It is important to distinguish rapid clearance from rapid redistribution of probe from plasma to tissue, since the former can lower background signal while the latter can significantly increase it (e.g. PEP05838, Figure 2.6[148]).

The plasma protein binding assay has the advantage of a cell free system (reduced variability) and simultaneously provides data on target uptake (since it is generally unbound probe that enters tissue). However, commercially available assays typically only work for probes less than 1-2 kDa in size and can have problems with agents that have extensive interactions with the dialysis membrane, making the cell uptake assay a viable alternative. As an example, four exendin peptide conjugates were synthesized with varying hydrophobic properties. Although plasma protein could not be quantified due to their higher molecular weight, the non-specific cell uptake rate was significantly higher for the more lipophilic conjugates and correlated with the 3 h plasma concentration in mice (Figure 2.7F).

The relative values of plasma protein binding and non-specific cell uptake can be used to rank order compounds, but an absolute guideline is helpful in determining if further molecular engineering is warranted. Similar to reductions in molecular weight and increases in affinity, there are benefits of increasing hydrophilicity to reduce background (such as addition of PEG to integrin binders[177]), but eventually there are diminishing returns with further effort. Based on the data presented here and literature values (SI), a significant reduction in background is not

expected below 60-80% plasma protein binding or $10^{-5}s^{-1}$ cellular uptake rate. (For comparison, pinocytosis rates[178] have been estimated around $1.1x10^{-5}s^{-1}$.) Further improvements beyond these levels may be obtained by reducing these parameters, but this is not without cost. Molecules in this size range that have no measurable plasma protein binding, inulin being a classic example, are very hydrophilic and flexible in direct contrast to most high affinity binding interfaces.

Given the increasing use of near-infrared probes for preclinical studies and clinical intraoperative imaging, we quantified the plasma protein binding of several commercially available dyes to guide fluorescent probe development. While the conjugates of these dyes will have altered plasma protein binding (and lose the carboxylic acid once they are conjugated to an amine), the relative magnitude can be used to estimate overall properties. For dyes in the 680-700 nm range, Alexa Fluor 680 had the lowest plasma protein binding of the dyes tested, while for the 750-800 nm range, ZW800-1 had the lowest plasma protein binding. These values, in addition to the dye residualization rates[179], are helpful in rational design of NIR probes.

2.6 Conclusion

In conclusion, we have analyzed data from 28 low molecular weight probes to provide a quantitative and mechanistic framework for comparing cell surface imaging agents. The qualities of optimal imaging agents are well known, but in practice, there are many trade-offs. This analysis is designed to quantitatively determine the magnitude of these impacts to select the most promising agents for preclinical analysis. For example, data on blood flow and permeability could be used to identify an appropriate scaffold and/or library for screening based on the target tissue (Table 2.1). The internalization and expression level of the target can be used to define a target affinity or compare predicted retention of lead compounds (Figure 2.2). A high throughput

test of plasma protein binding and/or non-specific cellular uptake can be used to quantitatively compare the background signal (Figure 2.7). Alternatively, for a series of *in vitro* characterized compounds, these plots can be used to quantitatively compare the expected TBR based on molecular weight, affinity, and lipophilicity/non-specific interactions. These data will help select the most promising candidates to move forward in a more quantitative and rational manner for molecular imaging agent design.

2.7 Experimental Methods

Computational Model Development

The original tissue simulation model was based on a non-linear partial differential equation model of tissue concentration with time-varying mixed boundary conditions and axial and radial gradients[180]. This model provides a self-consistent framework for simulating the distribution of agents from small molecule drugs to biologics and nanoparticles[181]. To limit the scope of the simulations, we used previous modeling results indicating that the highest target uptake occurs for very low molecular weight agents and those similar in size to antibodies[25]. In addition to high uptake, low molecular weight compounds benefit from rapid clearance and have demonstrated target to muscle ratios over 100[182, 183]. To focus on the design of imaging agents for extracellular targets, lipophilic compounds that can diffuse across plasma membranes with significant retained intracellular signal were excluded[184]. Finally, since imaging agents are ideally delivered at tracer doses, a subsaturating dose was assumed. Based on the four classes of pharmacokinetic behavior in tissue (blood flow-limited, permeability-limited, diffusion-limited, or binding/metabolism-limited agents)[181], the lack of transcellular extravasation of highly lipophilic compounds and tracer dose eliminates the diffusion-limited and binding/metabolism-

limited regimes, respectively, narrowing the analysis to blood-flow and permeability limited probes. Since peptide and protein-based agents form a large contingent of extracellular imaging agents, we focused on a permeability-limited model subject to blood-flow limitations.

A compartmental analysis assuming equilibrium binding was performed on plasma, tissue, and internal compartments (SI). Briefly, the imaging agent extravasates from the plasma compartment into the tissue compartment, where it is either receptor-bound or free. Bound imaging agent is then trafficked to the internal compartment. Binding equilibrium is assumed to be very fast relative to diffusion of the imaging agent out of the plasma. The model also assumes a sub-saturating tracer dose of imaging agent with the receptor in excess. It can be shown (SI) that the concentration of imaging agent in the extracellular tissue and internal compartments as a function of time can be represented by

$$P_{tissue} = (1-x)P_{plasma,0}\frac{2PR_{cap}}{R_{Krogh}^2}\left[\frac{A}{\Omega - k_\alpha}\left(e^{-k_\alpha t} - e^{-\Omega t}\right) + \frac{B}{\Omega - k_\beta}\left(e^{-k_\beta t} - e^{-\Omega t}\right)\right] \tag{2}$$

and

$$P_{\text{int}} = \Phi\left[\frac{A}{\Omega - k_\alpha}\left(\frac{e^{-k_\alpha t} - e^{-k_{\text{deg}} t}}{k_{\text{deg}} - k_\alpha} + \frac{e^{-k_{\text{deg}} t} - e^{-\Omega t}}{k_{\text{deg}} - \Omega}\right) + \frac{B}{\Omega - k_\beta}\left(\frac{e^{-k_\beta t} - e^{-k_{\text{deg}} t}}{k_{\text{deg}} - k_\beta} + \frac{e^{-k_{\text{deg}} t} - e^{-\Omega t}}{k_{\text{deg}} - \Omega}\right)\right] \tag{3}$$

where

$$\Omega = \frac{2PR_{cap}}{\varepsilon R_{Krogh}^2}\left(\frac{K_d}{R/\varepsilon + K_d}\right) + k_{\text{int}}\left(\frac{R/\varepsilon}{R/\varepsilon + K_d}\right) \tag{4}$$

$$\Phi = k_{\text{int}}(1-x)P_{plasma,0}\left(\frac{R/\varepsilon}{R/\varepsilon + K_d}\right)\left(\frac{2PR_{cap}}{R_{Krogh}^2}\right) \tag{5}$$

The parameters are described in the supplementary file. This model was used in conjunction with experimental data and simplifying assumptions to quantify the impact of probe and tissue parameters on target to background signal. While high contrast is not always necessary for an imaging agent, in most cases (delineating diseased tissue, quantifying changes in receptor expression) high contrast is beneficial and reduces artifacts from surrounding tissue signal.

The strategy outlined in this approach aims to maximize TBR by internalizing the probe within the target cells and minimizing binding/sticking and internalization in non-target tissues. An alternative approach is to select targets that are slowly internalizing and design probes that rapidly leak out of cells once they are metabolized. This would lower the signal intensity in off-target and clearance organs such as the liver and kidney. While this has been shown to improve target to background ratios for these organs[185], there are several limitations to this approach. The internalization, metabolism, and clearance of the probe from non-target tissue has to occur much faster than in the target tissue. Since metabolism and clearance often takes several hours to a day or more, ideally the target would not be internalized significantly over this time frame. Because most cell surface proteins have a constitutive rate of several hours[186], this greatly limits the number of applicable targets. As noted in Figure 2.3, this can increase the required affinity for high target uptake by 10 to 100-fold. Finally, the lipophilic chelate can increase plasma protein binding and liver uptake, lowering targeting efficiency. Although this approach can decrease the liver signal more than it decreases the target signal[185], in contrast, the approach discussed in the current work decreases non-specific uptake while *increasing* target signal. This may explain why the reported TBR values for the current approach are much higher than those achieved by a non-residualizing agent[185].

Permeability versus Molecular Weight

The relationship between molecular radius and permeability was modeled using a two-pore representation as described by Schmidt et al[25]. Previously reported measurements for permeability (P) for small molecules, peptides, proteins, polymers, and liposomes were compiled from literature (SI) and fit to determine the radii and fractional area of small and large pores. To quantify the extraction ratio of various molecular weight molecules, the permeability was first calculated using the two-pore prediction with the appropriate tissue vasculature. Then, using experimentally measured values for plasma flow rate and S/V (SI), a mixed flow and permeability-limited model was adopted from Tofts et al. to predict the fraction of imaging agent extracted from blood to tissue[24]. Organ systems were categorized as either fenestrated (kidney, pancreas), non-fenestrated (bone, heart, lung, muscle), or tumor for analysis (SI). A two-pore model was used to generate optimized fits for each of the three categories based on vasculature type.

Affinity versus Expression and Internalization

To predict uptake in various tissue types, a previously published model was used[180]. In short, the non-linear partial differential equation (PDE) model utilizes a Krogh cylinder geometry of tissue vessels with both axial and radial gradients for the imaging agent. Plasma concentration is modeled with biexponential decay with local concentrations determined by blood velocity and vessel permeability. A list of parameters used for tumor and endocrine pancreas uptake predictions are found in the supplementary data (SI). Experimentally measured affinity values were adjusted for temperature assuming constant free energy of binding. MATLAB was used to solve the system of nonlinear PDEs using finite differences to quantify

tissue uptake. To generate a full %ID/g contour, internalization rates were varied between 10^{-6} s^{-1} to 10^{-2} s^{-1}. Fixing antigen concentration and varying affinity generated a range of binding potential from 10^{-1} to 1000. Identical results were obtained when varying the binding potential by fixing affinity and varying the antigen concentration. Predicted uptake values were compared with experimentally determined values reported in the literature. For endocrine pancreas simulations, whole organ %ID/g was converted to islet %ID/g assuming islets are 1 wt% of the pancreas. Uptake values with 10% increases and decreases in internalization rate, affinity, and antigen expression were used as simulation error.

Plasma Clearance versus Contrast

The impact of plasma clearance on TBR was investigated using previously published data from mammary and prostate tumor models (SI). In short, small molecule inhibitors targeting prostate-specific membrane antigen (PSMA) with various dissociation constants and blood clearance rates were used to target LNCaP or PC3 xenografts in mouse models. Measured values for tumor and skeletal muscle uptake were used to calculate the TBR, which was then plotted against the blood concentration. A similar analysis was performed for various integrin binders targeting mammary adenocarcinomas in a mouse model and HER2-binding affibodies. TBR for both sets of compounds were also plotted against the total compound charge at physiological pH to demonstrate a lack of trend between uptake and molecular charge (SI). An analysis of non-target uptake was performed as well for molecules of varying hydrophobicity using previously published data of anti-HER2 affibodies (SI). Additionally, a correlation between plasma clearance and non-specific interactions was explored for exendin, a 4 kDa therapeutic peptide used to treat type 2 diabetes. The hydrophilic dye Alexa Fluor 680 or a lipophilic non-sulfonated

Cy7 dye were conjugated to exendin[147] using either directly to the 14th position or using a helix-stabilizing linker[187] to generate four variants. The peptides were administered intravenously in C57BL/6 mice and the plasma concentration monitored over time. Non-specific cellular uptake for peptide conjugates in HT1080 cells was quantified as well using *in vitro* assays (SI).

Plasma Clearance versus Non-specific Interactions

The targeting ligand was synthesized by ChemPartner (Waltham, MA) as an ester. The ester was hydrolyzed with 150 μL of ethanol and 7 μL of 1M NaOH per mg of drug overnight, neutralized with 1M HCl, and dried under vacuum. IRDye 800CW NHS ester was obtained from LI-COR (Lincoln, NE), ZW800-1 NHS ester was obtained from Curadel ResVet Imaging (Worcester, MA), and Alexa Fluor 680 NHS ester and BODIPY 650/665-X NHS ester were obtained from Life Technologies (Carlsbad, CA). The hydrolyzed integrin binder was reacted with the fluorescent dyes in a 1:1.5 molar ratio in the presence of 2 μL of triethylamine per mg of drug overnight and purified using a preparative scale Luna C18(2) column (Phenomenex; Torrance, CA) on a Shimadzu reverse phase HPLC unit. Successful conjugation was confirmed by ESI-MS and MALDI-TOF (SI).

All animal experiments were approved by the University of Michigan Institutional Animal Care and Use Committee (IACUC) and carried out in accordance with their guidelines. To quantify the blood clearance, the fluorescent compounds (15 nmol) were injected via the tail vein in C57BL/6 mice. Blood samples were collected at predetermined time points and the plasma concentration of the compounds was quantified using an Odyssey CLx. To quantify non-specific uptake rates, MDA-MB-231 cells were plated in 96 well plates and allowed to attach overnight. The cells were incubated with 200 nM of non-fluorescent ligand for 15 minutes followed by a

co-incubation with 10 nM or 20 nM of fluorescent ligand and 100 nM of non-fluorescent probe. At 15, 30, 45, and 60 min, the cellular uptake was quantified using an Attune Acoustic Focusing Cytometer (Applied Biosystems) with fluorescent beads (Bangs Laboratories, Inc.) to quantify the non-specific uptake rate. Plasma protein interactions were quantified for commonly used, commercially available far-red and near-infrared fluorescent dyes. For IRDye 800CW, ZW800, BODIPY 650, Alexa Fluor 680, and integrin conjugates, a Rapid Equilibrium Dialysis (RED) plate was used following the manufacturer's protocol.

Rapid Equilibrium Dialysis (RED) was used to quantify plasma protein binding for various fluorescent dyes (carboxylate form) and fluorescent conjugates. RED plates are available with membrane molecular weight cutoffs of either 8 kDa or 12 kDa. Given that many of the fluorescent conjugates are >1 kDa, the 12 kDa plate were used to reduce the equilibration time between chambers. The 12 kDa RED plate gave consistent results with small variation for all compounds tested except for ZW800 carboxylate, as seen in the higher standard deviations reported. It is possible the overall net positive charge on the molecule is responsible for interactions with the dialysis membrane. The 8 kDa RED plate resulted in lower plasma protein binding, which would be unexpected based simply on equilibration time. An ultrafiltration method (Centrifree Ultrafiltration Device, Millipore) resulted in lower but variable values of 41 +/- 9% bound for ZW800 carboxylate.

With the exception of ICG and SIDAG, which do not have functional handles for conjugation, the other dyes contain a carboxylate group that will not be present once the dye is conjugated to the targeting ligand. The optical properties of ICG are highly dependent on the microenvironment of the dye, which is impacted by plasma protein binding and partitioning[188, 189]. Additionally, ICG is often delivered at very high doses, which can potentially saturate some

binding sites in plasma and increase the free fraction. The estimates here are based on a subsaturating concentration of ICG[190].

For cellular uptake experiments, HEK-293 cells were used initially. However, the high blocking dose of integrin binder caused dissociation of these cells, so the cancer line MDA-MB-231 was used instead. Pinocytosis rates for macrophages and some tumor cell lines can approach $1.1x10^{-5}$/s from fluid phase uptake[178]. Therefore, the measured uptake rates are postulated to be higher due to non-specific association with the cell surface and internalization.

Exendin non-specific uptake

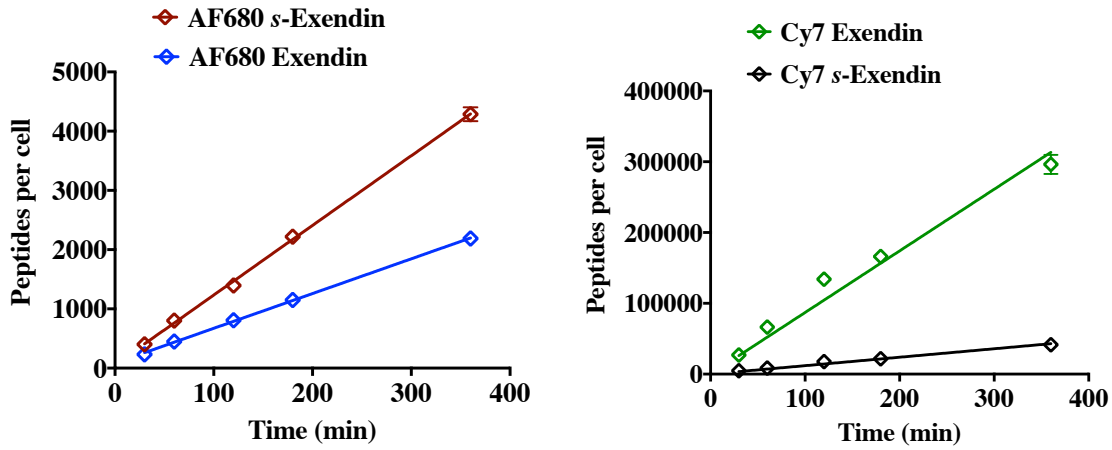

Figure 2.8 non-specific uptake assay of exendin in HT-1080 cells

HT1080 cells were grown in 24-well tissue culture plates. After adhering overnight, cells were incubated with 100 nM of different fluorescent exendin conjugates at 37°C. Fluorescent exendin conjugates are conjugated with either lipophilic or hydrophilic fluorophores to increase or decrease non-specific plasma protein and membrane interactions. After the each time point, cells were harvested and analyzed on an Attune Focusing cytometer to quantify the intracellular signal as a function of time. A blocking control was performed with excess non-fluorescent exendin to demonstrate the fluorescent signal is from non-specific uptake. The number of

internalized molecules per cell as a function of time was used to calculate the non-specific uptake rate.

Modeling Simplifications and Analysis

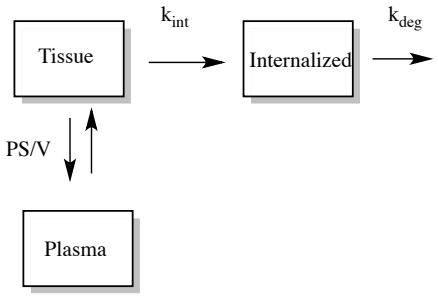

Figure 2.9 Simplified compartmental model for imaging agent concentration

It is assumed the compartments are well-mixed, at equilibrium, and "tissue" compartment consists of bound and free imaging agent. In actuality, imaging agent leaves plasma and into the target tissue; once in the tissue, the free imaging agent binds to target receptors. We assume binding equilibrium is very fast compared to diffusion of the imaging agent out of the plasma. The model assumes the receptor in excess. For these two reasons: 1) fast equilibrium and 2) receptor in excess, target tissue and receptor-expressing cells are combined into one compartment.

Assuming biexponential decay in plasma, the governing equations are shown below:

$$\frac{P_{plasma}}{P_{plasma,0}} = Ae^{-k_\alpha t} + Be^{-k_\beta t}$$

In the tissue, the peptide can be either bound or free

$$R + P_{free} \rightleftharpoons P_{bound}$$

The binding affinity, K_d, can be used to relate bound, free, and receptor concentrations:

$$K_d = \frac{P_{free} R}{P_{bound}}$$

Assuming P_{tissue} is the total imaging agent concentration in the islet is the sum of P_{free} and P_{bound}. Assume receptor R is in excess, following equilibria equations are obtained.

$$P_{free} = \left(\frac{K_d}{R/\varepsilon + K_d} \right) P_{tissue}$$

$$P_{bound} = \left(\frac{R/\varepsilon}{R/\varepsilon + K_d} \right) P_{tissue}$$

The overall balance on extracellular islet concentration P_{islet} can be written

$$\frac{dP_{tissue}}{dt} = \frac{2PR_{cap}}{R_{Krogh}^2}((1-x)P_{plasma} - \frac{P_{free}}{\varepsilon}) - k_{\text{int}} P_{bound}$$

The initial condition is $P(t=0)_{tissue}=0$. Substitute $P_{plasma}(t)$, and the equation can be written in the form

$$\frac{dx}{dt} + ax = be^{-k_\alpha t} + ce^{-k_\beta t}$$

Multiplying both sides by the integrating factor e^{at} and reverse product rule the RHS to give

$$\frac{d}{dt}(xe^{at}) = e^{at}(be^{-k_\alpha t} + ce^{-k_\beta t})$$

integration and application of the boundary condition gives (with appropriate coefficients)

$$P_{tissue} = (1-x)P_{plasma,0} \frac{2PR_{cap}}{R_{Krogh}^2}[\frac{A}{\Omega - k_\alpha}(e^{-k_\alpha t} - e^{-\Omega t}) + \frac{B}{\Omega - k_\beta}(e^{-k_\beta t} - e^{-\Omega t})]$$

with

$$\Omega = \frac{2PR_{cap}}{\varepsilon R_{Krogh}^2}(\frac{K_d}{R/\varepsilon + K_d}) + k_{\text{int}}(\frac{R/\varepsilon}{R/\varepsilon + K_d})$$

This will model the extracellular concentration of probe in the tissue.

To find the intracellular concentration, we use the governing equation for the intracellular compartment

$$\frac{dP_{\text{int}}}{dt} = k_{\text{int}} P_{bound} - k_{\text{deg}} P_{\text{int}}$$

Boundary condition is at t=0, P_{int}=0. With appropriate substitutions, the resulting ODE can be written in the form

$$\frac{dP_{\text{int}}}{dt} + k_{\text{deg}} P_{\text{int}} = be^{-k_\alpha t} + ce^{-k_\beta t} - de^{-\Omega t}$$

Multiplying both sides by the integrating factor $e^{k_{\text{deg}} t}$ and reverse product rule the RHS to give

$$\frac{d}{dt}(P_{\text{int}} e^{k_{\text{deg}} t}) = e^{k_{\text{deg}} t}(be^{-k_\alpha t} + ce^{-k_\beta t} - de^{-\Omega t})$$

integration and application of the boundary condition gives (with appropriate coefficients)

$$P_{\text{int}} = \Phi\left[\frac{A}{(\Omega - k_\alpha)}\left(\frac{e^{-k_\alpha t} - e^{-k_{\text{deg}} t}}{k_{\text{deg}} - k_\alpha} + \frac{e^{-k_{\text{deg}} t} - e^{-\Omega t}}{k_{\text{deg}} - \Omega}\right) + \frac{B}{(\Omega - k_\beta)}\left(\frac{e^{-k_\beta t} - e^{-k_{\text{deg}} t}}{k_{\text{deg}} - k_\beta} + \frac{e^{-k_{\text{deg}} t} - e^{-\Omega t}}{k_{\text{deg}} - \Omega}\right)\right]$$

with

$$\Omega = \frac{2PR_{cap}}{\varepsilon R_{Krogh}^2}\left(\frac{K_d}{R/\varepsilon + K_d}\right) + k_{\text{int}}\left(\frac{R/\varepsilon}{R/\varepsilon + K_d}\right)$$

and

$$\Phi = k_{\text{int}}(1-x)P_{plasma,0}\left(\frac{R/\varepsilon}{R/\varepsilon + K_d}\right)\left(\frac{2PR_{cap}}{R_{Krogh}^2}\right)$$

Table 2.3 Assumptions for model validation

Model assumptions	
1. Subsaturating dose	higher doses will lower TBR, so optimal assumption

2. No blood flow limitations	Important for tumors, which have slower blood flow rates. An extremely rapid clearance may not allow the tumor vessels to fill with probe.
3. Non-specific uptake is linear with concentration	There could be non-linear background uptake (e.g. target specific), but pinocytosis, non-specific binding, etc. are often linear.
Simplifying assumptions	
4. High affinity	Assumes all probe that enters tissue binds and does not dissociate, so optimal assumption. Internalization may help put a limit on the affinity, since once $k_e >> k_{off}$, all of the bound probe internalizes.
5. $k_{deg} << k_\alpha$ and $k_{deg} << k_{int}$	This is an optimal estimate to maximize the signal.
6. The imaging time is greater than k_α so the majority of probe is cleared from the blood	This is a optimal estimate. The signal in blood (both target and non-target) will lower the specific TBR since it is non-specific signal.
The combination of assumptions 4 and 5 above allows us to assume $k_{deg} \sim 0$ so $\exp(-k_{deg}t) \sim 1$ and $\exp(-k_\alpha t) \sim 0$	

Target Tissue

For the target tissue, starting with the model solution above:

At long times, all the blood and surface signal is gone, so only P_{int} determines the signal.

$$P_{\text{int}} = \Phi\left[\frac{A}{(\Omega - k_\alpha)}\left(\frac{e^{-k_\alpha t} - e^{-k_{\text{deg}}t}}{k_{\text{deg}} - k_\alpha} + \frac{e^{-k_{\text{deg}}t} - e^{-\Omega t}}{k_{\text{deg}} - \Omega}\right) + \frac{B}{(\Omega - k_\beta)}\left(\frac{e^{-k_\beta t} - e^{-k_{\text{deg}}t}}{k_{\text{deg}} - k_\beta} + \frac{e^{-k_{\text{deg}}t} - e^{-\Omega t}}{k_{\text{deg}} - \Omega}\right)\right]$$

Assuming high affinity ($K_d \rightarrow 0$),

$$\Omega = k_{\text{int}}$$

and

$$\Phi = k_{\text{int}}(1-x)P_{plasma,0}\left(\frac{2PR_{cap}}{R_{Krogh}^2}\right)$$

$$P_{\text{int}} = \Phi\left[\frac{A}{(k_{\text{int}} - k_\alpha)}\left(\frac{e^{-k_\alpha t} - e^{-k_{\text{deg}} t}}{k_{\text{deg}} - k_\alpha} + \frac{e^{-k_{\text{deg}} t} - e^{-k_{\text{int}} t}}{k_{\text{deg}} - k_{\text{int}}}\right) + \frac{B}{(k_{\text{int}} - k_\beta)}\left(\frac{e^{-k_\beta t} - e^{-k_{\text{deg}} t}}{k_{\text{deg}} - k_\beta} + \frac{e^{-k_{\text{deg}} t} - e^{-k_{\text{int}} t}}{k_{\text{deg}} - k_{\text{int}}}\right)\right]$$

If the imaging time is after clearance, and degradation is negligible

$$P_{\text{int}} = \Phi\left[\frac{A}{(k_{\text{int}} - k_\alpha)}\left(\frac{-1}{k_{\text{deg}} - k_\alpha} + \frac{1}{k_{\text{deg}} - k_{\text{int}}}\right) + \frac{B}{(k_{\text{int}} - k_\beta)}\left(\frac{-1}{k_{\text{deg}} - k_\beta} + \frac{1}{k_{\text{deg}} - k_{\text{int}}}\right)\right]$$

$$P_{\text{int}} = \Phi\left[\left(\frac{A}{\left(k_{\text{deg}} - k_\alpha\right)\left(k_{\text{deg}} - k_{\text{int}}\right)}\right) + \left(\frac{B}{\left(k_{\text{deg}} - k_\beta\right)\left(k_{\text{deg}} - k_{\text{int}}\right)}\right)\right]$$

Using assumption that $k_{deg} << k_{alpha/beta}$ and k_{int} and adding phi:

$$P_{\text{int}} = k_{\text{int}}(1-x)P_{plasma,0}\left(\frac{2PR_{cap}}{R_{Krogh}^2}\right)\left[\left(\frac{A}{\left(k_\alpha\right)\left(k_{\text{int}}\right)}\right) + \left(\frac{B}{\left(k_\beta\right)\left(k_{\text{int}}\right)}\right)\right]$$

$$P_{\text{int}} = (1-x)P_{plasma,0}\left(\frac{2PR_{cap}}{R_{Krogh}^2}\right)\left[\left(\frac{A}{k_\alpha}\right) + \left(\frac{B}{k_\beta}\right)\right]$$

$$P_{\text{int}} = (1-x)P_{plasma,0}\left(\frac{PS}{V}\right)\left[\left(\frac{A}{k_\alpha}\right) + \left(\frac{B}{k_\beta}\right)\right]$$

Non-target tissue

For non-target tissue, assuming first order internalization of probe non-specifically in the tissue. This in place of the high affinity assumption, but all other assumptions apply.

Looking at long times after the probe has cleared from the blood:

$$P_{\text{int}} = \Phi\left[\frac{A}{(\Omega - k_\alpha)}\left(\frac{e^{-k_\alpha t} - e^{-k_{\text{deg}} t}}{k_{\text{deg}} - k_\alpha} + \frac{e^{-k_{\text{deg}} t} - e^{-\Omega t}}{k_{\text{deg}} - \Omega}\right) + \frac{B}{(\Omega - k_\beta)}\left(\frac{e^{-k_\beta t} - e^{-k_{\text{deg}} t}}{k_{\text{deg}} - k_\beta} + \frac{e^{-k_{\text{deg}} t} - e^{-\Omega t}}{k_{\text{deg}} - \Omega}\right)\right]$$

If the uptake is non-specific and linear with concentration, this is the same as a very low affinity antibody where the bound portion is linear with concentration (Kd → large):

$$\Omega = \frac{2PR_{cap}}{\varepsilon R_{Krogh}^2}\left(\frac{K_d}{R/\varepsilon + K_d}\right) + k_{\text{int}}\left(\frac{R/\varepsilon}{R/\varepsilon + K_d}\right) = \frac{2PR_{cap}}{\varepsilon R_{Krogh}^2} + k_{\text{int}}\left(\frac{R/\varepsilon}{K_d}\right)$$

The first term incorporates washout from the tissue for the unbound probe, and the second term is linear in concentration. The form is first order, but the mechanism is completely different, so we will substitute a new constant, $k_{int,ns}$, which stands for k internalization, non-specific (ns):

$$\Omega = \frac{2PR_{cap}}{\varepsilon R_{Krogh}^2} + k_{\text{int},ns}$$

We will also assume that the imaging time as after plasma clearance but before significant degradation (assumptions 5 and 6)

$$P_{\text{int}} = \Phi\left[\frac{A}{(\Omega - k_\alpha)}\left(\frac{-1}{k_{\text{deg}} - k_\alpha} + \frac{1}{k_{\text{deg}} - \Omega}\right) + \frac{B}{(\Omega - k_\beta)}\left(\frac{-1}{k_{\text{deg}} - k_\beta} + \frac{1}{k_{\text{deg}} - \Omega}\right)\right]$$

$$P_{\text{int}} = \Phi\left[\frac{A}{(\Omega - k_\alpha)}\left(\frac{\Omega - k_\alpha}{\left(k_{\text{deg}} - k_\alpha\right)\left(k_{\text{deg}} - \Omega\right)}\right) + \frac{B}{(\Omega - k_\beta)}\left(\frac{\Omega - k_\beta}{\left(k_{\text{deg}} - k_\beta\right)\left(k_{\text{deg}} - \Omega\right)}\right)\right]$$

$$P_{\text{int}} = \Phi\left[\left(\frac{A}{\left(k_{\text{deg}} - k_\alpha\right)\left(k_{\text{deg}} - \Omega\right)}\right) + \left(\frac{B}{\left(k_{\text{deg}} - k_\beta\right)\left(k_{\text{deg}} - \Omega\right)}\right)\right]$$

Substituting

$$k_{\text{int},ns} = k_{\text{int}}\left(\frac{R/\varepsilon}{K_d}\right)$$

similar to above:

$$\Phi = k_{\text{int},ns}(1-x)P_{plasma,0}(\frac{2PR_{cap}}{R_{Krogh}^2})$$

Substituting

$$P_{\text{int}} = k_{\text{int},ns}(1-x)P_{plasma,0}(\frac{2PR_{cap}}{R_{Krogh}^2})\left[\left(\frac{A}{\left(k_{\text{deg}}-k_{\alpha}\right)\left(k_{\text{deg}}-\Omega\right)}\right)+\left(\frac{B}{\left(k_{\text{deg}}-k_{\beta}\right)\left(k_{\text{deg}}-\Omega\right)}\right)\right]$$

Using assumption 5 (specifically that $k_{deg} << k_{int,ns}$ and clearance, in this case

$$P_{\text{int}} = k_{\text{int},ns}(1-x)P_{plasma,0}(\frac{2PR_{cap}}{R_{Krogh}^2})\left(\frac{1}{\left(k_{\alpha}\right)\left(\Omega\right)}\right)$$

$$P_{\text{int}} = k_{\text{int},ns}(1-x)P_{plasma,0}(\frac{2PR_{cap}}{R_{Krogh}^2})\left[\left(\frac{A}{\left(k_{\alpha}\right)\left(\Omega\right)}\right)+\left(\frac{B}{\left(k_{\beta}\right)\left(\Omega\right)}\right)\right]$$

$$P_{\text{int}} = k_{\text{int},ns}(1-x)P_{plasma,0}(\frac{2PR_{cap}}{R_{Krogh}^2})\frac{1}{\Omega}\left[\left(\frac{A}{\left(k_{\alpha}\right)}\right)+\left(\frac{B}{\left(k_{\beta}\right)}\right)\right]$$

$$P_{\text{int}} = (1-x)P_{plasma,0}\left(\frac{PS}{V}\right)\left[\left(\frac{A}{\left(k_{\alpha}\right)}\right)+\left(\frac{B}{\left(k_{\beta}\right)}\right)\right]\left(\frac{k_{\text{int},ns}}{\left(\frac{2PR_{cap}}{\varepsilon R_{Krogh}^2}+k_{\text{int},ns}\right)}\right)$$

Maximizing TBR:

$$TBR = \frac{\left(P_{\text{int}}\right)_{target}}{\left(P_{\text{int}}\right)_{non-target}} = \frac{(1-x)P_{plasma,0}\left(\frac{PS}{V}\right)\left[\left(\frac{A}{k_\alpha}\right)+\left(\frac{B}{k_\beta}\right)\right]}{(1-x)P_{plasma,0}\left(\frac{PS}{V}\right)\left[\left(\frac{A}{k_\alpha}\right)+\left(\frac{B}{k_\beta}\right)\right]\left(\frac{k_{\text{int},ns}}{\left(\frac{2PR_{cap}}{\varepsilon R_{Krogh}^2}+k_{\text{int},ns}\right)}\right)}$$

$$TBR = \left[\frac{\left(\frac{PS}{V}\right)_{target}}{\left(\frac{PS}{V}\right)_{non-target}}\right]\left[\frac{\frac{2PR_{cap}}{\varepsilon R_{Krogh}^2}+k_{\text{int},ns}}{k_{\text{int},ns}}\right]$$

The initial plasma concentration (dose) and plasma clearance cancel from the analysis. The PS/V terms do not cancel, since these are the permeability surface area products for the target and non-target tissues, which can be different.

The permeability surface area product on the right is for the non-target tissue:

$$TBR = \left[\frac{\left(\frac{PS}{V}\right)_{target}}{\left(\frac{PS}{V}\right)_{non-target}}\right]\left[\frac{\left(\frac{PS}{V}\right)_{non-target}+\varepsilon k_{\text{int},ns}}{\varepsilon k_{\text{int},ns}}\right]$$

If the washout rate is higher than non-specific internalization (which is critical for imaging), the ratio is:

$$TBR = \left[\frac{\left(\frac{PS}{V}\right)_{\text{target}}}{\varepsilon k_{\text{int},ns}}\right]$$

Since the physiology of the target tissue is difficult to manipulate, the probe should be designed to have minimal non-specific uptake.

Additional points of distinction:

a. If there is no non-specific uptake in the background tissue, then the background always goes to zero at long times. This assumption is likely not true and ignores the background from autofluorescence or instrument noise (for radioactivity).

b. Faster clearance helps to keep assumption 5 and 6 true (imaging after everything cleared from the blood but little degradation), which is not the case for antibodies, for example.

c. The internalization rate, k_{int}, can help if there is low expression of target in the tissue. The internalization and recycle will prevent the dose from reaching saturation (since super-saturating doses lower the TBR). In other words, it helps maintain assumption 1.

d. Lower affinity would increase washout from the target tissue, lowering the TBR.

e. The MW of the probe affects clearance, but this appears to cancel out for TBR. However, the permeability of the target and non-target organs are a function of MW. For certain tissues (such as tumors), maximizing the ratio of permeabilities between target and non-target tissue would maximize the TBR.

Probe synthesis and characterization

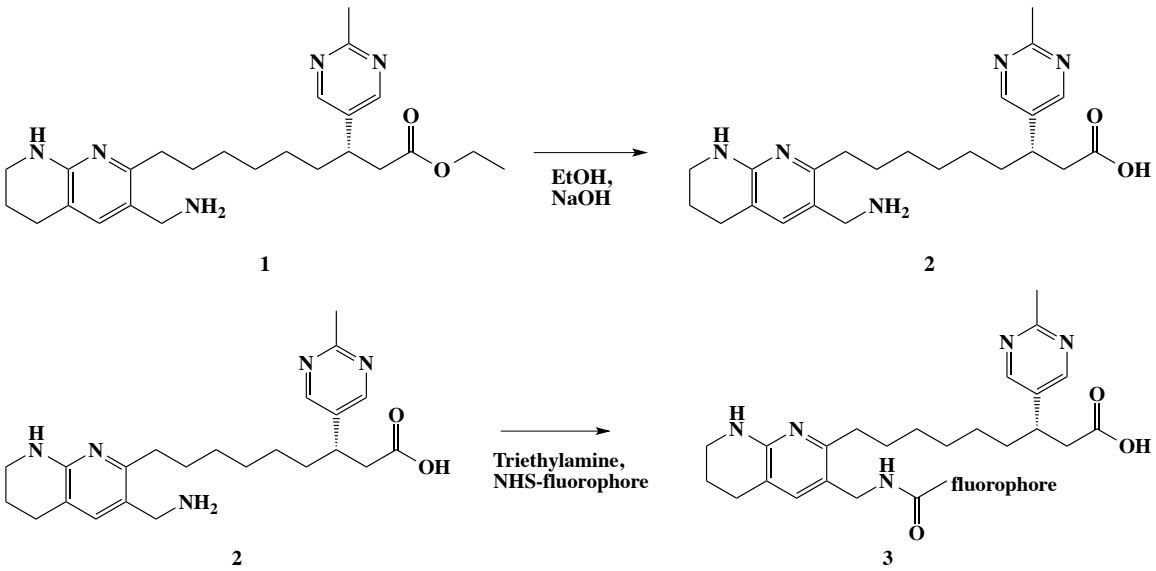

Scheme 2.2 Reaction for generating fluorescent αvβ3 targeting ligands
Hydrolysis (top) yields a carboxylic acid. Primary amine (bottom) reacts with NHS ester on various fluorophores. **1** was modified from Coleman et al.[191] and Kossodo et al.[192] and obtained from ChemPartner.

Table 2.4 Purification and characterization of fluorescent conjugates

Compound	Mobile phase	Expected MW	Observed MW	Ionization
800CW conjugate	A: 50 mM TEAA in H_2O B: MeCN	1394.70	1395.922	MALDI-TOF
AF680 conjugate	A: 0.1 % TFA in H_2O B: 0.1 % TFA in MeCN	1250.35	1253.314	MALDI-TOF
B650 conjugate	A: 0.1 % TFA in H_2O B: 0.1 % TFA in MeCN	940.92	940.1	MALDI-TOF
ZW800 conjugate	A: 0.1 % TFA in H_2O B: 0.1 % TFA in MeCN	1337.77	1335.6817	ESI

Table 2.5 Capillary permeability data

Compound	MW (Da)	Radius (nm)	Organ	Permeability ($*10^7$ cm/s)	Vasculature	Reference
Dextran	3300	1.5	LS174T tumor	154	Fenestrated, immature	[193]
Mouse Fc fragment	25000	2.66	LS174T tumor	3.74	Fenestrated, immature	[194]
Mouse Fab fragment	25000	2.66	LS174T tumor	4.61	Fenestrated, immature	[194]
Dextran	10000	2.7	LS174T tumor	32	Fenestrated, immature	[193]
Ovalbumin	45000	3.24	LS174T tumor	5.77	Fenestrated, immature	[194]
Evans blue albumin	66000	3.55	A-07 Tumor	15	Fenestrated, immature	[195]
Evans blue albumin	66000	3.55	R-18 Tumor	11	Fenestrated, immature	[195]
Evans blue albumin	66000	3.55	U-25 Tumor	9	Fenestrated, immature	[195]
Concanavalin A	104000	4.28	LS174T tumor	1.53	Fenestrated, immature	[194]
Mouse F(ab')2 fragment	110000	4.36	LS174T tumor	1.51	Fenestrated, immature	[194]
Mouse igG	160000	4.94	LS174T tumor	2.82	Fenestrated, immature	[194]
Dextran	40000	5	LS174T tumor	9.5	Fenestrated, immature	[193]
Dextran	70000	6.5	LS174T tumor	9.8	Fenestrated, immature	[193]
Dextran	2000000	22.1	LS174T tumor	1.7	Fenestrated, immature	[193]
Liposome	-	45	LS174T tumor	0.2	Fenestrated, immature	[194]
Liposome	-	60	LS174T tumor	0.155	Fenestrated, immature	[196]
Na	23	0.1	Kidney	7600	Fenestrated	[197]
Na	23	0.1	Pancreas	3600	Fenestrated	[98]
Urea	60	0.18	Kidney	36000	Fenestrated	[197]
Cr-EDTA	357	0.22	Pancreas	2200	Fenestrated	[98]
B12	1353	0.85	Pancreas	1100	Fenestrated	[98]

Inulin	5000	1.52	Kidney	1440	Fenestrated	[198]
Insulin	6000	1.66	Pancreas	348	Fenestrated	[98]
Albumin	66000	3.55	Kidney	71	Fenestrated	[199]
Albumin	66000	3.55	Pancreas	26	Fenestrated	[98]
Hydrophilic solute	-	0.24	Muscle	350	Non-fenestrated	[200]
Hydrophilic solute	-	0.26	Muscle	270	Non-fenestrated	[200]
Hydrophilic solute	-	0.44	Muscle	69	Non-fenestrated	[200]
Hydrophilic solute	-	0.58	Muscle	51	Non-fenestrated	[200]
Hydrophilic solute	-	1.5	Muscle	11	Non-fenestrated	[200]
Hydrophilic solute	-	3.6	Muscle	0.47	Non-fenestrated	[200]
Hexose	180	0.42	Human forearm	130	Non-fenestrated	[201]
Hexose	180	0.42	Dog heart	93	Non-fenestrated	[201]
Sucrose	342	0.52	Human forearm	87	Non-fenestrated	[201]
Sucrose	342	0.52	Dog heart	71.5	Non-fenestrated	[201]
Sucrose EDTA	342	0.52	Cardiac muscle	350	Non-fenestrated	[202]
Sucrose EDTA	342	0.52	Skeletal muscle	140	Non-fenestrated	[203]
Raffinose	504	0.56	Human forearm	54.6	Non-fenestrated	[201]
Inulin	5300	1.52	Human forearm	9.3	Non-fenestrated	[201]
Inulin	5300	1.52	Dog heart	24	Non-fenestrated	[201]
Inulin	5300	1.52	Cardiac muscle	40	Non-fenestrated	[202]
Inulin	5500	1.52	Skeletal muscle	20	Non-fenestrated	[202]
α-Globulin	45000	3.55	Dog heart	0.606	Non-fenestrated	[201]
Albumin	66000	3.55	Dog paw	0.519	Non-fenestrated	[201]
Albumin	66000	3.55	Dog heart	0.313	Non-fenestrated	[201]
Albumin	66000	3.55	Dog intestine	0.304	Non-fenestrated	[201]

Capillary permeability data for various compounds in different types of tissue. All permeability (P) values are experimentally determined and reported in literature as effective permeability, which account for convective and diffusive contributions. Molecular radii of compounds for kidney and pancreas permeability were compiled from literature[204, 205]. For tumor permeability, molecular radii of compounds were calculated based on previously reported methods for globular proteins and PEG chains when not stated in the reference[25]. Vasculature type, whether fenestrated or non-fenestrated, followed criteria listed by Sarin et al[206].

Table 2.6 Organ flow rate data

Organ	Plasma flow (mL/min)	Organ volume (mL)	Organ mass %	References
Bone	0.17	1.5	10.73	[207, 208]
Heart	0.28	0.28	0.5	[208, 209]
Kidney	0.8	0.298	1.67	[207, 208]
Liver	1.1	0.951	5.49	[208, 209]
Lung	4.38	0.191	0.73	[207, 208]
Muscle	0.8	7.9	38.4	[208, 209]
Spleen	0.05	0.1	0.50	[207]

Plasma flow rate, organ volume, and organ mass % were compiled from the literature. To convert plasma flow rates to mL/min/g, organ masses were used. Organ masses were either reported or calculated using organ mass % and total animal mass of 25 g for mouse data[208]. For tumor, a literature reported value of 0.1 mL/min/g was used as the blood flow rate and converted to plasma flow rate assuming a hematocrit of 0.45[210]. Endocrine and exocrine pancreas plasma flow rates were reported in literature[4].

Table 2.7 Islet simulation parameters for Krogh cylinder predictions

Symbol	Parameter	Value	Notes	Reference
C_0	Initial Plasma Conc	1 fM	Dose dependent	
Q	Blood flow	0.029mL/s/g	Not rate limiting	[98, 211]
v	Vessel velocity	0.6 mm/s		[212]
[T]	GLP-1 Receptor Conc	Varied		
P	Permeability	$2.1x10^{-5}$ cm/s	10-fold higher than non-fenestrated normal tissue	[98, 213]
k_{on}	Binding rate	$1.4x10^{6}$ /M/s		[214]
D	Diffusion Coefficient	100 um^2/s	Not rate-limiting	[25]
S/V	Capillary surface area to tissue volume	505 cm^2/cm^3	Extremely high in islets	[5]
ε	Void fraction	0.1	Interstitial space in pancreas (adapted from insulin)	[98]
R_{cap}	Capillary radius	3 μm		[215]
k_{deg}	Residualization rate	0.012 /hr	Fluorescent dye specific	[179]
A	Fraction fast	0.91		[147]
k_{fast}	Alpha clearance	0.174 min^{-1}		[147]
k_{slow}	Beta clearance	0.0169 min^{-1}		[147]
V_{plasma}	Plasma volume	1.4 mL		[216]
Kd	Dissociation constant	Varied		
k_e	Receptor internalization	Varied		
ρ	Tissue density	1000 g/L		
$Plasma_{Bound}$	Fraction Plasma protein bound	0.43	Measured	
Simulation time		3 h		

Table 2.8 Tumor simulation parameters for Krogh cylinder predictions

Symbol	Parameter	Value	Notes	References
C_0	Initial Plasma Conc	1 fM	Dose dependent	
Q	Blood flow	0.0016 mL/s/g	Not rate limiting	[217]
[T]	Receptor Conc	Varied		
P	Permeability	$8x10^{-6}$ cm/s	Figure 2.1	Figure 2.1
k_{on}	Binding rate	$4.4x10^{6}$ /M/s		[218]
D	Diffusion Coefficient	100 um^2/s	Not rate-limiting	[25]
R_{krogh}	Krogh cylinder radius	60 um		[219]
ε	Void fraction	0.2		[220]
R_{cap}	Capillary radius	10 μm		[221]
k_{deg}	Residualization rate	$4x10^{-6}$ s^{-1}	In^{111} half life of 48h	[222]
A	Fraction fast	0.9972		[218, 223]
k_{fast}	Alpha clearance	2.83 h^{-1}		[218, 223]
k_{slow}	Beta clearance	0.03 h^{-1}		[218, 223]
V_{plasma}	Plasma volume	1.4 mL		[216]
K_d	Dissociation constant	Varied		
k_e	Internalization	Varied		
ρ	Tissue density	1000 g/L		
$Plasma_{Bound}$		0.43	Assumed similar PPB as exendin	
Simulation time		4 h		

Table 2.9 HER2 and GLP-1R ligand properties for Krogh cylinder predictions

Compound	K_d (M)	k_e (s^{-1})	[T] (M)	%ID/g (measured)	Radiolabel	Receptor saturation	Reference
ZHER2:2395	$2.7*10^{-11}$	$3.9*10^{-6}$	$1*10^{-6}$	15	^{99m}Tc	N	[23, 161, 224]
ZHER2:4	$5.0*10^{-8}$	$3.9*10^{-6}$	$1*10^{-6}$	2.4	^{125}I	N	[23, 161, 223]
ZHER2:342	$2.2*10^{-11}$	$3.9*10^{-6}$	$1*10^{-6}$	9.46	^{125}I	N	[23, 161, 223]
A1-ZHER2:S1	$1.3*10^{-10}$	$3.9*10^{-6}$	$1*10^{-6}$	16	^{111}In	N	[23, 161, 225]
K50-ZHER2:S1	$1.1*10^{-10}$	$3.9*10^{-6}$	$1*10^{-6}$	13	^{111}In	N	[23, 161, 225]
K58-ZHER2:S1	$9.7*10^{-11}$	$3.9*10^{-6}$	$1*10^{-6}$	15	^{111}In	N	[23, 161, 225]
PEP05541	$1.2*10^{-10}$	$3.9*10^{-6}$	$1*10^{-6}$	12.9	^{111}In	N	[23, 148, 161]
PEP05838	$1.6*10^{-10}$	$3.9*10^{-6}$	$1*10^{-6}$	15.5	^{111}In	N	[23, 148, 161]
PEP07127	$3.8*10^{-9}$	$3.9*10^{-6}$	$1*10^{-6}$	14.3	^{111}In	N	[23, 148, 161]
ZHER2:2395	$2.7*10^{-11}$	$3.9*10^{-6}$	$2.5*10^{-8}$	6.9	^{99m}Tc	Y	[161, 224, 226]
ZHER2:342	$2.7*10^{-11}$	$3.9*10^{-6}$	$2.5*10^{-8}$	19	^{111}In	N	[159, 161, 226]
PEP05541	$1.2*10^{-10}$	$3.9*10^{-6}$	$2.5*10^{-8}$	7.4	^{111}In	N	[148, 161, 226]
PEP05838	$1.6*10^{-10}$	$3.9*10^{-6}$	$2.5*10^{-8}$	10.8	^{111}In	N	[148, 161, 226]
PEP07127	$3.8*10^{-9}$	$3.9*10^{-6}$	$2.5*10^{-8}$	1.71	^{111}In	N	[148, 161, 226]
800CW monomer	$2.6*10^{-9}$	0.002	$6.3*10^{-8}$	50	-	N	[147]
800CW dimer	$8.3*10^{-9}$	0.002	$6.3*10^{-8}$	45.7	-	N	[147]
800CW trimer	$2.1*10^{-8}$	0.002	$6.3*10^{-8}$	24	-	N	[147]

Previously published data on tumor and endocrine pancreas uptake. For tumor, several affibody probes were considered in addition to various radiolabels. For islet targeting, three exendin-based compounds were considered. For predicted uptake values, dissociation constants were recalculated assuming constant activation energy to account for temperature differences between affinity measurements and the *in vivo* experiments.

Chapter 3

Quantitative Impact Of Plasma Clearance And Down-Regulation On GLP-1 Receptor Molecular Imaging

3.1 Publication Information

Zhang, L. and G.M. Thurber. *Quantitative Impact of Plasma Clearance and Down-regulation on GLP-1 Receptor Molecular Imaging*. Molecular Imaging and Biology, 2016;18(1): 79-89.

Modifications have been made to the published document to adapt the content to this text. The previous chapter helped identify key imaging agent properties for targeting the endocrine pancreas. Based on those recommendations, this chapter explores *in vivo* targeting of beta cells in mouse models.

3.2 Abstract

Quantitative molecular imaging of beta cell mass (BCM) would enable early detection and treatment monitoring of type-1 diabetes. The glucagon like peptide-1 (GLP-1) receptor is an attractive target due to its beta cell specificity and cell surface location. We quantitatively investigated the impact of plasma clearance and receptor internalization on targeting efficiency in healthy B6 mice. Four exenatide-based probes were synthesized that varied in molecular weight, binding affinity, and plasma clearance. The GLP-1 receptor internalization rate and *in vivo* receptor expression were quantified. Receptor internalization (54,000 receptors/cell *in vivo*) decreased significantly within minutes, reducing the benefit of a slower clearing agent. The multimers and albumin binding probes had higher kidney and liver uptake, respectively. Slow

plasma clearance is beneficial for GLP-1 receptor peptide therapeutics. However, for peptide-based imaging agents, exendin-based probes are used to demonstrate downregulation of GLP-1 receptor and non-specific background uptake in the exocrine pancreas results in a higher TBR for fast-clearing agents.

3.3 Background

Type-1 diabetes mellitus (T1DM) is the result of an autoimmune destruction of beta cells, leading to loss of endogenous insulin production and unregulated blood glucose levels. Although the pathophysiology of T1DM is under investigation, the ability to monitor and measure the pancreatic beta cell mass (BCM) is important for assessing the magnitude of autoimmune destruction[12, 227-232]. Most patients display symptoms after losing the majority of their beta cell mass, complicating efforts to prevent further destruction using immunomodulatory therapy[233, 234]. The ability to accurately measure beta cell mass would also be informative during clinical trials to test the efficacy of treatment [235]. Although the regional distribution of beta cells within islets of Langerhans differs across species, the BCM makes up fewer than 2% of the pancreatic mass in humans[102, 236]. Due to this low fraction of beta cells in the pancreas, a robust, non-invasive technique for monitoring and measuring BCM to predict disease onset has proven elusive[84, 235]. Currently, stimulated insulin secretion to indirectly measure the BCM showed success with healthy animal models but failed to predict the development of diabetes because of its limited ability to monitor BCM functionality[12, 237, 238]. Other studies were able to correlate hyperglycemia only with large reductions in BCM[239, 240]. Imaging agents developed for targeting beta cells such as antibodies, sulfonylureas, and vesicular monoamine transporter (VMAT) receptor agonists have been used in the past but face problems due to low target-to-background

ratios (TBR) during imaging, often from low target expression or poor specificity[70, 241-244]. There is a strong demand in the diabetes community to establish an imaging technique to quantify and monitor the beta cell mass as the destruction of these cells is responsible for the onset of type-1 diabetes[76]. However, quantitative imaging is challenging because islets are 100-300 microns in diameter, much smaller than the resolution of PET and SPECT. Consequently, quantification of probe concentration will be diluted significantly by partial volume effects[245-250]. Additionally, the loss of beta cell mass requires measurement of a reduction in signal in the context of increased non-specific uptake due to inflammatory conditions during insulitis[17]

Exendin-4, a 39-amino acid peptide originally isolated from *Heloderma suspectum*, is used for the treatment of type 2 diabetes, and the ligand-receptor interaction between exendin and glucagon-like peptide-1 receptor (GLP-1R) has been characterized for imaging beta cells in T1DM[5, 47, 76, 251]. Expression of GLP-1R in beta cells, high vascularization of tissue within the islets of Langerhans, rapid binding kinetics, and *in vivo* target specificity have led to the development of multiple radiolabeled exendin molecules to track the beta cell mass as well as detection of insulinomas[5, 76, 251-257]. Owing to its fast binding kinetics, rapid uptake in target tissue, and ability to be stabilized to resist protease degradation, exendin and related peptides have been investigated as molecular imaging agents for measuring beta cell mass *in vivo*[45, 76, 187]. However, current approaches lack the sensitivity required for clinical application[252], so more development is needed. Modifications such as PEGylation have shown prolonged therapeutic effects[258, 259], which may benefit a slower-clearing imaging agent if rapid distribution and blood clearance result in low targeting. An imaging agent that clears from the blood slowly has more time to accumulate in the target tissue, and in the well-vascularized islets, endocytosis of GLP-1R agonists occurs rapidly[214], suggesting a slower clearing agent may theoretically result in a

higher TBR in the pancreas. However, potential downregulation of GLP-1R expression may reduce beta cell internalization rates to values lower than non-target uptake at longer times, and TBR will be reduced due to high background signal from lack of clearance. The multiple competing factors require quantitative analysis of molecular probe properties to design efficient imaging agents. The paucity of data on several parameters, including the number of GLP-1 receptors per cell and transient changes in internalization rate and down-regulation prevented accurate simulations of optimal probe properties. To quantify the internalization rate of GLP-1R and determine the role of receptor recycling, downregulation, and plasma clearance on imaging contrast, we synthesized a series of molecular imaging probes based on the exendin-4 peptide that vary in molecular weight and plasma clearance to determine the impact on TBR (Scheme 3.1). We also measured the time-dependent internalization rate using a quenchable probe and quantified the *in vivo* receptor expression. The data will help the design of improved imaging agents and predict scaling to the clinic.

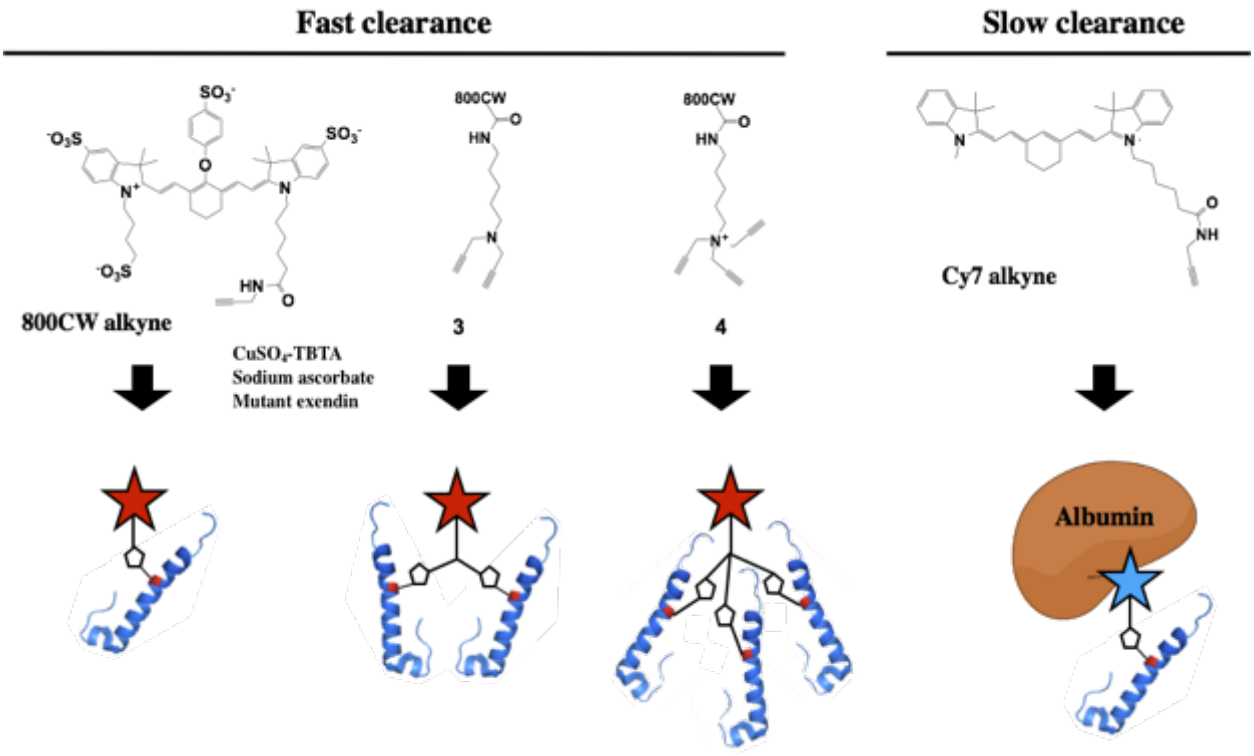

Scheme 3.1 Design and synthesis of various near-infrared exendin-based imaging agents
Design and synthesis of fast clearing IRDye 800CW conjugates and a slow clearing Cy7 monomer. Di-alkyne and tri-alkyne linkers were used to simultaneously generate exendin multimers and conjugate IRDye 800CW. Exendin crystal structures (PDB 3C59) are shown with the modified residues highlighted in red.

3.4 Results

To test the effect of plasma clearance on beta cell TBR, both fast and slow clearing exendin conjugates were synthesized. Based on its position pointing away from the binding pocket of GLP-1R, the methionine at the 14th position (M-14) was substituted with azidohomoalanine (AHA) during solid phase peptide synthesis. Novel heterobifunctional linkers were synthesized to simultaneously link multiple exendin molecules and enable fluorophore conjugation using copper catalyzed click chemistry. Three conjugates of varying molecular weight— IRDye 800CW (800CW) monomer, 800CW dimer, and 800CW trimer— that rapidly clear from blood were synthesized. Careful consideration was taken when choosing dyes, since

they can strongly influence the rate of extravasation and renal filtration due to interactions with albumin[165]. A highly charged and hydrophilic IRDye 800CW fluorophore was used to generate fast clearing multimers of exendin and a hydrophobic Cy7 fluorophore was selected to synthesize a slow clearing exendin monomer. Additionally, AF488 and AF647 conjugates were synthesized for internalization rate measurements and receptor expression quantification, respectively.

After synthesizing **1** and **2**, the linkers were conjugated with the fluorophores and peptides. All fluorescent exendin probes were purified using HPLC and characterized by MALDI-TOF (Figure 3.1). MALDI spectra for monomers were collected using reflectron positive mode; spectra for 800CW dimer and 800CW trimer were collected using linear positive mode.

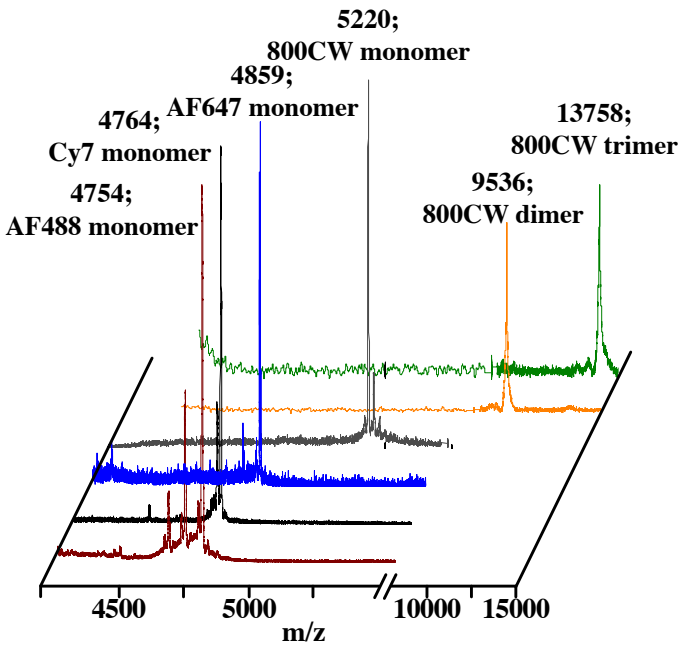

Figure 3.1 MALDI traces of purified imaging agents demonstrating successful synthesis
Lower molecular weight conjugates ionized using reflectron-positive mode whereas larger molecular multimers were ionized using linear-positive mode. CHCA matrix used for all samples.

Although crystallography for the receptor-ligand interaction for exendin indicate the M14 residue points away from the binding pocket[42], the affinity was measured to test the impact of fluorophore conjugation to the 14th position as well as confirm avidity effects of the 800CW dimer and trimer. Eleven or twelve-point affinity curves were generated in triplicate from binding assays using NIT-1 cells (Figure 3.2).

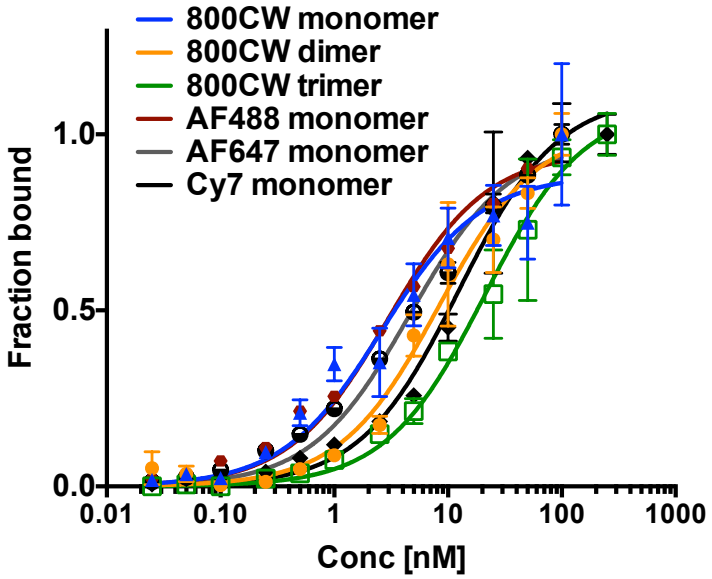

Figure 3.2 In vitro receptor binding assay to quantify binding affinity
Affinity curves indicate a strong affinity of all conjugates to GLP-1R with fitted K_d values. Data collected using flow cytometry and GLP-1R expressing NIT-1 cell line.

Fluorophore conjugation had minimal impact on the affinity, and all fluorescent conjugates of exendin maintained high affinity for GLP-1R (Table 3.1). For 800CW dimer and 800CW trimer, despite multivalency, the affinity decreased to values of K_d = 8.3 ± 1.2 nM and K_d = 20.9 ± 2.5 nM, respectively. It is likely that the steric hindrance resulting from adjacent exendin helices for the dimer and trimer overshadowed gains from avidity.

Table 3.1 Summary of binding affinity and molecular weight information for conjugates

Compound	Fluorophore	Expected MW	Binding affinity (nM)
AF488 monomer	Alexa Fluor 488	4750	3.0 ± 0.2
AF647 monomer	Alexa Fluor 647	--	4.6 ± 0.4
800CW monomer	IRDye 800CW	5219	2.6 ± 0.5
800CW dimer	IRDye 800CW	9523	8.3 ± 1.2
800CW trimer	IRDye 800CW	13745	20.9 ± 2.5
Cy7 monomer	Cy7	4768	12.4 ± 1.4

Glucagon-like peptide-1 receptor, a member of the seven-transmembrane family of GPCRs, has been shown to internalize GLP-1 peptide with a rapid half-life of 2-3 min and a recycle half-life of 15 min [214]. To verify that M14 exendin has no impact on receptor activation and subsequent endocytosis, internalization rates were measured on NIT-1 cells using a modified protocol from Schmidt et al[186]. After cells were allowed to internalize continuously for predetermined amounts of time, the total intensity per cell was compared to the surface quenched intensity per cell. The intensities plotted against time (Figure 3.3a) were then fitted to a compartmental binding and internalization model to yield a rapid, early internalization half-life of 5.7 ± 0.9 min and a slower, long-term internalization half-life of 220 ± 10 min (Figure 3.3c). The biexponential fit indicates that the early, rapid binding and internalization phase accounts for 68% of fluorescent intensity in the first 3 h of GLP-1R internalization. Additionally, by comparing the quenching of surface receptors incubated on ice (no internalization) with those after extended internalization, we estimate that the surface expression of GLP-1 receptor is downregulated between 55-60%. The slower internalization that is apparent at longer times (>30 min) is likely a result of GLP-1R downregulation and slower receptor dynamics. Qualitatively, live cell time lapse imaging of NIT-1 (Figure 3.3b) and HEK-293 cells transfected with GFP-GLP-1R agree with the results of the internalization assay. Surface binding and internalization

occur rapidly at early times, while images at longer times (60 and 180 min images) show small increases in fluorescence intensity.

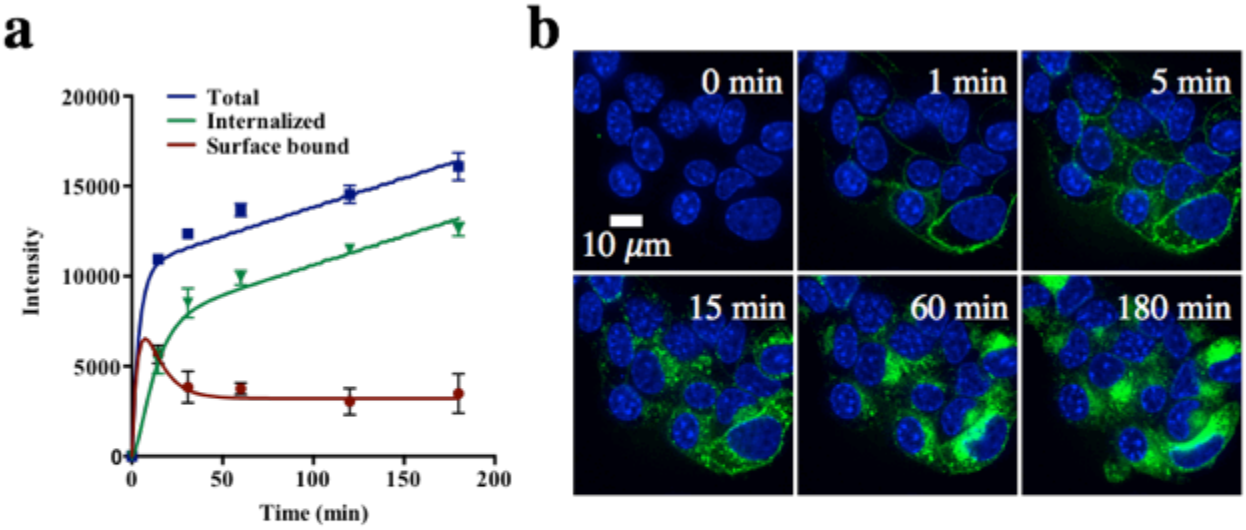

c

Compound	$t_{1/2,int,fast}$ (min)	$t_{1/2,int,slow}$ (min)	Fraction fast	In vitro expression (NIT-1)	In vivo expression (MIP-GFP beta cells, AF647 monomer)
AF488 monomer	5.7±0.9	220±10	0.68±0.05	17,000±4000 receptors/cell	54,000±3000 receptors/cell

Figure 3.3 In vitro internalization assay results to quantify GLP-1R internalization rate
In vitro internalization assay indicates rapid surface binding and internalization followed by slower internalization and GLP-1R downregulation (a). Live cell imaging of NIT-1 cells labeled with AF488 monomer (green intensity, b). Cells nuclei stained with Hoechst 33342 (blue). Fitted values for internalization and receptor expression (c).

To measure *in vivo* clearance and biodistribution of the 800CW monomer, dimer, trimer, and Cy7 monomer, 0.5 nmol of fluorescent probe was injected via tail vein in C57BL/6 mice and allowed to circulate. Blood samples were taken at multiple time points, and the half-lives of exendin conjugates in plasma were calculated by fitting the data to a biexponential decay (Figure 3.4a). As anticipated, the 800CW conjugates cleared rapidly. We observed a fast decay of the majority of probe within a few minutes followed by a slower (~30 min) clearance phase for each

(Table 3.2). The clearance half-lives for all molecular weight variants were rapid and there was no significant difference among the different constructs (fast clearance $p = 0.68$; slow clearance $p = 0.69$). Cy7 monomer had much slower (> 7-fold) plasma clearance due to the hydrophobic nature of the fluorophore and plasma protein binding[165]. After the last blood sample was taken, the animal was sacrificed and the organs were weighed, homogenized, serial-diluted, and imaged to quantify normalized uptake (Figure 3.4b).

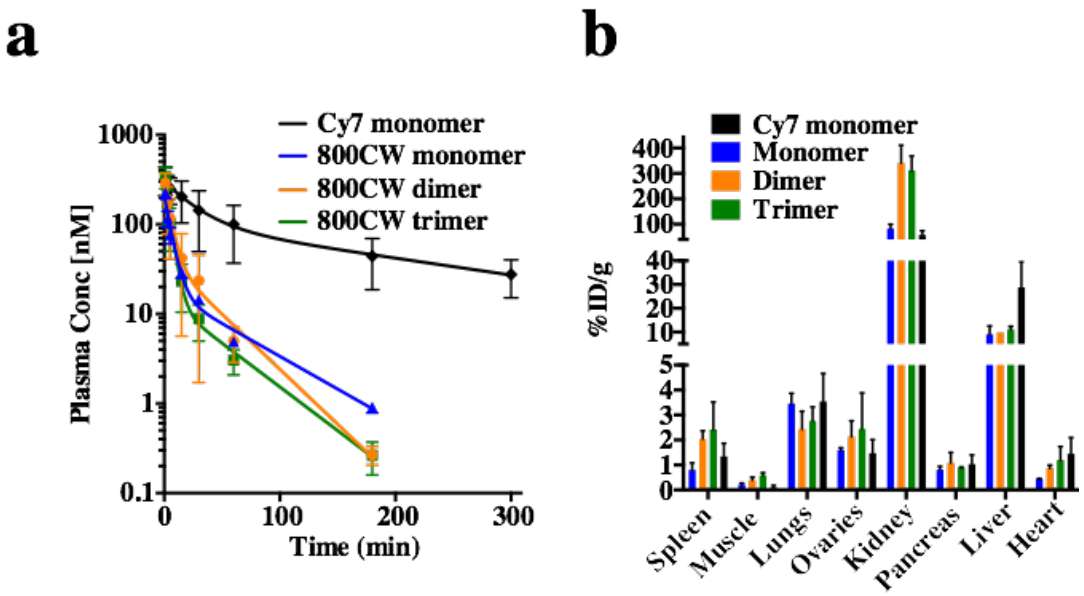

Figure 3.4 Plasma clearance of IRDye 800CW and Cy7 conjugates
Plasma clearance is rapid for all the hydrophilic IRDye 800CW conjugates, while the lipophilic agent clears slowly (a). Biodistribution shows higher non-specific uptake of multimers in the kidney and Cy7 uptake in the liver (b). Clearance rates were not significantly different between the monomer, dimer, and trimer.

Uptake was higher in the kidney for the dimer and trimer compared to the 800CW and Cy7 monomers, and the Cy7 monomer was higher in the liver than the 800CW probes ($p = 0.03$). No significant differences were detected in the total pancreatic uptake between all constructs. With a blocking injection, non-specific/exocrine pancreatic uptake for the slower-clearing Cy7 monomer measured 0.55 ± 0.04 %ID/g whereas 800CW monomer was 0.3 ± 0.1 %ID/g.

Subtracting %ID/g of blocked pancreata from experiments without blocking, the specific uptake in the islets was quantified to be 0.5 ± 0.1 %ID/g and 0.5 ± 0.4 %ID/g for the 800CW monomer at 3 h and Cy7 monomer at 5 h, respectively.

Table 3.2 Plasma biexponential decay data of various exendin conjugates in mice

Compound	Fast decay half-live (min)	Slow decay half-live (min)	Fraction fast	AUC (nM*min)
800CW monomer	3.9 ± 0.6	41 ± 3	0.91 ± 0.02	2180
800CW dimer	4.0 ± 2.0	25 ± 3	0.86 ± 0.06	2780
800CW trimer	3.0 ± 0.5	30 ± 3	0.96 ± 0.01	2140
Cy7 monomer	17.0 ± 7.0	160 ± 30	0.67 ± 0.08	20180

An AlexaFluor-647 monomer was injected intravenously in MIP-GFP mice to quantify receptor expression. *Ex vivo* labeling of isolated beta cells resulted in inconsistent signal intensity, so *in vivo* saturation was used to quantify expression levels. Macroscopic pancreas scans (Figure 3.6a) show AF647 signal in punctate spots several hundred microns in diameter, and confocal imaging of the pancreas from MIP-GFP mice indicate colocalization between the exendin-647 monomer and GFP expression (Figure 3.6b). Macroscopic images of the pancreas from mice injected with 800CW monomer, 800CW dimer, 800CW trimer, and Cy7 monomer (Figure 3.6c) indicate similar islet specific targeting across all constructs tested. Digestion of the pancreas into a single-cell suspension followed by fluorescence intensity measurements by flow cytometry indicated GLP-1R expression levels at 54,000 ± 3000 receptors/cell *in vivo*. A GLP-1R expression measurement with NIT-1 cells indicated 17,000 ± 4000 receptors/cell. Cells incubated with collagenase for 15 min had < 5% change in cell surface labeling.

To quantitatively analyze the impact of plasma clearance, molecular weight, binding affinity, and receptor internalization and down-regulation on targeting, we used a previously validated tissue transport simulation[5, 76, 180, 181] incorporating the parameter values measured in this work (SI). The results showed this partial differential equation simulation can be simplified to an ordinary differential equation (compartmental) model without loss in accuracy (Figure 3.5). In short, the imaging agent extravasates out of the pancreatic vasculature and is either specifically internalized after binding to GLP-1R, nonspecifically internalized by the exocrine pancreas, or washes out of the tissue. Both specific uptake in the islets and the non-specific internalization in the exocrine pancreas and nearby non-target organs such as liver and kidney are important for determining the target to background ratio in the pancreas.

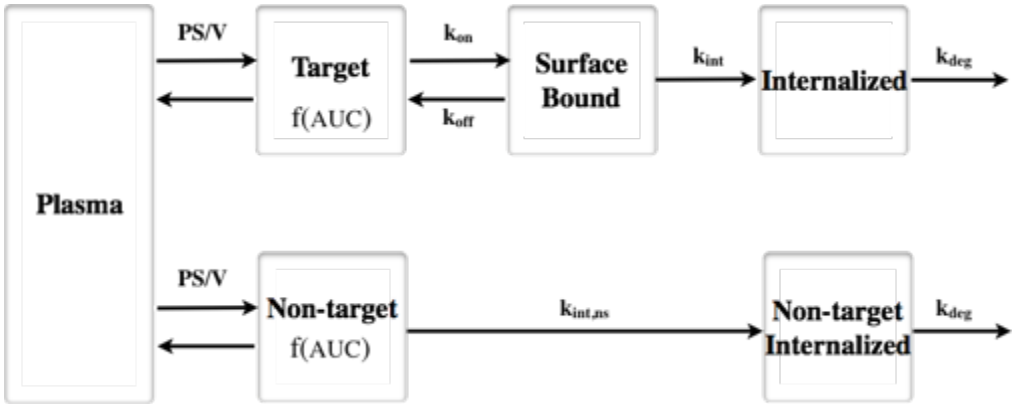

Figure 3.5 Compartmental analysis of transient probe concentrations
Analysis of transient probe concentrations using receptor expression, binding rates, internalization kinetics, and biodistribution parameters. At later times, the majority of the probe is predicted to be in the internalized compartments for both target and non-target tissue, highlighting the importance of minimizing non-specific internalization.

Additionally, kidneys express GLP-1R[260, 261] but signal is dominated by non-specific uptake due to scavenger receptors and transporters in the proximal tubule. In the pancreas, GLP-1R is weakly expressed in acinar cells of the exocrine pancreas whereas endocrine expression dominates[53, 54]. With the experimentally determined time-dependent internalization rates as

inputs for the compartmental model, we demonstrate TBR is maximized with rapidly cleared agents and decreases as uptake in non-target tissue increases. This is primarily due to the down-regulation in receptor internalization at longer times and increased non-target tissue uptake for slow clearing agents.

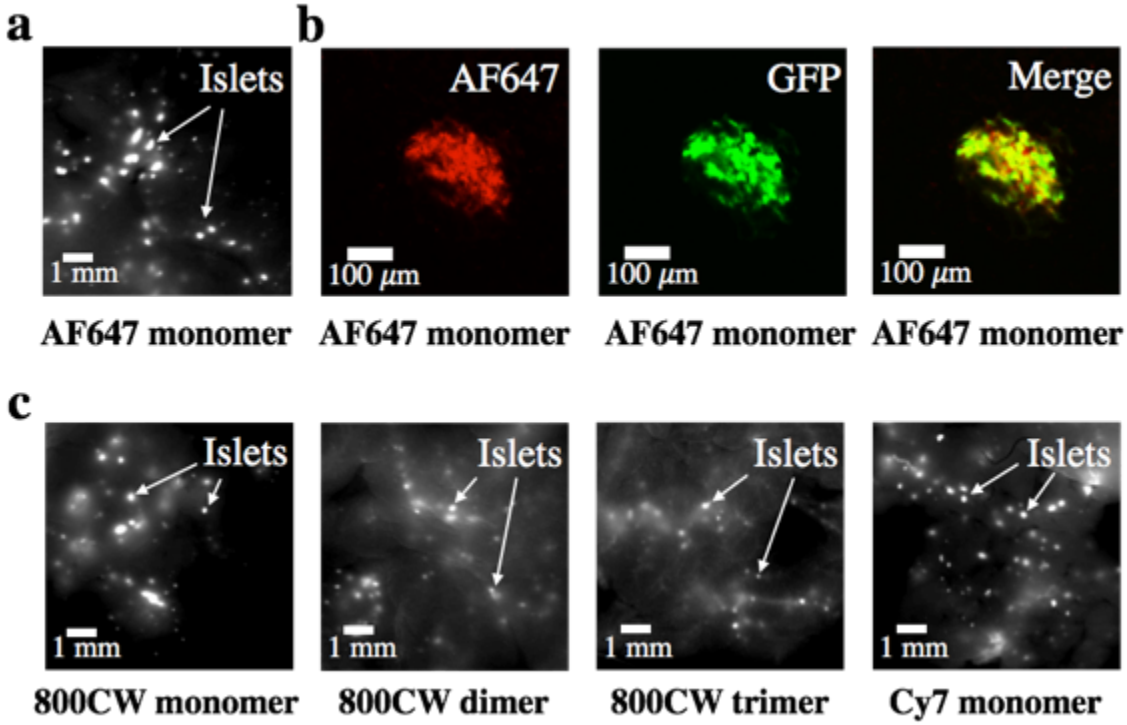

Figure 3.6 Macroscopic pancreas scans and confocal microscopy images using a transgenic mouse model
Macroscopic pancreas scans indicate punctate spot formation for all exendin conjugates (a, c). Confocal microscopy demonstrates islet specificity using a transgenic MIP-GFP mouse through colocalization of GFP and probe (b).

Additionally, dose of Cy7 monomer was optimized. Although the dose was subsaturating for the faster clearing agents, the slower clearance of the Cy7 monomer could potentially super-saturate the pancreas and lower the %ID/g. To verify 0.5 nmol of Cy7 monomer does not saturate the pancreas, the dose was reduced (Figure 3.7) and %ID/g measurements were

repeated. %ID/g values were not statistically significantly different between the higher and lower dose of Cy7 monomer, indicating the original dose of 0.5 nmol was sub-saturating.

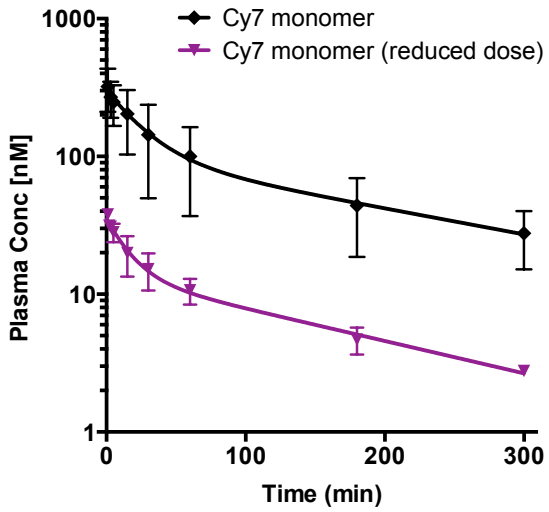

Figure 3.7 Plasma clearance of various Cy7 dosage to demonstrate linear plasma pharmacokinetics

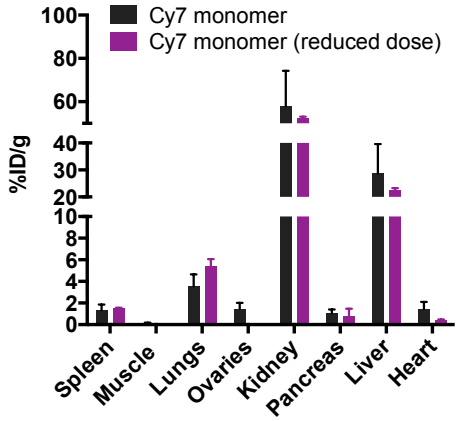

Figure 3.8 Normalized uptake comparison between dosages to demonstrate subsaturating kinetics

To compare the predictive model and experimental results, the concentration in the islet must be converted into the organ level percent injected dose per gram of pancreas tissue

(%ID/g). To make this conversion, the fraction of beta cells within the pancreas must be known. Using the data from Figure 3.4b, the simulations (details below) indicate that both 800CW and Cy7 monomer probes yield approximately 60-80 nM concentration within the islets. If we assume the islet fraction is 2% in the tissue, and use an algebraic equation to convert the signal into specific uptake in the pancreas[262], then the predictive model is in agreement with our experimental results.

$$\%\,ID/g = \frac{[C]_{islet}(fraction\ islet)100\%}{[C]_{0,plasma}V_{plasma}\rho_{tissue}}$$

$$\%\,ID/g = \frac{(70\ nM)(0.02)100\%}{(211\ nM)(1.4\ mL)(1\ g/mL)} = 0.47\ \%ID/g$$

However, this result requires further discussion. We and others have measured the beta cell fraction to be lower than 2% in rodents, closer to 0.7%[76, 263]. This would mean a higher concentration in the islets is required to agree with the experimentally measured %ID/g. The current concentration is close to a saturating dose, so it is unlikely that higher uptake in the islets (assuming receptor concentration and internalization estimates are correct) could come from the islets themselves. Low-level expression on exocrine cells may explain this specific uptake [52, 264]. Using the same formula above, assuming the islet fraction is 0.7%, and assuming the remaining specific uptake is from GLP1-R expressed on exocrine cells, we estimate ~850 receptors per exocrine cell. If this is indeed the case, a low 'cold' dose that saturates the exocrine pancreas but not the islets may help in specificity. (The ratio of delivery to receptors is much higher in the exocrine pancreas than the islets, making it feasible to preferentially saturate these cells.) A

similar approach is used in the clinic for radioimmunotherapy (RIT) by blocking normal tissue receptors prior to delivering the radioactive dose to tumor tissue [265].

Another aspect of the model that we could not directly measure was the plasma protein binding of the fluorescent peptides. In the absence of more specific data, we assumed the bound fraction of the dye-peptide conjugates was the same as literature reports of IRDye 800CW and cypate after conjugation to a small tumor-targeting peptide[165]: 31% and 97.5% for IRDye 800CW and Cy7, respectively[165]. Plasma protein binding has a major impact on the transient distribution of imaging agents. If no plasma protein binding were present, the predicted uptake in the islets would be far above saturation, which does not agree with our experimental results. This is in part due to the very high vessel surface area, blood flow, and permeability of the fenestrated capillaries. In addition, plasma protein binding is the mechanism for slower plasma clearance of Cy7, so it must be incorporated into the model. For a rapidly cleared monomer, reducing this plasma protein binding may be another way to improve the efficiency in islet uptake, achieving the same amount of specific targeting with a lower dose. A radiolabeled exendin with a residualizing, low plasma protein bound ^{111}In tag has been used to demonstrate higher pancreas uptake in mice[48].

To determine the impact of affinity, the wash out rate is compared with the internalization rate. Assuming binding reaches equilibrium in the tissue (which would occur within seconds given the effective antigen concentration and on rate), the rate of wash out depends on the PS/V and unbound probe. It is also assumed the on-rate is not significantly impacted by the trimer, which could be violated given the lower affinity. However, if the trimer has the same off-rate, then the on-rate would only change by 10-fold given the 10-fold higher K_d.

Additional results include simulated islet and exocrine pancreas concentrations for the fast clearing IRDYE 800CW monomer and slow clearing Cy7 monomer.

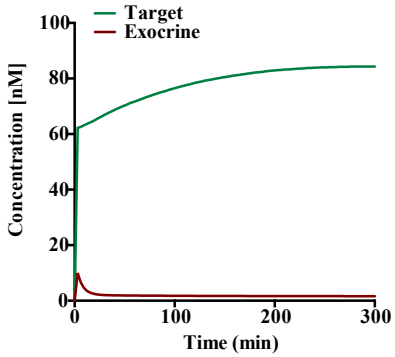

Figure 3.9 Simulation concentrations for islet and exocrine pancreas for 800CW

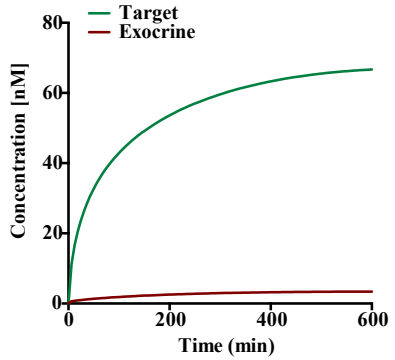

Figure 3.10 Simulation concentrations for islet and exocrine pancreas for Cy7

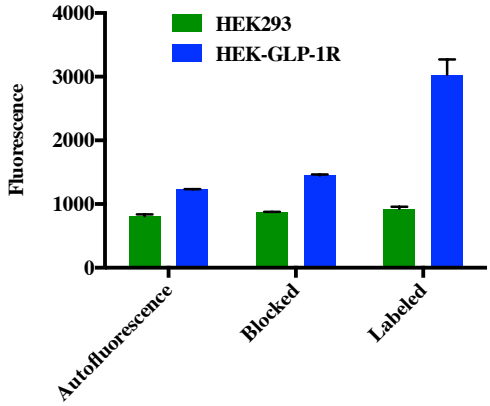

Figure 3.11 HEK-293 binding assay
Blocking both transfected and untransfected HEK-293 cells with non-fluorescent exendin prior to labeling with fluorescent exendin suggests non-specific binding to non-GLP-1R sites are low compared to receptor specific binding.

3.5 Discussion

Despite growing interest in developing GLP-1R imaging agents, the impact of plasma clearance and receptor kinetics on targeting efficiency have not been fully elucidated. The plasma clearance of exenatide has been manipulated through peptide/protein fusions[266-268] and PEGylation[258, 259] for drug treatment. However, ideal pharmacokinetics for imaging agents are typically very different than effective therapeutics. For example, rapid internalization of the GLP-1 receptor has been demonstrated upon peptide binding[76, 214]. While this can be problematic for therapeutics as endocytic pH changes and protease activity may rapidly degrade the molecule[115], internalization is often beneficial for imaging agents by trapping a pH-tolerant residualizing label within the cell[269]. To quantify the impact of plasma clearance and internalization on the molecular imaging of GLP-1 receptors, we generated a series of exenatide-based probes, measured GLP-1 receptor expression and internalization rates, and tested probe pharmacokinetics and imaging properties *in vivo*.

To investigate the effects of molecular weight on uptake in target and non-target tissue, a bifunctional linker was created to simultaneously crosslink multiple exendin peptides and conjugate a highly charged and fast clearing 800CW dye (Scheme 3.1). Additionally, a slower clearing exendin conjugate was synthesized using a more hydrophobic Cy7 dye that binds to plasma proteins[165]. All conjugates were synthesized with moderate yield (32-70%) with expected molecular weights as shown by MALDI-TOF and maintained strong binding affinity for GLP-1R. Exendin-4 is reported to bind to GLP-1R with single-digit nanomolar affinity, and all fluorescent monomers maintain high affinity after conjugation due to the M14 position oriented away from the receptor binding interface[42]. Unexpectedly, the 800CW dimer and 800CW trimer molecules resulted in weakened affinity upon crosslinking. This is likely due to steric effects that

outweigh any benefit from avidity. A longer linker between the peptides may reduce this effect, but the cellular kinetics mitigate any benefit. The rapid internalization of GLP-1 receptor results in most of the probe being internalized before it can dissociate, similar to many antibodies[270].

Literature reports on the internalization of GLP-1 receptor ligands vary in both rate and time-dependence, with some showing linear uptake over time[271] and others indicating rapid internalization followed by down-regulation[214, 272]. To determine the potential amplification of cell labeling by internalization and recycling, NIT-1 cells were incubated with excess probe at 37°C to allow for continuous uptake. The surface signal was quenched at each time point to decouple surface-bound and internalized probe. Fast surface labeling and internalization indicated by punctate vesicles in the cytosol occurred within minutes, consistent with previous observations. A time-lapse video (SI) along with live cell images at short times (<5 min) indicate the presence of numerous punctate, intracellular spots indicative of receptor trafficking upon internalization. This initial phase of uptake was followed by a much slower rate of continual internalization (half-life 220 min versus 5.7 min). This 38-fold reduction is predicted to lower the impact of sustained targeting on islet signal.

Additionally, we sought to measure the endogenous expression level of GLP-1 receptor in mice. Reports of absolute receptor expression levels are rare and often variable in the literature. Levels on RIN-m5f cells have been reported as 1,107 receptors/cell[273]. However, our results *in vivo* indicate a higher expression based on signal intensity[76]. The reduced expression on the insulinoma cell line may be a result of adaptation to cell culture. Because labeling islet cells *ex vivo* resulted in variable signal, we injected a saturating dose (1.2 nmol) of AF647 monomer into MIP-GFP mice and harvested the pancreas after only 30 min to minimize continuous uptake. After obtaining a single cell suspension, the cells were run on flow cytometry

and compared to quantitative beads. The results indicate 54,000 receptors per cell in B6 mice and 17,000 receptors per cell for NIT-1 cells.

To test whether slow clearance can be used to increase islet labeling, the different constructs were injected into B6 mice, and the plasma clearance was measured. At 3 h (for the rapidly cleared probes) or 5 h (for the slowly cleared monomer), the animals were sacrificed and biodistribution was quantified[274]. For plasma clearance, no statistically significant difference occurred for the monomer (5.3 kDa), dimer (9.5 kDa), and trimer (13.7 kDa) labeled with 800CW. This is consistent with molecules that are well below the ~60 kDa cut-off for renal filtration[275]. However, the monomer with a lipophilic Cy7 dye showed over a 7-fold increase in AUC due to plasma protein binding and reduced renal clearance[165].

The targeting of islets for each probe was confirmed by imaging the pancreas of each mouse, with islets readily apparent as bright, punctate foci ~100-300 microns in diameter. Using a MIP-GFP mouse, which expresses GFP exclusively in the beta cells, colocalization confirmed islet specificity. All 4 constructs showed excellent islet specificity, but no statistically significant differences occurred in the pancreas %ID/g. The lack of higher uptake from the more slowly cleared agent is likely due to the down-regulation and slower net internalization of GLP-1 receptors upon sustained exposure to exendin peptide. Since the initial rapid internalization is responsible for the majority of specific beta cell signal, a slow clearing imaging agent with detectable concentrations in the blood at longer times is not advantageous when the goal is to maximize the TBR.

Off-target uptake is equally important in designing effective imaging agents as demonstrated by the biodistribution. Despite similar plasma clearance rates, the renal uptake of the dimer and trimer are 3-fold higher than the monomer. After filtration by the glomerulus,

degradation and scavenger receptors in the renal proximal tubule recycle amino acids and peptides, preventing excretion in the urine[118]. Uptake of the dimer and trimer in the proximal tubule by scavenging receptors appears to be more efficient than the monomer and highlights a drawback of multimerization. Our results here are consistent with other reports[276, 277] showing higher renal uptake for multimers, motivating the development of high affinity monovalent constructs[132, 275, 278] rather than using avidity to compensate for low affinity. Although not statistically significant in all cases, the dimer and trimer generally have higher signal in other tissues as well. Non-specific internalization in off-target tissues is a major determinant of probe TBR, particularly for rapidly cleared low molecular weight agents. The rapid plasma clearance allows imaging after the majority of probe is removed from the blood (< 0.5% in the case of the monomer, dimer, and trimer). However, due to the residualizing IRDye 800CW label[179], both specifically and non-specifically internalized IRDye 800CW label wash out of tissue extremely slowly, negating any benefit of later imaging times.

The lipophilic Cy7-conjugate had ~10-fold slower clearance than the IRDye 800CW monomer, but tissue differences were more modest when the majority of probe had cleared from the plasma. One significant difference was the higher liver uptake of the Cy7 monomer. An alternative approach to slow clearance is to add an albumin binding peptide sequence through solid-phase synthesis [267], but increased liver uptake due to longer plasma exposure and/or scavenger uptake[279, 280] and down-regulation of GLP-1R may not provide any targeting benefit over the more rapidly cleared monomer. In the pancreas, total uptake of 800CW and Cy7 monomers was not statistically different ($p = 0.26$). To measure the specific uptake in the pancreas (versus total uptake), mice were given a large dose of wild-type exendin-4 45 minutes prior to injection of either 800CW monomer or Cy7 monomer. The higher non-specific uptake in

the pancreas ($p = 0.024$), despite having 5 h to clear (versus 3 h for 800CW), is consistent with the internalization conclusions: the majority of specific uptake in the target tissue occurs on the time scale of minutes given the rapid internalization rate of GLP-1R. Slower clearance does not increase specific uptake as demonstrated by similar specific %ID/g between the Cy7 monomer and 800CW monomer. Considering the fact that islets only make up 1-2% of the pancreas mass, specific uptake of 0.5% ID/g on a whole pancreas basis means the efficiency of uptake within the islets must be 25-50% ID/g. Although the high blood flow, fenestrated capillaries, and large capillary surface area provide excellent delivery to the islet, this analysis suggests equal consideration should be paid to reducing non-specific uptake in the tissue due to charge and hydrophobic interactions[148, 167, 168]. Additionally, ratio imaging may help normalize the non-specific uptake to better quantify specific targeting[281]. Being able to quantify plasma protein binding, blood clearance rate, and non-specific uptake rate in the exocrine pancreas as well as nearby organs such as kidney and liver will aid in imaging agent design when scaling to the clinic. Given the penetration depth limitations of whole-body optical and fluorescence imaging, a radiolabeled agent will ultimately quantify BCM in patients. However, fluorescence imaging with animal models will precede radiolabeling because optimal physicochemical probe properties are measured more readily using fluorescence.

To determine the impact of down-regulation and plasma clearance on imaging, a mechanistic, quantitative, and predictive model was used to examine the interdependent parameters. No experimental data were fit to the kinetic model, allowing for an independent comparison of islet targeting. A full distributed-parameter simulation[180, 181] was first conducted to show that the rapid diffusion and highly vascularized islet results in relatively homogeneous islet distribution, enabling the use of a compartmental analysis. The kinetic analysis using the

receptor expression, internalization kinetics/downregulation, and biodistribution parameters from this work indicate a rapidly cleared agent provides higher TBR than a slowly cleared agent (SI). The predicted uptake values were within experimental error of the measured uptake values. However, some small discrepancies suggest the possibility of low-level exocrine pancreas binding, and plasma protein binding of the fluorescent-exendin derivatives was an important parameter in the simulations (SI). The model also predicts that after the imaging agent is eliminated from blood and the interstitium at longer times, TBR remains relatively constant due to similar clearance (k_{deg}) of specifically and nonspecifically internalized probe. This TBR is higher for the fast clearing monomer due to lower exocrine uptake.

Sweet et al. estimated that the signal from islets would need to be 10-fold higher than non-specific exocrine signal for accurate BCM quantification[17] Since beta cells form ~1% of the pancreas, the beta cell signal needs to be 1,000-fold higher than exocrine cells. Our results indicate that the overall islet specific signal is 1.7 to 2-fold higher than exocrine signal, within reach of the 10-fold specificity required for accurate BCM imaging. A quantitative and mechanistic understanding of other targeting molecules[71, 282] rather than exclusively biodistribution data will help make rational comparisons between agents. These quantitative simulations can also focus design efforts for improvements in the development of new agents to achieve the necessary specificity.

3.6 Conclusion

We investigated the impact of plasma clearance and receptor down-regulation using four different GLP-1 receptor imaging agents varying in molecule weight and plasma clearance. The high affinity of the monomeric probe was sufficient for specific targeting, whereas higher non-

target tissue uptake, particularly in the kidney, highlights the drawbacks of imaging with multimeric peptides. Targeting of a plasma protein binding probe was mitigated by the rapid down-regulation of the receptor. Our results indicate the ideal BCM imaging agent clears quickly from blood to benefit from early rapid internalization while avoiding non-target uptake at later times. High levels of receptor expression (> 50,000 receptors per cell), rapid internalization, and an easily accessible cell surface location make GLP-1 receptor an attractive target for BCM quantitation, and simulations help identify the most important areas for improvement. Lowering non-specific interactions through peptide stabilization[187, 283] and/or accounting for this signal through ratio imaging[281] will help increase the precision and sensitivity of beta cell mass measurements for the early detection of type 1 diabetes.

3.7 Experimental Methods

All chemicals, unless specified, were purchased from Sigma-Aldrich (Milwaukee, WI) and were used as received. Fluorochromes AF647 alkyne and AF488 alkyne were purchased from Life Technologies (Carlsbad, CA); Cy7 was purchased from Lumiprobe (Hallandale Beach, FL); IRDye 800CW was purchased from Licor (Lincoln, NE). Mutant exendin-4 (HGEGTFTSDLSKQXEEEAVRLFIEWLKNGGPSSGAPPPS), where X is the non-natural amino acid azidohomoalanine, was purchased from Innopep (San Diego, CA). Reversed phase high performance liquid chromatography (RP-HPLC) and size-exclusion chromatography were performed on a Shimadzu LC unit using Luna C18(2) and Yarra SEC-2000 columns, respectively (Torrance, CA). ESI-MS data were obtained using an Agilent Q-TOF 1200 series. MALDI-MS spectra were collected using a Bruker Autoflex mass spectrometer. NMR spectra were collected using a Varian MR400 spectrometer. All MALDI-TOF and ESI-Mass

Spectrometry data were collected at the University of Michigan Department of Chemistry's Core Facility. Fluorescence microscopy was performed using an Olympus FV 1200 microscope and an Olympus-IX81 spinning disk confocal microscope.

Preparation of N,N'-di(prop-2-yn-1-yl)pentane-1,5-diamine (1) and 5-amino-N,N,N-tri(prop-2-yn-1-yl)pentan-1-aminium (2)

N-Boc-cadaverine (800 μmol) was added to potassium carbonate (2.4 mmol) in 2 mL acetonitrile (MeCN). Propargyl bromide in toluene was added dropwise (2.0 mmol) and the reaction mixture was stirred overnight at room temperature before being concentrated under reduced pressure. The reaction mixture was filtered and deprotected using 50% trifluoroacetic acid in dichloromethane, and purified using preparative RP-HPLC using a constant gradient of 5:95 of MeCN:H_2O to yield **1** and **2** (212 μmol, 27%;127 μmol, 16%). **1**: ^{1}H NMR (400 MHz, CD_3OD): *d*: 4.22 [d, *J* = 2.4, 4 H], 3.37 [t, *J* = 2.8, 2 H], 3.32 [t, *J* = 7.6, 2 H], 2.94 [t, *J* = 7.6, 2 H], 1.82 - 1.68 [m, 4 H], 1.47 [quint, *J* = 7.6, 2 H]. HRMS: *m/z* calculated for $C_{11}H_{18}N_2$: 178.1470, found: 179.1543 [MH^+]. **2**: ^{1}H NMR (400 MHz, CD_3OD): *d*: 4.50 [d, *J* = 2.4, 6 H], 3.64 - 3.59 [m, 5 H], 2.95 [t, *J* = 7.6, 2 H], 1.89 - 1.85 [m, 2 H], 1.75 [quint, *J* = 7.6, 2 H], 1.48 [quint, *J* = 7.6, 2 H]. HRMS: *m/z* calculated for $C_{14}H_{21}N_2$: 217.1705, found: 217.1699.

IRDye 800CW conjugation to (1) and (2)

IRDye 800CW NHS ester (1 μmol in DMSO) was added to an aqueous solution containing either **1** or **2** (10 μmol) buffered with 7.5% sodium bicarbonate. The reaction was stirred at room temperature for 30 min followed by purification on preparative RP-HPLC (12 mL/min; A: 0.1% trifluoroacetic acid in water, B: 0.1% trifluoroacetic acid in acetonitrile; 20-

60% B 0.1-10 min) to give fluorescent di-alkyne and tri-alkyne **3** and **4**, respectively; **3**: t_R = 8.4 min; **4**: t_R = 7.3 min MALDI-TOF: **3**: *m/z* calculated: 1160.42, found: 1163.49; **4**: *m/z* calculated: 1198.47, found: 1201.49;

Preparation of Cy7 alkyne

Propargylamine (5 μmol) was added to 200 μL of 1:1 water:acetonitrile buffered with 7.5% sodium bicarbonate. Cy7 NHS ester (0.5 μmol in DMSO) was added and the reaction was stirred at room temperature for 30 min followed by purification on preparative RP-HPLC (Cy7 alkyne: 65% B 0.1-20 min: t_R = 16.4 min). HRMS: *m/z* calculated for $C_{14}H_{21}N_2$: 586.3797, found: 586.3795.

Preparation of fluorescent exendin monomers

AF488 alkyne (0.2 μmol), AF647 alkyne (0.2 μmol), IRDye 800CW alkyne (0.2 μmol), or Cy7 alkyne (0.2 μmol) was added to 200 μL of water followed by $CuSO_4$-TBTA (20 nmol) and sodium ascorbate (1 μmol). Lastly, mutant exendin (0.2 μmol) was added and the reaction mixture was stirred at room temperature for 12 h followed by purification using preparative RP-HPLC (AF488 monomer: 20-55% B 0.1-17 min: t_R = 15.3 min; AF647 monomer: 20-30% B 0.1-4 min, 30% B 4-7 min, 30-55% B 7-17 min: t_R = 15.3 min; IRDye 800CW monomer: 20-70% B 0.1-15 min: t_R = 9.7 min; Cy7 monomer: 30-90% B 0.1-22 min: t_R = 11.1 min). MALDI-TOF: AF488 monomer: *m/z* calculated: 4750, found: 4754; AF647 monomer: *m/z* calculated: MW of dye unpublished, found: 4859; IRDye 800CW monomer: *m/z* calculated: 5219, found: 5220; Cy7 monomer: *m/z* calculated: 4768, found: 4764.

Preparation of IRDye 800CW dimer and IRDye 800CW trimer

3 or **4** (0.2 μmol) was added to 200 μL of water followed by $CuSO_4$-TBTA (20 nmol) and sodium ascorbate (1 μmol). Lastly, mutant exendin (0.6 μmol for IRDye 800CW dimer, 0.8 μmol for IRDye 800CW trimer) was added and the reaction mixture was stirred at room temperature for 12 h followed by purification using SEC-HPLC at a flow rate of 1 mL/min phosphate buffered saline (PBS), pH 7.4. MALDI-TOF: 800CW dimer: *m/z* calculated: 9523, found: 9536; IRDye 800CW trimer: *m/z* calculated: 13745, found: 13758.

Cell culture and stable transfection cell line generation

NIT-1 cells were generously provided by Dr. Ralph Weissleder's Laboratory and used for *in vitro* receptor binding assays due to NIT-1 expression of GLP-1R. Cells were grown in F12K containing 10% (v/v) FBS, 50U/mL penicillin, 50 μg/mL streptomycin, and 1.5 g/L sodium bicarbonate. The passage number for NIT-1 cells was between 4-8 for affinity measurements of all fluorescent exendin conjugates as well as internalization rate determination. For transfected cells, human embryonic kidney cells (HEK293) were grown in DMEM containing 10% (v/v) FBS, 50U/mL penicillin, and 50 μg/mL streptomycin. To generate a stable cell line, HEK293 cells were first cultured in 6-well plates and transfected using Lipofectamine 2000 following the manufacturer's instructions to express GLP-1R (GFP-tagged, Origene) and then selected with 1 mg/mL G-418.

In vitro receptor binding assay

NIT-1 cells were plated, grown for 48 hours, harvested with 0.05% trypsin-EDTA, washed, and resuspended in PBS with 0.1% bovine serum albumin (BSA). The cells were then

aliquoted and suspended in binding buffer containing fluorescent exendin conjugates ranging in concentration on ice (0.025-250 nM). The cells were then washed two times with 0.1% BSA in PBS and then immediately analyzed using an Attune Acoustic Focusing Cytometer (Applied Biosystems) or a LICOR Odyssey CLx scanner (Lincoln, NE). Affinity curves and statistical analyses were carried out using Prism 6.0 software.

Internalization assay

The internalization protocol was adapted from a previously published method for antibodies and antibody fragments[186]. Briefly, NIT-1 cells were subcultured into 24-well tissue culture plates, allowed to adhere, and grown for 48 h. After washing once with media, cells were incubated in binding buffer containing 40 nM AF488 monomer in media and allowed to internalize continuously at 37°C for 3 h, while controls were kept at 4°C. At 15, 30, 60, 120, and 180 min, cells were washed once with chilled 0.1% FBS in PBS and placed on ice. Cells were then incubated with 100 μL cell dissociation buffer (Gibco) for 5 min, lifted, and pelleted in microcentrifuge tubes. Lastly, cells were then resuspended in PBS or a dilution of 0.4% trypan blue in PBS (dilution factor 4) and analyzed using an Attune Acoustic Focusing Cytometer to differentiate between surface and internal fluorescence at various time points. Live cell time lapse images were collected at 37°C on an Olympus-IX81 spinning disk confocal microscope using a 488 nm laser line to corroborate the cytometry results. The cytometry results were fit to a multi-compartmental model with linear kinetics on MATLAB to calculate the internalization half-life of GLP-1R (SI).

Animals

All animal experiments were conducted in compliance with the University of Michigan University Committee on Use and Care of Animals (IACUC). For determining plasma clearance half-life, IRDye 800CW monomer, IRDye 800CW dimer, IRDye 800CW trimer, or Cy7 monomer (0.5 nmol) was injected in the tail vein of C57BL/6 mice. Blood samples were collected at 1, 3, 5, 15, 30, 60, and 180 min; in the case of the Cy7 monomer, blood was also collected at 300 min. 10 μL of whole blood was mixed with 20 μL of 10 mM EDTA in PBS, and spun down to isolate the plasma. Plasma samples were quantified with controls using a LICOR Odyssey CLx scanner to determine absolute concentration in the blood. After the last time point, the mice were sacrificed and the organs resected and visualized macroscopically on the Odyssey CLx. To confirm *in vivo* specificity of the fluorescent exendin conjugates, a 15 nmol dose of non-fluorescent, wild-type exendin-4 was administered via the tail vein 45 min prior to injecting the fluorescent conjugate. All *in vivo* receptor expression and biodistribution experiments (blocked, unblocked for each probe) were done in triplicate.

In vivo GLP-1R quantification

To measure the expression level of GLP-1R *in vivo*, a saturating dose of 1.2 nmol of AF647 monomer was injected in the tail vein of transgenic mice containing GFP under the control of the mouse insulin promoter (MIP-GFP mice, Jackson Laboratory Strain B6.Cg-Tg(Ins1-EGFP)1Hara/J). At 30 min post-injection, the mice were sacrificed and the pancreas resected. Successful islet targeting was confirmed using an Odyssey CLx scanner and by verifying colocalization of GFP and AF647 signal using fluorescence microscopy. After confirming specific islet targeting, the pancreas was incubated at 37°C for 15 min in 1 mg/mL collagenase type XI in PBS with continuous mixing to obtain a single cell suspension. The cells

were analyzed with an Attune Acoustic Focusing Cytometer to determine the fluorescence intensity of AF647 on the GFP-positive β-cells. After accounting for quenching effects of conjugating AF647 to exendin, a calibration curve generated with Quantum Alexa Fluor 647 MESF beads (Bangs Laboratories, Inc.) was used to determine the GLP-1R expression level *in vivo*.

Ex vivo biodistribution

The following protocol was modified from a previously published protocol for measuring uptake of fluorescent antibodies *ex vivo*[274]. Briefly, after animals were sacrificed, organs were resected, weighed, and incubated at 37°C in a mixture of RIPA buffer in PBS supplemented with 6 mg/mL collagenase type IV for 30 min. Next, 0.05% trypsin/EDTA was added and the digest solution was incubated for another 30 min at 37°C before being homogenized using an FB-120 Sonic Dismembrator. Each homogenized organ was then serial diluted in a 96-well plate and the fluorescence was quantified using an Odyssey CLx scanner. A calibration curve was generated using known amounts of fluorescent exendin in the digest solution and the %ID/g was calculated for each of the organs based on organ weight and homogenate volume.

Model Equations

Parameters:
Nomenclature:
R_{slow}: Free receptor/antigen undergoing slow internalization
R_{fast}: Free receptor/antigen undergoing fast internalization
P_{free}: Free peptide in the interstitium
$P_{bound,slow}$: Surface bound peptide on a slow internalizing receptor
$P_{bound,fast}$: Surface bound peptide on a fast internalizing receptor
$P_{exocrine}$: Free peptide in exocrine pancreas
P_{int}: Internalized peptide
$P_{int,nonspec}$: Internalized peptide in the exocrine pancreas (assumed to be non-specifically internalized)

P_{plasma}: Concentration of peptide in plasma
k_{on}: On rate for binding
k_{off}: Off rate for binding
$k_{int,slow}$: Slow internalization rate
$k_{int,fast}$: Fast internalization rate
$k_{int,nonspec}$: Non-specific uptake rate in exocrine and non-target tissues
k_{deg}: Degradation rate – includes protease digestion and loss of probe (residualization rate[179])
A: Fraction fast for plasma clearance or fraction fast internalization
S/V_{target}: capillary surface area to tissue volume ratio for target tissue
$S/V_{exocrine}$: capillary surface area to tissue volume ratio for exocrine/background
P: Vascular permeability
$X_{plasma,bound}$: Fraction of probe in plasma bound to plasma proteins

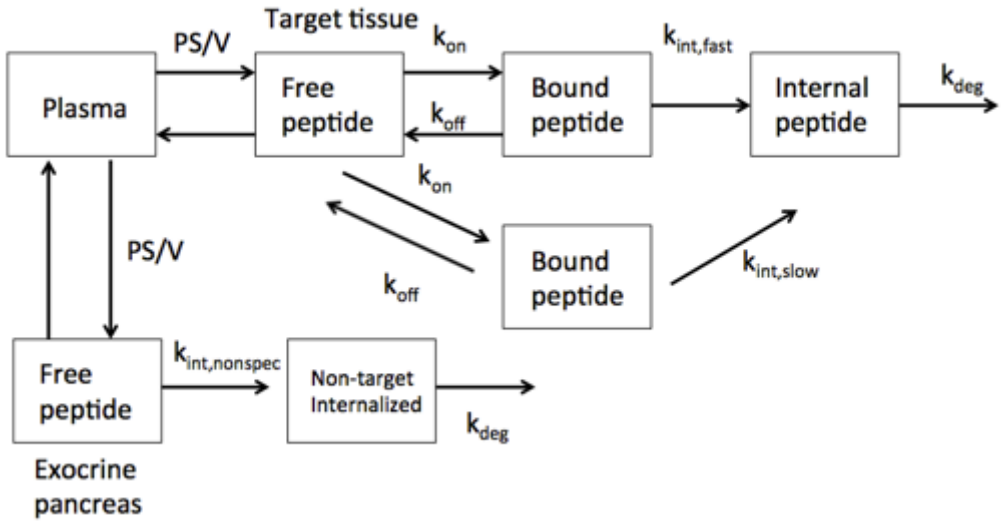

Figure 3.12 Compartmental analysis for *in vivo* studies

Plasma clearance is modeled as a biexponential decay function:

$$P_{plasma}(t) = P_{plasma,0}(Ae^{-k_\alpha t} + (1-A)e^{-k_\beta t})$$

Target tissue pathway:

Free peptide compartment:

$$\frac{dP_{free}}{dt} == -k_{on}P_{free}\frac{R_{slow}}{\varepsilon} - k_{on}P_{free}\frac{R_{fast}}{\varepsilon} + k_{off}P_{bound,slow} + k_{off}P_{bound,fast} + P\frac{S}{V_{target}}\left\{P_{plasma,0}(1-X_{plasma,bound})\left(Ae^{-k_\alpha t} + (1-A)e^{-k_\beta t}\right) - \frac{P_{free}}{\varepsilon}\right\}$$

Bound peptide (fast) compartment:

$$\frac{dP_{bound,fast}}{dt} = k_{on}P_{free}\frac{R_{fast}}{\varepsilon} - k_{off}P_{bound,fast} - k_{\mathrm{int},fast}P_{bound,fast}$$

Bound peptide (slow) compartment:

$$\frac{dP_{bound,slow}}{dt} = k_{on}P_{free}\frac{R_{slow}}{\varepsilon} - k_{off}P_{bound,slow} - k_{\mathrm{int},slow}P_{bound,slow}$$

Internal compartment:

$$\frac{dP_{\mathrm{int}ernal}}{dt} = k_{\mathrm{int},fast}P_{bound,fast} + k_{\mathrm{int},slow}P_{bound,slow} - k_{\deg}P_{\mathrm{int}ernal}$$

Receptor/Antigen balance:

$$\frac{dR_{fast}}{dt} = k_{\mathrm{int},slow}R_{fast,0} - k_{\mathrm{int},slow}R_{fast} - k_{on}P_{free}\frac{R_{fast}}{\varepsilon} + k_{off}P_{bound,fast}$$

$$\frac{dR_{slow}}{dt} = k_{\mathrm{int},slow}R_{slow,0} - k_{\mathrm{int},slow}R_{slow} - k_{on}P_{free}\frac{R_{slow}}{\varepsilon} + k_{off}P_{bound,slow}$$

$$R_{fast,0} + R_{slow,0} = 63nM$$

This concentration is calculated using 54,000 receptors/cell and 7e8 cells/mL.

Non-target tissue pathway

$$\frac{dP_{exocrine}}{dt} = P\frac{S}{V_{exocrine}}\left\{P_{plasma,0}(1-X_{plasma,bound})\left(Ae^{-k_\alpha t} + (1-A)e^{-k_\beta t}\right) - \frac{P_{exocrine}}{\varepsilon}\right\} - k_{\mathrm{int},nonspec}P_{exocrine}$$

$$\frac{dP_{\mathrm{int},nonspec}}{dt} = k_{\mathrm{int},nonspec}P_{exocrine} - k_{\deg}P_{\mathrm{int},nonspec}$$

Cellular model of internalization (in vitro)

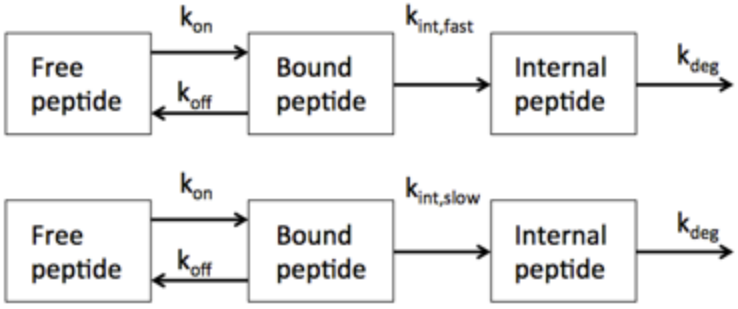

Figure 3.13 Compartmental model for fitting fast and slow internalization rate constants

Fast pathway:

Free receptor compartment:

$$\frac{dR_{fast}}{dt} = k_{\text{int},slow} A * P_{surface,initial} - k_{on} P_{free} * R_{fast} + k_{off} P_{bound,fast} - k_{\text{int},slow} R_{fast}$$

Bound peptide (fast) compartment:

$$\frac{dP_{bound,fast}}{dt} = k_{on} P_{free} * R_{fast} - k_{off} P_{bound,fast} - k_{\text{int},fast} P_{bound,fast}$$

Internal compartment:

$$\frac{dP_{\text{int},fast}}{dt} = k_{\text{int},fast} P_{bound,fast} - k_{\text{deg}} P_{\text{int},fast}$$

Slow pathway:

Free receptor compartment:

$$\frac{dR_{slow}}{dt} = k_{\text{int},slow} (1 - A) * P_{surface,initial} - k_{on} P_{free} * R_{slow} + k_{off} P_{bound,slow} - k_{\text{int},slow} R_{slow}$$

Bound peptide (fast) compartment:

$$\frac{dP_{bound,slow}}{dt} = k_{on} P_{free} * R_{slow} - k_{off} P_{bound,slow} - k_{\text{int},slow} P_{bound,slow}$$

Internal compartment:

$$\frac{dP_{\text{int},slow}}{dt} = k_{\text{int},slow} P_{bound,slow} - k_{\text{deg}} P_{\text{int},slow}$$

Table 3.3 Measured and literature parameters used in mechanistic and predictive model

Symbol	Parameter	Value	Notes	References
C_0	Initial Plasma Conc	211 nM	Dose dependent	Measured
T_{cell}	Receptors/cell	54,000	C57BL/6 Mouse	Measured
Q	Blood flow	173 mL/min/100g	Not rate limiting	[98, 211]
[Cell]	Beta cell density	$7x10^8$ cells/mL		[21]
[T]	GLP-1 Receptor Conc	63 nM	Based on $7x10^8$ cells/mL	Calculated
P	Permeability	$2.1x10^{-5}$ cm/s	10-fold higher than non-fenestrated normal tissue	[98, 213]
k_{on}	Binding rate	$1.4x10^6$ /M/s		[214]
K_d	Binding Affinity	2.6/12.4 nM		Measured
D	Diffusion Coefficient	100 um^2/s	Not rate-limiting	[25]
S/V	Capillary surface area to tissue volume	505 cm^2/cm^3	Extremely high in islets	[5]
ε	Void fraction	0.1	Interstitial space in pancreas (adapted from	[98]

			insulin)	
R_{cap}	Capillary radius	3 μm		[284]
k_e	Internalization rate	See Results		Measured in vitro
k_{deg}	Residualization rate	0.012 /hr	Fluorescent dye specific	[179]
A	Fraction alpha	See Chapter		Measured
k_{fast}	Alpha clearance			
k_{slow}	Beta clearance			
V_{plasma}	Plasma volume	1.4 mL		[285, 286]

The uptake in islets was simulated using an adaptation of a previously published and validated tissue transport model [97, 287]. Literature values for the parameters are listed in Table 3.3 along with experimentally measured parameters. For the islet uptake, no parameters were fit to the experimentally measured %ID/g values.

To model the exocrine/background concentration, the non-target uptake rate in the exocrine pancreas was experimentally determined for both the 800CW and Cy7 monomers. By first blocking GLP-1R in vivo with non-fluorescent exendin, the non-target uptake in the exocrine pancreas was approximated using the %ID/g of fluorescent exendin post-blocking. Subtracting %ID/g of blocked pancreata from experiments without blocking, the specific uptake in the islets was quantified to be 0.5 ± 0.1 %ID/g and 0.5 ± 0.4 %ID/g for the 800CW monomer at 3 h and Cy7 monomer at 5 h, respectively. Assuming plasma protein binding fractions of the free IRDye 800CW and Cy7 for the monomers (31% and 97.5%, respectively), non-target uptake

rates were fit for the exocrine pancreas using a compartmental model and found to have an uptake half-life of 61 ± 18 min and 9.2 ± 0.7 min for 800CW monomer and Cy7 monomer, respectively. Using this non-target uptake rate, an exocrine concentration was modeled. The target tissue (islet) concentration was simulated by combining surface bound and internalized probe. The exocrine concentrations match experimentally determined pancreatic concentrations from blocked experiments. However, the predicted islet concentrations were lower than experimental values (if there is a < 2% beta cell fraction in the pancreas). This could be due to error in the total receptor concentration (receptors/cell and islet cell density) or exocrine cell receptor expression (discussed above). However, islet expression is still high enough to quantify loss in beta cell mass[76].

Chapter 4

Blocking Exocrine Glucagon-Like Peptide-1 Receptor In The Mouse Pancreas For Accurate Beta Cell Mass Quantification In Diabetic Models

4.1 Abstract

The ability to measure beta cell mass early in the development of type-1 diabetes (T1DM), before insulin insufficiency and elevated glucose levels, would be transformative for the diabetes community. Exendin imaging agents have shown promising results in preclinical animal models of disease. However, results in the clinic have so far failed to accurately quantify beta cell mass. One of the surprising outcomes was higher than expected signal in long-term T1DM patients, which should have no beta cells. Recent evidence by our lab and others indicates that a very low level of expression on exocrine cells could be contributing to this falsely high signal due to their much higher abundance. The goal of this work is to develop a successful imaging strategy in animal models of T1DM by blocking non-specific/exocrine probe uptake to increase beta cell specificity. Using a multi-dose strategy with a lipophilic blocking agent, it was possible to block near-100% of exocrine signal while sparing a sufficient amount (15-20%) of the endocrine receptor for imaging. This provides a feasible method to block exocrine receptors and specifically label beta cells in a clinically translatable manner.

4.2 Background

Unregulated blood glucose levels resulting from diabetes negatively impact over 400 million patients worldwide. In addition to the financial burden, which constitutes approximately 10% of all healthcare costs in developed countries, patients are at risk of kidney disease, peripheral artery disease, and stroke and must rely on medications for life as no cure currently exists. Understanding disease pathophysiology has long been an interest for both the medical community and patients. However, diabetes remains challenging to study due to the inability to directly monitor the human pancreas, the central organ in the disease. Insulin-secreting beta cells play a pivotal role in disease progression but they cannot be directly observed. Functional studies, such as measuring insulin secretion or glucose monitoring, are not sensitive to early stages of the disease due to excess insulin secretion capacity of the beta cells. A non-invasive molecular imaging method for quantifying the beta cell mass (BCM) will prove invaluable for monitoring disease progression and assessing treatment efficacy.

There is currently no method for measuring the insulin-secreting BCM during the progression and treatment of diabetes. Molecular imaging approaches are promising, but the small size of islets of Langerhans where beta cells reside and low fraction of beta cells in the pancreas (~1% in healthy patients) have prevented the development of a translatable method. The inability to measure beta cell mass (BCM) in the clinic is a major roadblock to understanding the basic etiology of the disease, monitoring islet transplants, and measuring the efficacy of immunomodulatory therapies. Extensive research has been conducted to develop an imaging approach, but the small size and low fraction of islets in the pancreas have so far prevented a translatable method. One of the most advanced imaging targets has recently shown

higher than expected signal in patients that completely lack beta cells. Recently, others and we have demonstrated that off-target binding of glucagon-like peptide 1 (GLP- 1) receptor imaging agents has confounded the development of a probe for measuring beta cell mass in diabetes. New evidence indicates that low-level expression of glucagon-like peptide 1 receptor (GLP-1R) on non-target (exocrine) cells in the pancreas is responsible for the lack of specificity of these agents. Low levels of GLP-1R expression on exocrine cells are reported in mice, monkeys, and humans and can be blocked with unlabeled peptide without saturating beta cells, thereby allowing a follow-up imaging dose to specifically quantify BCM in animals and humans. This problem presents an opportunity to develop a translatable approach for beta cell imaging. By blocking non-specific/exocrine probe uptake, beta cell specificity can be improved for clinical translation.

To preferentially block the exocrine GLP-1R while maintaining free beta cell receptor for imaging agent labeling, a multiple dose strategy will be demonstrated using mouse models. Multiple doses are required to completely block the exocrine cells due to trafficking of the receptor. An exocrine saturating dose of lipophilic fluorescent exendin is first administered to block surface receptors and intracellular receptor that is recycled to the surface (due to the slow plasma clearance of the lipophilic peptide). The lipophilic molecule may also have slower diffusion into the Islets of Langerhans, sparing some of the desired target (endocrine receptor). An imaging dose is then administered to rapidly target the endocrine beta cells.

4.3 Results

Exendin is Taken Up Specifically by Low GLP-1 Receptor Expression in the Exocrine Pancreas

To independently verify exocrine GLP-1R expression, either blocking or imaging agent doses were administered intravenously to GLP-1R knockout mice. Comparing the fluorescence intensities quantified by flow cytometry, the exocrine signal from a wild type mouse receiving a high blocking dose of non-fluorescent exendin was lower than an unblocked mouse but the same as GLP-1R knockout mice (blocked or labeled). This indicates exendin binds specifically to GLP-1R (but not to any other receptors) and confirms a low level of exocrine GLP-1R expression.

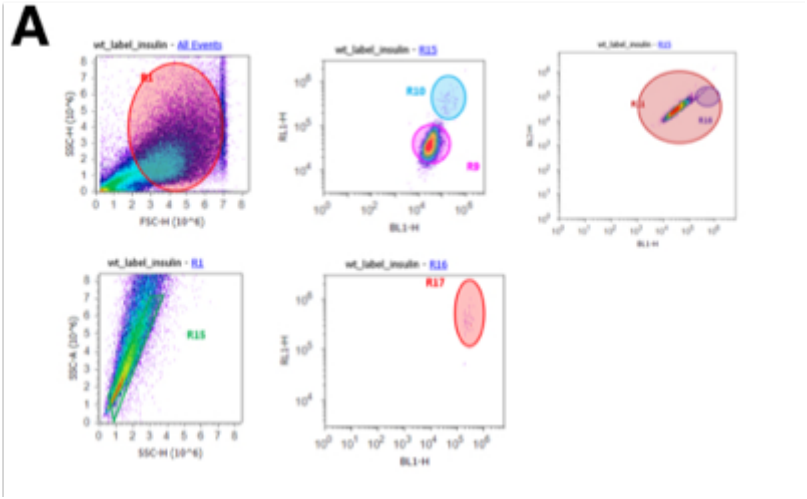

Figure 4.1 Flow cytometry for quantitative analysis of beta cell fluorescence.
The gating scheme is as follows: whole cells➔singlets➔insulin (+) or (-). This helped quantify exendin probe uptake in endocrine and exocrine pancreas populations.

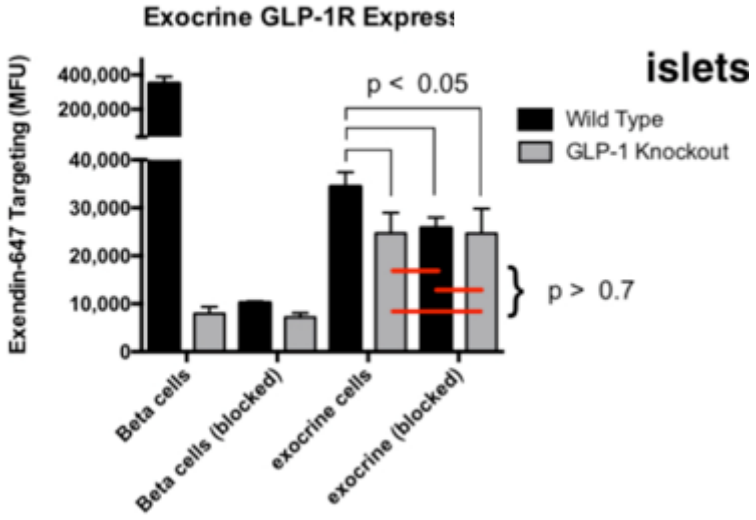

Figure 4.2 Demonstration of GP-1R expression in exocrine cells.
Three wild-type and 3 GLP-1R KO mice were injected with saturating doses of AF647 exendin. Three mice each were also injected with 15-fold excess of unlabeled peptide followed by AF647 exendin. The single cell suspension was run on flow cytometry. Exocrine cells showed a low but robust signal that could be blocked. Endocrine cells showed a much higher specific signal that could be blocked, as expected.

Exocrine Pancreas GLP-1R Can be Selectively Blocked

Three sets of healthy B6 mice were injected with either labeling, blocking, or low "exocrine-blocking" doses of exendin. For the labeled mice, 1 nmol of AF647 probe was injected via the tail vein, and the mouse was sacrificed 15 min after the probe injection. For complete blocking of GLP-1R, 15 nmol of exendin are injected followed 10 min later by 1 nmol of AF647-exendin, and sacrificed 15 min after the imaging probe injection. For the low "exocrine-blocking" dose, 170 pmol of Cy7-exendin is injected i.v. followed 10 min later by 1 nmol of AF647-exendin. 5 min after the imaging dose, a 15 nmol "post-block" dose of exendin is injected i.v. to "quench" any remaining receptor that traffics to the surface of exocrine cells. 10 min later (15 min after imaging probe injection), the mouse is sacrificed. The pancreas were removed and digested into a single cell suspension followed by cytometric analysis. The results

indicated near 100% of exocrine pancreas blocked in all sets of mice. A significant fraction of the endocrine beta cell receptors were blocked as well (80-86%).

Preliminary results showed that a hydrophilic probe could not selectively saturate the exocrine pancreas relative to islets. The working hypothesis is that the probe could rapidly diffuse into the islets such that blocking was limited by the thermodynamics of binding rather than the kinetics of delivery. Multiple doses of the Cy7 probe were required to completely block the exocrine cells due to trafficking of the receptor. To prevent trafficking in the exocrine while waiting for the imaging dose to clear from the blood, a high non-fluorescent post-block dose was injected 5 minutes after the imaging agent dose.

Table 4.1 Endocrine and exocrine blocked values for exocrine blocking dosing strategy

	Endocrine (beta cells), % blocked	Exocrine, % blocked
Set 1	86	100
Set 2	80	100
Set 3	85	98

Preliminary results with streptozotocin (STZ)-induced diabetic mice indicated a lack of islets both macroscopically (whole organ image) and at a cellular level (flow cytometry). Endocrine fluorescence intensity for STZ-treated mice, whether receiving a high-blocking dose or only an imaging dose, indicated a complete lack of beta cells in the pancreas. The exocrine intensity, however, was significantly higher for mice that received only the imaging agent dose. The results suggest GLP-1R expression in the exocrine tissue for mice treated with STZ.

Blood sugar levels were recorded for all animals before injection to ensure all healthy animals had significantly lower blood glucose levels than diseased animals. Healthy animals had levels ranging from 140-250 mg/dL of glucose, whereas STZ-treated animals had levels ranging from 400-600 mg/dL.

4.4 Discussion

Exendin remains a promising targeting ligand for measuring BCM, but clinical translation has not been as successful as anticipated. Recently, multiple labs have demonstrated imaging agent signal from non-beta cell have confounded the development of a probe for quantifying the beta cell mass for type 1 diabetes. This inability to monitor the functioning BCM in real time is a hindrance to understanding disease progression, monitoring islet transplants, and assessing treatment efficacy of immunomodulatory therapies.

The two most promising targeted molecular ligands for beta cells, namely agents for VMAT2 and GPL-1R, have shown higher than expected pancreas signal in long-term diabetics where there should be no beta cells remaining. Recent evidence by our lab and the literature has demonstrated low-level expression of GLP-1R in the exocrine tissue. This low level expression on non-target tissue, which remained elusive and controversial for many years due to the lack of specific antibodies against the receptor, is responsible for the lack of specificity of radiolabeled exendin-based imaging agents in the clinic. For this reason, there is a need to overcome the low expression in the exocrine pancreas tissue in order to develop a robust strategy for quantifying the beta cell mass in the clinic. The goal of this work is to develop a delivery strategy to specifically target beta cells to improve specificity. The strategy includes blocking the low level of GLP-1R expression in the exocrine tissue due to the large differences in receptor density (~850 receptors/cell versus 53,000 receptors per cell in exocrine and endocrine, respectively). A subsequent imaging dose can then specifically quantify BCM in animals and humans. Endocrine and exocrine receptor expression level was previously quantified and appropriate blocking doses were formulated to simultaneously saturate exocrine tissue while subsaturating the beta cells.

To generate the blocking peptide, a lipophilic Cy7 fluorophore was covalently conjugated to exendin peptide via copper-catalyzed click chemistry. The molecular weight was verified via ESI-MS and targeting specificity was verified using an *in vitro* binding assay. The imaging dose was similarly synthesized by conjugating a hydrophilic Alexa Fluor 647 fluorophore to exendin. The more lipophilic Cy7 exendin conjugate has a lower diffusion coefficient in tissue, which prevents unwanted diffusion of the blocking dose to the endocrine beta cells. As a result, the blocking dose is delivered 'locally' (i.e. it doesn't diffuse significantly between the endocrine and exocrine tissue) at a rate proportional to the permeability surface area product (PS/V). This is consistent with previous work (data not shown) using a hydrophilic exendin as the blocking dose where high amounts of endocrine GLP-1R were blocked, presumably from diffusion into the islets from the exocrine tissue. Additionally, a lipophilic Cy7 exendin will clearly slowly from the blood allowing for the blocking dose to block recycled intracellular receptor. Previous data indicate islets of Langerhans reach maximum imaging agent signal 3-5 minutes post intravenous injection in mice. For this reason, a hydrophilic imaging agent dose was chosen to quickly saturate the endocrine beta cells.

Given the similar GLP-1R mRNA profiles between mice and rats but large difference in exocrine uptake of exendin imaging probes, other groups have speculated that the probes may be binding a different receptor in mice. To confirm that these probes are only binding to GLP-1R in both the islets and exocrine pancreas, a GLP-1R knockout mouse model (courtesy of Dr. Dan Drucker) was imaged with our fluorescent probes. Fluorescence provides the single-cell resolution needed to quantify endocrine versus exocrine signal compared to radiolabels. It was demonstrated fluorescent exendin probes bind exclusively to GLP-1R in the pancreas (both beta cells and exocrine cells). To obtain this result, both wild type and knockout ($GLP\text{-}1R^{-/-}$) mice

were injected with 1 nmol of exendin-AF647 intravenously, and the pancreas was harvested 20 min later, digested, and analyzed by flow cytometry. A second set of mice received a large (15 nmol) blocking dose of exendin 10 min prior to the 1 nmol fluorescent dose. The wild type controls show very high signal in the beta cells as expected. Importantly, unblocked GLP- 1R knockout mice showed the same exocrine signal as blocked mice, indicating that only GLP-1R is contributing to the exocrine uptake. The signal intensity ratio between beta cells and exocrine cells is ~40 which is consistent with our published estimate from biodistribution data. These fluorescent probes and flow cytometry data provide the extreme sensitivity necessary for measuring the very low but specific exocrine cell uptake. Despite these challenges and the controversy surrounding expression in different cell types, these data support a low-level expression of GLP-1 receptor in exocrine cells, which is consistent with other animal studies, physiological function of the receptor in exocrine cells, multiple reports showing *ex vivo* expression in humans, and the high signal intensity in some patients in clinical trials but not others (due to patient-to-patient variability in exocrine expression).

After verifying exocrine GLP-1R, a blocking dose was implemented to preferentially block exocrine GLP-1R. This presents several challenges: the target and non-target cells are in the same tissue, and the blocking dose is more efficiently delivered to the undesired target tissue due to increased S/V (505 cm^2/cm^3 versus 180 cm^2/cm^3). As previously described, the first challenge was overcome using a lipophilic blocking dose with slow tissue diffusion. The binding and rapid internalization of the blocking dose allows for the selective blocking of exocrine cells through rapid binding. The challenge of more efficient delivery to the beta cells can be overcome by comparing the absolute GLP-1R expression on exocrine and endocrine cells. Despite a 3-fold higher surface area to volume in the endocrine tissue, there is a 50-fold greater receptor

expression. This indicates a 17-fold lower dose is required to saturate the exocrine compared to the islets of Langerhans. Although these predictions suggest a 17-fold difference, experiments indicated a 6-fold difference using a lipophilic Cy7-exendin blocking dose. The data indicate it is possible to block all exocrine receptors in the mouse pancreas while retaining approximately 15-20% of the receptors on beta cells for probe binding. The remaining receptors are dramatically higher than required for PET or SPECT imaging given the high sensitivity of the modalities. Therefore, the ability to completely block the exocrine signal was the highest priority.

4.5 Conclusions

A successful imaging agent capable of quantifying changes in BCM during the progression of type-1 diabetes mellitus (T1DM), type-2 diabetes, and during therapeutic intervention would be invaluable to the diabetes community. Based on our data and literature reports, the pancreatic uptake of exendin probes in humans and animal models is sufficient for detection, but the major problem is the high signal in T1DM patients where there should be no signal. The goal of this work is to develop a successful imaging strategy in T1DM by blocking non- specific/exocrine probe uptake to increase beta cell specificity. Our central hypothesis was that the low level of GLP-1R expression on exocrine cells in mice could be blocked with unlabeled peptide without saturating beta cells, thereby allowing a follow-up imaging dose to specifically quantify BCM. Using a multi-dose strategy by pre-blocking exocrine cells with a lipophilic exendin followed by an imaging dose and a large post-imaging dose block (to prevent uptake during plasma clearance of the imaging probe), near-100% exocrine blocking could be achieved while sparing a sufficient amount (15-20%) of the endocrine receptors. This strategy provides a feasible path forward for a clinically translatable approach to quantifying beta cell

mass.

4.6 Experimental Methods

Preparation of fluorescent exendin monomers

AF488 alkyne (0.2 μmol) was added to 200 μL of water followed by $CuSO_4$-TBTA (20 nmol) and sodium ascorbate (1 μmol). Lastly, mutant exendin (0.2 μmol) was added and the reaction mixture was stirred at room temperature for 12 h followed by purification using preparative RP-HPLC (AF647 monomer: 20-30% B 0.1-4 min, 30% B 4-7 min, 30-55% B 7-17 min: t_R = 15.3 min). MALDI-TOF: AF647 monomer: *m/z* calculated: MW of dye unpublished, found: 4859.

Animals

All animal experiments were conducted in compliance with the University of Michigan University Committee on Use and Care of Animals (IACUC). To block exocrine GLP-1R, 170 pmol of Cy7 exendin was injected intravenously. After 10 min, 1 nmol of AF647 exendin was administered. After 5 min 15 nmol of non-fluorescent exendin was administered to block recycling exocrine receptors while the imaging agent cleared from the circulation. 10 min later, the animal was euthanized and the pancreas removed for macroscopic imaging to confirm targeting specificity. 'Labeled' and 'blocked' mice were used to determine the range of exocrine values. For 'labeled' conditions, the animal received 1 nmol of AF647 exendin and was euthanized 15 minutes after injection. For 'blocked' conditions, the animal received 15 nmol of

non-fluorescent exendin; 15 min later, the animal received 1 nmol of AF647 exendin and was euthanized 15 min later.

The Jackson Laboratory treated mice with streptozotocin (STZ). Animals were given daily IP (interperitoneal) injections of STZ once per day for 5 consecutive days. At the same time, control mice will be injected with saline solution following the same protocol. On the 16th day after the initial injection, blood glucose levels were measured.

Pancreas Digest

Pancreas were digested in 1000U/ml collagenase IV at 37°C for 15 min with intermittent shaking. The digest solution was filtered, washed 2 x with media (F12K w/ 10% FBS), and washed 2 x with PBS before quantified using flow cytometry (Attune). The remaining cells were fixed using 4% paraformaldehyde.

Insulin Stain

The fixed cells were incubated overnight at 4 ^{o}C with a rabbit anti-insulin primary antibody (dilution 1:150 in PBS with 0.1% BSA supplemented with 1% goat plasma), followed by a 30 min room temperature incubation with goat anti-rabbit IgG FITC secondary antibody (dilution 1:50 in PBS with 0.1% BSA). Insulin positive cells were shown to be labeled with AF647 exendin using flow cytometry.

Chapter 5

A Dual-Purpose Linker For Alpha Helix Stabilization And Imaging Agent Conjugation To Glucagon-Like Peptide-1 Receptor Ligands

5.1 Publication Information

Zhang, L., T. Navaratna, J. Liao**,** and G.M. Thurber. *A dual-purpose linker for alpha helix stabilization and imaging agent conjugation to glucagon-like Peptide-1 receptor ligands*. Bioconjugate Chemistry. 2015; 26(2): 329-37.

Modifications have been made to the published document to adapt the content to this text. Previous chapters demonstrate successful beta cell targeting strategies using the exendin peptide. This chapter illustrates peptide stabilization strategies to address the limitations of peptide-based imaging agents and therapeutics.

5.2 Abstract

Peptides display many characteristics of efficient imaging agents such as rapid targeting, fast background clearance, and low non-specific cellular uptake. However, poor stability, low affinity, and loss of binding after labeling often preclude their use *in vivo*. Using the glucagon-like peptide-1 receptor (GLP-1R) ligands exendin and GLP-1 as a model system, we designed a novel alpha helix stabilizing linker to simultaneously address these limitations. The stabilized and labeled peptides showed an increase in helicity, improved protease resistance, negligible loss or an improvement in binding affinity, and excellent *in vivo* targeting. The ease of incorporating azidohomoalanine in peptides and efficient reaction with the dialkyne linker enables this technique to potentially be used as a general method for labeling alpha helices. This strategy should be useful for imaging beta cells in diabetes research and in developing and testing other peptide targeting agents.

5.3 Background

The ability to image and observe cellular phenomena both *in vivo* and *in vitro* plays a crucial role in understanding disease progression and treatment response [288, 289]. Molecular imaging agents enable investigators to probe the dynamics of specific biologic interactions in normal and pathological conditions. In principle, peptides are ideal imaging agents due to their low molecular weight[275], rapid clearance from background tissues, and ability to mimic protein-protein interactions for high binding specificity[290]. However, these agents suffer from several problems including poor stability due to proteases, low affinity from lack of a stable conformation, and difficulty in labeling with fluorescent and/or radioactive probes without disrupting binding[291]. Due to recent advances in synthesis techniques, there is renewed interest in using stabilized alpha helices with improved protease resistance and binding affinity for targeting both intracellular[292, 293] and extracellular[294] proteins. Side chain cross-linking reactions to promote an alpha helix conformation include olefin metathesis[295], copper catalyzed azide-alkyne reactions[296, 297], lactam ring formation[298], and disulfide bonds[299, 300] among others[294].

In many cases, stabilizing the alpha helix increases helicity, improves binding affinity, and/or increases protease resistance[301]. However, this is not universally true since the introduction of the side chain cross linker necessarily introduces two mutations into the sequence and the linker addition itself, which can each change intra- and inter- molecular interactions[302-304]. The sequence mutations and cross linker can impart both positive and negative contributions to the free energy of helix formation and free energy of binding, making the net impact challenging to predict *a priori* from structural considerations alone.

In the context of imaging agent development, while these stabilizing structures have the potential to improve protease stability and binding affinity by locking molecules in a helical

conformation, this exacerbates the problem of labeling the peptide since multiple modifications must now be done without disrupting the binding interface. To address this issue, we synthesized probes using a novel linker to simultaneously label and stabilize an alpha helix to improve protease stability while maintaining *in vitro* and *in vivo* binding affinity. This was compared with two non-fluorescent stabilizing linkers (Scheme 5.1) to separate the impact of the fluorophore from helix stabilization.

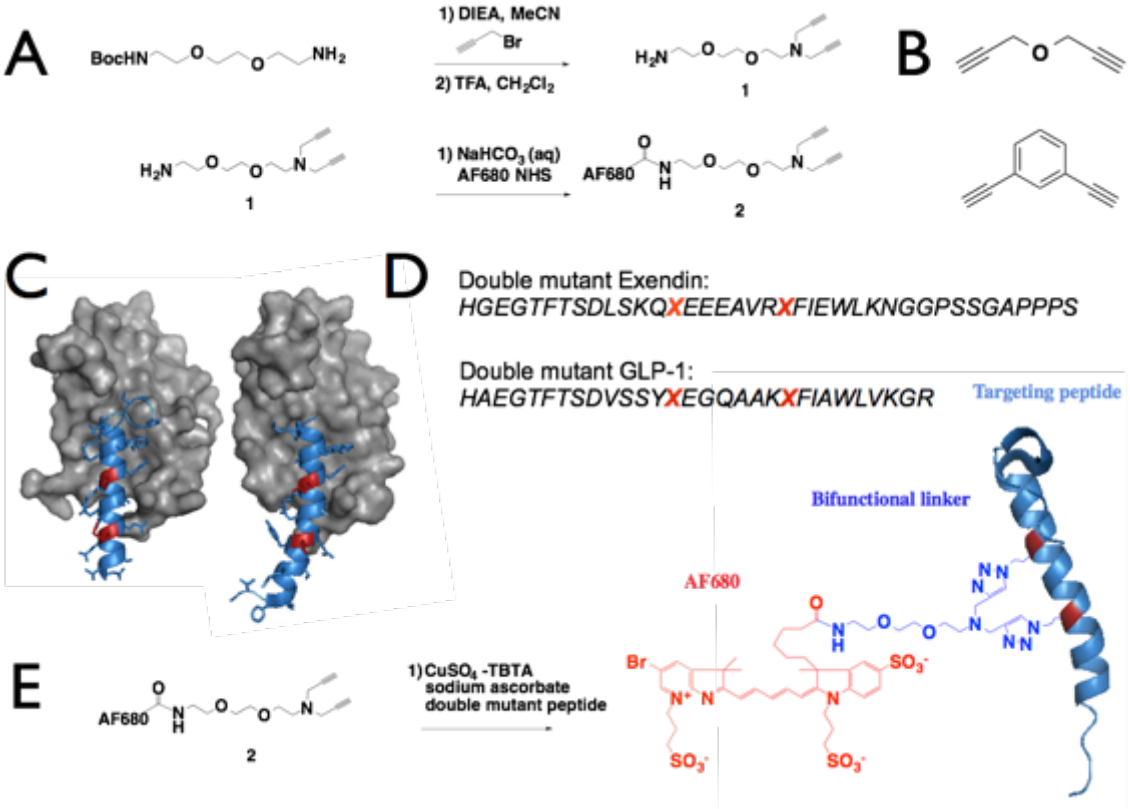

Scheme 5.1 Linker design and synthesis
A Boc-protected hydrophilic spacer was alkylated with propargyl bromide and deprotected to provide a free amine for fluorophore conjugation (A). Propargyl ether (top) and 1,3-diethynylbenzene (bottom) were used to test steric effects of the dye and rigidity of the linker (B). The crystal structure of exendin (left, PDB 3C59) and GLP-1 (right, PDB 3IOL) are shown with the modified residues highlighted in red (C) and the double mutant sequences (D). The peptides were reacted with the linker to form labeled and stabilized alpha helices (E).

One promising application of targeting peptides is to utilize modified glucagon-like peptide 1 receptor (GLP-1R) binding peptides for imaging beta cells in diabetes[305, 306]. Beta cells express moderate to high levels of GLP-1 receptor resulting in excellent target specificity versus exocrine cells within the pancreas. These properties have led several investigators to explore the use of radiolabeled exendin molecules for tracking beta cell mass in diabetes[45, 65, 253, 254, 287, 305, 306]. However, the molecular properties of the radiolabeled peptide require further optimization before obtaining clinical utility[65, 254]. Using a novel dialkyne linker with a functional handle for attaching an imaging agent, we synthesized a dual-purpose linker to simultaneously stabilize and label alpha helices. Here we demonstrate the improved protease resistance and *in vivo* targeting of these stabilized glucagon-like peptide-1 receptor (GLP-1R) ligands for visualizing the beta cell mass in the pancreas.

The ligands GLP-1 and exendin share significant homology and bind the same pocket on GLP-1R, but they exhibit distinct differences. Exendin binds in a straight alpha helix while GLP-1 has a small kink around glycine-22[307]. Exendin also has significant helical structure in solution while GLP-1 is almost completely disordered[308]. This allowed us to investigate several aspects of the linker including the impact on helicity, flexibility, affinity, and stability.

One turn of an alpha helix constitutes approximately 3.6 amino acid residues. As a result, i, i+4 and i, i+7 are frequent candidates for crosslinking residues between either one or two adjacent loops[298]. To generate a staple across two loops, we postulated that non-natural azide-containing amino acids could be introduced and crosslinked at i, i+7 residues in exendin-4 and GLP-1 through incorporation of azidohomoalanine (AHA) during solid phase peptide synthesis (SPPS). A novel dialkyne linker is used to bridge the two AHA side chains and stabilize the helix while introducing a functional handle for labeling. The chemistry utilizes the well-studied copper

catalyzed azide alkyne cycloaddition (CuAAC) for high-yielding and specific crosslinking of the desired residues.

The AHA substitution locations were selected using crystal structures[42, 307] for the receptor-ligand interaction as well as alanine scan data of GLP-1 with sequence alignment for exendin-4[309]. Previous work labeling exendin with fluorescent tags has shown variable tolerance (negligible impact to >30-fold reduction in binding) at several positions with different fluorophores along the peptide backbone[105]. The requirements for a stabilizing linker are even more stringent. First, the linker must be located within the alpha helix portion of the peptide, ruling out labeling of the c-terminal and n-terminal regions. Second, the cross-link necessitates a larger structure adjacent to the peptide compared to a single fluorophore. Ultimately, methionine at the 14th position (M-14) and leucine at the 21st (L-21) were substituted with AHA for exendin-4 to generate double mutant exendin. Similarly, L-20 and E-27 substitutions were made to GLP-1 (7-36) for double mutant GLP-1. We present novel stabilized GLP-1R ligands crosslinked with dialkyne linkers (Scheme 5.1E) of varying rigidity and demonstrate that all conjugates maintain GLP-1R specific targeting. To abbreviate the structure names, the stabilized alpha helices of exendin generated with the AlexaFluor 680 linker, propargyl ether linker, and 1,3-diethynylbenzene are labeled AF680 sExendin, PropE sExendin, and DEB sExendin, respectively. AlexaFluor 680 linker, propargyl ether, and 1,3-diethynyl stabilized GLP-1 are named AF680 sGLP-1, PropE sGLP-1, and DEB sGLP-1. The novel structures should prove useful for developing stabilized alpha helix imaging agents.

5.4 Results

Stabilized alpha helical imaging peptides were generated using a novel dialkyne linker as shown in Scheme 5.1A. To generate the dual-purpose linker, N-Boc- 2,2'-(ethylenedioxy)diethylamine was alkylated with excess propargyl bromide, followed by deprotection with trifluoroacetic acid and subsequent purification via flash chromatography. The resulting intermediate **1** was further purified on HPLC followed by conjugation to AF680 NHS ester to yield **2**.

GLP-1R ligands exendin-4 and GLP-1 were chosen to demonstrate the ability of the dual-purpose linker to simultaneously stabilize and fluorescently tag targeting peptides under investigation for imaging in diabetes[105, 287, 306]. Based on crystallography data for the receptor-ligand interaction, the M14 and L21 residues in exendin and L20 and E27 residues of GLP-1 were substituted with azidohomoalanine (Scheme 5.1B, C). The i, i+7 residues on exendin-4 and GLP-1 double mutant peptides were then reacted with **2** to stabilize and label the agents (Scheme 5.1D). In addition to alpha helix stabilization with **2**, we also investigated the effect of linker rigidity on the stabilized peptide with propargyl ether and the more rigid crosslinker 1,3-diethynylbenzene on the i, i+7 residues of the GLP-1R ligands. A non-stabilized single mutant exendin-4 labeled with AF647 was synthesized for quantifying the binding affinity of propargyl ether and 1,3-diethynylbenzene stabilized peptides in competition assays. Both AF647-exendin and stabilized peptides were purified using HPLC and characterized by MALDI-TOF (Figure 5.1).

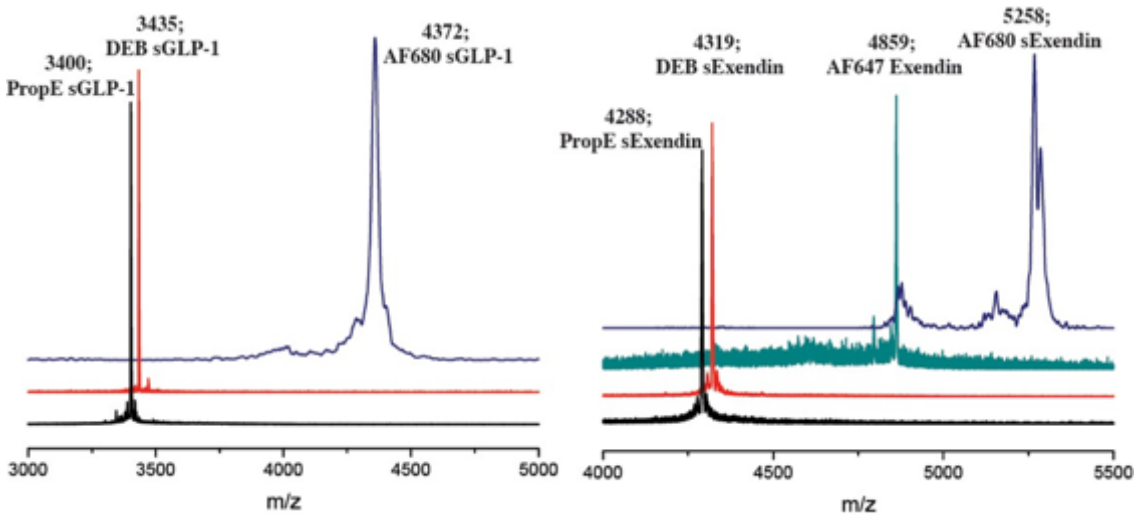

Figure 5.1 MALDI-ToF mass spectrometry traces of purified peptides showing successful synthesis of stabilized helices

To determine the effect of the alpha helix stabilization on protease resistance, both double mutant GLP-1R ligands with and without i, i+7 crosslinks were subject to 500 ng/μl trypsin digests at room temperature. Unstabilized double mutant exendin with M14X and L21X modifications digested rapidly in the presence of trypsin (half life of 0.7 h, Figure 5.2). In contrast, the stabilizing crosslinker improved protease resistance over six-fold in the case of propargyl ether (half-life of 4.5 h) and almost five-fold for 1,3 diethynylbenzene (half-life of 3.2 h). The fluorescent crosslinker-stabilized exendin demonstrated an almost six-fold increase (half-life of 3.9 h). Stabilization of wild-type GLP-1 increased protease stability by 6-14 fold for PropE sGLP-1, DBE sGLP-1, and AF680 sGLP-1, respectively.

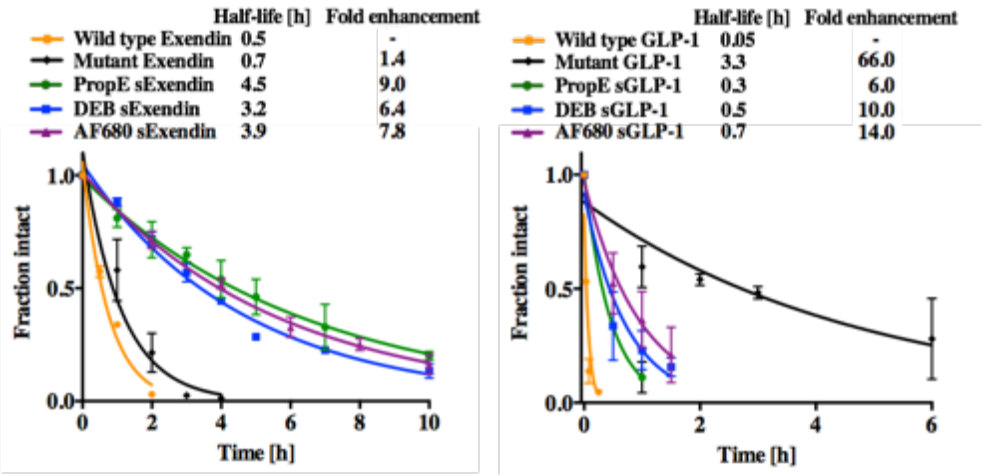

Figure 5.2 Protease stability of stabilized peptides
Digests were run on HPLC and monitored at 254 nm to separate intact versus degraded fragments and areas fit to an exponential decay.

The stabilizing linker increased protease resistance for exendin, but the impact on binding affinity from the stabilizing linker was unknown. To test the influence on target binding, the affinity was measured in a binding assay using NIT-1 cells (Figure 5.3). Eleven or 12 point curves were done in triplicate for each experiment, and all experiments were repeated on 2 or 3 separate days. M-14, L-21 azidohomoalanine (AHA) substitutions in exendin-4 did not significantly lower the binding affinity as anticipated by their orientation away from the binding pocket (Table 5.1). Similarly, GLP-1 also maintained high affinity despite the two substitutions. Stabilization of exendin with propargyl ether and 1,3 diethynylbenzene yielded a K_d = 0.9 ± 0.9 nM and K_d = 0.8 ± 0.2 nM, respectively. Neither affinity was statistically significantly different than the double mutant exendin (p value of 0.6 compared to prop exendin and 0.3 for 1,3 exendin), demonstrating that steric hindrance from the linker did not significantly increase the K_d. The AF680 linker-stabilized peptide had a K_d slightly above the original peptide but still maintained high affinity. For GLP-1, the propargyl ether stabilizer resulted in increased affinity with a K_d = 3.5 ± 0.8 nM. In the case of the more rigid 1,3 diethynylbenzene, alpha helix

stabilization resulted in similar affinity values. Stabilization with the new dual-purpose crosslinker also gave higher affinity for GLP-1R despite the presence of the fluorophore (K_d = 3.1 ± 0.7 nM). Both AF680 GLP-1 and prop GLP-1 were statistically significantly higher affinity than GLP-1 (p value of 0.04 for both), although 1,3 GLP-1 was not (p = 0.08).

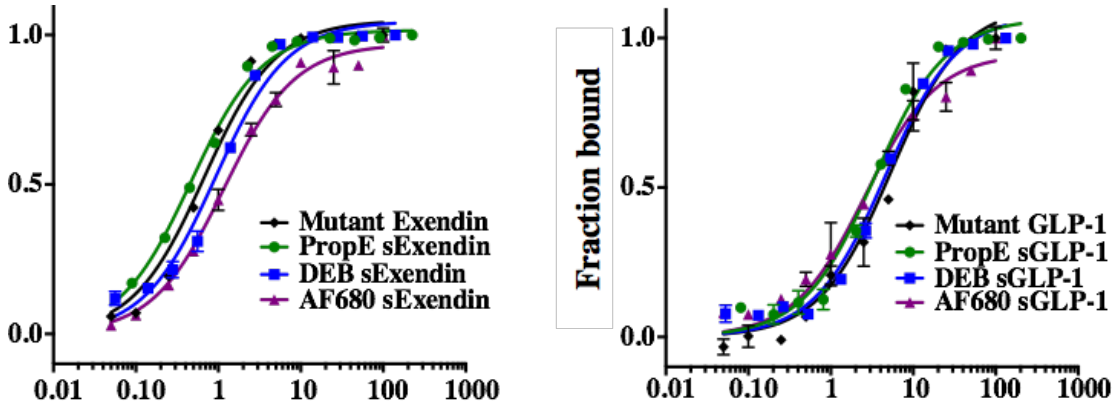

Figure 5.3 Representative affinity curves
In vitro cell binding affinity assays show negligible loss of affinity for exendin and a small improvement in binding for GLP-1 stabilized peptides.

Table 5.1 Summary of binding affinity values for multiple stabilized peptides

Peptide	Crosslinker	Binding affinity (nM)
Exendin (M14X, L21X)	None	0.5 (± 0.2)
Exendin (M14X, L21X)	Propargyl Ether	0.9 (± 0.7)
Exendin (M14X, L21X)	1,3-Diethynylbenzene	0.8 (± 0.2)
Exendin (M14X, L21X)	AF680	1.4 (± 0.3)
GLP-1 (L20, E27)	None	5.6 (± 0.2)
GLP-1 (L20, E27)	Propargyl Ether	3.5 (± 0.8)
GLP-1 (L20, E27)	1,3-Diethynylbenzene	4.8 (± 0.3)
GLP-1 (L20, E27)	AF680	3.1 (± 0.7)

The increase in affinity for GLP-1 was unexpected given the typical negative impact of steric hindrance on K_d[310]. Helix stabilization is known to decrease the entropic penalty of binding

by locking the peptide in an alpha helix and limiting the number of conformations[294]. To investigate the effect of the dialkyne cross-linker on the helix structure, circular dichroism measurements were taken to determine the % helicity. Non-stabilized double mutant exendin-4 contained intermediate helicity (57%) in phosphate buffer (Figure 5.4), consistent with the significant helicity of exendin[308]. The propargyl ether and 1,3 diethynylbenzene linkers had small increases in helicity (67 and 59%, respectively), and the fluorescent derivative had 55% helicity. Calculations of the fractional helicity are based on estimates of the number of helical residues within the peptide sequence[308]. To experimentally validate these estimates, 50% trifluoroethanol (TFE) was used as a solvent to drive the peptides into a helical conformation. The highest values for exendin and GLP-1 were between 93-104% indicating the number of helical residues used in the calculation was accurate.

Table 5.2 Summary of binding affinity values for multiple stabilized peptides in different solvents

Peptide	Crosslinker	χ^{helix} (buffer)	χ^{helix} (50% TFE)
Exendin (M14X, L21X)	None	0.57	0.93
Exendin (M14X, L21X)	Propargyl Ether	0.67	0.9
Exendin (M14X, L21X)	1,3-Diethynylbenzene	0.59	0.93
Exendin (M14X, L21X)	AF680	0.55	0.82
GLP-1 (L20, E27)	None	0.07	0.6
GLP-1 (L20, E27)	Propargyl Ether	0.38	1.04
GLP-1 (L20, E27)	1,3-Diethynylbenzene	0.23	0.81
GLP-1 (L20, E27)	AF680	0.3	0.71

All the peptides had elevated helicity (> 80%). On the contrary, GLP-1 has very little helicity in phosphate buffer (7%), but stabilization with propargyl ether, 1,3 diethynylbenzene, and the AF680 stabilizing linker resulted in a significant increase in % helicity (38, 23, and 30%). The higher helicity for stabilized peptides was maintained in 50% TFE buffer with 60% for the GLP-1 peptide and 104%, 82%, and 71% for the propargyl ether, 1,3 diethynylbenzene, and AF680 cross-linked peptides.

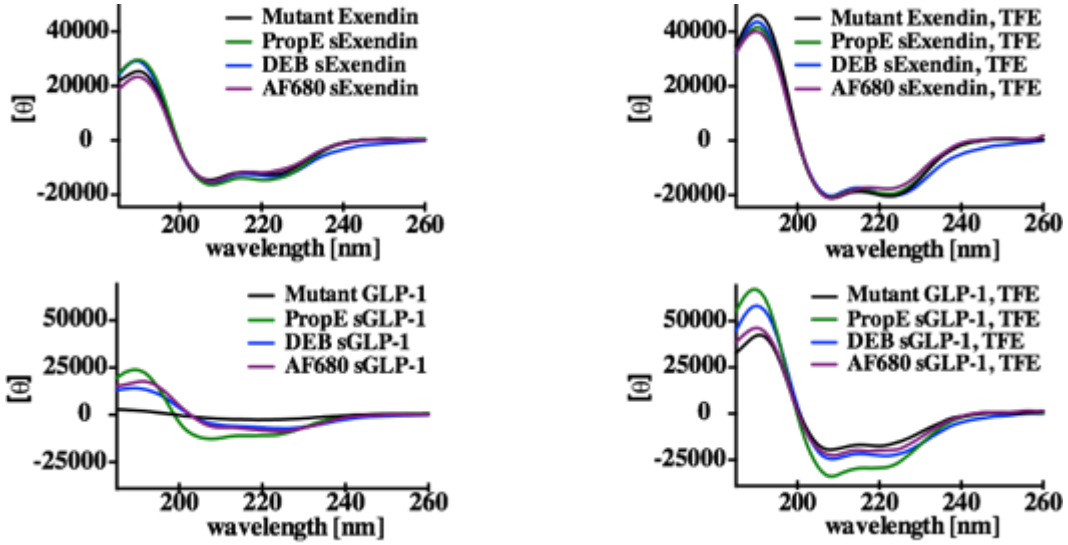

Figure 5.4 Circular Dichroism spectra of stabilized peptides in different solvents
The stabilizing linker dramatically improves the helicity of GLP-1 with a smaller increase in helicity for the more highly structured exendin peptide.

Owing to its higher stability, AF680 stabilized exendin-4 was used to demonstrate the *in vivo* imaging potential of the fluorescent helix stabilizing crosslinker. To show the specificity of the imaging agent for beta cells in the islets of Langerhans, AF680 exendin-4 was injected in C57BL/6 mice and allowed to circulate for 3 h. Blood samples were taken and the half life of AF680 exendin-4 in plasma was determined by fitting to a biexponential decay. We observed a fast decay $t_{1/2}$ of 2.7 min and a slow decay $t_{1/2}$ of 67 min (Figure 5.5). To confirm specific beta cell targeting, the animal was sacrificed after 3 h and the pancreas removed.

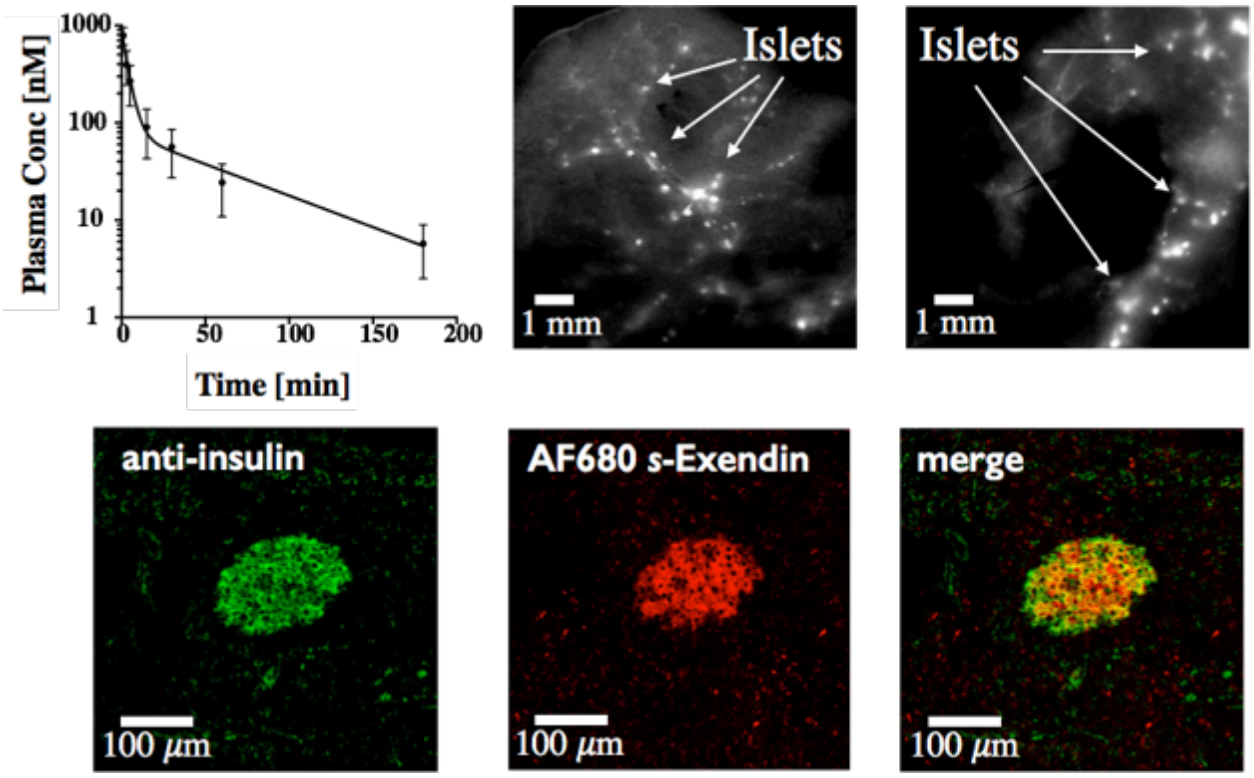

Figure 5.5 Plasma clearance and successful *in vivo* targeting of stabilized peptides
Stabilized fluorescent exendin clears rapidly from the plasma (top left) and efficiently targets islets, providing high tissue contrast (top middle). Beta cells form ~1-2% of the pancreas and are located in 100-300 μm Islets of Langerhans that are labeled intensely by the fluorescent peptides (arrows). K12C labeled fluorescent exendin is shown for comparison (top right). Histology slide of pancreas showing *ex vivo* anti-insulin staining of islets (left), *in vivo* delivered AF680 sExendin (middle) and merge (right).

Macroscopic scans of the organ indicate AF680 exendin-4 signal in distinct, punctate spots spread along the pancreatic vasculature indicating efficient targeting of the islets of Langerhans (Figure 5.5). A validated K12 labeled exendin peptide[227, 287] is shown for comparison.

5.5 Discussion

Peptides possess many properties that are ideal for imaging agents[311, 312]. Their low molecular weight allows rapid uptake in target tissue, fast clearance from background regions,

and low non-specific uptake. Despite these advantages, significant challenges exist including poor stability, low affinity, and difficulty in labeling without lowering affinity due to steric hindrance of binding. To help address some of these issues, we designed a dual-purpose linker to simultaneously label an alpha helix peptide while stabilizing the secondary structure.

For the linker design, propargyl bromide was used to react with the hydrophilic spacer for optimal cross-linker length. Previous reports of i, i+7 linkers indicated that a 13-atom linker stabilizes an alpha helix conformation[294]. Linker design was critical to avoid the stabilization of other types of helices[313] or longer linkers that lack stability[314]. The facile incorporation of azidohomoalanine, either by synthetic techniques (SPPS) or biological systems[315] makes this cross-linking chemistry advantageous for synthesizing stabilized helices. The 7-carbon span of the dialkyne generates a 13-atom cross-link for efficient stabilization of an alpha helix.

Stabilization of alpha helices reduces the solvent interaction of the hydrophilic backbone and can increase cell permeability[292, 316]. While membrane permeability is desirable for intracellular targets, this would increase the background signal of an imaging agent. A diethylene glycol spacer was placed between the amine functional handle and the dialkyne to impart additional hydrophilicity to the linker. Although the fluorescent dyes used in this work are charged and hydrophilic, the linker will aid in radiolabelling applications where the tag may be more lipophilic.

As a model system for testing the dual-purpose linker, we chose exendin and GLP-1 peptides. We and others[65, 105, 227, 254, 287, 305, 306] have used exendin and stabilized GLP-1[45] for imaging beta cells and increasing therapeutic efficacy, and the peptides are well characterized. Several GLP-1R agonists are in the clinic for treating type 2 diabetes[317], and the crystal structures of both peptides bound to their target have been published.

The stabilized peptides were synthesized with moderate yield (9-63%) with the expected molecular weight shown by MALDI-TOF. Despite the homobifunctional cross-linking chemistry, little to no oligomerization was detected. This is likely due to templating effects from the peptide backbone[297] and is in agreement with the higher yield for the more helical exendin-4 peptide compared to GLP-1. An additional linker, 1,4 diethynylbenzene, was tested to see if the increased strain from a more rigid linear cross-linking agent would stabilize or destabilize the helix. However, yields of this reaction were extremely low likely due to inefficient cross-linking (data not shown). The stabilized helices showed up to a 6-fold increase in trypsin protease stability. For exendin, the three predicted cleavage sites include one site within the cross-link, one just outside the cross-link, and a third several residues away. The increased helicity along with direct steric hindrance likely contributes to the lack of protease digestion.

Despite the larger cross-linking label, the K_d for AF680 stabilized exendin only increased by 0.9 nM. Locating the linker opposite the binding interface and including a hydrophilic spacer allowed the peptide to maintain high binding affinity in addition to the increased protease stability. The other cross-linking agents did not have a significant impact on the affinity of exendin. This is likely due to the high helicity of the peptide even without a stabilizing side chain crosslink. To corroborate this argument, a three state thermodynamic model of binding for helical peptides (supplementary data) was used to show a negligible predicted increase in the binding affinity (0.42 to 0.53 nM) for exendin. The larger increase in helicity for GLP-1 results in a small but significant predicted increase in binding affinity (K_d ~ 1.5 nM) in the absence of steric effects and enthalpy changes.

The trade-off between a more rigid alpha helix (lowering the entropic penalty but reducing the enthalpy of binding) and a more flexible linker has been established for stabilized

helices[294]. The stabilized GLP-1 peptides demonstrated a small but statistically significant increase in affinity and a large increase in helicity, consistent with the thermodynamic model. GLP-1 is disordered in solution, so stabilizing the alpha helix increases the affinity by a lower entropic penalty upon binding. In principle, locking the GLP-1 peptide in a straight alpha helix could lower affinity by removing the kink present in the crystal structure. This level of detail is not captured in the simple three state model. For GLP-1, it appears that the i,i+7 cross link is flexible enough to allow for high affinity interactions, or at the very least, the reduction in the entropic penalty dominates the free energy of binding and affinity.

Comparing the more rigid 1,3 diethynylbenzene cross-linker versus the propargyl ether, it appears the latter has more helix inducing propensity in these two peptides. While both increased the protease stability of exendin, the affinity of GLP-1, and the helicity in phosphate buffer for both peptides, the propargyl ether did so to a larger extent in each case. The additional flexibility likely makes the alpha helix more energetically favorable thereby increasing protease stability, affinity, and helicity.

The stabilized fluorescent peptide maintained efficient targeting of beta cells *in vivo*. The rapid clearance from the plasma is beneficial for lowering background fluorescence but could potentially reduce targeting if insufficient amounts reach the beta cells. Intravital microscopy experiments of exendin show rapid uptake in islets within several minutes after injection[227]. Islets are highly vascularized (500 cm^2/cm^3 blood vessel surface area to volume[287]) with fenestrated endothelium which should allow efficient access to the target cells. For tumors, an analysis of molecular weight versus targeting efficiency concluded that lower molecular weight high-affinity binders have more efficient targeting[275]. Small agents were all filtered rapidly by

the kidneys, but the lower molecular weight agents extravasated more quickly. It remains to be seen whether the same quantitative conclusions apply to the pancreas.

We anticipate this dual-purpose linker will have many applications with other peptides in imaging and therapeutic development. Recently, Lau et al. used a poly-arginine conjugated 1,3 diethynylbenzene cross-linker to increase cellular uptake of a p53 alpha helix[137]. In their MDM2 targeting peptide, they found a similar trend where a more flexible aliphatic dialkyne produced better stabilization than a more rigid 1,3 dialkylbenzene[318]. This is analogous to our findings where propargyl ether resulted in more efficient binding and helicity. Importantly, the propargyl ether and fluorescent linkers maintain hydrophilicity for this extracellular target compared to the intracellular MDM2-targeting peptides. The ability to both stabilize the alpha helix and impart additional functionality through the tertiary amine in our linker minimizes the impact of sterically bulky groups. Successful alpha helix stabilization in both the GLP-1R targeting peptides and MDM2 peptides provides evidence that this method will work as a general strategy. The functional linker should have applications in many stabilized alpha helix applications including imaging agents, drug design, surface modification, and affinity separations[319, 320].

5.6 Conclusion

We have reported a novel dual-purpose linker that is capable of labeling GLP-1 receptor ligands with an imaging agent modality, stabilizing the alpha helix structure, and increasing protease stability while having minimal impact or an improvement on binding affinity. This approach should have utility in engineering novel stabilized alpha helices with improved properties for molecular imaging.

5.7 Experimental Methods

Double mutant exendin-4 (HGEGTFTSDLSKQXEEEAVRXFIEWLKNGGPSSG APPPS), double mutant GLP-1 (7-36, HAEGTFTSDVSSYXEGQAAKXFIAWLVKGR), and single mutant exendin-4 (HGEGTFTSDLSKQXEEEAVRLFIEWLKNGGPSSGAPPPS), where X is the non-natural amino acid AHA, were purchased from Innopep (San Diego, CA). Fluorochromes AF647 alkyne and AF680 N-hydroxysuccinimidyl (NHS) ester were purchased from Life Technologies (Carlsbad, CA). N-Boc- 2,2'-(ethylenedioxy)diethylamine, rabbit anti-insulin, and goat anti-rabbit IgG FITC antibodies were purchased from Santa Cruz Biotechnology (Dallas, TX). All other reagents, unless specified, were purchased from Sigma-Aldrich (Milwaukee, WI) and were used as received. Reverse phase high performance liquid chromatography (RP-HPLC) was performed on a Shimadzu LC unit using analytical and preparative reversed phase Phenomenex Luna C18(2) columns. MALDI-MS spectra were collected using a Bruker Autoflex mass spectrometer, and ESI-MS analysis was performed on an Agilent Q-TOF 1200 series. NMR spectra were collected using a Varian MR400 spectrometer. Fluorescence microscopy images were collected using an Olympus FV 1200 confocal microscope.

Preparation of (1)

N-Boc- 2,2′-(ethylenedioxy)diethylamine (805 μmol) was added to diisopropylethylamine (2.40 mmol) in 3.8 mL MeCN. Propargyl bromide in toluene was added dropwise (2.62 mmol). The reaction mixture was stirred overnight at room temperature before being concentrated under reduced pressure and then subjected to flash chromatography (80:7:1 $CHCl_3$: MeOH: NH_4OH). The desired fraction was concentrated, deprotected using 50%

trifluoroacetic acid in dichloromethane, and purified using preparative RP-HPLC using a linear gradient of MeCN in H_2O to yield **1** (475 μmol, 59%).^{1}H NMR (400 MHz, CD_3OD) δ 3.89 (4H, d), 3.77 (2H, t), 3.73 (2H, t), 3.70 (4H, s), 3.18 (2H, t), 3.15 (2H, t), 3.04 (2H, t). ^{13}C NMR(400 MHz, CD_3OD) δ 76.8, 74.6, 69.9, 69.8, 66.5, 51.9, 42.2, 39.2. HRMS: *m/z* calculated for $C_{12}H_{20}N_2O_2$: 225.1603, found: 225.1600.

Preparation of (2)

AF680 NHS ester (1 μmol in DMSO) was added to an aqueous solution containing **1** (10 μmol) buffered with 7.5% sodium bicarbonate. The reaction was stirred at room temperature for 30 min followed by purification on preparative RP-HPLC (12 mL/min; A: 0.1% trifluoroacetic acid in water, B: 0.1% trifluoroacetic acid in acetonitrile; 20% B 0.1-3 min, 20-40% B 3-11 min) to give **2**: t_R = 10.2 min. MALDI-TOF: *m/z* calculated: 1063.11, found: 1064.38. All MALDI-TOF and ESI-Mass Spectrometry data were collected at the University of Michigan Department of Chemistry's Core Facility.

Preparation of Stabilized Peptides

Propargyl ether (0.3 μmol), 1,3 diethynylbenzene (0.3 μmol), **2** (0.3 μmol), or AF647 alkyne (0.3 μmol) was first added to 200 μL of 1:1 water:tert-butanol, followed by Cu-TBTA (30 nmol) and sodium ascorbate (0.3 μmol). Lastly, double mutant peptide (0.3 μmol) was added and the solution was gently stirred at room temperature for 12 h followed by purification on preparative RP-HPLC (propargyl ether stabilized exendin (PropE sExendin) and 1,3-diethynylbenzene stabilized exendin (DEB sExendin): 28% B 0.1-7 min, 28-70% B 7-23 min (PropE sExendin: 97% purity; DEB sExendin: 98% purity); AF680 linker stabilized exendin

(AF680 sExendin), AF680 linker stabilized GLP-1 (AF680 sGLP-1), AF647 labeled exendin: 25% B 0.1-7 min, 25-70% B 7-20 min (AF680 sExendin: 92% purity; AF680 sGLP-1: 89% purity; AF647 exendin: 94% purity); propargyl ether stabilized GLP-1 (PropE sGLP-1): 37% B 0.1-7 min (PropE sGLP-1: 93% purity); 1,3-diethynylbenzene stabilized GLP-1 (DEB sGLP-1): 23-38% B 0.1-12 min, 38-50% B 12-20 min (DEB sGLP-1: 92% purity)) at a flow rate of 12 mL/min. MALDI-TOF: PropE Exendin: *m/z* calculated 4288, found: 4288; DEB sExendin: *m/z* calculated 4320, found: 4319; AF680 sExendin: *m/z* calculated 5257, found: 5258; AF680 sGLP-1: *m/z* calculated 4370, found: 4372; AF647 sExendin: *m/z* calculated: MW of dye unpublished, found: 4859; PropE sGLP-1: *m/z* calculated 3401, found: 3400; DEB sGLP-1: *m/z* calculated 3433, found: 3435. For quantifying peptide concentrations to determine yield and circular dichroism measurements, amino acid analysis was carried out by the University of Michigan Proteomics and Peptide Synthesis Core.

Cell Culture

NIT-1 cells, a GLP-1R positive mouse beta cell line, were generously provided by Dr. Ralph Weissleder's Laboratory and used for receptor binding studies. Cells were grown in F12K containing 10% (v/v) heat-inactivated FBS, 50U/mL penicillin, 50 μg/mL streptomycin, and 1.5 g/L sodium bicarbonate. The passage number for NIT-1 cells used in affinity measurements for all peptides was between 4 and 16

In Vitro Receptor Binding Assay

NIT-1 cells were grown for 48 hours before being harvested with trypsin-EDTA. The cells were then washed with PBS, centrifuged, and resuspended in PBS with 1.0% BSA. Cells

were aliquoted and suspended in binding buffer containing stabilized GLP-1 or exendin on ice (0.05-250 nM). After 3 h, cells were centrifuged and washed (for fluorescent constructs) or the buffer was replaced with a second binding buffer containing 20 nM of AF647 exendin. After 1 h, cells were washed with PBS with 1.0% BSA and immediately analyzed using an Attune Acoustic Focusing Cytometer (Applied Biosystems). Binding affinity curves and statistical analysis were carried out using Prism 6.0 software.

Animals

All animal experiments were conducted in compliance with the University of Michigan University Committee on Use and Care of Animals (UCUCA). For measuring plasma clearance, AF680 sExendin (1.2 nmol) or a validated K12C fluorescent exendin control peptide[227, 287] was injected in the lateral tail vein of C57BL/6 mice (6 mice total). At predetermined time points (1, 3, 5, 15, 30, 60, 180 min), retro orbital blood samples were collected. A LICOR Odyssey CLx scanner (Lincoln, NE) was used to measure the fluorescence intensity for each sample and the intensities were converted to concentration using a dilution series of AF680 sExendin in mouse plasma. After 3 h, the mice were sacrificed and the pancreas resected. Islets were visualized by a near-infrared scan on a LICOR Odyssey CLx scanner.

Histology and Microscopy

Pancreata resected from C57BL/6 mice injected with AF680 sExendin were submerged in OCT and frozen in chilled 2-methylbutane. The organ was then sectioned into 6 μm slices, fixed with 4% paraformaldehyde for 10 min, and incubated overnight at 4 ^{o}C with a rabbit anti-insulin primary antibody (dilution 1:150 in PBS with 0.1% BSA supplemented with 1% goat

plasma), followed by a 30 min room temperature incubation with goat anti-rabbit IgG FITC secondary antibody (dilution 1:50 in PBS with 0.1% BSA).

Trypsin Digest

To assess the proteolytic resistance of stabilized peptides, both stapled and unstapled peptides (75 μM) were subject to a trypsin digest (500 ng/μL, pH 7.4, room temperature). Enzymatic digest was monitored at 254 nm using RP-HPLC to determine the degradation half-life.

Circular Dichroism (CD) Measurements

To quantify peptide secondary structure, CD spectra were collected on a Jasco-815 CD spectrometer with a 1 mm Hellma quartz cuvette at 23 ^{o}C. Five scans from 185 nm to 260 nm at 20 nm/min were averaged for peptide samples prepared in 5 mM potassium phosphate buffer, pH 7.0 at concentrations ranging between 5 μM to 20 μM as determined by amino acid analysis. A scan containing only buffer/buffer with cross-linker was subtracted from sample scans. Helicity was calculated using mean residue ellipticity at 221 nm and maximum ellipticity as reported elsewhere[308].

Chapter 6

A Helix-Stabilizing Linker Improves Subcutaneous Bioavailability Of A Helical Peptide Independent Of Linker Lipophilicity

6.1 Publication Information

Zhang, L., T. Navaratna, and G.M. Thurber. *A Helix-Stabilizing Linker Improves Subcutaneous Bioavailability of a Helical Peptide Independent of Linker Lipophilicity*. Bioconjugate Chemistry. 2016; 27(7): 1663–1672

Modifications have been made to the published document to adapt the content to this text. The use of double click chemistry for peptide helix stabilization indicated multiple improvements such as affinity, helicity, and protease resistance. The advantages of stabilized peptides for subcutaneous delivery are discussed in this chapter.

6.2 Abstract

Stapled peptides address several limitations to peptide-based imaging agents and therapeutics such as poor stability and low affinity due to conformational flexibility. There is also active research in developing these compounds for intracellular drug targeting. A significant effort has been invested in determining the effects of helix stabilization on intracellular delivery, but much less is known about the impact on other pharmacokinetic parameters such as plasma clearance and bioavailability. We investigated the effect of different fluorescent helix-stabilizing linkers with varying lipophilicity on subcutaneous (SC) bioavailability using the glucagon-like peptide-1 (GLP-1) receptor ligand exendin as a model system. The stapled peptides showed significantly higher bioavailability independent of linker hydrophilicity owing to increased protease resistance, and all subcutaneously delivered conjugates were able to successfully target

the islets of Langerhans with high specificity. The lipophilic peptide variants had slower absorption and plasma clearance than their respective hydrophilic peptides, and the absolute bioavailability was also lower due to the longer residence times in the skin. The ease and efficiency of double-click helix stabilization chemistries is a useful tool for increasing the bioavailability of peptide therapeutics, many of which suffer from rapid *in vivo* protease degradation. Helix stabilization using linkers of varying lipophilicity can further control SC absorption rates to customize plasma pharmacokinetics.

6.3 Background

Peptides acting as hormones and growth factors serve selective and crucial signaling roles via binding to specific cell surface receptors[43]. These characteristics make peptides and peptidomimetics attractive candidates as therapeutics, but their rapid renal clearance and poor stability from *in vivo* proteases have limited their broader use in the clinic[25, 290]. Recently, improvements in synthetic and analytical techniques, high throughput screening, and helix stabilization chemistries have generated a resurgence in the research and development of therapeutic peptides, as demonstrated by the increasing number of peptide therapeutics in clinical trials[43, 292, 321].

Peptide therapeutics are often delivered through subcutaneous injection. Although oral administration is the preferred route of delivery for therapeutics, it is generally not applicable to peptides as the harsh environment of the gastrointestinal tract is abundant with proteases. Peptides also suffer from permeability limitations across the intestinal epithelium[322, 323]. Studies that tested stapled peptides (chemically cross-linked helices) for oral administration showed increases in oral availability, and while promising, further improvements are needed before

clinical translation[124]. Alternatively, IV delivery requires technically trained personnel (with associated risks[324-326]) and is particularly cumbersome for peptides with fast clearance that require frequent dosing. Given the limitations of intravenous and oral routes, subcutaneously administered peptide therapeutics have seen commercial success with multiple FDA approved molecules and more in clinical trials, notably cancer vaccines, GLP-1 agonists used to treat type 2 diabetes, and anti-inflammatory agents[43, 327, 328].

SC doses are given as a bolus, and the injected therapeutic is absorbed from the site of injection into the blood or lymph capillaries to enter systemic circulation[327, 329]. These injections are readily self-administered and exhibit a slower absorption rate when compared to the instantaneous systemic delivery of an IV bolus. This provides effective, long-term treatment and may alleviate side effects attributed to high serum concentrations[330]. The longer residence time in the body is especially important for peptide therapeutics given their rapid clearance, and SC administration allows the molecule to circumvent the short residence time from renal filtration through absorption-limited pharmacokinetics[331].

Molecular characteristics impacting interstitial transport include shape, molecular weight, charge, and stability in the presence of extracellular proteases[326, 329, 332, 333]. The bioavailability of a subcutaneously injected therapeutic, defined as the fraction of the dose that makes it to the systemic circulation, has been shown to be dose and injection site-dependent for multiple antibody treatments[334, 335]. Further complicating drug design is a lack of robust models to explain SC absorption kinetics. For certain antibody treatments, the SC route has been approved, but the wide range in bioavailability remains unexplained, although factors such as interstitial pressure, applied heat, protein size, formulation, and in the case of IgGs, FcRn binding, are thought to play a major role[336-339]. Assuming negligible cellular uptake/trapping at the site of injection, SC

bioavailability is theoretically 100% for a catabolically stable molecule[340]. However, peptide and protein drugs exhibit highly variable SC bioavailability, suggesting degradation during the absorption process[329, 337, 341]. Pretreatment of the site of injection with protease inhibitor-containing ointments increases the bioavailability of subcutaneously injected insulin[342]. Others have found evidence of degradation products of injected protein and peptides using *in vitro* assays of subcutaneous tissue homogenates or by examining the site of injection[343, 344]. Given the role of proteases in hindering absorption, the design of protease-resistant peptides is crucial for the development of highly bioavailable peptide and protein-based therapeutics. Using stabilization strategies that can impart varying lipophilic and hydrophilic properties can further fine-tune the absorption rate as shown by favorable pharmacokinetics of transdermally applied stabilized exendin[345], but the impact on bioavailability for the subcutaneous route and effects of peptide stability is not well understood.

One increasingly common way to improve peptide stability is through helix stabilization. Although several techniques for generating stapled peptides have been reported, including olefin metathesis, lactam ring formation, and disulfide bond formation among others, another promising alternative is to use a double copper (I)-catalyzed click reaction between two azidohomoalanine (AHA) amino acid substitutions along the peptide sequence[137, 187, 295, 298-300]. Azidohomoalanine is easily incorporated during solid phase peptide synthesis (SPPS) and has been previously used to generate fluorescent imaging agents via alkyne fluorophore conjugation as well as stapled fluorescent and non-fluorescent peptides such as exendin and Mdm2 inhibitors[137, 187, 346, 347]. Based on past results focused on glucagon-like peptide-1 receptor (GLP-1R) ligand exendin and FDA approval of multiple subcutaneously administered exendin analogues for treating type 2 diabetes including exenatide, liraglutide, and dulaglutide, exendin

was chosen as the model system for investigating the effect of lipophilicity and stability on SC bioavailability[267, 348]. Helix stabilization and lipophilicity impact the absorption and bioavailability in complex ways. Increased protein binding and/or membrane interaction slows absorption and can sequester the peptide from proteolytic enzymes but simultaneously increases exposure time to epithelial proteases. Many lipophilic agents have been utilized to increase plasma protein binding of peptides including fatty acids[349], diphenyl cyclohexanol[279], and lipophilic fluorescent dyes[175, 176]. Alternatively, albumin-binding peptides can be used for a similar purpose [280, 350, 351], although these peptides would also be subject to degradation following subcutaneous delivery. Alpha helix stabilization may alter absorption and clearance rates in addition to improving protease stability.

Due to the interplay of these factors, we studied the impact of helix stabilization and lipophilicity on SC absorption and bioavailability of stabilized and non-stabilized exendin derivatives with hydrophilic or lipophilic fluorescent linkers. Here we report increased bioavailability of these stapled peptides compared to their non-stapled counterparts and extended plasma exposure using lipophilic linkers. A stronger understanding of the impact of these modifications on bioavailability and clearance is crucial for generating predictive models to aid in clinical translation.

6.4 Results

To investigate the effects of peptide stabilization on *in vivo* subcutaneous (SC) absorption using linkers with different lipophilicity, two series of fluorescently labeled exendin probes were synthesized (Scheme 6.1). Based on crystallography data for the binding pocket of glucagon-like peptide-1 receptor (GLP-1R) for exendin, AHA substitutions were made at the 14th position for

single mutant exendin and both 14th and 21st positions for double mutant exendin. These substitutions allow for a direct comparison between stapled and non-stapled peptide. A more hydrophilic set of peptides was generated by first functionalizing Alexa Fluor 680 NHS ester with either 1 or 2 reactive alkynes followed by a single-click cycloaddition for non-stapled peptide or a double-click cycloaddition for stapled peptide. Similar syntheses were performed using Cy7 NHS ester to generate a lipophilic pair of exendin conjugates. Careful consideration was taken when choosing dyes, as dye structure and molecular charge can greatly impact non-specific cellular and plasma protein interactions[165, 352]. Cy7 and Alexa Fluor 680 were chosen based on plasma protein binding of the free dye as determined by rapid equilibrium dialysis as well as previously published data on Cy7 exendin and *s*-AF680 exendin[147, 187].

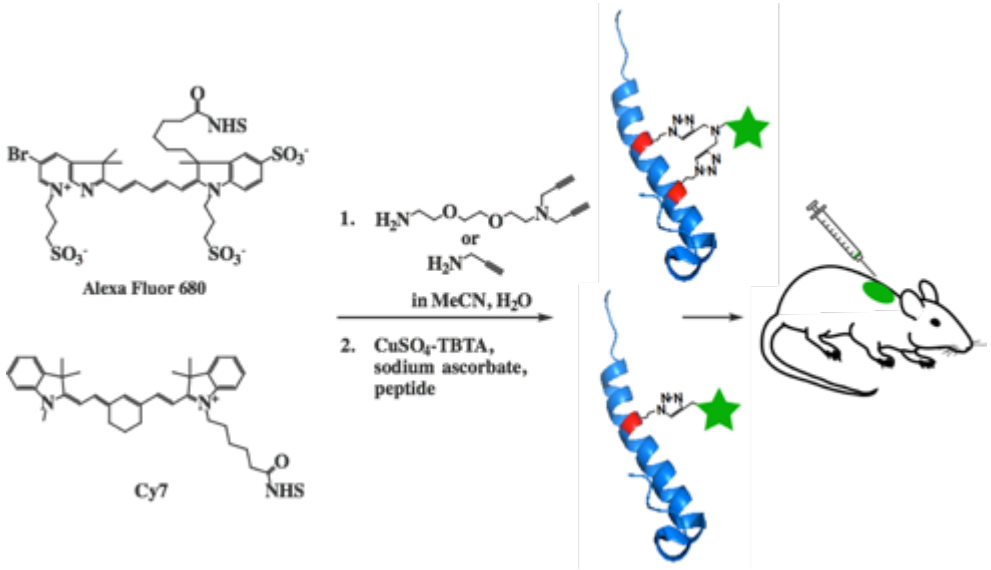

Scheme 6.1 Design of stabilized and non-stabilized exendin conjugates
The modified residues are highlighted in red. Fluorophores are first functionalized with one or two alkynes using amine-NHS chemistry, followed by either single or double click reactions to generate the fluorescent conjugates.

Successful synthesis of fluorescently stapled and non-stapled exendin was verified using ESI-MS and purity determined on RP-HPLC while monitoring both 214 nm and peak

fluorophore absorbance (SI). Alexa Fluor 680 conjugates were ionized in negative mode while Cy7 conjugates were ionized in positive mode for ESI-MS. Spectra are shown below.

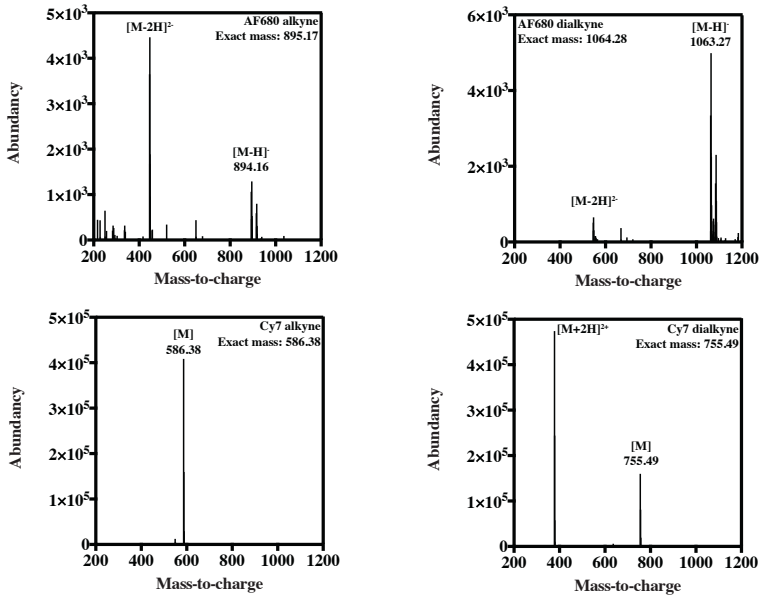

Figure 6.1 ESI spectra of alkyne functionalized fluorophores for peptide conjugation
Fluorescent alkyne and dialkyne linkers were purified using RP-HPLC with water with 0.1 % TFA (A) and acetonitrile with 0.1% TFA (B).AF680 alkyne: 10-60% B 0.1-16 min; t_R=12.1 min. AF680 dialkyne: 10-60% B 0.1-16 min; t_R=11.7 min. Cy7 alkyne: 70% B 0.1 -15 min; t_R=11.3 min. Cy7 dialkyne: 50% B 0.1-4 min, 50-80% B 4-20 min; t_R=14.0 min.

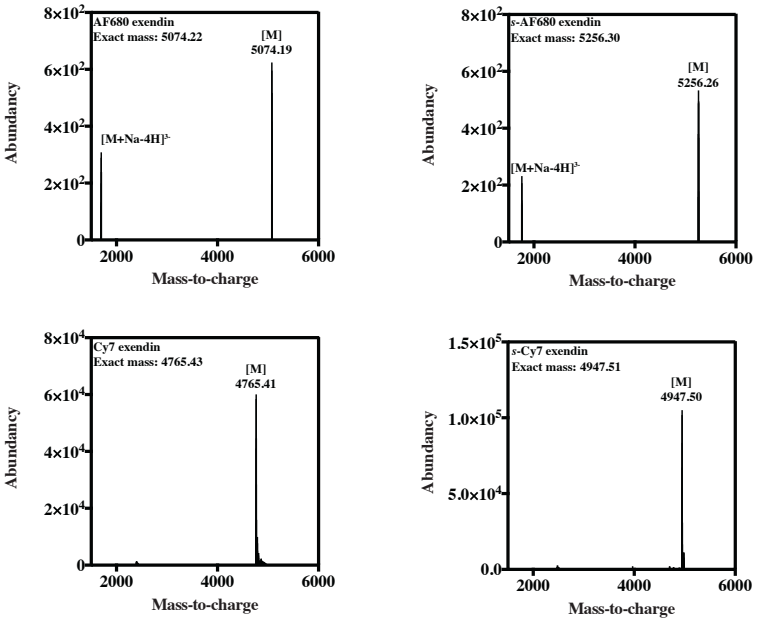

Figure 6.2 ESI spectra of fluorescent exendin conjugates

AF680 exendin: 20-50% B 0.1-24 min; t_R=21.4 min. *s*-AF680 exendin: 20-50% B 0.1-24 min; t_R=20.1 min. Cy7 exendin: 30-80% B 0.1 -20 min; t_R=11.1 min. *s*-Cy7 exendin: 30-80% B 0.1-20 min; t_R=11.7 min.

Post-purification, stabilized peptides were reacted with excess fluorescent AlexaFluor 647 alkyne to verify no unreacted azides were present. HPLC and MALDI-TOF indicated no new species were formed. Isotopic spacing for deconvoluted peptide ESI spectra indicates no multimerization of peptide species.

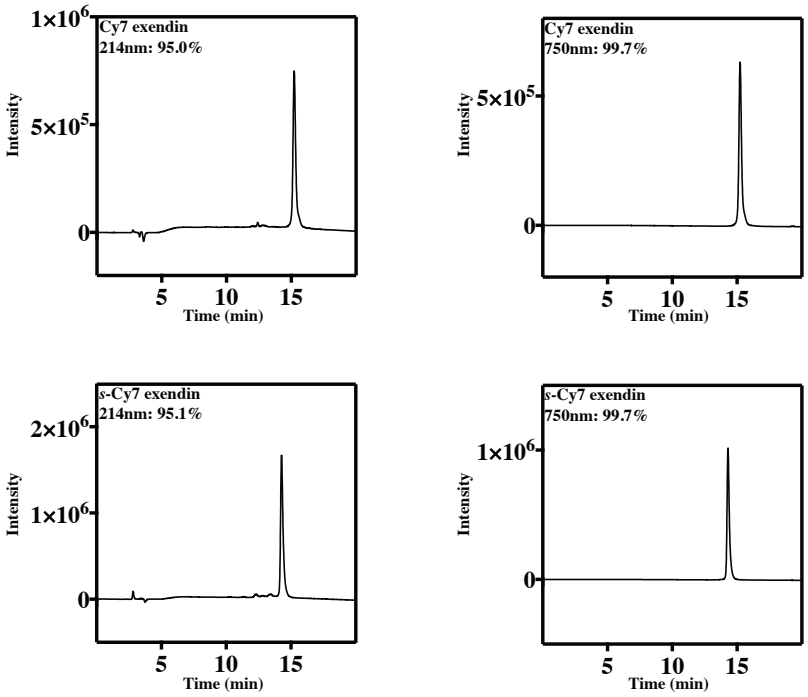

Figure 6.3 HPLC chromatogram of alkyne functionalized fluorophores
HPLC traces for alkyne functionalized dyes demonstrating high purity at 214 nm and fluorophore absorbance wavelengths. Purity check method is 10-70% B 0.1-19 min.

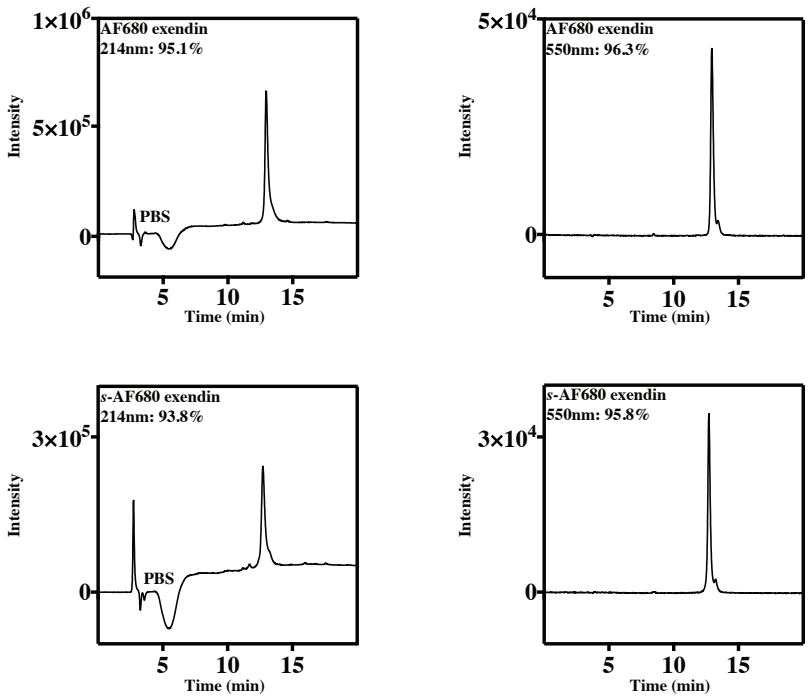

Figure 6.4 HPLC chromatogram of fluorescent peptides
HPLC traces for fluorescent exendin conjugates demonstrating high purity at 214 nm and fluorophore absorbance wavelengths. Purity check method is 10-70% B 0.1-19 min.

The binding affinity of each exendin conjugate to GLP-1R was experimentally determined to quantify impact of stabilization and dye lipophilicity. *In vitro* twelve-point affinity curves indicate all conjugates maintain the low nanomolar affinity unmodified exendin exhibits[5, 48, 251, 255]. The results also indicate stabilization resulted in a higher affinity (lower K_d) when compared to the non-stapled counterpart for each dye (Figure 6.5). Stabilization with Cy7 resulted in values of K_d = 7.2 ± 0.3 nM whereas single-click Cy7 exendin resulted in K_d = 11.2 ± 0.6 nM. Stabilization with AF680 resulted in values of K_d = 2.3 ± 0.1 nM whereas single-click AF680 exendin resulted in K_d = 3.3 ± 0.2 nM. The affinity improvement is not surprising given helix stabilization is known to lessen entropic penalties to binding through conformational constraints[294].

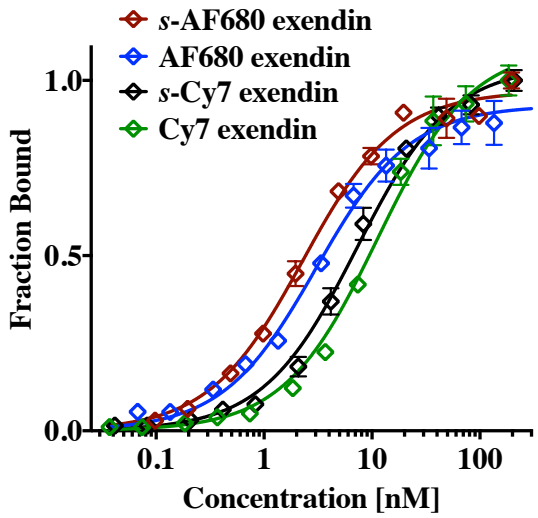

Figure 6.5 Cellular binding affinity assay indicating successful binding of peptide probes

Changes in proteolytic stability due to helix stabilization were investigated through a trypsin digest adapted from a previously published protocol[187]. Digest of fluorescently stapled and non-stapled peptides (Figure 6.6) and unreacted double mutant exendin (SI) in 5 ng/µl trypsin indicate the double-click stabilization across the i, i+7 residues significantly improves protease resistance. Non-stapled AF680 and Cy7 exendin demonstrated digest half-lives of 4.9 ± 0.2 h and 9 ± 1 h, respectively. The stapled counterparts showed improvements with digest half-lives of 13 ± 1 h and 14 ± 1 h, respectively. Unreacted double mutant exendin digested with a half-life of 0.8 ± 0.2 h (SI). Digests were monitored using HPLC; the area-under-curve of the intact species was quantified over time to fit a degradation rate.

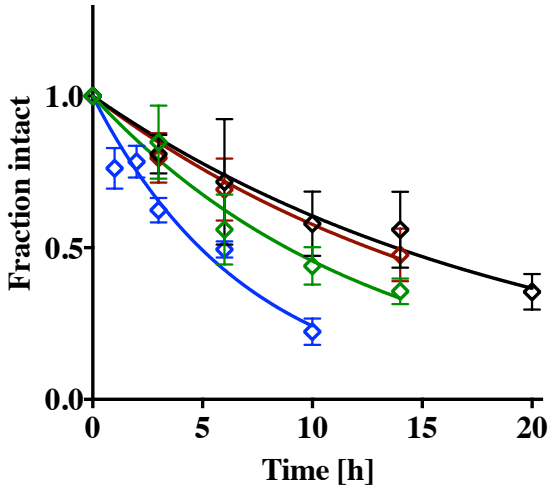

Figure 6.6 Trypsin digest of stabilized versus non-stabilized exendin probes

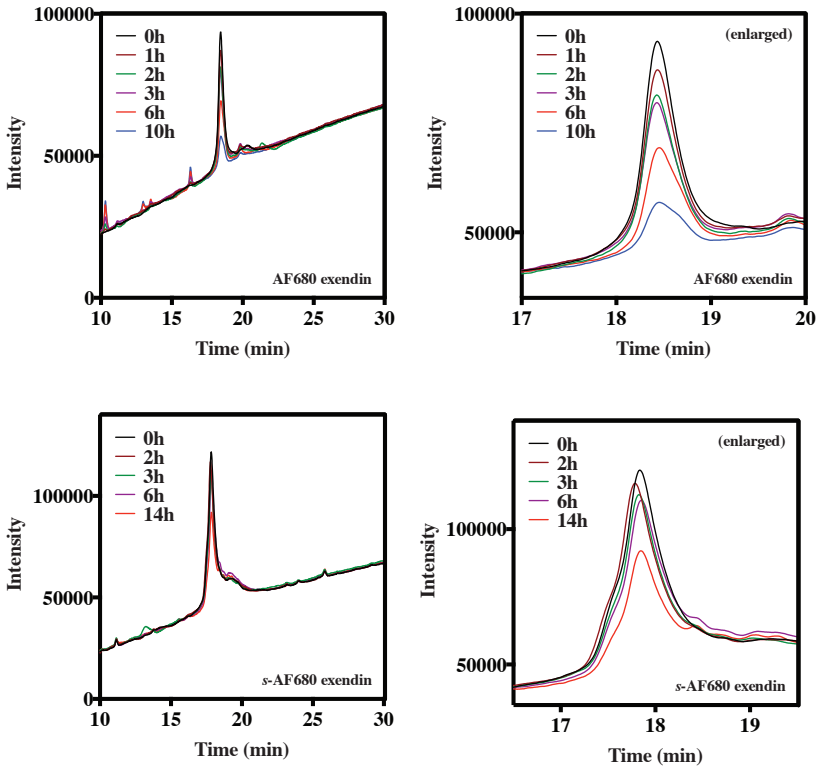

Figure 6.7 HPLC chromatogram of trypsin digest for exendin (AF680)
Traces show trypsin digest of unstabilized (top) and stabilized (bottom) AF680 exendin. As time increases, intact peptide peaks diminishes. Area under curve (AUC) used to determine digest rate.

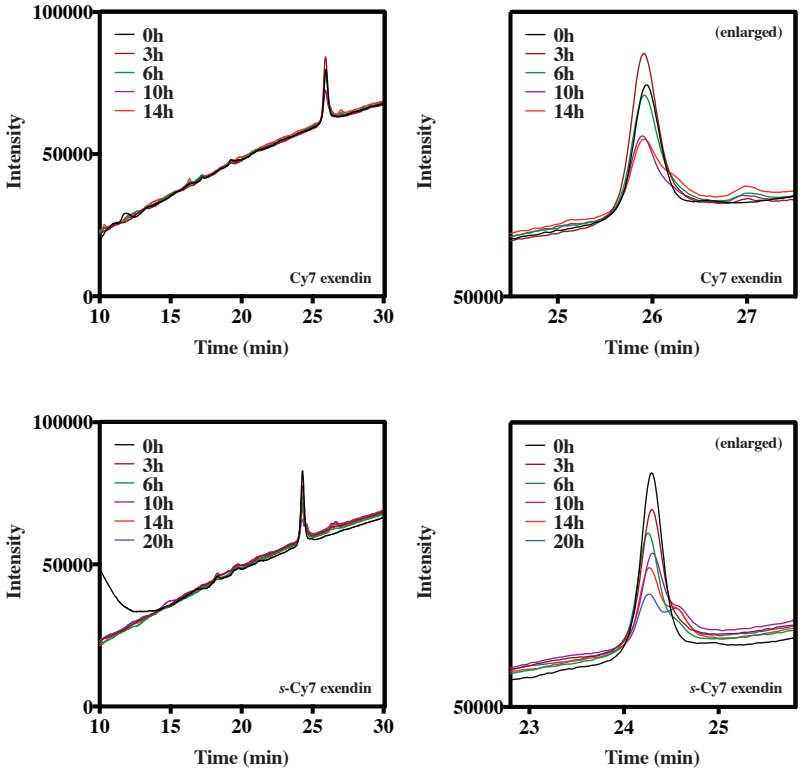

Figure 6.8 HPLC chromatogram of trypsin digest for exendin (Cy7)
Traces show trypsin digest of unstabilized (top) and stabilized (bottom) Cy7 exendin. As time increases, intact peptide peaks diminishes. Area under curve (AUC) used to determine digest rate.

Gradient used for analysis were all the same: B (0.1% TFA in acetonitrile), 20-60%: 28 min. Unreacted double mutant exendin was subject to the same digest conditions as well. The results indicated the unreacted double mutant exendin digested with a half-life of 0.8 ± 0.2 h, consistent with our previous findings. Interestingly, the digest of *s*-AF680 exendin in this manuscript is significantly slower than our previously published values. This is likely due to multiple reasons including an increase in overall stapled peptide purity in the current digest as well as differences in post-purification work-up of the stapled peptide. Previously, stapled peptides were concentrated on a rotary evaporator. The acidic pH resulting from residual TFA was then adjusted to pH 7.4 with sodium bicarbonate. All exendin conjugates were rotary evaporated with methanol 3x to remove residual TFA and then lyophilized. The current methods

as reported in this manuscript do not require any additional pH adjustment steps. The pH of the reaction digest mixture was measured to confirm the appropriate pH. Digests were performed in triplicate with the exception of the double mutant unreacted peptide, which was digested once to compare with previously published digests in triplicate.

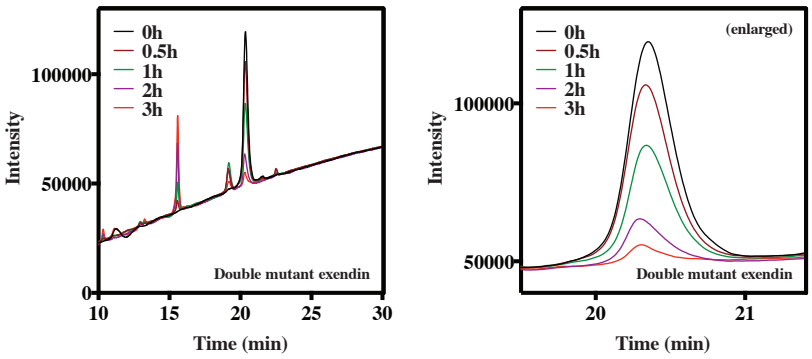

Figure 6.9 HPLC chromatogram of trypsin digest for exendin
Trypsin digested double mutant exendin is shown. Digest is rapid without helix stabilization.

CD spectra of stapled and non-stapled peptides were collected in 1:1 water:acetonitrile. Although CD spectra of peptides are typically collected in a mild potassium phosphate buffer, the Cy7 conjugates absorbance spectra in aqueous solutions showed a broad shoulder near 700 nm, inconsistent with the original fluorophore absorbance spectra. The absorbance spectra in 1:1 water:acetonitrile gave the expected result (SI). Due to concerns about potential aggregation of the more lipophilic species, CD characterization was performed in 1:1 water:acetonitrile. Though less common, organic solvents have been used for collecting CD spectra of poorly soluble peptides[137, 347]. The 221 nm absorbance on CD indicated a minor increase in helicity due to stabilization for AF680 conjugates. AF680 conjugate helicity and the small increase upon stabilization agree with previously published values for exendin helicity and are consistent with the significant helicity of wild-type exendin. Cy7 conjugates displayed higher helicity, regardless

of the double-click staple (χ^{helix}=0.84) possibly due to side chain interactions with the lipophilic dye. Absorption spectra for the Cy7 conjugates in the mentioned solvents are discussed below.

In the presence of 0.1% TFA added to the mobile phase, AlexaFluor 680 absorbance max shifts from 680 nm to ~550 nm, hence detection at 550 nm on HPLC. This change in absorbance is reversible once TFA is removed/neutralized. Cy7 peptides are monitored at 750 nm. Stabilized/non-stabilized conjugate purity evaluated at both fluorophore absorbance and 214nm absorbance. There was no statistically significant difference in fluorescence intensity between stapled and non-stapled conjugates using either Cy7 or AF680 using a dilution series. Absorbance spectra of fluorescently stabilized/non-stabilized peptides indicate no changes in maximum excitation compared to unreacted fluorophore. Compounds are dissolved in 1:1 water:acetonitrile.

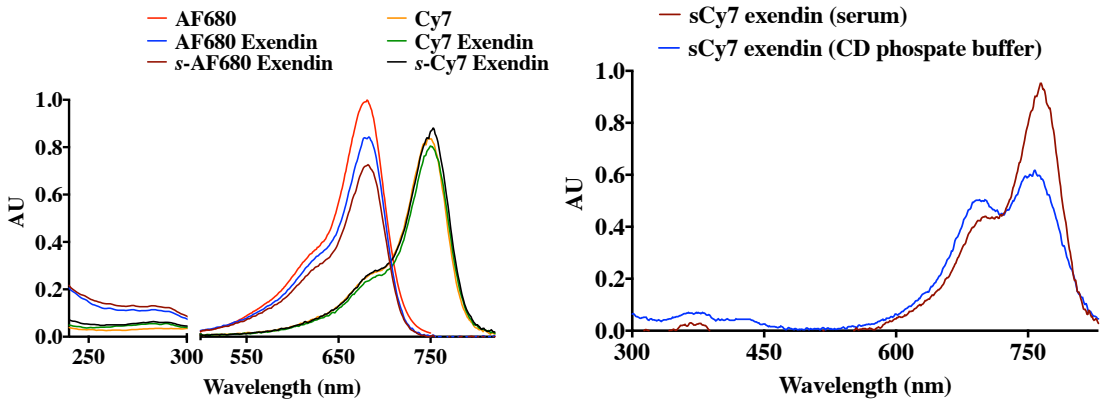

Figure 6.10 Absorbance spectra for exendin conjugates
(Left): absorbance profiles are as expected in 1:1 acetonitrile water; (right): for Cy7 conjugates, absorbance in 5 mM potassium phosphate buffer shows a much stronger shoulder, indicative of H-aggregates of Cy7 at these high concentrations[353].

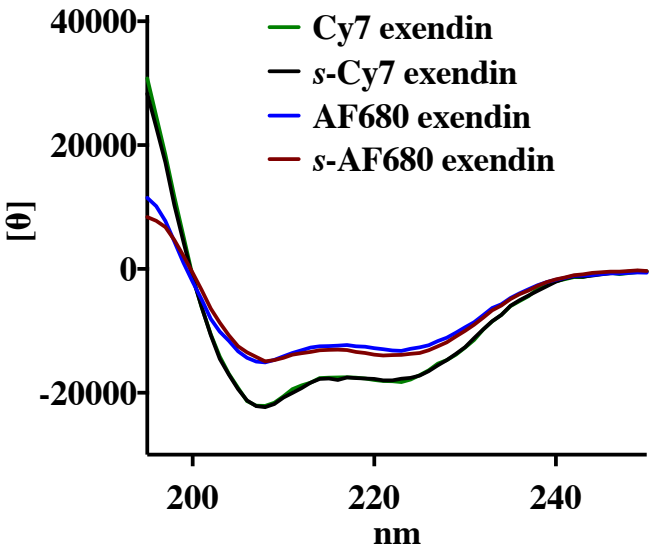

Figure 6.11 CD spectra for stabilized and non-stabilized exendin probes

Table 6.1 Summary of binding affinity, digest half-life, and helicity

Compound	Affinity (nM)	Half life (h)	χ^{helix}
s-AF680 exendin	2.3 (± 0.1)	13 (± 1)	0.65
AF680 exendin	3.3 (± 0.2)	4.9 (± 0.2)	0.61
s-Cy7 exendin	7.2 (± 0.3)	14 (± 1)	0.84
Cy7 exendin	11.2 (± 0.6)	9 (± 1)	0.84

Given the specificity of these exendin conjugates for beta cell targeting, the subcutaneous bioavailability of the compounds was investigated. One set of C57BL/6 mice was given 1 nmol of stapled or non-stapled Cy7 or AF680 exendin intravenously (Figure 6.12). A second set of

mice was given the same dose subcutaneously. AUC calculated from the subcutaneous delivery divided by the plasma concentration AUC provided the absolute bioavailability. The *s*-AF680 exendin demonstrated complete bioavailability (103 ± 6%) when compared to non-stapled AF680 exendin (65 ± 6%). Similarly, stabilization via a lipophilic Cy7 linker yielded improved bioavailability of 82 ± 12% vs. 57 ± 9% for stapled and non-stapled, respectively. The differences in bioavailability between stapled and non-stapled peptides are statistically significant (p value = 0.0004 and 0.02 for AF680 and Cy7 conjugates, respectively Figure 6.13).

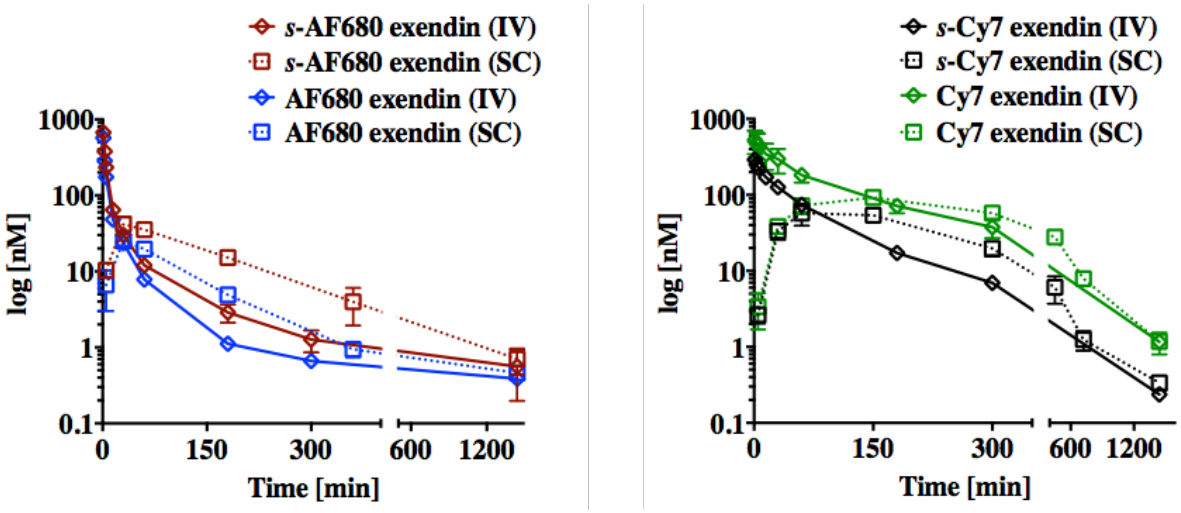

Figure 6.12 Plasma clearance of various exendin probes in mice for IV and SC routes
Fluorescent exendin with and without helix stabilization were administered either intravenously or subcutaneously in mice. The plasma concentration was quantified and plotted versus time to determine the effect of helix stabilization on SC bioavailability. Stabilized AF680 and Cy7 exendin displays significantly higher bioavailability than their non-stabilized counterparts.

Table 6.2 Summary of bioavailability and clearance rate data

Compound	% Bioavailable	IV clearance
s-AF680 exendin	103 (± 6)	$k_\alpha = 0.173\ min^{-1}$ $k_\beta = 0.011\ min^{-1}$ %fast = 96
AF680 exendin	65 (± 6)	$k_\alpha = 0.142\ min^{-1}$ $k_\beta = 0.011\ min^{-1}$ %fast = 97
s-Cy7 exendin	82 (± 12)	$k_\alpha = 0.034\ min^{-1}$ $k_\beta = 0.008\ min^{-1}$ %fast = 76
Cy7 exendin	57 (± 9)	$k_\alpha = 0.032\ min^{-1}$ $k_\beta = 0.005\ min^{-1}$ %fast = 64

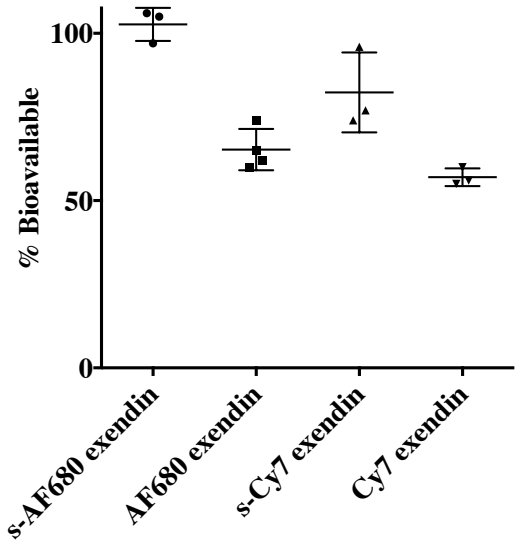

Figure 6.13 Unpaired t-test for differences in bioavailability

The fluorescent non-stabilized exendin bioavailabilities agree well with previously reported values for exendin-4 in rats[354-356]. SC injection of non-stapled Cy7 exendin resulted in higher plasma concentration than stapled Cy7 due to slower clearance, although overall bioavailability increased through helix stabilization. An efficient therapeutic that is able to both reach high systemic concentrations and high bioavailability through protease resistance could potentially be engineered with a longer, lipophilic linker to increase plasma protein interactions.

SDS-PAGE was used to verify that experimentally measured plasma intensities were a result of intact peptide absorbed from the skin rather than degradation products (SI). Degradation byproducts are fluorescent as well and can lead to errors while quantifying bioavailability, but no fluorescent degradation byproducts were detected in the plasma. Fluorescent exendin peptides subject to a trypsin digest were also analyzed using SDS-PAGE to verify that fragments differ significantly from intact, control peptide.

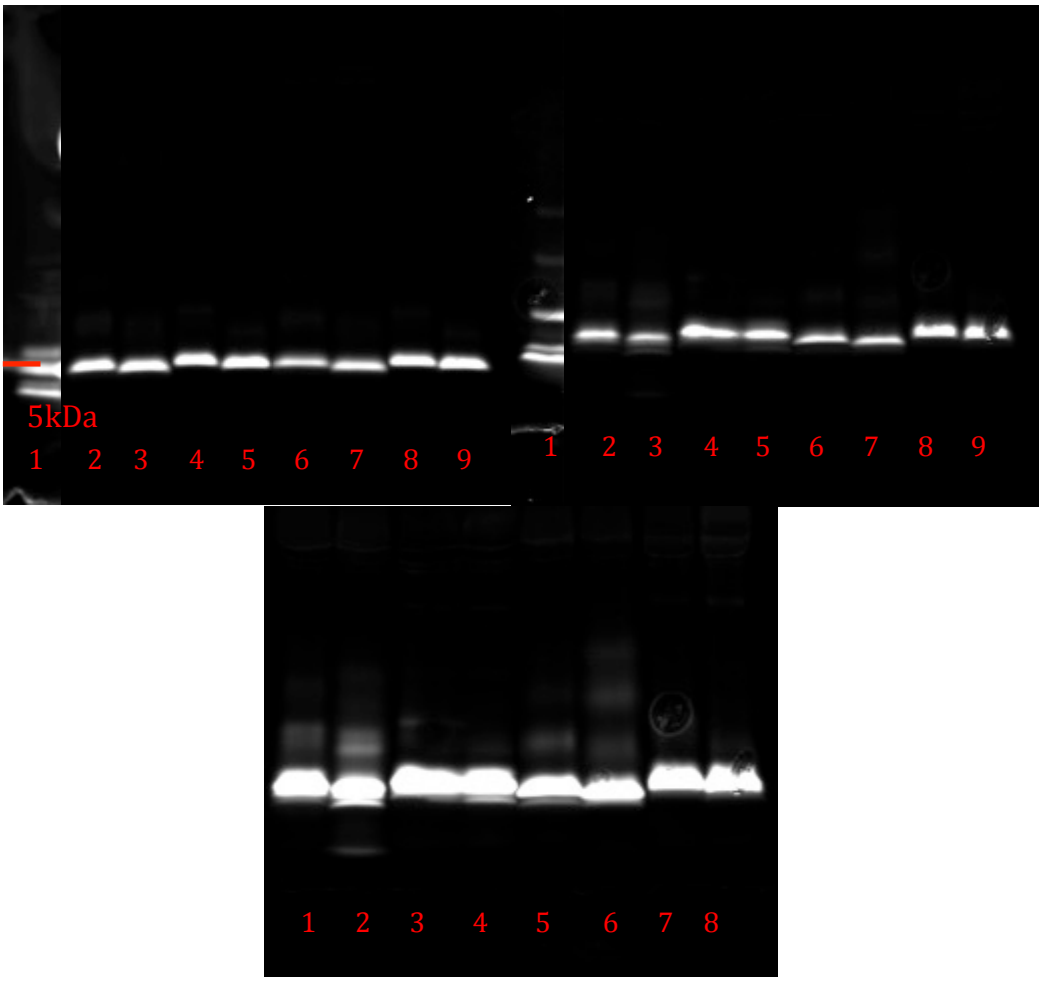

Figure 6.14 Exendin serum stability (SDS-PAGE)
Left, top: 0 h incubation; right, top: 24 h incubation; left, bottom: 24 h incubation (window leveled to bring out fragments). Fluorescent values indicate little degradation of all conjugates in either fresh mouse serum or frozen plasma at 37°C over 24 h. The ladder has been window leveled differently from the other lanes for ease of visualization.

Lane ID (Figure 6.14)
1. Ladder
2. *s*-680 exendin (serum)
3. 680 exendin (serum)
4. *s*-Cy7 exendin (serum)
5. Cy7 exendin (serum)
6. *s*-680 exendin (plasma)
7. 680 exendin (plasma)
8. *s*-Cy7 exendin (plasma)
9. Cy7 exendin (plasma)

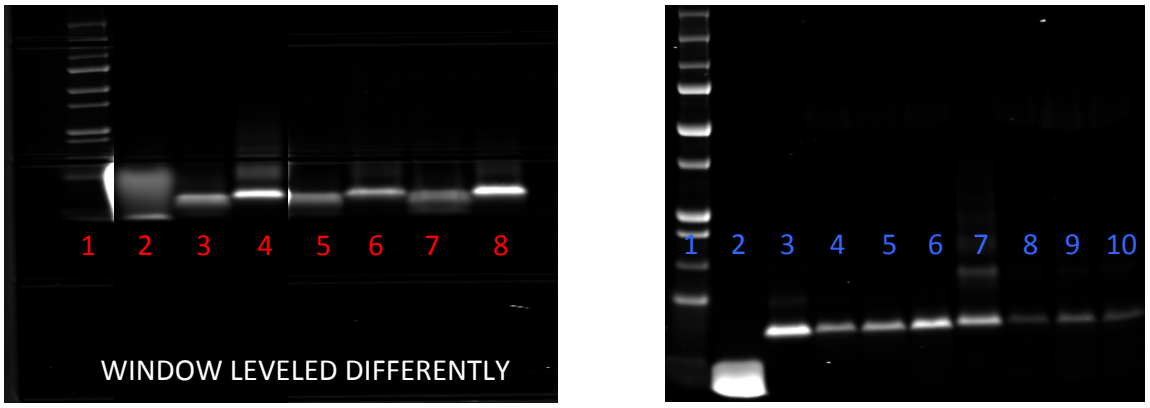

Figure 6.15 SDS-PAGE for plasma samples of mice injected with fluorescent exendin
Plasma samples collected from SC injections. The protein gels (above) indicate plasma fluorescence intensity, which is used to calculate bioavailability, is primarily from intact peptide.

Lane ID (Figure 6.15)
Left:
1. Ladder
2. AF680 dialkyne (free fluorophore, not injected)
3. 680 exendin (not injected)
4. *s*-680 exendin (not injected)
5. 680 exendin (30 min)
6. *s*-680 exendin (30 min)
7. 680 exendin (1 h)
8. *s*-680 exendin (1 h)
Right:
1. Ladder
2. Cy7 (free fluorophore, not injected)
3. Cy7 exendin (not injected)
4. Cy7 exendin (30 min)
5. Cy7 exendin (1 h)
6. Cy7 exendin (2.5 h)
7. *s*-Cy7 exendin (not injected)
8. *s*-Cy7 exendin (30 min)
9. *s*-Cy7 exendin (1 h)

10. *s*-Cy7 exendin (2.5 h)

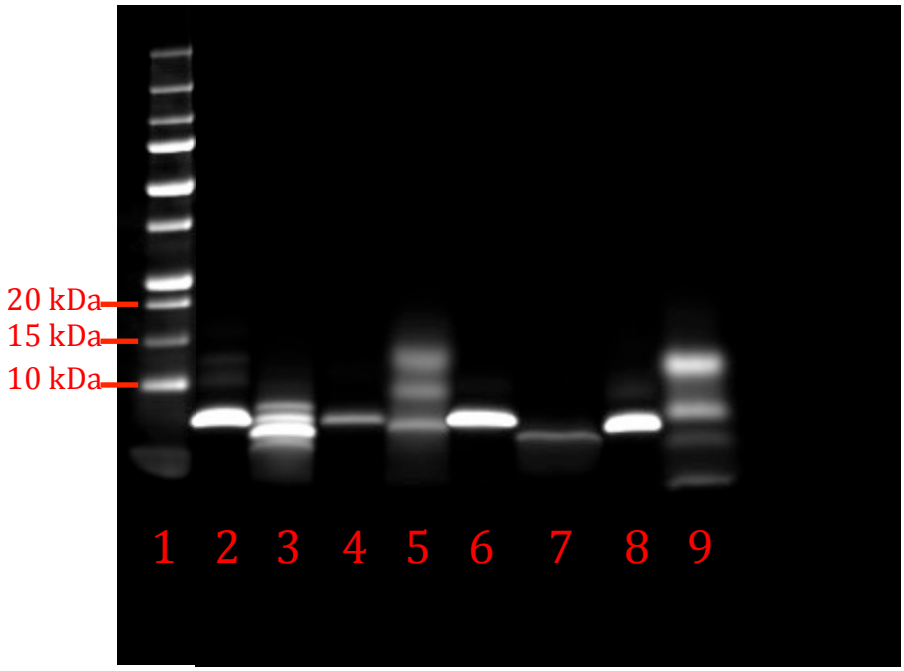

Figure 6.16 SDS-PAGE for fluorescent exendin peptide digested *in vitro*

Lane ID (Figure 6.16)
1. Ladder
2. *s*-Cy7 exendin (undigested)
3. *s*-Cy7 exendin (digested)
4. *s*-680 exendin (undigested)
5. *s*-680 exendin (digested)
6. Cy7 exendin (undigested)
7. Cy7 exendin (digested)
8. 680 exendin (undigested)
9. 680 exendin (digested)

Following the last blood sample, each animal was sacrificed, and the pancreas was removed for macroscopic imaging to confirm beta cell targeting specificity. As expected, all conjugates successfully targeted the islets of Langerhans, visualized as punctate white spots scattered across the organ (Figure 6.17) and consistent with previous work showing overlap with insulin staining and MIP-GFP[76, 187]. The combination of *in vitro* and *in vivo* sample analysis on

SDS-PAGE and specific beta cell targeting demonstrates that intact and functional peptide is absorbed into the plasma.

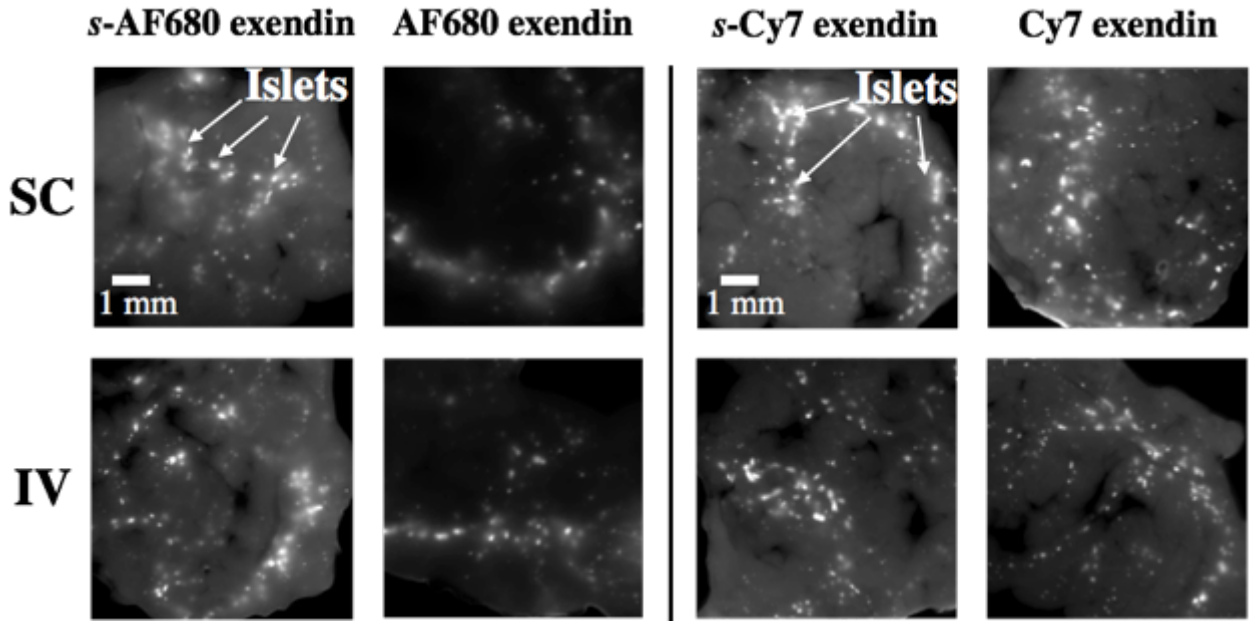

Figure 6.17 Macroscopic pancreas images (*ex vivo*)
Macroscopic pancreas images demonstrate islet targeting whether peptide is administered subcutaneously or intravenously for all exendin conjugates. Beta cells are located in the islets of Langerhans and appear as distinct punctate spots

To quantify the impact of stabilization and lipophilicity on absorption, degradation and bioavailability, a simple three-compartment model was used to calculate first-order absorption and degradation rate constants (Figure 6.18). The exchange rates between the central and peripheral compartment and the clearance rate were fit using the intravenous plasma clearance. These values were then fixed, and the absorption rate and extracellular degradation rate were fit to the subcutaneous absorption data.

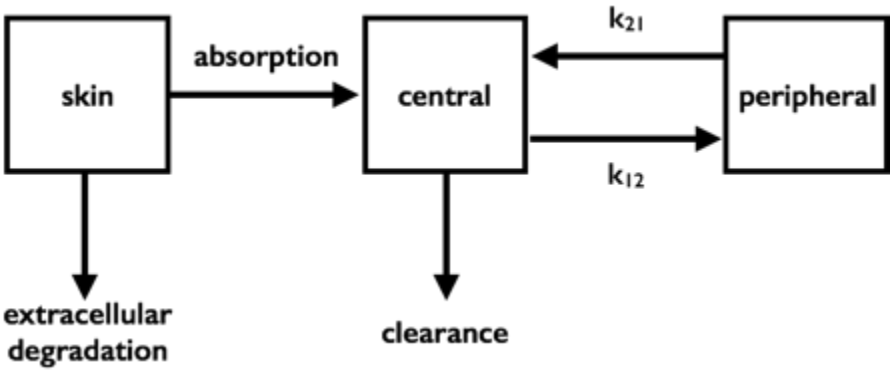

Figure 6.18 Three-compartment model for rates affecting SC absorption

Model Derivation

A: skin
B: central compartment
C: peripheral compartment
k_{abs}: first order absorption, min^{-1}
k_{deg}: first order degradation, min^{-1}
V_A: skin compartment volume, L
k_{cl}: clearance from central compartment, min^{-1}
k_{12}: transport from central to peripheral, min^{-1}
k_{21}: transport from peripheral to central, min^{-1}
C_B=central compartment concentration (measured for each peptide), nM
C_c=peripheral compartment concentration, nM
X_A=moles in skin compartment, nmole
$X_{A,0}$=injected SC dose, 1 nmole
$X_{B,0}$=0
$X_{C,0}$=0
k_α=alpha clearance (biexponential)
k_β=beta clearance (biexponential)
f_A=fraction fast (fit from biexponential)

Balance on skin compartment:

$$\frac{dX_A}{dt} = -k_{abs}X_A - k_{\deg}X_A$$ with the initial condition, t=0, $X_A=X_{A,0}$=1 nmol

$$X_A = X_{A,0}\exp(-(k_{abs}+k_{\deg})*t)$$

Balance on central compartment:

$$\frac{dC_B}{dt} = \frac{k_{abs}}{V_A} * X_{A,0} * \exp(-(k_{abs}+k_{\deg})*t) - k_{cl} * C_B - k_{12}C_B + k_{21}C_C$$

Balance on peripheral compartment:

$$\frac{dC_C}{dt} = k_{12}C_B - k_{21}C_C$$

k_{21}, k_{12}, and k_{cl} are calculated using the following relationships for biexponential decay:

$$k_\alpha + k_\beta = k_{cl} + k_{12} + k_{21}$$

$$k_\alpha * k_\beta = k_{cl} * k_{21}$$

$$f_A = \frac{k_{21} - k_\alpha}{k_\beta - k_\alpha}$$

Experimental plasma concentrations (C_B) are used to determine alpha and beta clearance half lives and are used as input to determine the rate constants between the central and peripheral compartments using Prism software. Using the injected dose of 1 nmol ($X_{A,0}$) and the experimentally determined bioavailability, the ODE for the central compartment was used to fit for k_{abs}, k_{deg}, and V_A simultaneously. Each peptide was fit separately with absorption and degradation half lives summarized in Table 6.3.

Table 6.3 Fitted rate constants and volumes for subcutaneous absorption

Compound	k_{abs} (min^{-1})	k_{deg} (min^{-1})	V_A (L)
s-AF680 exendin	0.0087 (± 0.0018)	0.00065 (± 0.00026)	0.0013 (± 0.00006)
AF680 exendin	0.0077 (± 0.0014)	0.0041 (± 0.00079)	0.0020 (± 0.00026)
s-Cy7 exendin	0.0059 (± 0.0015)	0.0013 (± 0.00034)	0.0026 (± 0.00033)
Cy7 exendin	0.0036 (± 0.0006)	0.0029 (± 0.00044)	0.0014 (± 0.00009)

6.5 Discussion

Owing to their low off-target effects, ease of synthesis via SPPS, and availability of tools for engineering including phage display, bacterial surface display, one-bead-one-compound selection and others, peptides hold clinical relevance both as imaging agents and therapeutics. There has also been a recent resurgence in investigating peptides for targeting intracellular protein-protein interactions. However, significant challenges such as poor affinity, low *in vivo* stability, and rapid systemic clearance exist and lower the potential for clinical efficacy. One strategy to address these shortcomings involves secondary structure stabilization[45, 124, 292, 357],

which has been shown to improve protease stability and affinity by decreasing the entropic penalty upon binding. This works by constraining the helix and confers protease resistance by increasing helicity[358] and sterically hindering digestive enzymes with non-natural amino acids and crosslinks. Significant effort has been spent investigating the impact of helix stabilization on binding affinity and intracellular delivery, but much less is known about the impact on subcutaneous bioavailability. This work used a model exendin system to quantify the interplay of helix stabilization and peptide lipophilicity on the absolute SC bioavailability and absorption profile of stabilized and non-stabilized alpha helical peptides.

Currently, multiple peptide therapeutics have FDA approval for SC delivery. However, abundant epidermal proteases (e.g. in the extracellular matrix[359] and on immune cells[360]) can degrade the peptide, often rendering a large fraction of the injected dose ineffective, especially if the dose reaches systemic circulation slowly[336]. Hydrophilic peptides that are absorbed more rapidly can escape the degradation pathway, but rapid plasma clearance of a quickly absorbed bolus dose is equally unwanted since the systemic dose may be too low to achieve a sustained therapeutic effect. In contrast, lipophilic compounds are known to interact with plasma proteins, and plasma protein binding is an established method for slowing the plasma clearance of molecules by conjugating lipophilic moieties[147, 175, 176, 267, 361]. The increase in lipophilicity may lower solubility in aqueous formulations compared to the hydrophilic counterparts and can result in self-association, aggregates, and/or precipitates. Consequently, poor solubility is a potential problem in protein pharmaceuticals[332, 362, 363]. Although free Cy7 dye is poorly soluble in aqueous solutions, the peptide conjugate is much more soluble due to exendin's high aqueous solubility. To further avoid aggregation, fluorescent conjugates were stored in a 1:1 dilution of water:acetonitrile and diluted in PBS prior to SC injection; no aggregation is visible prior to

injection. Given the complex interactions between self-association, non-specific interactions, proteolysis, and absorption rates, the degradation and absorption rates must be considered together. Peptide stability and absorption rates were independently changed to quantify the impact on absolute bioavailability. A quantitative and mechanistic understanding of these rates is critical since variability in animals makes it challenging to scale to the clinic.

Peptides were synthesized using either single alkyne or dialkyne linkers functionalized with Alexa Fluor 680 or Cy7 to independently modify the protease stability and lipophilicity (Scheme 6.1). As demonstrated by *in vitro* cellular affinity assays, all peptides maintained low nanomolar affinity. Helix stabilization was able to improve the affinity 1.4-1.6 fold, and this small increase for an already helical native peptide agrees well with a three-state thermodynamic model of binding[187]. CD spectra were collected to compare with the differences in binding affinity. Interestingly, both Cy7 exendin conjugates displayed high helicity regardless of helix stabilization. Non-covalent side chain interactions (such as phenylalanine-phenylalanine interactions at i, i+4 residues[364, 365] and phenylalanine-lipid interactions[366]) have been shown to contribute to the overall peptide helix stability. The CD measurements presented here indicate that a fluorescent pharmacokinetic modifier (Cy7) may have a similar impact as non-fluorescent modifiers (lipids) by inducing helicity of peptides with hydrophobic side chains as shown by various lipidated GLP-1 peptides[366]. Intrahelix associations with a nearby F22 residue may explain both the increased helicity for the Cy7 variants and reduced affinity. The F22 residue is in the center of the hydrophobic binding pocket[42], where steric hindrance could lower the affinity despite the higher helicity.

To observe how the improved affinity and increased protease resistance of the stabilized peptides impact SC bioavailability, 1 nmol of each of the four fluorescent exendin conjugates was delivered intravenously or subcutaneously to mice (Figure 6.12). The lipophilic Cy7 conjugates were absorbed more slowly with the maximum plasma concentration (C_{max}) occurring at ~2 h compared to the hydrophilic AF680 peptides, which reached C_{max} at ~30 min. This is expected due to increased non-specific interactions and protein binding when compared to hydrophilic molecules[348]. CD spectra also indicate higher helicity for Cy7 conjugates, and the physical state of the peptide at the site of injection is known to affect the pharmacokinetics of absorption[332]. Although helical forms can be readily absorbed from the SC site, increased non-specific interactions from the lipophilic dye likely dominate compared to helicity, hence the slower absorption rates.

The higher bioavailability of the stabilized peptides correlates with improved proteolytic resistance. Although subcutaneous absorption is a complex process and incompletely understood[327], the epidermis contains abundant proteases necessary for maintaining homeostasis of the skin[359]. These enzymes have been implicated in degrading peptide therapeutics before reaching systemic clearance, reducing their efficacy. Proteases almost universally cleave amide bonds in an extended beta strand conformation, rendering the alpha helix conformation more stable than linear peptides[367]. The non-stabilized fluorescent conjugates were not able to achieve total bioavailability although the amount was high (65% and 57% for AF680 and Cy7, respectively). Cy7 stabilization also showed improved bioavailability over non-stabilized Cy7 exendin (82% vs. 57%), and complete bioavailability was possible through helix stabilization using AF680 (103%). All peptides maintained efficient targeting of islets following subcutaneous delivery. These improvements are likely due to the reduced proteolysis from the

stabilized secondary structure. Improved absorption has been demonstrated using protease inhibitors concurrent with treatment, but these approaches may cause unwanted side effects given that defective proteolytic enzymes in the epidermis cause multiple skin disorders[359]. Engineering peptides that are more resistant to these degradation pathways avoids special formulation requirements.

The absorption rate of the peptide in the skin inversely correlated with the plasma AUC following intravenous injection. For example, the non-stabilized Cy7 peptide had the highest AUC (SI) and also the slowest absorption rate, while the AF680 peptides had the lowest AUC and fastest absorption rates. This likely results from the amount of interaction with skin and plasma proteins. These data are also consistent with non-specific cellular interactions measured *in vitro,* where non-stabilized Cy7 had the highest level of uptake, correlating to the highest plasma protein binding[352]. Interestingly, when comparing liraglutide and semaglutide, Lau et al. found that the slowest clearing peptide (semaglutide) also had the highest subcutaneous bioavailability (94% versus 66%)[348]. They argued that the higher protein binding of semaglutide reduced clearance and protected the molecule from protease degradation. For the fluorophore-clicked peptides, the slower clearing unstabilized Cy7 peptide would then be expected to have increased bioavailability (in contrast to the results) in the absence of helix-stabilizing effects. Therefore, the more rapidly clearing *s*-Cy7 peptide likely had to overcome increased protease exposure to still attain improved bioavailability, which could explain the lower magnitude of improved bioavailability for the lipophilic peptides than with AF680 peptides. This also provides guidance for designing stabilizing linkers with increased plasma protein binding[345, 348].

In situ measurement of the peptide degradation and absorption rates is challenging, which contributes to the incomplete understanding of subcutaneous bioavailability. To estimate these values, a 3-compartmental model was modified from Lu et al. with parameters fitted using MATLAB (Figure 6.18)[368]. The fitted degradation rates are qualitatively consistent with the *in vitro* degradation rates (SI); slower absorption rates with the lipophilic exendin conjugates are also consistent with the compartmental model. The slower absorption of the lipophilic peptides likely explains the lower bioavailability of Cy7 conjugates compared to AF680 conjugates due to a longer residence time in the skin. The factors affecting delivery are complex and include size, pKa, solubility, concentration, injection depth, body movement, blood supply, injection site, among many others[327, 332]. There is a limited understanding how these factors quantitatively impact bioavailability, hence the lack of strong predictive models for SC delivery. The current model lumps these factors into overall absorption and degradation mechanisms, but a more detailed and quantitative understanding of the underlying steps in SC drug delivery will allow for better predictions and scaling to the clinic in the future.

Stabilized alpha helices allow researchers to investigate the impact of physicochemical properties on absorption at the site of injection. Adding lipophilic moieties through side chain substitution or conjugation is an increasingly used strategy to engineer 'long-acting' pharmaceutics because patients require fewer doses to maintain an efficacious systemic concentration[349, 369, 370]. However, long residence times in the skin can lower the bioavailability of these formulations[371]. Stabilizing peptides via double-click reaction using a lipophilic dye-linker molecule simultaneously remedies low bioavailability and promotes plasma protein interactions to slow systemic clearance.

6.6 Conclusion

We independently modified the protease stability and lipophilicity of present four fluorescently labeled exendin molecules including using stapled stabilized and non-stapled stabilized variants with either lipophilic Cy7 or hydrophilic AF680 dyes as pharmacokinetic modifiers. Helix stabilization via the double-click staple linker resulted in improved bioavailability when all peptides were administered subcutaneously in mice likely from improved protease resistance. This result occurred for both hydrophilic and lipophilic derivatives, providing an independent method for improving bioavailability. Lipophilicity of the stabilizing crosslinker also significantly impacted absorption rates and AUC. The combination of imparting lipophilicity to slow systemic clearance and protease resistance to increase bioavailability is an attractive strategy for engineering peptide therapeutics.

6.7 Experimental Methods

Similar to previously published work, either one or two AHA substitutions were made to generate single-mutant and double-mutant exendin[147, 187]. A methionine residue at the 14th position was substituted with AHA during solid phase peptide synthesis based on its position pointing away from the binding pocket of GLP-1R[42]. An additional substitution replaced leucine at the 21st position with AHA to generate a double mutant exendin; i, i+7 residues correspond to positions located two helix turns apart and enabled subsequent helix stabilization.

Materials

Double mutant exendin-4 (HGEGTFTSDLSKQXEEEAVRXFIEWLKNGGPSSGAPPP S) and single mutant exendin-4 (HGEGTFTSDLSKQXEEEAVRLFIEWLKNGGPSSGAPPPS),

where is X is the non-natural amino acid azidohomoalanine, were obtained from Innopep (San Diego, CA). Alexa Fluor 680 NHS ester and Cy7 NHS ester were purchased from Life Technologies (Carlsbad, CA) and Lumiprobe (Hallandale Beach, FL), respectively. *N*-boc-2m2'-(ethylenedioxy)-diethylamine was purchased from Santa Cruz Biotechnology (Dallas, TX). Other reagents were purchased from Sigma-Aldrich (Milwaukee, WI). ESI-MS spectra were collected using an Agilent Q-TOF 1200 series. RP-HPLC was performed on a Shimadzu LC unit using Phenomenex Luna C18(2) analytical and semi-prep columns.

Preparation of Fluorescent Alkyne and Dialkyne

Fluorescent dialkynes are synthesized from a previously published *N*-(2-(2-(2-aminoethoxy)ethoxy)ethyl)-*N*-(prop-2-yn-1-yl)prop-2-yn-1-amine linker (**1**)[187]. Propargylamine or **1** (5 μmol) was added to 200 μl of 1:1 water:acetonitrile with 20 μl 7.5% sodium bicarbonate. Either Cy7 NHS ester or Alexa Fluor 680 NHS ester (0.5 μmol in DMSO) was added and the reaction was stirred at room temperature for 30 min followed by purification on preparative RP-HPLC (AF680 alkyne: calcd: 895.17, found: $[M-H]^-$ = 894.16; AF680 dialkyne: calcd: 1064.28, found: $[M-H]^-$ = 1063.27; Cy7 alkyne: calcd: 586.38, found: [M] = 586.38; Cy7 dialkyne: calcd: 755.49, found: [M] = 755.49).

Preparation of Stabilized (s-)/non-stabilized Exendin

AF680 alkyne, AF680 dialkyne, Cy7 alkyne, or Cy7 dialkyne (300 nmol) was added to 100 μl of 1:1 water:*tert*-butanol followed by $CuSO_4$-TBTA (10 nmol in 1:1 water:DMSO) and sodium ascorbate (300 nmol in water). Lastly, single mutant or double mutant exendin was added (350 nmol) and the reaction was gently stirred at room temperature for 5 h followed by

purification using RP-HPLC. The purified peptides were dissolved in methanol and concentrated under reduced pressure three times followed by overnight lyophilization (AF680 exendin: calcd: 5074.22, found: 5074.19; *s*-AF680 exendin: calcd: 5256.30, found: 5256.26; Cy7 exendin: calcd: 4765.43, found: 4765.41; *s*-Cy7 exendin: calcd: 4947.51, found: 4947.50).

Cell Culture

NIT-1, a GLP-1R positive mouse beta cell line, were grown in F12K containing 10% (v/v) FBS, 50 U/mL penicillin, 50 μg/mL streptomycin, and 1.5 g/L sodium bicarbonate. Passage number used for cellular assays was between 6-10.

In Vitro Receptor Binding Assay

NIT-1 cells were grown for 48 h before being harvested with 0.05% trypsin-EDTA, washed and resuspended in PBS containing 0.1% bovine serum albumin (BSA). Cells were aliquoted and suspended in binding buffer containing fluorescent exendin conjugates ranging in concentration (0.01 nM - 340 nM) for 3 h on ice. Cells were then washed two times with 0.1% BSA in PBS and immediately analyzed using an Attune Acoustic Focusing Cytometer (Applied Biosystems). The binding affinity (K_d) was calculated using Prism 6.0 software.

Trypsin Digest

To compare the digest half-lives between stapled and non-stapled fluorescent exendin conjugates, both peptides were subject to a trypsin digest adapted from previously published methods[187]. In short, 0.05% trypsin-EDTA was diluted to a digest concentration of 5 ng/μL (DF100) with PBS (pH 7.4, room temperature). Peptide (45-50 μM) was added and the digest

was monitored at 214 nm using HPLC to quantify the AUC of intact peptide (SI). AUC of the intact peptide peak was plotted against time and fit to an exponential decay to determine a degradation half-life.

Circular Dichroism Spectra

To quantify and compare changes in peptide secondary structure, CD spectra were collected on a Jasco-815 CD spectrometer. Peptides were dissolved in 1:1 water:acetonitrile at concentrations determined by amino acid analysis. Scans containing only 1:1 water:acetonitrile were collected and subtracted as background. Helicity values for peptides were quantified using CD absorbance at 221 nm and the maximum ellipticity[372372].

Animals

Animal experiments were in compliance with the University of Michigan Institutional Animal Care and Use Committee (IACUC). All fluorescent exendin conjugates (1 nmol in 100 μL PBS) were injected in triplicate subcutaneously in the dorsal skin between the shoulders or intravenously (1 nmol in 150 μL PBS) via the tail vein of C57BL/6 mice. For SC injections, mice were anesthetized with 2.5 % isoflurane. Animals were kept under anesthesia for no longer than 5 min for each blood draw and no heating elements were used to reduce local variability in heating of the skin. Because injections were localized in the dorsal region, animals were oriented on their stomach during the injection and while under anesthesia. Animals were briefly oriented to the side during retro-orbital blood sampling but promptly reoriented after the blood draw. Previous experiments with inconsistencies in orientation, temperature, and isoflurane concentration resulted in inconsistent absorption rates and plasma concentrations (data not

shown). For intravenous injections, blood samples were collected at 1, 3, 5, 15, 30, 60, 180, 300, and 1440 min and fluorescent peptide concentration quantified using a LICOR Odyssey CLx scanner (Lincoln, NE). SC injected peptides were quantified similarly through blood samples at pre-determined time points to capture absorption into the blood and plasma clearance. Area under curve (AUC) was calculated by applying the trapezoidal rule to a plot of plasma concentration as a function of time. For each fluorescent compound, the AUC ratio was taken between the SC injection and the intravenous injection to quantify the bioavailability. After 24 h, animals were sacrificed and the pancreas removed and macroscopically imaged using the Odyssey CLx to verify successful islet of Langerhans targeting. Plasma samples were then run on a reducing SDS-PAGE gel and scanned to confirm fluorescent signal from plasma corresponded to intact peptide rather than degraded byproducts (SI).

Chapter 7

Concluding Remarks And Future Directions

7.1 Summary of Work

In this dissertation, we developed new methods and materials for molecular imaging probes to measure beta cell mass (BCM) in diabetes. Chapters 1 and 2 focused on the challenges of developing an imaging agent for measuring BCM in diabetes and on the optimal physicochemical properties needed for these probes. The molecular weight of exendin probes are near optimal for targeting the endocrine pancreas, and this molecule was analyzed in more detail. Chapter 3 examined the receptor trafficking properties and modifications in plasma clearance to obtain more efficient beta cell targeting. Due to rapid downregulation of the receptor, slow plasma clearance does not allow for continual beta cell uptake, so the slower clearance results in higher background and lower targeting efficiency. A rapidly cleared agent is therefore ideal for measuring BCM. Additionally, the receptor expression of GLP1-R was measured for the first time and provided evidence for low exocrine expression of GLP1-R in addition to the high endocrine expression. This low level expression on exocrine cells, due to their much higher prevalence than beta cells, could explain the failure in the clinic of current imaging agents to accurately measure BCM. Chapter 4 investigated this exocrine expression in more detail. Using wild type mice alongside a GLP-1R knockout transgenic mouse model, a very low expression of GLP1-R was confirmed on exocrine cells. Although absolute expression is very low (850 receptors per cell on exocrine cells versus 53,000 receptors per cell on beta cells), the much

higher prevalence of exocrine cells (99%) relative to beta cells (1%) results in a significant total signal from the exocrine pancreas. Chapter 4 tested a method to preferentially block this uptake to provide more specific beta cell signal, and near 100% blocking of exocrine signal was achievable while sparing 15-20% of the receptor on endocrine cells for quantitative imaging. Chapter 5 looked at stabilizing the alpha helix to improve its physicochemical properties. Using a unique cross-linker with exendin and GLP1 as model peptides, the properties of alpha helical imaging agents could be improved. Due to the high helicity of exendin, this was not needed for beta cell imaging agents but could be used for other helical probes. The increase protease stability of the cross-linked peptides and use as a therapeutic led us to test the subcutaneous bioavailability. These cross-linkers were able to improve SC bioavailability for both rapidly absorbed hydrophilic peptides and slowly absorbed hydrophobic conjugates. This method could be used to improve the bioavailability of therapeutic peptides in addition to imaging agents.

For developing clinically translatable agents, we first identified key challenges facing a successful imaging agent for quantifying the beta cell mass for type 1 diabetes research (Chapter 1). Two key challenges include the small size of islets of Langerhans as well as the low volume fraction of islets in the pancreas organ. As a result, a probe with high specificity for the beta cells over the exocrine pancreas and low non-specific uptake in tissue is required for successful clinical translation.

Building on previously published work, which indicated peptides have the potential for high tissue uptake due to high permeability, we identified a 3-step screening approach for imaging agent design (Chapter **2**). The three steps include screening for the optimal molecular weight, determining the required binding affinity, and reducing the non-specific signal during imaging. The screening step is used to determine the optimal molecular weight range, which is a

function of the target tissue physiology. To do this, first, a relationship between vessel permeability and molecular weight was identified for a variety of tissue types and a wide range of imaging agent molecular weights. Using these predicted permeability values, the extravasation/extraction fraction into the target tissue was predicted as a function of size for different tissue types. 3 kDa and 6.9 kDa were predicted for efficient extravasation into the endocrine (beta cell) and exocrine pancreas, respectively. The next step was to identify binding affinity. A previously published tissue uptake model was first validated and then used to predict the impact of binding affinity on uptake. The internalization rate was a key parameter that determined the required affinity for efficient retention in the tissue. This model helped identify affinity requirements for different tissue types, including endocrine pancreas. Lastly, two *in vitro* assays were used to determine the impact of different fluorophores on background signal. The combination of extravasation predictions, affinity requirements, and plasma protein binding and non-specific uptake assays focused our efforts on an exendin agonist as a suitable peptide for beta cell quantification.

Given our live cell imaging of the exendin/GLP-1R system, rapid internalization was observed and we wanted to assess the impact of this internalization on *in vivo* targeting. On one hand, a slow clearing molecule can be repeatedly internalized for high specific signal; on the other hand, a rapidly cleared imaging agent results in low background signal. The relative rate between these competing factors determines the overall imaging contrast. A series of fast and slow clearing fluorescent exendin-based conjugates were synthesized to quantitatively assess the impact of these phenomena (Chapter **3**). We first verified that moderate expression of the GLP-1R *in vivo* precluded the use of avidity for improved binding. Although we achieved slower clearance using a lipophilic Cy-7 exendin, the specific pancreas uptake was similar for both fast

and slow clearing imaging agents. A detailed *in vitro* internalization assay revealed a high degree of receptor downregulation, indicating that a slow clearing probe will not be repeatedly internalized. The work suggested a rapidly cleared exendin is ideal for imaging beta cell mass.

Measuring specific signal from the beta cells is important for accurate quantification. However, clinical attempts have proven challenging due to non-beta cell GLP-R signal. Mouse studies indicated expression of GLP-1R in the exocrine pancreas. Since the time of that publication, additional literature evidence has surfaced; GLP-1R is expressed in mice, non-human primates, and humans. Evidence of GPL-1R in the exocrine pancreas has been challenging to identify; antibodies for the receptor are notoriously unreliable and expression is low. Additionally, the expression in the exocrine pancreas is extremely low, varies between species, and displays heterogeneous distribution across the tissue. However, the confirmation of GLP-1R in the exocrine tissue helped explain why radiolabeled exendin has performed poorly in the clinic. After independently verifying GLP-1R expression in the exocrine tissue, a multiple dosing strategy was explored to preferentially block the exocrine pancreas (Chapter **4**). Preliminary results look promising as the exocrine GLP-1R is completely blocked. Although the majority of beta cell receptors are blocked as well (80-85%), the free receptors are well above the number needed to detect using radiolabeled probes (PET or SPECT) for clinical translation.

Lastly, due to much of the work and motivation in this dissertation pertaining to peptides and peptide-based imaging agents, our final goal was to generate new tools to address the shortcomings of peptide-based agents. Though peptides have an optimal molecular weight for tissue extravasation, they suffer from poor binding and instability. To address these shortcomings, we designed a novel heterobifunctional linker (Chapter **5**) to simultaneously stabilize the peptide and attach a fluorophore. We demonstrated superior protease resistance

through *in vitro* trypsin digestion as well as improved binding and helicity through *in vitro* cell assays and circular dichroism, respectively. After demonstrating *in vivo* specificity, the impact of helix stabilization on subcutaneous bioavailability was investigated. Comparing the intravenously and subcutaneously delivered doses, it was confirmed that stabilization—and likely the improved protease resistance conferred—significantly improved subcutaneous delivery. Varying the lipophilicity of the fluorescent staple could further control the absorption rates.

7.2 Future Work and Directions

The work in this thesis opens the door to several new avenues of research. This section briefly describes two major new avenues for this work, and other members in the group are already exploring some of these directions.

Stabilized Alpha Helices for Imaging and Therapy

Chapter **2** focused on identifying optimal properties of extracellular molecular imaging agents with an emphasis on molecular weight, affinity, and background signal. The emphasis on extracellular targets such as GLP1-R, though important to this dissertation, does not encompass all possible targets, many of which are intracellular. Some of the most important intracellular targets for biopharmaceuticals include mitochondrial, nuclear, and cytoplasmic targets including intracellular pathogens. Though many of the same considerations such as molecular weight are important for extravasation to the target tissue, there is the challenge of efficient cellular uptake. "Stapled peptides" using an all hydrocarbon cross-linker have been reported to reach therapeutic concentrations in cells and *in vivo*. However, the results have been controversial, and progress in the field has been slow. The stabilization method developed in this thesis can be used to generate

novel alpha helices and test cellular uptake rates and cytosolic access to determine if this is a feasible class of agents. Design of successful therapeutics for intracellular targets will need to place much greater emphasis on membrane permeability and the properties of the payload or ligand that will allow for passive cellular uptake. The membrane permeability of molecules within this size range (500 to 5,000 Da) are also important for the transient distribution of payloads from nanoparticles and antibody drug conjugates, a current area of investigation in the lab.

Regardless of the utility of stabilized helices for intracellular therapeutics, helix stabilization can be beneficial for peptide-based imaging agents. This strategy offers the potential for a platform technology to develop stabilized alpha helices for imaging agents, therapeutics, and separations. Our linker can be used to stabilize any helical peptide that can be readily solid phase synthesized. Much research has been conducted in our group on p53-like peptides with promising results including improved pepsin stability and increased cell permeability. The ability to surface display peptides on bacteria with residues modified for stabilization also holds promise for a rapid screening method to identify stabilized peptides, which is currently under development by others in the lab. The kinetics of subcutaneous absorption, while initially developed for therapeutic delivery, are useful in designing subcutaneously delivered near-infrared imaging agents for a safe and patient compliant method of disease screening. Finally, the ease of synthesis, stability, and small size make stabilized peptides useful for affinity chromatography applications. These are only a few projects that showcase the potential of this peptide stabilization technology.

Imaging Beta Cell Mass

To date, biochemical tests using blood samples are the standard for assessing beta cell mass functionality. However, these methods are insensitive to early stages of type 1 diabetes when the pancreas has excess capacity to control blood glucose levels. In fact, greater than 90% of the pancreas beta cell mass (BCM) may be destroyed before insulin insufficiency and elevated blood glucose levels. The inability to detect early stages of the disease has been problematic in studying immunomodulatory therapies and the success of islet transplants.. Although methods exist to target and quantify the BCM in healthy animal models, these techniques fail in disease models and the clinic. An imaging technique with the resolution and sensitivity to quantify the BCM would greatly benefit the diabetes community but has so far remained out of reach. Particularly for type 1 diabetes, extensive research has been conducted on islet transplantation, since this treatment has the potential for curative results. The ability to track transplanted islets would improve transplantation technique and post-surgical monitoring. The results of this dissertation indicate accurate quantification of BCM in disease models is possible by blocking non-beta cell GLP-1R in the exocrine tissue. The studies in this dissertation illustrate the need for robust quantification in order to avoid the failure of prematurely engaging in a clinical trial. This work will not only be instrumental in designing a clinical trial with current probes but will also spark new areas of research. Given the controversy over GLP-1R expression on exocrine cells and pancreatitis and the variable patient-to-patient differences (where 50% appear to have exocrine GLP-1R expression and the others don't), our exocrine blocking strategy could identify patients who are susceptible to these effects for further study. Comparing the pancreas signal with and without an exocrine blocking dose would determine if they had significant GLP-1R exocrine expression (a drop in signal) or not (negligible change). Most importantly, our studies

will help spearhead the development of a clinical imaging protocol for measuring BCM in patients to study the etiology of diabetes and treatment response

Much of this thesis was focused on developing better imaging agents for measuring beta cell mass in diabetes. This included studying the details of the exendin/GLP-1R receptor system in mice, with an emphasis on the impacts of slower plasma clearance and avidity on specific uptake in the pancreas. One goal of the project was to design stronger binders to GLP-1R while another was to slow clearance to increase internalization and target uptake. Unfortunately, low to moderate expression of GLP-1R prevented avidity effects, and rapid downregulation stymied attempts to increase target uptake. Despite these attempts, the approach led to probably the most interesting finding from this project, which was the expression of GLP-1R in the exocrine pancreas. Future work should focus on blocking these receptors prior to *in vivo* imaging. Although some have argued that any exocrine expression is grounds for rejection of a potential target for imaging beta cell mass, many attempts have been made to discover more specific targets to no avail. The rapid internalization, high affinity, and ideal molecular weight of exendin solve many of the problems for imaging this challenging target. By using a strategy to block the exocrine GLP1-R, the decades of research in developing efficient radiolabeled probes and experience with early clinical results can be leveraged to more rapidly develop a suitable approach.

References

1. Scully, T. Diabetes in numbers. *Nature* **485**, S2-3 (2012).

2. Laurent, D., Vinet, L., Lamprianou, S., Daval, M., Filhoulaud, G., Ktorza, A. et al. Pancreatic beta-cell imaging in humans: fiction or option? *Diabetes Obes. Metab.* **18**, 6-15 (2016).

3. Cabrera, O., Berman, D.M., Kenyon, N.S., Ricordi, C., Berggrern, P.O. & Caicedo, A. The unique cytoarchitecture of human pancreatic islets has implications for islet cell function. *Proceedings of the National Academy of Sciences of the United States of America* **103**, 2334-2339 (2006).

4. Carlsson, P.O., Berne, C. & Jansson, L. Angiotensin II and the endocrine pancreas: effects on islet blood flow and insulin secretion in rats. *Diabetologia* **41**, 127-133 (1998).

5. Keliher, E.J., Reiner, T., Thurber, G.M., Upadhyay, R. & Weissleder, R. Efficient18F-Labeling of Synthetic Exendin-4 Analogues for Imaging Beta Cells. *ChemistryOpen* **1**, 177-183 (2012).

6. Zhang, L., Bhatnagar, S., Deschenes, E. & Thurber, G.M. Mechanistic and quantitative insight into cell surface targeted molecular imaging agent design. *Scientific Reports* **6** (2016).

7. Di Gialleonardo, V., de Vries, E.F.J., Di Girolamo, M., Quintero, A.M., Dierckx, R.A.J.O. & Signore, A. Imaging of beta-Cell Mass and Insulitis in Insulin-Dependent (Type 1) Diabetes Mellitus. *Endocr Rev* **33**, 892-919 (2012).

8. Foulis, A.K., Liddle, C.N., Farquharson, M.A., Richmond, J.A. & Weir, R.S. The Histopathology of the Pancreas in Type-1 (Insulin-Dependent) Diabetes-Mellitus - a 25-Year Review of Deaths in Patients under 20 Years of Age in the United-Kingdom. *Diabetologia* **29**, 267-274 (1986).

9. Olokoba, A.B., Obateru, O.A. & Olokoba, L.B. Type 2 diabetes mellitus: a review of current trends. *Oman Med J* **27**, 269-273 (2012).

10. Kahn, C.R. Banting Lecture. Insulin action, diabetogenes, and the cause of type II diabetes. *Diabetes* **43**, 1066-1084 (1994).

11. Defronzo, R.A. Banting Lecture. From the triumvirate to the ominous octet: a new paradigm for the treatment of type 2 diabetes mellitus. *Diabetes* **58**, 773-795 (2009).

12. Ichise, M. & Harris, P.E. Imaging of beta-Cell Mass and Function. *J Nucl Med* **51**, 1001-1004 (2010).

13. Shapiro, A.M.J., Lakey, J.R.T., Ryan, E.A., Korbutt, G.S., Toth, E., Warnock, G.L. et al. Islet transplantation in seven patients with type 1 diabetes mellitus using a glucocorticoid-free immunosuppressive regimen. *N Engl J Med* **343**, 230-238 (2000).

14. Brennan, D.C., Kopetskie, H.A., Sayre, P.H., Alejandro, R., Cagliero, E., Shapiro, A.M. et al. Long-Term Follow-Up of the Edmonton Protocol of Islet Transplantation in the United States. *American journal of transplantation : official journal of the American Society of Transplantation and the American Society of Transplant Surgeons* **16**, 509-517 (2016).

15. Carlsson, P.O., Palm, F., Andersson, A. & Liss, P. Markedly decreased oxygen tension in transplanted rat pancreatic islets irrespective of the implantation site. *Diabetes* **50**, 489-495 (2001).

16. Pattou, F., Kerr-Conte, J. & Wild, D. GLP-1-receptor scanning for imaging of human beta cells transplanted in muscle. *N Engl J Med* **363**, 1289-1290 (2010).

17. Sweet, I.R., Cook, D.L., Lernmark, A., Greenbaum, C.J. & Krohn, K.A. Non-invasive imaging of beta cell mass: a quantitative analysis. *Diabetes Technology & Therapeutics* **6**, 652-659 (2004).

18. Blomberg, B.A., Codreanu, I., Cheng, G., Werner, T.J. & Alavi, A. Beta-cell imaging: call for evidence-based and scientific approach. *Mol. Imaging Biol.* **15**, 123-130 (2013).

19. Frangioni, J.V. New technologies for human cancer imaging. *J. Clin. Oncol.* **26**, 4012-4021 (2008).

20. Bock, T., Svenstrup, K., Pakkenberg, B. & Buschard, K. Unbiased estimation of total beta-cell number and mean beta-cell volume in rodent pancreas. *APMIS* **107**, 791-799 (1999).

21. Herbach, N., Bergmayr, M., Goke, B., Wolf, E. & Wanke, R. Postnatal development of numbers and mean sizes of pancreatic islets and beta-cells in healthy mice and GIPR(dn) transgenic diabetic mice. *PLoS ONE* **6**, e22814 (2011).

22. Nir, T., Melton, D.A. & Dor, Y. Recovery from diabetes in mice by beta cell regeneration. *The Journal of clinical investigation* **117**, 2553-2561 (2007).

23. Engfeldt, T., Orlova, A., Tran, T., Bruskin, A., Widstrom, C., Karlstrom, A.E. et al. Imaging of HER2-expressing tumours using a synthetic Affibody molecule containing the Tc-99m-chelating mercaptoacetyl-glycyl-glycyl-glycyl (MAG3) sequence. *Eur. J. Nucl. Med. Mol. Imaging* **34**, 722-733 (2007).

24. Tofts, P.S., Brix, G., Buckley, D.L., Evelhoch, J.L., Henderson, E., Knopp, M. et al. Estimating kinetic parameters from dynamic contrast-enhanced T(1)-weighted MRI of a diffusable tracer: Standardized quantities and symbols. *J. Magn. Reson. Imaging* **10**, 223-232 (1999).

25. Schmidt, M.M. & Wittrup, K.D. A modeling analysis of the effects of molecular size and binding affinity on tumor targeting. *Mol Cancer Ther* **8**, 2861-2871 (2009).

26. Turvey, S.E., Swart, E., Denis, M.C., Mahmood, U., Benoist, C., Weissleder, R. et al. Noninvasive imaging of pancreatic inflammation and its reversal in type 1 diabetes. *J Clin Investig* **115**, 2454-2461 (2005).

27. Kriz, J., Jirak, D., Girman, P., Berkova, Z., Zacharovova, K., Honsova, E. et al. Magnetic resonance imaging of pancreatic islets in tolerance and rejection. *Transplantation* **80**, 1596-1603 (2005).

28. Medarova, Z., Castillo, G., Dai, G., Bolotin, E., Bogdanov, A. & Moore, A. Noninvasive magnetic resonance imaging of microvascular changes in type 1 diabetes. *Diabetes* **56**, 2677-2682 (2007).

29. Dodd, C.H., Hsu, H.C., Chu, W.J., Yang, P., Zhang, H.G., Mountz, J.D., Jr. et al. Normal T-cell response and in vivo magnetic resonance imaging of T cells loaded with HIV transactivator-peptide-derived superparamagnetic nanoparticles. *J Immunol Methods* **256**, 89-105 (2001).

30. Moore, A., Sun, P.Z., Cory, D., Hogemann, D., Weissleder, R. & Lipes, M.A. MRI of insulitis in autoimmune diabetes. *Magn Reson Med* **47**, 751-758 (2002).

31. Gaglia, J.L., Harisinghani, M., Aganj, I., Wojtkiewicz, G.R., Hedgire, S., Benoist, C. et al. Noninvasive mapping of pancreatic inflammation in recent-onset type-1 diabetes patients. *Proc Natl Acad Sci U S A* **112**, 2139-2144 (2015).

32. Gaglia, J.L., Guimaraes, A.R., Harisinghani, M., Turvey, S.E., Jackson, R., Benoist, C. et al. Noninvasive imaging of pancreatic islet inflammation in type 1A diabetes patients. *J. Clin. Invest.* **121**, 442-445 (2011).

33. Karlsson, F., Antonodimitrakis, P.C. & Eriksson, O. Systematic screening of imaging biomarkers for the Islets of Langerhans, among clinically available positron emission tomography tracers. *Nucl Med Biol* **42**, 762-769 (2015).

34. Eriksson, O., Espes, D., Selvaraju, R.K., Jansson, E., Antoni, G., Sorensen, J. et al. Positron Emission Tomography Ligand [C-11]5-Hydroxy-Tryptophan Can Be Used as a Surrogate Marker for the Human Endocrine Pancreas. *Diabetes* **63**, 3428-3437 (2014).

35. Freeby, M., Goland, R., Ichise, M., Maffei, A., Leibel, R. & Harris, P. VMAT2 quantitation by PET as a biomarker for beta-cell mass in health and disease. *Diabetes Obesity & Metabolism* **10**, 98-108 (2008).

36. Schafer, M.K., Hartwig, N.R., Kalmbach, N., Klietz, M., Anlauf, M., Eiden, L.E. et al. Species-specific vesicular monoamine transporter 2 (VMAT2) expression in mammalian pancreatic beta cells: implications for optimising radioligand-based human beta cell mass (BCM) imaging in animal models. *Diabetologia* **56**, 1047-1056 (2013).

37. Saisho, Y., Harris, P.E., Butler, A.E., Galasso, R., Gurlo, T., Rizza, R.A. et al. Relationship between pancreatic vesicular monoamine transporter 2 (VMAT2) and insulin expression in human pancreas. *J Mol Hist* **39**, 543-551 (2008).

38. Goswami, R., Ponde, D.E., Kung, M.P., Hou, C., Kilbourn, M.R. & Kung, H.F. Fluoroalkyl derivatives of dihydrotetrabenazine as positron emission tomography imaging agents targeting vesicular monoamine transporters. *Nucl Med Biol* **33**, 685-694 (2006).

39. Freeby, M.J., Kringas, P., Goland, R.S., Leibel, R.L., Maffei, A., Divgi, C. et al. Cross-sectional and Test-Retest Characterization of PET with [F-18]FP-(+)-DTBZ for beta Cell Mass Estimates in Diabetes. *Mol. Imaging Biol.* **18**, 292-301 (2016).

40. Normandin, M.D., Petersen, K.F., Ding, Y.S., Lin, S.F., Naik, S., Fowles, K. et al. In Vivo Imaging of Endogenous Pancreatic beta-Cell Mass in Healthy and Type 1 Diabetic Subjects Using F-18-Fluoropropyl-Dihydrotetrabenazine and PET. *J Nucl Med* **53**, 908-916 (2012).

41. Goland, R., Freeby, M., Parsey, R., Saisho, Y., Kumar, D., Simpson, N. et al. C-11-Dihydrotetrabenazine PET of the Pancreas in Subjects with Long-Standing Type 1 Diabetes and in Healthy Controls. *Journal of Nuclear Medicine* **50**, 382-389 (2009).

42. Runge, S., Thogersen, H., Madsen, K., Lau, J. & Rudolph, R. Crystal structure of the ligand-bound glucagon-like peptide-1 receptor extracellular domain. *J Biol Chem* **283**, 11340-11347 (2008).

43. Fosgerau, K. & Hoffmann, T. Peptide therapeutics: current status and future directions. *Drug Discov Today* **20**, 122-128 (2015).

44. Wu, Z. & Kandeel, F. Radionuclide probes for molecular imaging of pancreatic beta-cells. *Adv Drug Deliv Rev* **62**, 1125-1138 (2010).

45. Gao, H., Niu, G., Yang, M., Quan, Q., Ma, Y., Murage, E.N. et al. PET of Insulinoma Using 18F-FBEM-EM3106B, a New GLP-1 Analogue. *Molecular Pharmaceutics* (2011).

46. Furman, B.L. The development of Byetta (exenatide) from the venom of the Gila monster as an anti-diabetic agent. *Toxicon : official journal of the International Society on Toxinology* **59**, 464-471 (2012).

47. Eng, J., Kleinman, W.A., Singh, L., Singh, G. & Raufman, J.P. Isolation and Characterization of Exendin-4, an Exendin-3 Analog, from Heloderma-Suspectum

Venom - Further Evidence for an Exendin Receptor on Dispersed Acini from Guinea-Pig Pancreas. *J Biol Chem* **267**, 7402-7405 (1992).

48. Gotthardt, M., Lalyko, G., van Eerd-Vismale, J., Keil, B., Schurrat, T., Hower, M. et al. A new technique for in vivo imaging of specific GLP-1 binding sites: First results in small rodents. *Regul Pept* **137**, 162-167 (2006).

49. Mukai, E., Toyoda, K., Kimura, H., Kawashima, H., Fujimoto, H., Ueda, M. et al. GLP-1 receptor antagonist as a potential probe for pancreatic beta-cell imaging. *Biochem Biophys Res Commun* **389**, 523-526 (2009).

50. Toyoda, K., Kimura, H., Mukai, E., Ogawa, Y., Fujimoto, H., Ueda, M. et al. Non-Invasive PET Imaging of Pancreatic Islets Targeting Glucagon-Like Peptide-1 Receptors. *Diabetes* **59**, A431-A431 (2010).

51. Brom, M., Woliner-van der Weg, W., Joosten, L., Frielink, C., Bouckenooghe, T., Rijken, P. et al. Non-invasive quantification of the beta cell mass by SPECT with In-111-labelled exendin. *Diabetologia* **57**, 950-959 (2014).

52. Korner, M., Stockli, M., Waser, B. & Reubi, J.C. GLP-1 receptor expression in human tumors and human normal tissues: Potential for in vivo targeting. *J Nucl Med* **48**, 736-743 (2007).

53. Pyke, C., Heller, R.S., Kirk, R.K., Orskov, C., Reedtz-Runge, S., Kaastrup, P. et al. GLP-1 Receptor Localization in Monkey and Human Tissue: Novel Distribution Revealed With Extensively Validated Monoclonal Antibody. *Endocrinology* **155**, 1280-1290 (2014).

54. Waser, B., Blank, A., Karamitopoulou, E., Perren, A. & Reubi, J.C. Glucagon-like-peptide-1 receptor expression in normal and diseased human thyroid and pancreas. *Mod Pathol* **28**, 391-402 (2015).

55. Zhang, L. & Thurber, G.M. Quantitative Impact of Plasma Clearance and Down-regulation on GLP-1 Receptor Molecular Imaging. *Mol. Imaging Biol.* **18**, 79-89 (2016).

56. Willekens, S.M., Joosten, L., Boerman, O.C., Balhuizen, A., Eizirik, D.L., Gotthardt, M. et al. Strain Differences Determine the Suitability of Animal Models for Noninvasive In Vivo Beta Cell Mass Determination with Radiolabeled Exendin. *Molecular imaging and biology : MIB : the official publication of the Academy of Molecular Imaging* **18**, 705-714 (2016).

57. Pyke, C. & Knudsen, L.B. The glucagon-like peptide-1 receptor--or not? *Endocrinology* **154**, 4-8 (2013).

58. Hou, Y., Ernst, S.A., Heidenreich, K. & Williams, J.A. Glucagon-like peptide-1 receptor is present in pancreatic acinar cells and regulates amylase secretion through cAMP. *American journal of physiology. Gastrointestinal and liver physiology* **310**, G26-33 (2016).

59. Nalin, L., Selvaraju, R.K., Velikyan, I., Berglund, M., Andreasson, S., Wikstrand, A. et al. Positron emission tomography imaging of the glucagon-like peptide-1 receptor in healthy and streptozotocin-induced diabetic pigs. *Eur J Nucl Med Mol Imaging* **41**, 1800-1810 (2014).

60. Hanafusa, T., Miyagawa, J., Nakajima, H., Tomita, K., Kuwajima, M., Matsuzawa, Y. et al. The NOD mouse. *Diabetes Res Clin Pract* **24 Suppl**, S307-311 (1994).

61. Pozzilli, P., Signore, A., Williams, A.J. & Beales, P.E. NOD mouse colonies around the world--recent facts and figures. *Immunol. Today* **14**, 193-196 (1993).

62. King, A.J.F. The use of animal models in diabetes research. *Br J Pharmacol* **166**, 877-894 (2012).

63. Mordes, J.P., Bortell, R., Blankenhorn, E.P., Rossini, A.A. & Greiner, D.L. Rat models of type 1 diabetes: genetics, environment, and autoimmunity. *ILAR J* **45**, 278-291 (2004).

64. Brom, M., Oyen, W.J., Joosten, L., Gotthardt, M. & Boerman, O.C. 68Ga-labelled exendin-3, a new agent for the detection of insulinomas with PET. *Eur J Nucl Med Mol Imaging* **37**, 1345-1355 (2010).

65. Mikkola, K., Yim, C.B., Fagerholm, V., Ishizu, T., Elomaa, V.V., Rajander, J. et al. 64Cu- and 68Ga-labelled [Nle(14),Lys(40)(Ahx-NODAGA)NH2]-exendin-4 for pancreatic beta cell imaging in rats. *Molecular imaging and biology : MIB : the official publication of the Academy of Molecular Imaging* **16**, 255-263 (2014).

66. Bandara, N., Zheleznyak, A., Cherukuri, K., Griffith, D.A., Limberakis, C., Tess, D.A. et al. Evaluation of Cu-64 and Ga-68 Radiolabeled Glucagon-Like Peptide-1 Receptor Agonists as PET Tracers for Pancreatic beta cell Imaging. *Molecular imaging and biology : MIB : the official publication of the Academy of Molecular Imaging* **18**, 90-98 (2016).

67. Schoffelen, R., Sharkey, R.M., Goldenberg, D.M., Franssen, G., McBride, W.J., Rossi, E.A. et al. Pretargeted immuno-positron emission tomography imaging of carcinoembryonic antigen-expressing tumors with a bispecific antibody and a 68Ga- and 18F-labeled hapten peptide in mice with human tumor xenografts. *Mol Cancer Ther* **9**, 1019-1027 (2010).

68. Buschard, K., Brogren, C.H., Ropke, C. & Rygaard, J. Antigen Expression of the Pancreatic Beta-Cells Is Dependent on Their Functional-State, as Shown by a Specific, Bb Rat Monoclonal Autoantibody Ic2. *APMIS* **96**, 342-346 (1988).

69. Konidaris, C., Simonson, W., Michelsen, B. & Papadopoulos, G.K. Specific monoclonal antibodies against the surface of rat islet beta cells. *Cell Biol Int* **26**, 817-828 (2002).

70. Moore, A., Bonner-Weir, S. & Weissleder, R. Noninvasive in vivo measurement of beta-cell mass in mouse model of diabetes. *Diabetes* **50**, 2231-2236 (2001).

71. Hampe, C.S., Wallen, A.R., Schlosser, M., Ziegler, M. & Sweet, I.R. Quantitative evaluation of a monoclonal antibody and its fragment as potential markers for pancreatic beta cell mass. *Exp Clin Endocrinol Diabetes* **113**, 381-387 (2005).

72. Wilson, M.E., Scheel, D. & German, M.S. Gene expression cascades in pancreatic development. *Mech Dev* **120**, 65-80 (2003).

73. Signore, A., Chianelli, M., Parisella, M.G., Capriotti, G., Giacalone, P., Di Leve, G. et al. In vivo imaging of insulitis in autoimmune diabetes. *J Endocrinol Investig* **22**, 151-158 (1999).

74. Weissleder, R. & Ntziachristos, V. Shedding light onto live molecular targets. *Nature Medicine* **9**, 123-128 (2003).

75. Hara, M., Dizon, R.F., Glick, B.S., Lee, C.S., Kaestner, K.H., Piston, D.W. et al. Imaging pancreatic beta-cells in the intact pancreas. *Am J Physiol Endocrinol Metab* **290**, E1041-1047 (2006).

76. Reiner, T., Thurber, G., Gaglia, J., Vinegoni, C., Liew, C.W., Upadhyay, R. et al. Accurate measurement of pancreatic islet beta-cell mass using a second-generation fluorescent exendin-4 analog. *Proc Natl Acad Sci U S A* **108**, 12815-12820 (2011).

77. Hu, G., Henke, A., Karpowicz, R.J., Jr., Sonders, M.S., Farrimond, F., Edwards, R. et al. New fluorescent substrate enables quantitative and high-throughput examination of vesicular monoamine transporter 2 (VMAT2). *ACS Chem. Biol.* **8**, 1947-1954 (2013).

78. Maresca, K.P., Marquis, J.C., Hillier, S.M., Lu, G., Femia, F.J., Zimmerman, C.N. et al. Novel polar single amino acid chelates for technetium-99m tricarbonyl-based radiopharmaceuticals with enhanced renal clearance: application to octreotide. *Bioconjug Chem* **21**, 1032-1042 (2010).

79. Ray Banerjee, S., Pullambhatla, M., Foss, C.A., Falk, A., Byun, Y., Nimmagadda, S. et al. Effect of chelators on the pharmacokinetics of (99m)Tc-labeled imaging agents for the prostate-specific membrane antigen (PSMA). *J Med Chem* **56**, 6108-6121 (2013).

80. Schmitt, A., Bernhardt, P., Nilsson, O., Ahlman, H., Kolby, L. & Forssell-Aronsson, E. Differences in biodistribution between 99mTc-depreotide, 111In-DTPA-octreotide, and 177Lu-DOTA-Tyr3-octreotate in a small cell lung cancer animal model. *Cancer Biother Radiopharm* **20**, 231-236 (2005).

81. Neri, E., Cappelli, C., Boggi, U., Salvatori, L., Vistoli, F., Del Chiaro, M. et al. Multirow CT in the follow-up of pancreas transplantation. *Transplant Proc* **36**, 597-600 (2004).

82. Haldorsen, I.S., Raeder, H., Vesterhus, M., Molven, A. & Njolstad, P.R. The role of pancreatic imaging in monogenic diabetes mellitus. *Nat Rev Endocrinol* **8**, 148-159 (2012).

83. Lee, D.E., Koo, H., Sun, I.C., Ryu, J.H., Kim, K. & Kwon, I.C. Multifunctional nanoparticles for multimodal imaging and theragnosis. *Chem Soc Rev* **41**, 2656-2672 (2012).

84. Medarova, Z., Evgenov, N.V., Dai, G., Bonner-Weir, S. & Moore, A. In vivo multimodal imaging of transplanted pancreatic islets. *Nat. Protoc.* **1**, 429-435 (2006).

85. Vats, D., Wang, H., Esterhazy, D., Dikaiou, K., Danzer, C., Honer, M. et al. Multimodal imaging of pancreatic beta cells in vivo by targeting transmembrane protein 27 (TMEM27). *Diabetologia* **55**, 2407-2416 (2012).

86. Iozzo, P. Metabolic imaging in obesity: underlying mechanisms and consequences in the whole body. *Ann N Y Acad Sci* **1353**, 21-40 (2015).

87. Osterholt, M., Sen, S., Dilsizian, V. & Taegtmeyer, H. Targeted metabolic imaging to improve the management of heart disease. *JACC Cardiovasc Imaging* **5**, 214-226 (2012).

88. Morooka, M., Kubota, K., Kadowaki, H., Ito, K., Okazaki, O., Kashida, M. et al. 11C-methionine PET of acute myocardial infarction. *J Nucl Med* **50**, 1283-1287 (2009).

89. Williams, K.V., Price, J.C. & Kelley, D.E. Interactions of impaired glucose transport and phosphorylation in skeletal muscle insulin resistance: a dose-response assessment using positron emission tomography. *Diabetes* **50**, 2069-2079 (2001).

90. Krssak, M., Falk Petersen, K., Dresner, A., DiPietro, L., Vogel, S.M., Rothman, D.L. et al. Intramyocellular lipid concentrations are correlated with insulin sensitivity in humans: a 1H NMR spectroscopy study. *Diabetologia* **42**, 113-116 (1999).

91. Borra, R., Lautamaki, R., Parkkola, R., Komu, M., Sijens, P.E., Hallsten, K. et al. Inverse association between liver fat content and hepatic glucose uptake in patients with type 2 diabetes mellitus. *Metabolism: clinical and experimental* **57**, 1445-1451 (2008).

92. Brehm, A., Krssak, M., Schmid, A.I., Nowotny, P., Waldhausl, W. & Roden, M. Increased lipid availability impairs insulin-stimulated ATP synthesis in human skeletal muscle. *Diabetes* **55**, 136-140 (2006).

93. Keshari, K.R., Wilson, D.M., Sai, V., Bok, R., Jen, K.Y., Larson, P. et al. Noninvasive in vivo imaging of diabetes-induced renal oxidative stress and response to therapy using hyperpolarized 13C dehydroascorbate magnetic resonance. *Diabetes* **64**, 344-352 (2015).

94. McGavock, J.M., Lingvay, I., Zib, I., Tillery, T., Salas, N., Unger, R. et al. Cardiac steatosis in diabetes mellitus: a 1H-magnetic resonance spectroscopy study. *Circulation* **116**, 1170-1175 (2007).

95. Tichauer, K.M., Wang, Y., Pogue, B.W. & Liu, J.T. Quantitative in vivo cell-surface receptor imaging in oncology: kinetic modeling and paired-agent principles from nuclear medicine and optical imaging. *Phys Med Biol* **60**, R239-269 (2015).

96. Poulin, P., Chen, Y.H., Ding, X., Gould, S.E., Hop, C.E., Messick, K. et al. Prediction of drug distribution in subcutaneous xenografts of human tumor cell lines and healthy tissues in mouse: application of the tissue composition-based model to antineoplastic drugs. *J Pharm Sci* **104**, 1508-1521 (2015).

97. Thurber, G.M. & Weissleder, R. A systems approach for tumor pharmacokinetics. *PLoS One* **6**, e24696 (2011).

98. Sweiry, J.H. & Mann, G.E. Pancreatic Microvascular Permeability in Cerulein-Induced Acute-Pancreatitis. *Am J Physiol* **261**, G685-G692 (1991).

99. Hernandez, M. & Knox, S. Radiobiology of radioimmunotherapy: targeting CD20 B-cell antigen in non-Hodgkin's lymphoma. *Int. J. Radiat. Oncol. Biol. Phys.* **59**, 1274-1287 (2004).

100. Kaminski, M.S., Zasadny, K.R., Francis, I.R., Milik, A.W., Ross, C.W., Moon, S.D. et al. Radioimmunotherapy of B-Cell Lymphoma with I-131 Anti-B1 (Anti-Cd20) Antibody. *New England Journal of Medicine* **329**, 459-465 (1993).

101. Boswell, C.A., Mundo, E.E., Zhang, C., Stainton, S.L., Yu, S.F., Lacap, J.A. et al. Differential effects of predosing on tumor and tissue uptake of an 111In-labeled anti-TENB2 antibody-drug conjugate. *Journal of nuclear medicine : official publication, Society of Nuclear Medicine* **53**, 1454-1461 (2012).

102. Saisho, Y., Butler, A.E., Manesso, E., Elashoff, D., Rizza, R.A. & Butler, P.C. beta-Cell Mass and Turnover in Humans Effects of obesity and aging. *Diabetes Care* **36**, 111-117 (2013).

103. Di Bella, E.V.R., Kadrmas, D.J. & Christian, P.E. Feasibility of dual-isotope coincidence/single-photon imaging of the myocardium. *Journal of Nuclear Medicine* **42**, 944-950 (2001).

104. Mathijs, I., Xavier, C., Peleman, C., Caveliers, V., Brom, M., Gotthardt, M. et al. A standardized method for in vivo mouse pancreas imaging and semiquantitative beta cell mass measurement by dual isotope SPECT. *Molecular imaging and biology : MIB : the official publication of the Academy of Molecular Imaging* **17**, 58-66 (2015).

105. Clardy, S.M., Keliher, E.J., Mohan, J.F., Sebas, M., Benoist, C., Mathis, D. et al. Fluorescent exendin-4 derivatives for pancreatic beta-cell analysis. *Bioconjug Chem* **25**, 171-177 (2014).

106. Adelhorst, K., Hedegaard, B.B., Knudsen, L.B. & Kirk, O. Structure-activity studies of glucagon-like peptide-1. *J Biol Chem* **269**, 6275-6278 (1994).

107. Sletten, E.M. & Bertozzi, C.R. From mechanism to mouse: a tale of two bioorthogonal reactions. *Acc. Chem. Res.* **44**, 666-676 (2011).

108. Sletten, E.M. & Bertozzi, C.R. Bioorthogonal chemistry: fishing for selectivity in a sea of functionality. *Angew. Chem. Int. Ed. Engl.* **48**, 6974-6998 (2009).

109. van Hest, J.C.M., Kiick, K.L. & Tirrell, D.A. Efficient incorporation of unsaturated methionine analogues into proteins in vivo. *J Am Chem Soc* **122**, 1282-1288 (2000).

110. Wang, L., Xie, J. & Schultz, P.G. Expanding the genetic code. *Annu Rev Biophys Biomol Struct* **35**, 225-249 (2006).

111. Wiltschi, B., Merkel, L. & Budisa, N. Fine Tuning the N-Terminal Residue Excision with Methionine Analogues. *Chembiochem* **10**, 217-220 (2009).

112. Link, A.J., Vink, M.K.S. & Tirrell, D.A. Presentation and detection of azide functionality in bacterial cell surface proteins. *J Am Chem Soc* **126**, 10598-10602 (2004).

113. Gong, N., Ma, A.N., Zhang, L.J., Luo, X.S., Zhang, Y.H., Xu, M. et al. Site-specific PEGylation of exenatide analogues markedly improved their glucoregulatory activity. *Br J Pharmacol* **163**, 399-412 (2011).

114. Thurber, G.M., Schmidt, M.M. & Wittrup, K.D. Antibody tumor penetration: transport opposed by systemic and antigen-mediated clearance. *Adv Drug Deliv Rev* **60**, 1421-1434 (2008).

115. Thurber, G.M., Schmidt, M.M. & Wittrup, K.D. Factors determining antibody distribution in tumors. *Trends Pharmacol Sci* **29**, 57-61 (2008).

116. Kim, T.H., Jiang, H.H., Lee, S., Youn, Y.S., Park, C.W., Byun, Y. et al. Mono-PEGylated Dimeric Exendin-4 as High Receptor Binding and Long-Acting Conjugates for Type 2 Anti-Diabetes Therapeutics. *Bioconjugate chemistry* **22**, 625-632 (2011).

117. Kim, T.H., Jiang, H.H., Lim, S.M., Youn, Y.S., Choi, K.Y., Lee, S. et al. Site-Specific PEGylated Exendin-4 Modified with a High Molecular Weight Trimeric PEG Reduces Steric Hindrance and Increases Type 2 Antidiabetic Therapeutic Effects. *Bioconjugate chemistry* **23**, 2214-2220 (2012).

118. Vegt, E., Melis, M., Eek, A., de Visser, M., Brom, M., Oyen, W.J.G. et al. Renal uptake of different radiolabelled peptides is mediated by megalin: SPECT and biodistribution studies in megalin-deficient mice. *Eur. J. Nucl. Med. Mol. Imaging* **38**, 623-632 (2011).

119. Kirsi, M., Cheng-Bin, Y., Veronica, F., Tamiko, I., Viki-Veikko, E., Johan, R. et al. Cu-64- and Ga-68-Labelled [Nle(14),Lys(40)(Ahx-NODAGA)NH2]-Exendin-4 for Pancreatic Beta Cell Imaging in Rats. *Mol. Imaging Biol.* **16**, 255-263 (2014).

120. Christensen, E.I. & Willnow, T.E. Essential role of megalin in renal proximal tubule for vitamin homeostasis. *J Am Soc Nephrol* **10**, 2224-2236 (1999).

121. Azzarito, V., Long, K., Murphy, N.S. & Wilson, A.J. Inhibition of alpha-helix-mediated protein-protein interactions using designed molecules. *Nat Chem* **5**, 161-173 (2013).

122. Harrison, R.S., Shepherd, N.E., Hoang, H.N., Ruiz-Gomez, G., Hill, T.A., Driver, R.W. et al. Downsizing human, bacterial, and viral proteins to short water-stable alpha helices that maintain biological potency. *Proc Natl Acad Sci U S A* **107**, 11686-11691 (2010).

123. Neumann, H., Wang, K., Davis, L., Garcia-Alai, M. & Chin, J.W. Encoding multiple unnatural amino acids via evolution of a quadruplet-decoding ribosome. *Nature* **464**, 441-444 (2010).

124. Bird, G.H., Madani, N., Perry, A.F., Princiotto, A.M., Supko, J.G., He, X. et al. Hydrocarbon double-stapling remedies the proteolytic instability of a lengthy peptide therapeutic. *Proc Natl Acad Sci U S A* **107**, 14093-14098 (2010).

125. Craik, D.J., Fairlie, D.P., Liras, S. & Price, D. The future of peptide-based drugs. *Chem. Biol. Drug Des.* **81**, 136-147 (2013).

126. Felix, A.M., Heimer, E.P., Wang, C.T., Lambros, T.J., Fournier, A., Mowles, T.F. et al. Synthesis, biological activity and conformational analysis of cyclic GRF analogs. *Int. J. Pept. Protein Res.* **32**, 441-454 (1988).

127. Phelan, J.C., Skelton, N.J., Braisted, A.C. & McDowell, R.S. A general method for constraining short peptides to an alpha-helical conformation. *J Am Chem Soc* **119**, 455-460 (1997).

128. Willmann, J.K., van Bruggen, N., Dinkelborg, L.M. & Gambhir, S.S. Molecular imaging in drug development. *Nat. Rev. Drug Discov.* **7**, 591-607 (2008).

129. Jain, A. & Jain, S.K. PEGylation: an approach for drug delivery. A review. *Crit Rev Ther Drug Carrier Syst* **25**, 403-447 (2008).

130. Hauert, S., Berman, S., Nagpal, R. & Bhatia, S.N. A computational framework for identifying design guidelines to increase the penetration of targeted nanoparticles into tumors. *Nano Today* **8**, 566-576 (2013).

131. Wu, A.M. & Senter, P.D. Arming antibodies: prospects and challenges for immunoconjugates. *Nat Biotechnol* **23**, 1137-1146 (2005).

132. Stern, L.A., Case, B.A. & Hackel, B.J. Alternative Non-Antibody Protein Scaffolds for Molecular Imaging of Cancer. *Current Opinion in Chemical Engineering* **2**, 425-432 (2013).

133. Veronese, F.M. Peptide and protein PEGylation: a review of problems and solutions. *Biomaterials* **22**, 405-417 (2001).

134. Choi, H.S., Nasr, K., Alyabyev, S., Feith, D., Lee, J.H., Kim, S.H. et al. Synthesis and In Vivo Fate of Zwitterionic Near-Infrared Fluorophores. *Angew Chem Int Edit* **50**, 6258-6263 (2011).

135. Choi, H.S., Gibbs, S.L., Lee, J.H., Kim, S.H., Ashitate, Y., Liu, F.B. et al. Targeted zwitterionic near-infrared fluorophores for improved optical imaging. *Nat Biotechnol* **31**, 148-153 (2013).

136. Zhang, L., Navaratna, T., Liao, J. & Thurber, G.M. Dual-purpose linker for alpha helix stabilization and imaging agent conjugation to glucagon-like peptide-1 receptor ligands. *Bioconjug Chem* **26**, 329-337 (2015).

137. Lau, Y.H., de Andrade, P., Quah, S.T., Rossmann, M., Laraia, L., Skold, N. et al. Functionalised staple linkages for modulating the cellular activity of stapled peptides. *Chemical Science* **5**, 1804-1809 (2014).

138. Vaupel, P. Tumor microenvironmental physiology and its implications for radiation oncology. *Semin. Radiat. Oncol.* **14**, 198-206 (2004).

139. Tredan, O., Galmarini, C.M., Patel, K. & Tannock, I.F. Drug resistance and the solid tumor microenvironment. *J. Natl. Cancer Inst.* **99**, 1441-1454 (2007).

140. Mukai, T., Namba, S., Arano, Y., Ono, M., Fujioka, Y., Uehara, T. et al. Synthesis and evaluation of a monoreactive DOTA derivative for indium-111-based residualizing label to estimate protein pharmacokinetics. *J Pharm Pharmacol* **54**, 1073-1081 (2002).

141. Boswell, C.A., Bumbaca, D., Fielder, P.J. & Khawli, L.A. Compartmental Tissue Distribution of Antibody Therapeutics: Experimental Approaches and Interpretations. *AAPS J.* **14**, 612-618 (2012).

142. Boswell, C.A., Mundo, E.E., Zhang, C., Bumbaca, D., Valle, N.R., Kozak, K.R. et al. Impact of Drug Conjugation on Pharmacokinetics and Tissue Distribution of Anti-STEAP1 Antibody-Drug Conjugates in Rats. *Bioconjug Chem* **22**, 1994-2004 (2011).

143. Wall, D.A. & Maack, T. Endocytic Uptake, Transport, and Catabolism of Proteins by Epithelial-Cells. *Am J Physiol* **248**, C12-C20 (1985).

144. Shih, L.B., Thorpe, S.R., Griffiths, G.L., Diril, H., Ong, G.L., Hansen, H.J. et al. The Processing and Fate of Antibodies and Their Radiolabels Bound to the Surface of Tumor-Cells in-Vitro - a Comparison of 9 Radiolabels. *J Nucl Med* **35**, 899-908 (1994).

145. Press, O.W., Shan, D., Howell-Clark, J., Eary, J., Appelbaum, F.R., Matthews, D. et al. Comparative metabolism and retention of iodine-125, yttrium-90, and indium-111 radioimmunoconjugates by cancer cells. *Cancer Res* **56**, 2123-2129 (1996).

146. Ferl, G.Z., Kenanova, V., Wu, A.M. & DiStefano, J.J., 3rd A two-tiered physiologically based model for dually labeled single-chain Fv-Fc antibody fragments. *Mol Cancer Ther* **5**, 1550-1558 (2006).

147. Zhang, L. & Thurber, G.M. Quantitative Impact of Plasma Clearance and Down-regulation on GLP-1 Receptor Molecular Imaging. *Mol. Imaging Biol.* (2015).

148. Tolmachev, V., Tran, T.A., Rosik, D., Sjoberg, A., Abrahmsen, L. & Orlova, A. Tumor Targeting Using Affibody Molecules: Interplay of Affinity, Target Expression Level, and Binding Site Composition. *J Nucl Med* **53**, 953-960 (2012).

149. Monera, O.D., Sereda, T.J., Zhou, N.E., Kay, C.M. & Hodges, R.S. Relationship of sidechain hydrophobicity and alpha-helical propensity on the stability of the single-stranded amphipathic alpha-helix. *J Pept Sci* **1**, 319-329 (1995).

150. Orcutt, K.D., Nasr, K.A., Whitehead, D.G., Frangioni, J.V. & Wittrup, K.D. Biodistribution and clearance of small molecule hapten chelates for pretargeted radioimmunotherapy. *Mol. Imaging Biol.* **13**, 215-221 (2011).

151. Berezin, M.Y., Guo, K.V., Akers, W., Livingston, J., Solomon, M., Lee, H. et al. Rational Approach To Select Small Peptide Molecular Probes Labeled with Fluorescent Cyanine Dyes for in Vivo Optical Imaging. *Biochemistry* **50**, 2691-2700 (2011).

152. Dijkers, E.C.F., Kosterink, J.G.W., Rademaker, A.P., Perk, L.R., van Dongen, G.A.M.S., Bart, J. et al. Development and Characterization of Clinical-Grade Zr-89-Trastuzumab for HER2/neu ImmunoPET Imaging. *J Nucl Med* **50**, 974-981 (2009).

153. Aerts, H.J., Dubois, L., Hackeng, T.M., Straathof, R., Chiu, R.K., Lieuwes, N.G. et al. Development and evaluation of a cetuximab-based imaging probe to target EGFR and EGFRvIII. *Radiother Oncol* **83**, 326-332 (2007).

154. Yin, H., Slusky, J.S., Berger, B.W., Walters, R.S., Vilaire, G., Litvinov, R.I. et al. Computational design of peptides that target transmembrane helices. *Science* **315**, 1817-1822 (2007).

155. Vanhee, P., van der Sloot, A.M., Verschueren, E., Serrano, L., Rousseau, F. & Schymkowitz, J. Computational design of peptide ligands. *Trends Biotechnol* **29**, 231-239 (2011).

156. Larsen, A.C., Gillig, A., Shah, P., Sau, S.P., Fenton, K.E. & Chaput, J.C. General approach for characterizing in vitro selected peptides with protein binding affinity. *Anal Chem* **86**, 7219-7223 (2014).

157. Gladich, I., Rodriguez, A., Hong Enriquez, R.P., Guida, F., Berti, F. & Laio, A. Designing High-Affinity Peptides for Organic Molecules by Explicit Solvent Molecular Dynamics. *J. Phys. Chem. B* **119**, 12963-12969 (2015).

158. Reynolds, F. & Kelly, K.A. Techniques for molecular imaging probe design. *Mol Imaging* **10**, 407-419 (2011).

159. Tolmachev, V., Wallberg, H., Sandstrom, M., Hansson, M., Wennborg, A. & Orlova, A. Optimal specific radioactivity of anti-HER2 Affibody molecules enables discrimination between xenografts with high and low HER2 expression levels. *Eur. J. Nucl. Med. Mol. Imaging* **38**, 531-539 (2011).

160. Feldwisch, J., Tolmachev, V., Lendel, C., Herne, N., Sjoberg, A., Larsson, B. et al. Design of an Optimized Scaffold for Affibody Molecules. *J Mol Biol* **398**, 232-247 (2010).

161. Wallberg, H. & Orloval, A. Slow internalization of anti-HER2 synthetic Affibody monomer In-111-DOTA-Z(HER2 : 342-pep2): Implications for development of labeled tracers. *Cancer Biother. Radiopharm.* **23**, 435-442 (2008).

162. Orlova, A., Wullberg, H., Stone-Elander, S. & Tolmachev, V. On the Selection of a Tracer for PET Imaging of HER2-Expressing Tumors: Direct Comparison of a I-124-Labeled Affibody Molecule and Trastuzumab in a Murine Xenograft Model. *J Nucl Med* **50**, 417-425 (2009).

163. Werle, M. & Bernkop-Schnurch, A. Strategies to improve plasma half life time of peptide and protein drugs. *Amino Acids* **30**, 351-367 (2006).

164. Harris, J.M., Martin, N.E. & Modi, M. Pegylation - A novel process for modifying pharmacokinetics. *Clin Pharmacokinet* **40**, 539-551 (2001).

165. Berezin, M.Y., Guo, K., Akers, W., Livingston, J., Solomon, M., Lee, H. et al. Rational approach to select small peptide molecular probes labeled with fluorescent cyanine dyes for in vivo optical imaging. *Biochemistry* **50**, 2691-2700 (2011).

166. Buse, J.B., Rosenstock, J., Sesti, G., Schmidt, W.E., Montanya, E., Brett, J.H. et al. Liraglutide once a day versus exenatide twice a day for type 2 diabetes: a 26-week randomised, parallel-group, multinational, open-label trial (LEAD-6). *Lancet* **374**, 39-47 (2009).

167. Geng, S.B., Cheung, J.K., Narasimhan, C., Shameem, M. & Tessier, P.M. Improving Monoclonal Antibody Selection and Engineering using Measurements of Colloidal Protein Interactions. *J Pharm Sci* **103**, 3356-3363 (2014).

168. Hotzel, I., Theil, F.P., Bernstein, L.J., Prabhu, S., Deng, R., Quintana, L. et al. A strategy for risk mitigation of antibodies with fast clearance. *MAbs* **4**, 753-760 (2012).

169. Sharkey, R.M., Natale, A., Goldenberg, D.M. & Mattes, M.J. Rapid blood clearance of immunoglobulin G2a and immunoglobulin G2b in nude mice. *Cancer Res* **51**, 3102-3107 (1991).

170. De Leon-Rodriguez, L.M. & Kovacs, Z. The synthesis and chelation chemistry of DOTA-peptide conjugates. *Bioconjug Chem* **19**, 391-402 (2008).

171. Liu, G.Z. & Hnatowich, D.J. Labeling biomolecules with radiorhenium - A review of the bifunctional chelators. *Anticancer Agents Med. Chem.* **7**, 367-377 (2007).

172. Konikowski, T., Hayhie, T.P., Glenn, H.J. & Farr, L.E. Iodohippurate sodium 131-I (OIH) clearance in mice bioassay of radiopharmaceuticals. *Proc Soc Exp Biol Med* **137**, 1343-1351 (1971).

173. Hackel, B.J., Sathirachinda, A. & Gambhir, S.S. Designed hydrophilic and charge mutations of the fibronectin domain: towards tailored protein biodistribution. *Protein Eng Des Sel* **25**, 639-647 (2012).

174. Kelly, R.L., Sun, T., Jain, T., Caffry, I., Yu, Y., Cao, Y. et al. High throughput cross-interaction measures for human IgG1 antibodies correlate with clearance rates in mice. *MAbs* **7**, 770-777 (2015).

175. Hughes, L.D., Rawle, R.J. & Boxer, S.G. Choose Your Label Wisely: Water-Soluble Fluorophores Often Interact with Lipid Bilayers. *PLoS ONE* **9** (2014).

176. Zanetti-Domingues, L.C., Tynan, C.J., Rolfe, D.J., Clarke, D.T. & Martin-Fernandez, M. Hydrophobic Fluorescent Probes Introduce Artifacts into Single Molecule Tracking Experiments Due to Non-Specific Binding. *PLoS ONE* **8** (2013).

177. Hernandez, R., Czerwinski, A., Chakravarty, R., Graves, S.A., Yang, Y., England, C.G. et al. Evaluation of two novel (64)Cu-labeled RGD peptide radiotracers for enhanced PET imaging of tumor integrin alphavbeta3. *Eur. J. Nucl. Med. Mol. Imaging* **42**, 1859-1868 (2015).

178. Thurber, G.M., Figueiredo, J.L. & Weissleder, R. Multicolor fluorescent intravital live microscopy (FILM) for surgical tumor resection in a mouse xenograft model. *PLoS ONE* **4**, e8053 (2009).

179. Cilliers, C., Liao, J., Atangcho, L. & Thurber, G.M. Residualization Rates of Near-Infrared Dyes for the Rational Design of Molecular Imaging Agents. *Mol. Imaging Biol.* (2015).

180. Thurber, G.M. & Weissleder, R. A Systems Approach for Tumor Pharmacokinetics. *PLoS ONE* **6** (2011).

181. Bhatnagar, S., Deschenes, E., Liao, J.S., Cilliers, C. & Thurber, G.M. Multichannel Imaging to Quantify Four Classes of Pharmacokinetic Distribution in Tumors. *J Pharm Sci* **103**, 3276-3286 (2014).

182. Hillier, S.M., Maresca, K.P., Femia, F.J., Marquis, J.C., Foss, C.A., Nguyen, N. et al. Preclinical evaluation of novel glutamate-urea-lysine analogues that target prostate-specific membrane antigen as molecular imaging pharmaceuticals for prostate cancer. *Cancer Res* **69**, 6932-6940 (2009).

183. Hillier, S.M., Maresca, K.P., Lu, G., Merkin, R.D., Marquis, J.C., Zimmerman, C.N. et al. 99mTc-labeled small-molecule inhibitors of prostate-specific membrane antigen for molecular imaging of prostate cancer. *J Nucl Med* **54**, 1369-1376 (2013).

184. Artursson, P., Palm, K. & Luthman, K. Caco-2 monolayers in experimental and theoretical predictions of drug transport. *Adv Drug Delivery Rev* **64**, 280-289 (2012).

185. Ono, M., Arano, Y., Mukai, T., Saga, T., Fujioka, Y., Ogawa, K. et al. Control of radioactivity pharmacokinetics of 99mTc-HYNIC-labeled polypeptides derivatized with ternary ligand complexes. *Bioconjug Chem* **13**, 491-501 (2002).

186. Schmidt, M.M., Thurber, G.M. & Wittrup, K.D. Kinetics of anti-carcinoembryonic antigen antibody internalization: effects of affinity, bivalency, and stability. *Cancer Immunol. Immunother.* **57**, 1879-1890 (2008).

187. Zhang, L., Navaratna, T., Liao, J.S. & Thurber, G.M. Dual-Purpose Linker for Alpha Helix Stabilization and Imaging Agent Conjugation to Glucagon-Like Peptide-1 Receptor Ligands. *Bioconjug Chem* **26**, 329-337 (2015).

188. Landsman, M.L., Kwant, G., Mook, G.A. & Zijlstra, W.G. Light-absorbing properties, stability, and spectral stabilization of indocyanine green. *J Appl Physiol* **40**, 575-583 (1976).

189. Mordon, S., Devoisselle, J.M., Soulie-Begu, S. & Desmettre, T. Indocyanine green: physicochemical factors affecting its fluorescence in vivo. *Microvasc Res* **55**, 146-152 (1998).

190. Ott, P. Hepatic elimination of indocyanine green with special reference to distribution kinetics and the influence of plasma protein binding. *Pharmacol Toxicol* **83 Suppl 2**, 1-48 (1998).

191. Coleman, P.J., Brashear, K.M., Askew, B.C., Hutchinson, J.H., McVean, C.A., Duong, L.T. et al. Nonpeptide alpha(v)beta(3) antagonists. Part 11: Discovery and preclinical evaluation of potent alpha v beta(3) antagonists for the prevention and treatment of osteoporosis. *J Med Chem* **47**, 4829-4837 (2004).

192. Kossodo, S., Pickarski, M., Lin, S.A., Gleason, A., Gaspar, R., Buono, C. et al. Dual In Vivo Quantification of Integrin-targeted and Protease-activated Agents in Cancer Using Fluorescence Molecular Tomography (FMT). *Mol. Imaging Biol.* **12**, 488-499 (2010).

193. Dreher, M.R., Liu, W., Michelich, C.R., Dewhirst, M.W., Yuan, F. & Chilkoti, A. Tumor vascular permeability, accumulation, and penetration of macromolecular drug carriers. *J. Natl. Cancer Inst.* **98**, 335-344 (2006).

194. Yuan, F., Dellian, M., Fukumura, D., Leunig, M., Berk, D.A., Torchilin, V.P. et al. Vascular permeability in a human tumor xenograft: molecular size dependence and cutoff size. *Cancer Res* **55**, 3752-3756 (1995).

195. Graff, B.A., Bjornaes, I. & Rofstad, E.K. Macromolecule uptake in human melanoma xenografts. relationships to blood supply, vascular density, microvessel permeability and extracellular volume fraction. *Eur J Cancer* **36**, 1433-1440 (2000).

196. Yuan, F., Leunig, M., Huang, S.K., Berk, D.A., Papahadjopoulos, D. & Jain, R.K. Microvascular permeability and interstitial penetration of sterically stabilized (stealth) liposomes in a human tumor xenograft. *Cancer Res* **54**, 3352-3356 (1994).

197. Pallone, T.L., Work, J., Myers, R.L. & Jamison, R.L. Transport of sodium and urea in outer medullary descending vasa recta. *J. Clin. Invest.* **93**, 212-222 (1994).

198. Crone, C. The Permeability of Capillaries in Various Organs as Determined by Use of the 'Indicator Diffusion' Method. *Acta Physiol Scand* **58**, 292-305 (1963).

199. Turner, M.R. & Pallone, T.L. Hydraulic and diffusional permeabilities of isolated outer medullary descending vasa recta from the rat. *Am J Physiol* **272**, H392-400 (1997).

200. Michel, C.C. & Curry, F.E. Microvascular permeability. *Physiol Rev* **79**, 703-761 (1999).

201. Dedrick, R.L. & Flessner, M.F. Pharmacokinetic considerations on monoclonal antibodies. *Prog Clin Biol Res* **288**, 429-438 (1989).

202. Crone, C., D.G. Levitt Capillary permeability to small solutes. *Handbook of Physiology. The Cardiovascular System. Microcirculation.* (1984).

203. Paaske, W.P. Capillary permeability in skeletal muscle. *Acta Physiol Scand* **101**, 1-14 (1977).

204. Heyrovska, R. Effective Radii of Alkali-Halide Ions in Aqueous-Solutions, Crystals and in the Gas-Phase and the Interpretation of Stokes Radii. *Chem. Phys. Lett.* **163**, 207-211 (1989).

205. Schultz, S.G. & Solomon, A.K. Determination of the effective hydrodynamic radii of small molecules by viscometry. *J Gen Physiol* **44**, 1189-1199 (1961).

206. Sarin, H. Physiologic upper limits of pore size of different blood capillary types and another perspective on the dual pore theory of microvascular permeability. *J Angiogenes Res* **2**, 14 (2010).

207. Gerlowski, L.E. & Jain, R.K. Physiologically based pharmacokinetic modeling: principles and applications. *J Pharm Sci* **72**, 1103-1127 (1983).

208. Brown, R.P., Delp, M.D., Lindstedt, S.L., Rhomberg, L.R. & Beliles, R.P. Physiological parameter values for physiologically based pharmacokinetic models. *Toxicol Ind Health* **13**, 407-484 (1997).

209. Barbee, R.W., Perry, B.D., Re, R.N. & Murgo, J.P. Microsphere and dilution techniques for the determination of blood flows and volumes in conscious mice. *Am J Physiol* **263**, R728-733 (1992).

210. Vaupel, P., Kallinowski, F. & Okunieff, P. Blood flow, oxygen and nutrient supply, and metabolic microenvironment of human tumors: a review. *Cancer Res* **49**, 6449-6465 (1989).

211. Friedman, H.S., Lowery, R., Shaughnessy, E. & Scorza, J. The Effects of Ethanol on Pancreatic Blood-Flow in Awake and Anesthetized Dogs. *Proc Soc Exp Biol Med* **174**, 377-382 (1983).

212. Menger, M.D., Vajkoczy, P., Leiderer, R., Jager, S. & Messmer, K. Influence of experimental hyperglycemia on microvascular blood perfusion of pancreatic islet isografts. *J. Clin. Invest.* **90**, 1361-1369 (1992).

213. Kvietys, P.R., Perry, M.A. & Granger, D.N. Permeability of Pancreatic Capillaries to Small Molecules. *Am J Physiol* **245**, G519-G524 (1983).

214. Widmann, C., Dolci, W. & Thorens, B. Agonist-induced internalization and recycling of the glucagon-like peptide-1 receptor in transfected fibroblasts and in insulinomas. *The Biochemical Journal* **310 (Pt 1)**, 203-214 (1995).

215. Kirkpatrick, J.P., Brizel, D.M. & Dewhirst, M.W. A mathematical model of tumor oxygen and glucose mass transport and metabolism with complex reaction kinetics. *Radiat Res* **159**, 336-344 (2003).

216. Kaliss, N. & Pressman, D. Plasma and Blood Volumes of Mouse Organs, as Determined with Radioactive Iodoproteins. *Proc Soc Exp Biol Med* **75**, 16-20 (1950).

217. Baxter, L.T., Zhu, H., Mackensen, D.G. & Jain, R.K. Physiologically based pharmacokinetic model for specific and nonspecific monoclonal antibodies and fragments in normal tissues and human tumor xenografts in nude mice. *Cancer Res* **54**, 1517-1528 (1994).

218. Tolmachev, V., Nilsson, F.Y., Widstrom, C., Andersson, K., Rosik, D., Gedda, L. et al. 111In-benzyl-DTPA-ZHER2:342, an affibody-based conjugate for in vivo imaging of HER2 expression in malignant tumors. *J Nucl Med* **47**, 846-853 (2006).

219. Baish, J.W., Gazit, Y., Berk, D.A., Nozue, M., Baxter, L.T. & Jain, R.K. Role of tumor vascular architecture in nutrient and drug delivery: an invasion percolation-based network model. *Microvasc Res* **51**, 327-346 (1996).

220. Krol, A., Nagaraj, S., Dewhirst, M. & Yuan, F. Available volume fraction of macromolecules in tumor tissues. *FASEB J* **14**, A167-A167 (2000).

221. Thurber, G.M., Zajic, S.C. & Wittrup, K.D. Theoretic criteria for antibody penetration into solid tumors and micrometastases. *J Nucl Med* **48**, 995-999 (2007).

222. Stein, R., Goldenberg, D.M., Ong, G.L., Thorpe, S.R. & Mattes, M.J. Manipulation of blood clearance to optimize delivery of residualizing label-antibody conjugates to tumor cells in vivo. *J Nucl Med* **38**, 1392-1400 (1997).

223. Orlova, A., Magnusson, M., Eriksson, T.L.J., Nilsson, M., Larsson, B., Hoiden-Guthenherg, I. et al. Tumor Imaging using a picomolar affinity HER2 binding affibody molecule. *Cancer Res* **66**, 4339-4348 (2006).

224. Ahlgren, S., Wallberg, H., Tran, T.A., Widstrom, C., Hjertman, M., Abrahmsen, L. et al. Targeting of HER2-Expressing Tumors with a Site-Specifically Tc-99m-Labeled Recombinant Affibody Molecule, Z(HER2:2395), with C-Terminally Engineered Cysteine. *J Nucl Med* **50**, 781-789 (2009).

225. Honarvar, H., Strand, J., Perols, A., Orlova, A., Selvaraju, R.K., Karlstrom, A.E. et al. Position for Site-Specific Attachment of a DOTA Chelator to Synthetic Affibody Molecules Has a Different Influence on the Targeting Properties of Ga-68-Compared to In-111-Labeled Conjugates. *Mol. Imaging* **13** (2014).

226. Milenic, D.E., Garmestani, K., Brady, E.D., Albert, P.S., Ma, D.S., Abdulla, A. et al. Targeting of HER2 antigen for the treatment of disseminated peritoneal disease. *Clin. Cancer Res.* **10**, 7834-7841 (2004).

227. Reiner, T., Kohler, R.H., Liew, C.W., Hill, J.A., Gaglia, J., Kulkarni, R.N. et al. Near-infrared fluorescent probe for imaging of pancreatic beta cells. *Bioconjug Chem* **21**, 1362-1368 (2010).

228. Bandara, N., Zheleznyak, A., Cherukuri, K., Griffith, D.A., Limberakis, C., Tess, D.A. et al. Evaluation of Cu-64 and Ga-68 Radiolabeled Glucagon-Like Peptide-1 Receptor Agonists as PET Tracers for Pancreatic beta cell Imaging. *Mol. Imaging Biol.* (2015).

229. Goke, B. What are the Potential Benefits of Clinical beta-Cell Imaging in Diabetes Mellitus? *Curr Pharm Des* **16**, 1547-1549 (2010).

230. Holmberg, D. & Ahlgren, U. Imaging the pancreas: from ex vivo to non-invasive technology. *Diabetologia* **51**, 2148-2154 (2008).

231. Arifin, D.R. & Bulte, J.W.M. Imaging of pancreatic islet cells. *Diabetes-Metab Res Rev* **27**, 761-766 (2011).

232. Boerman, O.C. & Gotthardt, M. F-18-Labelled exendin to image GLP-1 receptor-expressing tissues: from niche to blockbuster? *Eur. J. Nucl. Med. Mol. Imaging* **39**, 461-462 (2012).

233. Foulis, A.K., Liddle, C.N., Farquharson, M.A., Richmond, J.A. & Weir, R.S. The histopathology of the pancreas in type 1 (insulin-dependent) diabetes mellitus: a 25-year review of deaths in patients under 20 years of age in the United Kingdom. *Diabetologia* **29**, 267-274 (1986).

234. Chmelova, H., Cohrs, C.M., Chouinard, J.A., Petzold, C., Kuhn, M., Chen, C. et al. Distinct roles of beta cell mass and function during type 1 diabetes onset and remission. *Diabetes* (2015).

235. Saudek, F., Brogren, C.H. & Manohar, S. Imaging the Beta-cell mass: why and how. *Review of Diabetic Studies* **5**, 6-12 (2008).

236. Steiner, D.J., Kim, A., Miller, K. & Hara, M. Pancreatic islet plasticity Interspecies comparison of islet architecture and composition. *Islets* **2**, 135-145 (2010).

237. McCulloch, D.K., Koerker, D.J., Kahn, S.E., Bonner-Weir, S. & Palmer, J.P. Correlations of in vivo beta-cell function tests with beta-cell mass and pancreatic insulin content in streptozocin-administered baboons. *Diabetes* **40**, 673-679 (1991).

238. Brom, M., Andraojc, K., Oyen, W.J.G., Boerman, O.C. & Gotthardt, M. Development of Radiotracers for the Determination of the Beta-Cell Mass In Vivo. *Curr Pharm Des* **16**, 1561-1567 (2010).

239. Goland, R., Freeby, M., Parsey, R., Saisho, Y., Kumar, D., Simpson, N. et al. 11C-dihydrotetrabenazine PET of the pancreas in subjects with long-standing type 1 diabetes and in healthy controls. *J Nucl Med* **50**, 382-389 (2009).

240. Gepts, W. & Lecompte, P.M. The pancreatic islets in diabetes. *Am J Med* **70**, 105-115 (1981).

241. Sweet, I.R., Cook, D.L., Lernmark, A., Greenbaum, C.J., Wallen, A.R., Marcum, E.S. et al. Systematic screening of potential beta-cell imaging agents. *Biochem Biophys Res Commun* **314**, 976-983 (2004).

242. Schneider, S., Feilen, P.J., Schreckenberger, M., Schwanstecher, M., Schwanstecher, C., Buchholz, H.G. et al. In vitro and in vivo evaluation of novel glibenclamide derivatives as imaging agents for the non-invasive assessment of the pancreatic islet cell mass in animals and humans. *Exp Clin Endocrinol Diabetes* **113**, 388-395 (2005).

243. Harris, P.E., Ferrara, C., Barba, P., Polito, T., Freeby, M. & Maffei, A. VMAT2 gene expression and function as it applies to imaging beta-cell mass. *Journal of Molecular Medicine-Jmm* **86**, 5-16 (2008).

244. Souza, F., Simpson, N., Raffo, A., Saxena, C., Maffei, A., Hardy, M. et al. Longitudinal noninvasive PET-based beta cell mass estimates in a spontaneous diabetes rat model. *J. Clin. Invest.* **116**, 1506-1513 (2006).

245. Basu, S. & Alavi, A. Partial volume correction of standardized uptake values and the dual time point in FDG-PET imaging: should these be routinely employed in assessing patients with cancer? *Eur. J. Nucl. Med. Mol. Imaging* **34**, 1527-1529 (2007).

246. Basu, S., Zaidi, H., Houseni, M., Bural, G., Udupa, J., Acton, P. et al. Novel quantitative techniques for assessing regional and global function and structure based on modern imaging modalities: implications for normal variation, aging and diseased states. *Semin Nucl Med* **37**, 223-239 (2007).

247. Chawluk, J.B., Alavi, A., Dann, R., Hurtig, H.I., Bais, S., Kushner, M.J. et al. Positron emission tomography in aging and dementia: effect of cerebral atrophy. *J Nucl Med* **28**, 431-437 (1987).

248. Hickeson, M., Yun, M.J., Matthies, A., Zhuang, H.M., Adam, L.E., Lacorte, L. et al. Use of a corrected standardized uptake value based on the lesion size on CT permits accurate characterization of lung nodules on FDG-PET. *Eur. J. Nucl. Med. Mol. Imaging* **29**, 1639-1647 (2002).

249. Srinivas, S.M., Dhurairaj, T., Basu, S., Bural, G., Surti, S. & Alavi, A. A recovery coefficient method for partial volume correction of PET images. *Ann. Nucl. Med.* **23**, 341-348 (2009).

250. Tanna, N.K., Kohn, M.I., Horwich, D.N., Jolles, P.R., Zimmerman, R.A., Alves, W.M. et al. Analysis of Brain and Cerebrospinal-Fluid Volumes with Mr Imaging - Impact on Pet Data Correction for Atrophy .2. Aging and Alzheimer Dementia. *Radiology* **178**, 123-130 (1991).

251. Brand, C., Abdel-Atti, D., Zhang, Y., Carlin, S., Clardy, S.M., Keliher, E.J. et al. In vivo imaging of GLP-1R with a targeted bimodal PET/fluorescence imaging agent. *Bioconjug Chem* **25**, 1323-1330 (2014).

252. Mikkola, K., Yim, C.B., Fagerholm, V., Ishizu, T., Elomaa, V.V., Rajander, J. et al. 64Cu- and 68Ga-labelled [Nle(14),Lys(40)(Ahx-NODAGA)NH2]-exendin-4 for pancreatic beta cell imaging in rats. *Mol. Imaging Biol.* **16**, 255-263 (2014).

253. Wicki, A., Wild, D., Storch, D., Seemayer, C., Gotthardt, M., Behe, M. et al. [Lys(40)(Ahx-DTPA-In-111)NH2]-Exendin-4 is a highly efficient radiotherapeutic for glucagon-like peptide-1 receptor-targeted therapy for insulinoma. *Clin. Cancer Res.* **13**, 3696-3705 (2007).

254. Wild, D., Wicki, A., Mansi, R., Behe, M., Keil, B., Bernhardt, P. et al. Exendin-4-Based Radiopharmaceuticals for Glucagonlike Peptide-1 Receptor PET/CT and SPECT/CT. *J Nucl Med* **51**, 1059-1067 (2010).

255. Goke, R., Fehmann, H.C., Linn, T., Schmidt, H., Krause, M., Eng, J. et al. Exendin-4 Is a High Potency Agonist and Truncated Exendin-(9-39)-Amide an Antagonist at the Glucagon-Like Peptide 1-(7-36)-Amide Receptor of Insulin-Secreting Beta-Cells. *J Biol Chem* **268**, 19650-19655 (1993).

256. Kolligs, F., Fehmann, H.C., Goke, R. & Goke, B. Reduction of the Incretin Effect in Rats by the Glucagon-Like Peptide-1 Receptor Antagonist Exendin(9-39) Amide. *Diabetes* **44**, 16-19 (1995).

257. Gotthardt, M., Fischer, M., Naeher, I., Holz, J.B., Jungclas, H., Fritsch, H.W. et al. Use of the incretin hormone glucagon-like peptide-1 (GLP-1) for the detection of insulinomas: initial experimental results. *Eur. J. Nucl. Med. Mol. Imaging* **29**, 597-606 (2002).

258. Kim, T.H., Jiang, H.H., Lee, S., Youn, Y.S., Park, C.W., Byun, Y. et al. Mono-PEGylated dimeric exendin-4 as high receptor binding and long-acting conjugates for type 2 anti-diabetes therapeutics. *Bioconjug Chem* **22**, 625-632 (2011).

259. Kim, T.H., Jiang, H.H., Lim, S.M., Youn, Y.S., Choi, K.Y., Lee, S. et al. Site-specific PEGylated Exendin-4 modified with a high molecular weight trimeric PEG reduces steric hindrance and increases type 2 antidiabetic therapeutic effects. *Bioconjug Chem* **23**, 2214-2220 (2012).

260. Fujita, H., Morii, T., Fujishima, H., Sato, T., Shimizu, T., Hosoba, M. et al. The protective roles of GLP-1R signaling in diabetic nephropathy: possible mechanism and therapeutic potential. *Kidney Int* **85**, 579-589 (2014).

261. Liu, W.J., Xie, S.H., Liu, Y.N., Kim, W., Jin, H.Y., Park, S.K. et al. Dipeptidyl Peptidase IV Inhibitor Attenuates Kidney Injury in Streptozotocin-Induced Diabetic Rats. *J Pharmacol Exp Ther* **340**, 248-255 (2012).

262. Thurber, G.M. & Dane Wittrup, K. A mechanistic compartmental model for total antibody uptake in tumors. *J Theor Biol* **314**, 57-68 (2012).

263. Nir, T., Melton, D.A. & Dor, Y. Recovery from diabetes in mice by beta cell regeneration. *J Clin Investig* **117**, 2553-2561 (2007).

264. Gier, B., Matveyenko, A.V., Kirakossian, D., Dawson, D., Dry, S.M. & Butler, P.C. Chronic GLP-1 receptor activation by exendin-4 induces expansion of pancreatic duct glands in rats and accelerates formation of dysplastic lesions and chronic pancreatitis in the Kras(G12D) mouse model. *Diabetes* **61**, 1250-1262 (2012).

265. Kaminski, M.S., Zasadny, K.R., Francis, I.R., Milik, A.W., Ross, C.W., Moon, S.D. et al. Radioimmunotherapy of B-Cell Lymphoma with [I-131] Anti-B1 (Anti-Cd20) Antibody. *N Engl J Med* **329**, 459-465 (1993).

266. Wang, Q.H., Chen, K., Liu, R., Zhao, F., Gupta, S., Zhang, N.N. et al. Novel GLP-1 Fusion Chimera as Potent Long Acting GLP-1 Receptor Agonist. *PLoS One* **5**, 9 (2010).

267. Levy, O.E., Jodka, C.M., Ren, S.S., Mamedova, L., Sharma, A., Samant, M. et al. Novel exenatide analogs with peptidic albumin binding domains: potent anti-diabetic agents with extended duration of action. *PLoS ONE* **9**, e87704 (2014).

268. Glaesner, W., Vick, A.M., Millican, R., Ellis, B., Tschang, S.H., Tian, Y. et al. Engineering and characterization of the long-acting glucagon-like peptide-1 analogue LY2189265, an Fc fusion protein. *Diabetes-Metab Res Rev* **26**, 287-296 (2010).

269. Reynolds, F. & Kelly, K.A. Techniques for Molecular Imaging Probe Design. *Mol. Imaging* **10**, 407-419 (2011).

270. Mattes, M.J., Griffiths, G., Diril, H., Goldenberg, D., Ong, G. & Shih, L. Processing of Antibody-Radioisotope Conjugates after Binding to the Surface of Tumor Cells. *Cancer* **73**, 787-793 (1994).

271. Wild, D., Behe, M., Wicki, A., Storch, D., Waser, B., Gotthardt, M. et al. [Lys(40) (Ahx-DTPA-In-111)NH2]exendin-4, a very promising ligand for glucagon-like peptide-1 (GLP-1) receptor targeting. *J Nucl Med* **47**, 2025-2033 (2006).

272. Roed, S.N., Wismann, P., Underwood, C.R., Kulahin, N., Iversen, H., Cappelen, K.A. et al. Real-time trafficking and signaling of the glucagon-like peptide-1 receptor. *Mol Cell Endocrinol* **382**, 938-949 (2014).

273. Bavec, A. & Licar, A. Functional Characterization of N-Terminally GFP-Tagged GLP-1 Receptor. *J Biomed Biotechnol* (2009).

274. Oliveira, S., Cohen, R., Walsum, M.S., van Dongen, G.A., Elias, S.G., van Diest, P.J. et al. A novel method to quantify IRDye800CW fluorescent antibody probes ex vivo in tissue distribution studies. *EJNMMI Res* **2**, 50 (2012).

275. Schmidt, M.M. & Wittrup, K.D. A modeling analysis of the effects of molecular size and binding affinity on tumor targeting. *Molecular Cancer Therapeutics* **8**, 2861 (2009).

276. Li, Z.B., Cai, W.B., Cao, Q.Z., Chen, K., Wu, Z.H., He, L.N. et al. 64Cu-Labeled "Tetrameric and octameric RGD peptides for small-animal PET of Tumor alpha(v)beta(3) integrin expression. *J Nucl Med* **48**, 1162-1171 (2007).

277. Cheng, Z., Wu, Y., Xiong, Z.M., Gambhir, S.S. & Chen, X.Y. Near-infrared fluorescent RGD peptides for optical imaging of integrin alpha(v)beta 3 expression in living mice. *Bioconjug Chem* **16**, 1433-1441 (2005).

278. Moore, S.J., Gephart, M.G.H., Bergen, J.M., Su, Y.R.S., Rayburn, H., Scott, M.P. et al. Engineered knottin peptide enables noninvasive optical imaging of intracranial medulloblastoma. *Proc Natl Acad Sci U S A* **110**, 14598-14603 (2013).

279. Hahnenkamp, A., Alsibai, W., Bremer, C. & Holtke, C. Optimizing the bioavailability of small molecular optical imaging probes by conjugation to an albumin affinity tag. *J Control Release* **186**, 32-40 (2014).

280. Pollaro, L., Raghunathan, S., Morales-Sanfrutos, J., Angelini, A., Kontos, S. & Heinis, C. Bicyclic Peptides Conjugated to an Albumin-Binding Tag Diffuse Efficiently into Solid Tumors. *Mol Cancer Ther* **14**, 151-161 (2015).

281. Samkoe, K.S., Tichauer, K.M., Gunn, J.R., Wells, W.A., Hasan, T. & Pogue, B.W. Quantitative In Vivo Immunohistochemistry of Epidermal Growth Factor Receptor Using a Receptor Concentration Imaging Approach. *Cancer Res* **74**, 7465-7474 (2014).

282. Kavishwar, A. & Moore, A. Sphingomyelin Patches on Pancreatic Beta-cells Are Indicative of Insulin Secretory Capacity. *J Histochem Cytochem* **61**, 910-919 (2013).

283. Gao, H.K., Niu, G., Yang, M., Quan, Q.M., Ma, Y., Murage, E.N. et al. PET of Insulinoma Using F-18-FBEM-EM3106B, a New GLP-1 Analogue. *Mol Pharm* **8**, 1775-1782 (2011).

284. Kirkpatrick, J.P., Brizel, D.M. & Dewhirst, M.W. A mathematical model of tumor oxygen and glucose mass transport and metabolism with complex reaction kinetics. *Radiation Research* **159**, 336-344 (2003).

285. Kaliss, N. & Pressman, D. Plasma and blood volumes of mouse organs as determined with radioactive iodoproteins. *Proceedings of the Society for Experimental Biology and Medicine* **75**, 16-20 (1950).

286. Green, E. Biology of the Laboratory Mouse. (Dover Publications & The Jackson Laboratory, New York; 1966).

287. Keliher, E.J., Reiner, T., Thurber, G.M., Upadhyay, R. & Weissleder, R. Efficient 18F-Labeling of Synthetic Exendin-4 Analogues for Imaging Beta Cells. *ChemistryOpen*, n/a-n/a (2012).

288. Weissleder, R. & Pittet, M.J. Imaging in the era of molecular oncology. *Nature* **452**, 580-589 (2008).

289. Zhao, B.S., Schwartz, L.H. & Larson, S.M. Imaging Surrogates of Tumor Response to Therapy: Anatomic and Functional Biomarkers. *Journal of Nuclear Medicine* **50**, 239-249 (2009).

290. Akers, W.J., Zhang, Z.R., Berezin, M., Ye, Y.P., Agee, A., Guo, K. et al. Targeting of alpha(v)beta(3)-integrins expressed on tumor tissue and neovasculature using fluorescent small molecules and nanoparticles. *Nanomedicine* **5**, 715-726 (2010).

291. Kimura, R.H., Cheng, Z., Gambhir, S.S. & Cochran, J.R. Engineered Knottin Peptides: A New Class of Agents for Imaging Integrin Expression in Living Subjects. *Cancer Research* **69**, 2435-2442 (2009).

292. Walensky, L.D., Kung, A.L., Escher, I., Malia, T.J., Barbuto, S., Wright, R.D. et al. Activation of apoptosis in vivo by a hydrocarbon-stapled BH3 helix. *Science* **305**, 1466-1470 (2004).

293. Bird, G.H., Madani, N., Perry, A.F., Princiotto, A.M., Supko, J.G., He, X.Y. et al. Hydrocarbon double-stapling remedies the proteolytic instability of a lengthy peptide therapeutic. *Proceedings of the National Academy of Sciences of the United States of America* **107**, 14093-14098 (2010).

294. Sia, S.K., Carr, P.A., Cochran, A.G., Malashkevich, V.N. & Kim, P.S. Short constrained peptides that inhibit HIV-1 entry. *Proc Natl Acad Sci U S A* **99**, 14664-14669 (2002).

295. Schafmeister, C.E., Po, J. & Verdine, G.L. An all-hydrocarbon cross-linking system for enhancing the helicity and metabolic stability of peptides. *J Am Chem Soc* **122**, 5891-5892 (2000).

296. Neumann, H., Wang, K.H., Davis, L., Garcia-Alai, M. & Chin, J.W. Encoding multiple unnatural amino acids via evolution of a quadruplet-decoding ribosome. *Nature* **464**, 441-444 (2010).

297. Torres, O., Yuksel, D., Bernardina, M., Kumar, K. & Bong, D. Peptide tertiary structure nucleation by side-chain crosslinking with metal complexation and double "click" cycloaddition. *Chembiochem* **9**, 1701-1705 (2008).

298. Yu, C.X. & Taylor, J.W. Synthesis and study of peptides with semirigid i and i+7 side-chain bridges designed for alpha-helix stabilization. *Bioorg Med Chem* **7**, 161-175 (1999).

299. Galande, A.K., Bramlett, K.S., Trent, J.O., Burris, T.P., Wittliff, J.L. & Spatola, A.F. Potent inhibitors of LXXLL-based protein-protein interactions. *Chembiochem* **6**, 1991-1998 (2005).

300. Jackson, D.Y., King, D.S., Chmielewski, J., Singh, S. & Schultz, P.G. General-Approach to the Synthesis of Short Alpha-Helical Peptides. *J Am Chem Soc* **113**, 9391-9392 (1991).

301. Bird, G.H., Gavathiotis, E., LaBelle, J.L., Katz, S.G. & Walensky, L.D. Distinct BimBH3 (BimSAHB) stapled peptides for structural and cellular studies. *ACS Chem Biol* **9**, 831-837 (2014).

302. Okamoto, T., Segal, D., Zobel, K., Fedorova, A., Yang, H., Fairbrother, W.J. et al. Further insights into the effects of pre-organizing the BimBH3 helix. *ACS Chem Biol* **9**, 838-839 (2014).

303. Okamoto, T., Zobel, K., Fedorova, A., Quan, C., Yang, H., Fairbrother, W.J. et al. Stabilizing the pro-apoptotic BimBH3 helix (BimSAHB) does not necessarily enhance affinity or biological activity. *ACS Chem Biol* **8**, 297-302 (2013).

304. Giordanetto, F., Revell, J.D., Knerr, L., Hostettler, M., Paunovic, A., Priest, C. et al. Stapled Vasoactive Intestinal Peptide (VIP) Derivatives Improve VPAC2 Agonism and Glucose-Dependent Insulin Secretion. *ACS medicinal chemistry letters* **4**, 1163-1168 (2013).

305. Reiner, T., Thurber, G., Gaglia, J., Vinegoni, C., Liew, C.W., Upadhyay, R. et al. Accurate measurement of pancreatic islet beta-cell mass using a second-generation fluorescent exendin-4 analog. *Proceedings of the National Academy of Sciences of the United States of America* **108**, 12815-12820 (2011).

306. Brand, C., Abdel-Atti, D., Zhang, Y., Carlin, S., Clardy, S.M., Keliher, E.J. et al. In vivo imaging of GLP-1R with a targeted bimodal PET/fluorescence imaging agent. *Bioconjug Chem* **25**, 1323-1330 (2014).

307. Underwood, C.R., Garibay, P., Knudsen, L.B., Hastrup, S., Peters, G.H., Rudolph, R. et al. Crystal Structure of Glucagon-like Peptide-1 in Complex with the Extracellular

Domain of the Glucagon-like Peptide-1 Receptor. *Journal of Biological Chemistry* **285**, 723-730 (2010).

308. Andersen, N.H., Brodsky, Y., Neidigh, J.W. & Prickett, K.S. Medium-dependence of the secondary structure of exendin-4 and glucagon-like-peptide-1. *Bioorganic & Medicinal Chemistry* **10**, 79-85 (2002).

309. Adelhorst, K., Hedegaard, B.B., Knudsen, L.B. & Kirk, O. Structure-Activity Studies of Glucagon-Like Peptide-1. *Journal of Biological Chemistry* **269**, 6275-6278 (1994).

310. Parker, J.C., Andrews, K.M., Rescek, D.M., Massefski, W., Jr., Andrews, G.C., Contillo, L.G. et al. Structure-function analysis of a series of glucagon-like peptide-1 analogs. *The journal of peptide research : official journal of the American Peptide Society* **52**, 398-409 (1998).

311. James, M.L. & Gambhir, S.S. A molecular imaging primer: modalities, imaging agents, and applications. *Physiol Rev* **92**, 897-965 (2012).

312. Lee, S., Xie, J. & Chen, X. Peptide-based probes for targeted molecular imaging. *Biochemistry* **49**, 1364-1376 (2010).

313. Jacobsen, O., Maekawa, H., Ge, N.H., Gorbitz, C.H., Rongved, P., Ottersen, O.P. et al. Stapling of a 3(10)-Helix with Click Chemistry. *J. Org. Chem.* **76**, 1228-1238 (2011).

314. Scrima, M., Le Chevalier-Isaad, A., Rovero, P., Papini, A.M., Chorev, M. & D'Ursi, A.M. Cu-I-Catalyzed Azide-Alkyne Intramolecular i-to-(i+4) Side-Chain-to-Side-Chain Cyclization Promotes the Formation of Helix-Like Secondary Structures. *European Journal of Organic Chemistry*, 446-457 (2010).

315. Johnson, J.A., Lu, Y.Y., Van Deventer, J.A. & Tirrell, D.A. Residue-specific incorporation of non-canonical amino acids into proteins: recent developments and applications. *Curr. Opin. Chem. Biol.* **14**, 774-780 (2010).

316. Muppidi, A., Wang, Z.Y., Li, X.L., Chen, J.D. & Lin, Q. Achieving cell penetration with distance-matching cysteine cross-linkers: a facile route to cell-permeable peptide dual inhibitors of Mdm2/Mdmx. *Chemical Communications* **47**, 9396-9398 (2011).

317. Ahren, B. & Schmitz, O. GLP-1 receptor agonists and DPP-4 inhibitors in the treatment of type 2 diabetes. *Hormone and Metabolic Research* **36**, 867-876 (2004).

318. Lau, Y.H., de Andrade, P., McKenzie, G.J., Venkitaraman, A.R. & Spring, D.R. Linear Aliphatic Dialkynes as Alternative Linkers for Double-Click Stapling of p53-Derived Peptides. *Chembiochem* (2014).

319. Li, H., Aneja, R. & Chaiken, I. Click chemistry in peptide-based drug design. *Molecules* **18**, 9797-9817 (2013).

320. White, C.J. & Yudin, A.K. Contemporary strategies for peptide macrocyclization. *Nat. Chem.* **3**, 509-524 (2011).

321. Kaspar, A.A. & Reichert, J.M. Future directions for peptide therapeutics development. *Drug Discov Today* **18**, 807-817 (2013).

322. Goldberg, M. & Gomez-Orellana, I. Challenges for the oral delivery of macromolecules. *Nat. Rev. Drug Discov.* **2**, 289-295 (2003).

323. Park, J.W., Kim, S.K., Al-Hilal, T.A., Jeon, O.C., Moon, H.T. & Byun, Y. Strategies for Oral Delivery of Macromolecule Drugs. *Biotechnol Bioprocess Eng* **15**, 66-75 (2010).

324. Schweighofer, C.D. & Wendtner, C.M. First-line treatment of chronic lymphocytic leukemia: role of alemtuzumab. *Onco Targets Ther* **3**, 53-67 (2010).

325. Launay-Vacher, V. An appraisal of subcutaneous trastuzumab: a new formulation meeting clinical needs. *Cancer Chemother Pharmacol* **72**, 1361-1367 (2013).

326. McDonald, T.A., Zepeda, M.L., Tomlinson, M.J., Bee, W.H. & Ivens, I.A. Subcutaneous administration of biotherapeutics: current experience in animal models. *Curr. Opin. Mol. Ther.* **12**, 461-470 (2010).

327. Richter, W.F. & Jacobsen, B. Subcutaneous absorption of biotherapeutics: knowns and unknowns. *Drug Metab Dispos* **42**, 1881-1889 (2014).

328. Asahara, S., Takeda, K., Yamao, K., Maguchi, H. & Yamaue, H. Phase I/II clinical trial using HLA-A24-restricted peptide vaccine derived from KIF20A for patients with advanced pancreatic cancer. *J Transl Med* **11**, 291 (2013).

329. Richter, W.F., Bhansali, S.G. & Morris, M.E. Mechanistic determinants of biotherapeutics absorption following SC administration. *AAPS J.* **14**, 559-570 (2012).

330. Hale, G., Rebello, P., Brettman, L.R., Fegan, C., Kennedy, B., Kimby, E. et al. Blood concentrations of alemtuzumab and antiglobulin responses in patients with chronic lymphocytic leukemia following intravenous or subcutaneous routes of administration. *Blood* **104**, 948-955 (2004).

331. Mager, D.E. & Jusko, W.J. Receptor-mediated pharmacokinetic/pharmacodynamic model of interferon-beta 1a in humans. *Pharm. Res.* **19**, 1537-1543 (2002).

332. Clodfelter, D.K., Pekar, A.H., Rebhun, D.M., Destrampe, K.A., Havel, H.A., Myers, S.R. et al. Effects of non-covalent self-association on the subcutaneous absorption of a therapeutic peptide. *Pharm. Res.* **15**, 254-262 (1998).

333. Reddy, S.T., Berk, D.A., Jain, R.K. & Swartz, M.A. A sensitive in vivo model for quantifying interstitial convective transport of injected macromolecules and nanoparticles. *J Appl Physiol* **101**, 1162-1169 (2006).

334. Kagan, L., Turner, M.R., Balu-Iyer, S.V. & Mager, D.E. Subcutaneous absorption of monoclonal antibodies: role of dose, site of injection, and injection volume on rituximab pharmacokinetics in rats. *Pharm. Res.* **29**, 490-499 (2012).

335. Tang, L., Persky, A.M., Hochhaus, G. & Meibohm, B. Pharmacokinetic aspects of biotechnology products. *J Pharm Sci* **93**, 2184-2204 (2004).

336. Porter, C.J. & Charman, S.A. Lymphatic transport of proteins after subcutaneous administration. *J Pharm Sci* **89**, 297-310 (2000).

337. Porter, C.J., Edwards, G.A. & Charman, S.A. Lymphatic transport of proteins after s.c. injection: implications of animal model selection. *Adv Drug Deliv Rev* **50**, 157-171 (2001).

338. McLennan, D.N., Porter, C.J., Edwards, G.A., Heatherington, A.C., Martin, S.W. & Charman, S.A. The absorption of darbepoetin alfa occurs predominantly via the lymphatics following subcutaneous administration to sheep. *Pharm. Res.* **23**, 2060-2066 (2006).

339. Deng, R., Meng, Y.G., Hoyte, K., Lutman, J., Lu, Y.M., Iyer, S. et al. Subcutaneous bioavailability of therapeutic antibodies as a function of FcRn binding affinity in mice. *Mabs* **4**, 101-109 (2012).

340. Theil, F.P. & Zhou, H. ADME and Translational Pharmacokinetics/Pharmacodynamics of Therapeutic Proteins. (2016).

341. Vugmeyster, Y., Xu, X., Theil, F.P., Khawli, L.A. & Leach, M.W. Pharmacokinetics and toxicology of therapeutic proteins: Advances and challenges. *World J Biol Chem* **3**, 73-92 (2012).

342. Takeyama, M., Ishida, T., Kokubu, N., Komada, F., Iwakawa, S., Okumura, K. et al. Enhanced bioavailability of subcutaneously injected insulin by pretreatment with ointment containing protease inhibitors. *Pharm. Res.* **8**, 60-64 (1991).

343. Wang, W.R., Chen, N., Shen, X.L., Cunningham, P., Fauty, S., Michel, K. et al. Lymphatic Transport and Catabolism of Therapeutic Proteins after Subcutaneous Administration to Rats and Dogs. *Drug Metab Dispos* **40**, 952-962 (2012).

344. Berger, M., Halban, P.A., Girardier, L., Seydoux, J., Offord, R.E. & Renold, A.E. Absorption Kinetics of Subcutaneously Injected Insulin - Evidence for Degradation at the Injection Site. *Diabetologia* **17**, 97-99 (1979).

345. Yang, P.Y., Zou, H., Chao, E., Sherwood, L., Nunez, V., Keeney, M. et al. Engineering a long-acting, potent GLP-1 analog for microstructure-based transdermal delivery. *Proc Natl Acad Sci U S A* (2016).

346. Lau, Y.H., Wu, Y.T., de Andrade, P., Galloway, W.R.J.D. & Spring, D.R. A two-component 'double-click' approach to peptide stapling. *Nat. Protoc.* **10**, 585-594 (2015).

347. Lau, Y.H., de Andrade, P., Wu, Y. & Spring, D.R. Peptide stapling techniques based on different macrocyclisation chemistries. *Chem Soc Rev* **44**, 91-102 (2015).

348. Lau, J., Bloch, P., Schaffer, L., Pettersson, I., Spetzler, J., Kofoed, J. et al. Discovery of the Once-Weekly Glucagon-Like Peptide-1 (GLP-1) Analogue Semaglutide. *J Med Chem* **58**, 7370-7380 (2015).

349. Madsen, K., Knudsen, L.B., Agersoe, H., Nielsen, P.F., Thogersen, H., Wilken, M. et al. Structure-activity and protraction relationship of long-acting glucagon-like peptide-1 derivatives: importance of fatty acid length, polarity, and bulkiness. *J Med Chem* **50**, 6126-6132 (2007).

350. Dennis, M.S., Jin, H.K., Dugger, D., Yang, R.H., McFarland, L., Ogasawara, A. et al. Imaging tumors with an albumin-binding Fab, a novel tumor-targeting agent. **67**, 254-261 (2007).

351. Nguyen, A., Reyes, A.E., Zhang, M., McDonald, P., Wong, W.L.T., Damico, L.A. et al. The pharmacokinetics of an albumin-binding Fab (AB.Fab) can be modulated as a function of affinity for albumin. *Protein Engineering Design & Selection* **19**, 291-297 (2006).

352. Zhang, L., Bhatnagar, S., Deschenes, E. & Thurber, G.M. Mechanistic and quantitative insight into cell surface targeted molecular imaging agent design. *Scientific reports*, In Press (2016).

353. Wurth, C., Grabolle, M., Pauli, J., Spieles, M. & Resch-Genger, U. Relative and absolute determination of fluorescence quantum yields of transparent samples. *Nat Protoc* **8**, 1535-1550 (2013).

354. Parkes, D., Jodka, C., Smith, P., Nayak, S., Rinehart, L., Gingerich, R. et al. Pharmacokinetic actions of exendin-4 in the rat: Comparison with glucagon-like peptide-1. *Drug Dev Res* **53**, 260-267 (2001).

355. Gao, W. & Jusko, W.J. Pharmacokinetic and pharmacodynamic modeling of exendin-4 in type 2 diabetic Goto-Kakizaki rats. *J Pharmacol Exp Ther* **336**, 881-890 (2011).

356. Egan, J.M., Meneilly, G.S. & Elahi, D. Effects of 1-mo bolus subcutaneous administration of exendin-4 in type 2 diabetes. *Am J Physiol Endocrinol Metab* **284**, E1072-1079 (2003).

357. Lau, Y.H., de Andrade, P., Skold, N., McKenzie, G.J., Venkitaraman, A.R., Verma, C. et al. Investigating peptide sequence variations for 'double-click' stapled p53 peptides. *Org. Biomol. Chem.* **12**, 4074-4077 (2014).

358. Tyndall, J.D.A., Nall, T. & Fairlie, D.P. Proteases universally recognize beta strands in their active sites. *Chem. Rev.* **105**, 973-999 (2005).

359. de Veer, S.J., Furio, L., Harris, J.M. & Hovnanian, A. Proteases: common culprits in human skin disorders. *Trends Mol Med* **20**, 166-178 (2014).

360. Karande, P. & Mitragotri, S. Transcutaneous immunization: an overview of advantages, disease targets, vaccines, and delivery technologies. *Annual review of chemical and biomolecular engineering* **1**, 175-201 (2010).

361. Decristoforo, C. & Mather, S.J. 99m-Technetium-labelled peptide-HYNIC conjugates: effects of lipophilicity and stability on biodistribution. *Nucl Med Biol* **26**, 389-396 (1999).

362. Chen, B.L., Arakawa, T., Morris, C.F., Kenney, W.C., Wells, C.M. & Pitt, C.G. Aggregation pathway of recombinant human keratinocyte growth factor and its stabilization. *Pharm. Res.* **11**, 1581-1587 (1994).

363. Manning, M.C., Matsuura, J.E., Kendrick, B.S., Meyer, J.D., Dormish, J.J., Vrkljan, M. et al. Approaches for increasing the solution stability of proteins. *Biotechnol Bioeng* **48**, 506-512 (1995).

364. Serrano, L., Bycroft, M. & Fersht, A.R. Aromatic Aromatic Interactions and Protein Stability - Investigation by Double-Mutant Cycles. *J Mol Biol* **218**, 465-475 (1991).

365. Butterfield, S.M., Patel, P.R. & Waters, M.L. Contribution of aromatic interactions to alpha-helix stability. *J Am Chem Soc* **124**, 9751-9755 (2002).

366. Ward, B.P., Ottaway, N.L., Perez-Tilve, D., Ma, D., Gelfanov, V.M., Tschop, M.H. et al. Peptide lipidation stabilizes structure to enhance biological function. *Molecular metabolism* **2**, 468-479 (2013).

367. Tyndall, J.D. & Fairlie, D.P. Conformational homogeneity in molecular recognition by proteolytic enzymes. *J Mol Recognit* **12**, 363-370 (1999).

368. Li, X.G., Li, L., Zhou, X., Chen, Y., Ren, Y.P., Zhou, T.Y. et al. Pharmacokinetic/pharmacodynamic studies on exenatide in diabetic rats. *Acta Pharmacol Sin* **33**, 1379-1386 (2012).

369. Buse, J.B., Rosenstock, J., Sesti, G., Schmidt, W.E., Montanya, E., Brett, J.H. et al. Liraglutide once a day versus exenatide twice a day for type 2 diabetes: a 26-week randomised, parallel-group, multinational, open-label trial (LEAD-6). *Lancet* **374**, 39-47 (2009).

370. Kolterman, O.G., Kim, D.D., Shen, L., Ruggles, J.A., Nielsen, L.L., Fineman, M.S. et al. Pharmacokinetics, pharmacodynamics, and safety of exenatide in patients with type 2 diabetes mellitus. *Am. J. Health. Syst. Pharm.* **62**, 173-181 (2005).

371. Wang, M., Defranco, D., Wright, K., Quazi, S., Chen, J., Spencer-Pierce, J. et al. Decreased Subcutaneous Bioavailability of an Oxyntomodulin Analog in a Controlled

Release Formulation could be Caused by Skin Metabolism in Rats. *Journal of Bioequivalence & Bioavailability* **4**, 69-77 (2012).

372. Andersen, N.H., Brodsky, Y., Neidigh, J.W. & Prickett, K.S. Medium-dependence of the secondary structure of exendin-4 and glucagon-like-peptide-1. *Bioorg Med Chem* **10**, 79-85 (2002).